HARVARD UNIVERSITY
Graduate School of Arts and Sciences

DISSERTATION ACCEPTANCE CERTIFICATE

The undersigned, appointed by the

Department of Physics

have examined a dissertation entitled

Optimizing Solid-State Spins in Diamond for Nano- to Millimeter-Scale Magnetic Field Sensing

presented by Erik Bauch

candidate for the degree of Doctor of Philosophy and hereby certify that it is worthy of acceptance.

Signature _____

Typed name: Professor Ronald Walsworth, Chair

Signature _____

Typed name: Professor Amir Yacoby

Signature _____

Typed name: Professor Markus Greiner

Date: January 8, 2018

Optimizing Solid-State Spins in Diamond for Nano- to Millimeter-Scale Magnetic Field Sensing

A thesis presented
by

Erik Bauch

to
The Physics Department
in partial fulfillment of the requirements
for the degree of
Doctor of Philosophy
in the subject of

Physics

Harvard University
Cambridge, Massachusetts
January 2018

Thesis advisor

Ronald L. Walsworth

Author

Erik Bauch

Optimizing Solid-State Spins in Diamond for Nano- to Millimeter-Scale Magnetic Field Sensing

Abstract

Solid-state defect impurities have established themselves as an impactful research platform providing novel pathways to a broad spectrum of problems in physics, biology, chemistry, geology, medicine and materials science. In this dissertation, we present several achievements to improve the sensing capabilities of nitrogen-vacancy (NV) center spins in diamond. The NV defect stands out among impurities currently being investigated. Its prominence in the field is facilitated by its exceptionally long ground-state spin lifetimes at room temperature, an optical spin polarization and readout mechanism, and its capability to be manipulated via coherent microwaves and static magnetic fields.

In the introductory chapter, we review the fundamental aspects of NV research, which encompasses modern applications, processing techniques, and primary sequences for manipulation of the NV spin state. In the second chapter, we describe the spin bath environment surrounding the NV center spins. In chapters three and four, we present two optical methods to extend the NV sensing capabilities to nanometric spatial resolution and to enhance the readout fidelity of NV spin ensembles.

Chapters five and six present a detailed study of dephasing and decoherence mechanisms for NV spin ensembles in a bath of paramagnetic nitrogen spins.

Contents

List of Figures

List of Tables

Citations to Previously Published Work

Parts of this dissertation cover research reported in the following articles:

1. Jaskula*, J.-C., Bauch*, E., Arroyo-Camejo, S., Lukin, M. D., Hell, S. W., Trifonov, A. S., & Walsworth, R. L. (2017). Superresolution optical magnetic imaging and spectroscopy using individual electronic spins in diamond. Optics Express, 25(10), 11048. doi.org/10.1364/OE.25.011048

2. Jaskula, J.-C., Shields, B. J., Bauch, E., Lukin, M. D., Trifonov, A. S., & Walsworth, R. L. (2017). Improved quantum sensing with a single solid-state spin via spin-to-charge conversion, http://arxiv.org/abs/1711.02023

3. Bauch*, E., Hart*, C. A., Schloss, J. M., Turner, M. J., Barry, J. F., Kehayias, P., & Walsworth, R. L. (2018). Ultralong Dephasing Times in Solid-State Spin Ensembles via Quantum Control. PRL, 5. http://arxiv.org/abs/1801.03793

4. Bauch, E., Jungyun, P., Hart, C., Singh, S., Schloss, J. M., Turner, M. J.,Barry., J. F., Pham, L., Bar-Gill, N., Walsworth, R. L. (2017). Quantum coherence of NV center solid-state spins in diamond. Manuscript in preparation.

5. Barry, J. F., Schloss, J. M., Turner, M. J., Bauch, E., Hart, C. A., & Walsworth, R. L. (2017). Optimizing NV ensemble magnetometer sensitivity. Manuscript in preparation.

Acknowledgments

I thank all the people in my life who have made this possible, who have believed in me, who taught me, who corrected me, who assisted me, who have followed up with me, who have shown interest in my work, who have seen potential in me, who helped me navigate through difficult waters when needed, who advised me, who consulted me, who fed me, who have spent time with me, who celebrated with me, and who love me.

Erik

January 19, 2018

Boston, USA

Abbreviations

AC	alternating current used to describe RF and MW fields
EPR	electron paramagnetic resonance
ESEEM	electron-spin-echo-envelope modulation
ESR	electron spin resonance
CVD	chemical vapor deposition
DC	direct current used to describe static fields
DQ	double quantum
DEER	double electron-electron resonance
FWHM	full width at half maximum
HPHT	high-pressure high-temperature
HWHM	half width at half max
IR	infrared, spectral range from 0.7 to 300 µm (1.77 eV to 4.1 meV)
ISC	intersystem crossing
JTE	Jahn-Teller effect
ppm	parts-per-million, $1.763\times10^{17}\,\mathrm{cm}^{-3}$ atoms in diamond
ppb	parts per billion, $1.763\times10^{14}\ \mathrm{cm}^{-3}$ atoms in diamond
MW	microwave, 1 to 4 GHz
NV	nitrogen-vacancy
NV^0	symbol for the neutral nitrogen-vacancy
NV^-	symbol for negatively charged nitrogen-vacancy
NV^+	symbol for positively charged nitrogen-vacancy
N_s^0	symbol for the subsitutional nitrogen defect (P1 center)
N_s^+	symbol for the ionized nitrogen defect

ODMR	optical detected magnetic resonance
P1 center	terminology for the subsitutional nitrogen defect, see N_s^0
PL	photoluminescence
PLS	photoluminescence spectroscopy
PSB	phonon sideband
RADOR	ramsey double electron resonance
RF	radio frequency, 1 - 1000 MHz
SEDOR	spin echo double electron resonance (see DEER)
SNR	signal-to-noise ratio
SQ	single quantum
UV	ultra-violet
VIS	visible
ZFS	zero field splitting
ZPL	zero-phonon line

Chapter 1

Introduction

Solid-state impurity spin defects have garnered an increasing interest in quantum science and quantum sensing applications. They are introduced into the solid as dopants and possess unique quantum properties that provide novel pathways to a wide range of physics-related problems. Nitrogen-vacancy (NV) defects, in particular, are well-known for their exceptionally long ground-state spin coherence and population lifetimes at room temperature, an optical spin polarization and readout mechanism, and the direct addressability via coherent microwaves (MW) and static magnetic fields. In this dissertation, we present several efforts to push further the already outstanding capabilities of NV center spins in diamond, with a special focus on the quantum sensing of magnetic fields. The relevance of the NV defect is exemplified by Fig. 1.1, which depict the number of related publications that were submitted to the open access preprint archive arxiv.org over the past 10 years. A steep increasing trend is visible. This statistic does not include all NV-related papers that have been published, but it rather includes papers that merely mention NV defects. Nonetheless,

it clearly emphasizes that this diamond defect has established itself as a remarkable research platform and possesses an increasing relevance to physics applications.

Impurity defects, however, are not unique to diamond or limited to NV center spins. In fact, a wide range of defects in numerous solids have been discovered and studied. Historically, electronic phosphor spins in silicon [1–4] and subsitutional nitrogen spins in diamond, termed P1 centers [5–10], have been the most well-studied solid-state defects. That said, a new generation of defect spins has recently come under investigation to challenge and provide capabilities beyond those of NV-based applications. Some of these defects include silicon-vacancies in diamond [11–14], photoluminescence defects in silicon-carbide [15–20], chromium defects in silicon-carbide and gallium-nitride [18, 21], and manganese and cobalt defects in zinc oxide [22, 23]. Still, the NV center has thus far maintained its top position among its contenders, which is supported by its combination of unique physical characteristics, extensive amount of available scientific literature, well-developed processing techniques, and long list of applications. A successor has yet to be discovered.

1.1 Historical Background & Applications

About 1000 NV center related papers have been submitted to the preprint website arxiv.org over the past 10 years alone and thus providing a comprehensive literature review herein would be a fruitless task. Consequently, we highlight a few important milestones and select applications in this section.

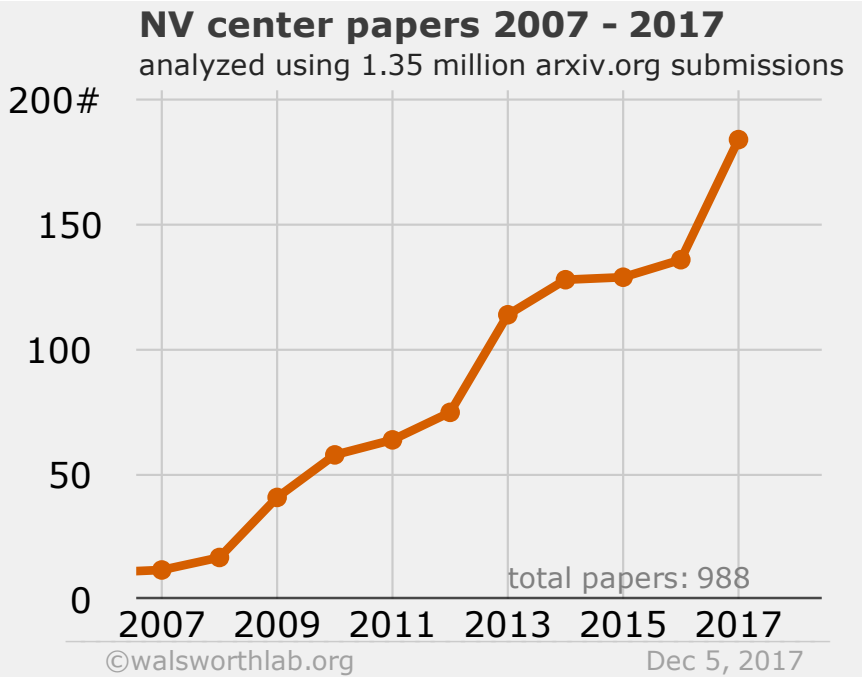

Figure 1.1: Submission statistics – The graph displays the number of NV center related submissions to the open access preprint archive *arxiv.org* over the last 10 years.

History

The foundation of diamond research was laid in 1955 when Bundy et al. presented the first man-made diamond to the world [24]. In Fig. 1.2, we summarize this and other early works relevant to the NV center field. At that time, Bundy and colleagues worked at General Electric, and the diamond growth technique they developed is known as the high-pressure high-temperature (HPHT), one of two major methods available to date (see Sec. 1.3.2). To confirm that their synthetic diamond crystals were indeed equivalent to a natural counterpart they performed x-ray diffractometry, chemical analysis, and scratch tests, and they demonstrated repeatability of growth. In the years leading up to and just after Bundy's seminal work, other scientists began

to investigate a wide range of dopants in diamond. These included boron, aluminum, silicon, phosphorous, and nitrogen, all elements which are elements that neighbor carbon in the periodic table (element 6, see Fig. 1.2). The first diamond defect was unambiguously identified in 1959 via paramagnetic resonance spectroscopy. The only explanation for the observed resonance features was the substitutional nitrogen atom, which is one of the only elements with a nuclear spin $I = 1$ [5]. Three studies in the 1960s and 1970s followed, all of which investigated fluorescence spectra in nitrogen-rich irradiated diamonds [25–27]. However, it was not until 1976 when Davies and Hamer summarized the three earlier studies and, presented new fluorescence and absorption spectra, that it could be concluded that the observed optical properties must be those of a substitutional nitrogen next to a vacancy [28]. Davies also gave an overview of the vacancy defect in 1977 [29], which was introduced into the diamond lattice via irradiation damage, a technique that was well-established by then. Still, vacancies form many compound defects and, exists in several charge states, and thus they produce an extensive range of optical fluorescence bands (e.g., ND1, GR1, GR2, etc.) [29]. Several NV studies in the 1970s and 1980s started to elucidate many of the common NV center properties [7, 30–34]. For example, in 1977, Loubser and van Wyk observed the first indication of ground-state spin polarization in NV centers upon light excitation [30]; in 1983, Collins et al. performed the first excited-state lifetime measurement ($\sim 13\,\text{ns}$) [31]; and van Oort demonstrated the first optically detected NV coherence measurements in 1988 [34]. In 1997, scientists in Germany reported the first single NV center measurement, performed via confocal microscopy [35]. Individual atomic-size NV defects were readily identified via their triplet spin

ground state, fluorescence spectroscopy, and the optical polarization mechanism already seen by Loubser and van Wyk. Several studies followed in the late 1990s and early 2000s [36–40] and demonstrated among other phenomena, photon-antibunching [37] and the first coherent measurement for single centers [40]. In 2008, a seminal study published by a research team at Harvard detailed the potential impact of NV spins for sensing applications [41]. Many groundbreaking experiments and publications in the field of NV center research have been spawned since that time.

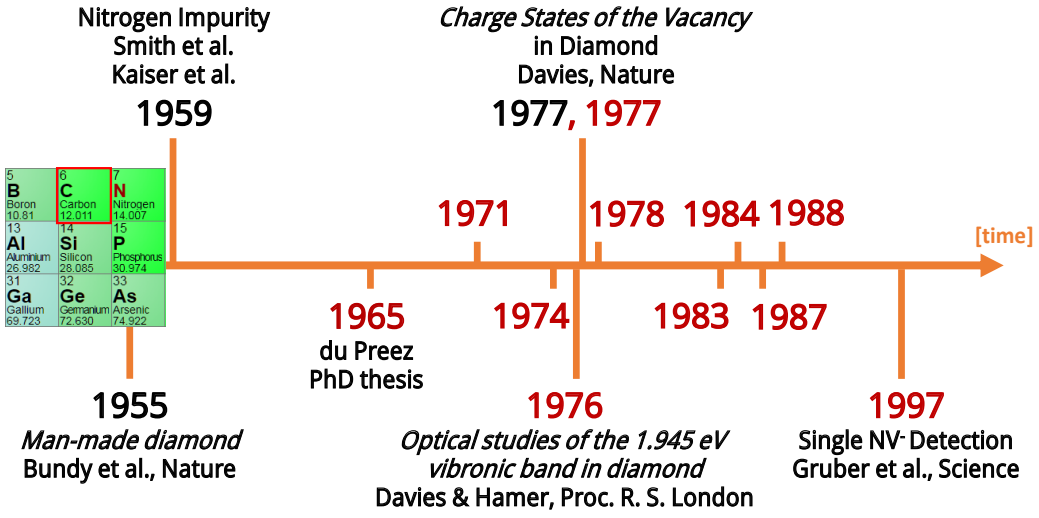

Figure 1.2: Summary of early NV center work – NV center publications are indicated in red. The first mention of NV fluorescence spectra was by du Preez in 1965 [25], but the work was not associated with NV centers until 1976 [28]. For additional references see main text.

The wide range of topics covered by NV researchers include quantum information [42–45] and control [46–56], fundamental physics [57–62], solid-state physics [63–65], quantum hybrid devices and cavity dynamics [66–71], chemistry applications and magnetic resonance spectroscopy (MRS)[72–79], biophysics and biomagnetism[80–

83], magnetic field sensing[41, 84–88], magnetic field imaging [80, 82, 89–95], magnetic navigation [96–98], paleomagnetism [99–101], electric field sensing [102–107], temperature sensing [81, 108–110], pressure sensing[111–113], NV radios [114], NV masers [115, 116], proposals for NV-based lasers [117, 118], and proposals for dark matter detection[119]. In addition, numerous startups have been recently registered to commercialize select NV-based technologies [120–122].

Applications

Experiments with NV centers are naturally separated into the two classes of single/few spin and ensemble, where the latter describes the interrogation of high spin densities over larger field of views. Although both experimental classes share many of the underlying NV specific properties, techniques developed for single spins are not straightforwardly transferable to ensemble measurements (and vice versa). First, the saturation intensity of a single center ($\sim 1\text{mW}/\mu\text{m}^2$) demands hundreds of milliwatts of excitation power in ensemble experiments. This need is attributed to the required illumination of a larger field of view compared to that of a confocal microscope setup ($\sim 1\,\mu\text{m}^2$) that is typically employed in single NV research. In addition, ensemble samples contain a higher abundance of additional absorptive defects, in particular subsitutional nitrogen centers, which are incorporated into the lattice during diamond growth (see Sec. 1.3.2). Second, in single NV measurements the *dephasing time*, which is related to the lifetime of the spin states in the ground state, is given by the time average over many experimental runs. In ensemble measurements, however, the average is determined from many NV centers located at different lattice sites, whose local

environments slightly vary. Consequently, the ensemble fluorescence is a spatially and temporally averaged signal, which is strongly influenced by inhomogeneities within the crystal. These distinctions leads to rather peculiar differences when comparing single and ensemble spin properties, some of which are discussed in Ch. 2 and 5. We therefore raise a word of caution that many of the excellent single center properties, such as state-of-the-art coherence times[81, 123], can only be considered as best-case scenarios when compared to ensembles.

Moreover, NV experiments can be also coarsely separated into quantum information/control and quantum sensing types, which have seen approximately equal shares of attention in the research community. Quantum information/control is geared towards exploiting single NV spin properties for a range of applications related to quantum computing and simulation [42–45], such as quantum entanglement or teleporation among pairs of spins [54–56], quantum memories for the storage of arbitrary quantum states [46, 52], and optimization of the readout fidelity of single spins [47, 51, 124]. Sensing experiments include any modalities in which the NV spin state's susceptibility to external fields and environmental parameters is exploited; this applies to single and ensemble measurements. These modalities include perturbations of the spin state due to temperature fluctuations of the diamond host crystal [81, 108–110], electric fields and crystal lattice strain [102–107, 125, 126], magnetic fields [41, 86, 88], magnetic noise intrinsic to the diamond[49, 127–129], and surface noise [74–79, 106, 130].

Lastly, we discuss a few recent exemplary sensing applications to provide insight into current NV capabilities. In a study published in 2010 it was shown that the NV spin resonance is affected by temperature-induced expansion of the diamond lattice which leads to a shift in resonance frequency of $-74\,\mathrm{kHz/K}$ [108]. This discovery would ultimately lay the foundation for NV thermometry in which the NV spin is employed as a well-localized temperature sensor[81, 109, 131]. For example, Reference [81] demonstrated that NV spins embedded into $\sim 100\,\mathrm{nm}$-sized nanodiamonds could be used to perform temperature measurements in living biological cells with sub-cellular spatial resolution. On the other hand, temperature sensitivities of $10\,\mathrm{mK}/\sqrt{\mathrm{Hz}}$ and below have been obtained from bulk ensemble measurements [81, 109].

Electric-field sensing is another application of NV centers. Electric fields affect the NV spin in various ways, and thus attaining a deeper understanding of these fields is a current research trend. Results of earlier studies have reported a linear Stark effect of the NV ground state [132] which was later employed to demonstrate DC and AC electric field sensing with a single NV center [103]. Such a single NV electric-field detector has also been used to measure the single electron charge of an adjacent NV [104]. For bulk NV centers, electric strain-field gradients are a dominant noise source of dephasing [133–135] and strain has been suggested as a means for dark-matter detection [119]. For shallow NV centers a few nanometers below the diamond surface, electric-field noise has been found to significantly limit the coherence and spin lifetime of the NVs [105–107], and shallow NVs may therefore provide sensitive charge sensing

for specimens placed on top of the diamond [105].

In addition to temperature and electric field sensing, multiple studies have explored methods to extend the NV sensing volume to larger, micron or millimeter-sized fields of views. In such wide-field imaging applications, NV ensembles are arranged in a thin ($1 - 10\,\mu$m-scale) layer of enhanced NV-density diamond and employed to image fields from sources placed on top of the diamond sample. Many experiments have thus far utilized wide-field imaging and include imaging of paramagnetic biological cell types [80, 82], current flow in graphene [93], MW fields [95], and magnetic dipoles in rocks [99, 101, 136].

For further reading, we suggest the following topical reviews: *Quantum Sensing* [137], *Single-spin magnetic resonance in the nitrogen-vacancy center of diamond* [138], *Probing condensed matter physics with magnetometry based on nitrogen-vacancy centres in diamond* [65], and *Spins and mechanics in diamond* [139].

1.2 Organization of the Dissertation

In this chapter, we focus on a few of the most relevant aspects of NV research, highlighting the NV optical and magnetic properties, and we also explore a range of fundamental MW control techniques, which act as the basis for the experiments described in the later chapters. Many excellent analyses on the specifics of NV center physics have been written already, and we recommend the theses by Linh Pham [140] and Victor Acosta [141], as well as the extensive NV center review by Doherty et al.

[142] to supplement the discussion in Ch. 1 and 2.

Chapter 2 shifts the focus from the NV to its immediate environment, the *diamond spin bath*, which typically consists of excess nuclear and electronic spins such as P1 substitutional nitrogen spins. Many NV spin properties relevant for applications are impacted by the spin bath and a detailed understanding is therefore crucial. We provide specifics about the nitrogen bath that consists of subsitutional nitrogen spins and a theoretical description of the underlying noise mechanisms. Three additional MW control techniques are introduced which, in combination with the techniques introduced in Ch. 1, form a powerful set of tools to study the bath environment in diamond.

The first experiment is presented in Ch. 3, and demonstrates how superresolution microscopy can be employed to localize individual NV centers with nanometer precision [143]. Using the sensing capabilities of individual spins, we detected the magnetic field from a nearby wire with a spatial resolution of $\sim 20\,\mathrm{nm}$, about $13\times$ smaller than the optical diffraction limit. Superresolution microscopy was awarded the Nobel prize in Chemistry in 2014, and awardee Stefan Hell is a co-author of this experiment [143].

The second experiment is described in Ch. 4 and focuses on an implementation of a new readout scheme that utilizes the charge state of $\mathrm{NV}^-/\mathrm{NV}^0$ centers [144]. By using three laser light sources at different wavelengths (532, 594, and 637 nm) the

spin ground state of NV^- is repetitively readout via charge state detection, which, in principle, allows for photon-shot-noise-free spin state readout and improved sensitivity in sensing applications.

Chapter 5 and 6 discuss two related sets of experiments to elucidate dephasing and decoherence mechanisms of NV^- ensemble spins in a bath of paramagnetic substitutional nitrogen spins [129, 135]. The first set of experiments investigates limitations to the inhomogeneous dephasing time T_2^* measured through linewidth or Ramsey experiments and demonstrate that T_2^* can be significantly enhanced by combining two unique quantum control techniques. The second set of experiments investigates limitations to the coherence time T_2 as measured through spin echo and dynamical decoupling. By combining results from both studies, we are able to consistently describe the dynamics of the spin bath and find solid agreement between experiment and simulations.

In Ch. 7, we conclude our work and offer outlooks for future research directions. Additional information and simulations are provided in the Appendices.

1.3 Nitrogen-Vacancy Center in Diamond

The NV center spin defects found in diamond have been extensively studied and deployed in a wide range of applications. Almost all of these advances are facilitated by the magnetic and optical properties of the negatively charged NV^- center [142]. For one, the NV^- center provides a readout and initialization of its spin state by

optical means. In addition, the spin ground state is long-lived (milliseconds) and allows coherent manipulation at ambient temperature. Lastly, the centers magnetic spin sublevels are addressable via external magnetic bias fields and microwaves in the gigahertz range. On the other hand, NV^0 and NV^+ centers are two additional known charge states [145], but their physical properties are less favorable for spin applications. In this section we discuss the properties of the negatively charged NV^- in more detail.

1.3.1 Crystal Structure

The NV center in diamond consists of a subsitutional nitrogen atom (N_s^0) next to a vacant carbon lattice site (see Fig. 1.3). For the NV^-, a natural quantization axis is given by the line that connects the nitrogen and vacancy (black arrow), which gives rise to an axial, C_{3V} point-group symmetry. The symmetry of the NV defect determines the structure of the NV energy levels and selection rules for dipole-allowed transitions, and it therefore plays a crucial role in determining the defect's optical properties, which are discussed in Sec. 1.3.3. For example, since the nitrogen atom could occupy any of the four lattice sites that neighbor the vacancy, four distinct NV *classes* exists and are denoted by the vectors [111], $[\bar{1}1\bar{1}]$, $[1\bar{1}\bar{1}]$, and $[\bar{1}\bar{1}1]$. In ensemble experiments, where all NV classes are typically equally abundant, a small magnetic field $B_0 \gtrsim 10\,\mathrm{G}$ (typically) can be applied along any of the [111] directions to use Zeeman splitting of individual resonances of a select NV class. Similarly, any combination of NV classes can be addressed with an appropriate combination of

magnetic fields and MW radiation applied along the individual crystal directions.

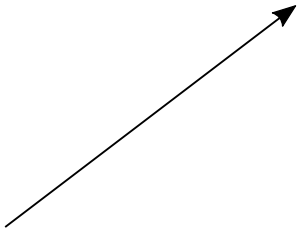

Figure 1.3: Nitrogen-vacancy (NV) center structure – The NV center in diamond consists of a subsitutional nitrogen atom adjacent to a vacant lattice site. A natural quantization axis for NV^- defect is given by the axis through the nitrogen and vacancy (black arrow) along the [111] crystal direction. Since the nitrogen atom can occupy any of the four lattice sites neighboring the vacancy, four distinct NV^- classes in diamond exist. In ensemble experiments, where typically all NV^- classes are equally abundant, a small magnetic field can be applied along any of the [111] directions to Zeeman split and spectrally separate individual resonances of a select class.

1.3.2 Formation of Centers

Two methods are commonly deployed to activate the formation of NV centers in diamond. In experiments, which require a homogeneous distribution of centers over micron- to millimeter scales, an irradiate-anneal recipe is used [146–148]. First, a diamond host crystal with a fixed concentration of nitrogen spins is manufactured. Second, vacancies are introduced into the lattice by irradiating the host crystal with high energy particles, which are usually electrons at several hundred kiloelectronvolts

energy. Lastly, the irradiated crystal is annealed at temperatures of $\sim$ 800 °C and above. At these temperatures, vacancies become mobile and form nitrogen-vacancy centers [149, 150]. In this procedure, the N-to-NV conversion efficiency, which is given by the ratio $[NV^-]/[N_{initial}]$, is an important measure to be optimized and values in the range from 1 - 40 % have been reported in the literature [71, 83, 85, 108, 151].

Alternatively, NV centers can be formed via implantation of $^{14}N^+$ or $^{15}N^+$ isotopes by bombarding the host crystal with a beam of nitrogen ions [54, 89, 90, 152–159]. During the impact, the nitrogen and vacancies are incorporated into the diamond lattice, and vacancy formation may be further increased by co-implantation of ions [154, 156, 160]. An annealing step either in-situ [161] or post-implantation promotes formation of NV centers by allowing migration of the introduced vacancies. Recently, a focus has been put on the precise placement of NV spins, such as by controlled spatial masking and tuning of the nitrogen beam implantation energy thus providing lateral localization within a few tens of nanometers [155, 158, 162]. In addition, shallow NV centers are nowadays routinely implanted nowadays mere nanometers below the diamond surface [159, 163], and implantation of molecular nitrogen (N_2^+) can be used for enhanced creation of dipolar-coupled NV center pairs [153, 157].

The diamond host properties play an important role in NV experiments as crystal qualities inevitably affect the embedded spins. Chemical vapor deposition (CVD) [164–166] of a carbonaceous gaseous source (typically methane) onto a substrate

is the preferred crystal growth method today. The technique provides high-grade single-crystalline diamond material while allowing fine control over concentrations and isotopic admixture of individual spin species. Nitrogen concentrations in CVD samples are selected in the $\approx 0.001 - 50\,\mathrm{ppm}$ (parts-per-million) range and manufactured depending on their particular application. Another powerful aspect of the CVD technology is the ability to grow diamond material from isotopically purified or enriched source gases. For example, by depleting the source gas of paramagnetic spin species such as ^{13}C isotopes with nuclear spin $I = 1/2$ (1.07 % natural abundance), an ultra-pure spin-free host diamond environment is built [123]. In such isotopically enriched samples, the coherence time of individual NV centers is essentially limited by the millisecond-long T_1 spin lifetime of diamond (given spin-lattice relaxation, see Sec. 2.3.3). The exhibited coherence times $T_2 \sim T_1 \sim 1\,\mathrm{ms}$ are some of the longest of an electronic solid-state spin to date. A smaller group of employed diamond samples can be grown with the older, high-pressure-high-temperature (HPHT) method [24, 166–170]. HPHT diamond samples typically contain a natural abundance of ^{13}C spins and high nitrogen concentrations $\sim 200\,\mathrm{ppm}$. A few studies reported the usage of HPHT diamond with a nitrogen content $\sim 1\,\mathrm{ppm}$ [85], and isotope purification is possible as well in principle. The greater flexibility in diamond growth and availability of diamond manufacturers, however, has made CVD the preferred technique for research diamond material.

1.3.3 Optical Properties

Over the past years, the optical properties of the NV center charge states have been an active field of research [34, 108, 124, 144, 145, 171–184]. In this section we focus on one important aspect: the initialization with green laser light and optical readout of the NV^- spin ground state.

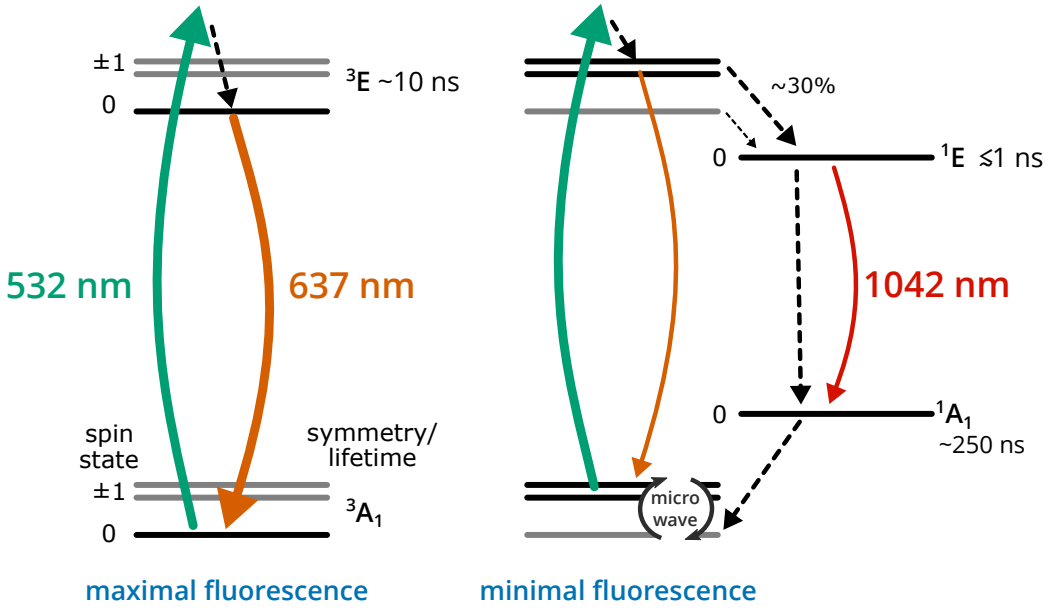

Figure 1.4: NV^- level structure – The NV center is optically identified by either its zero-phonon-line (ZPL) in the visible at 637 nm (orange) or the much weaker ZPL at 1042 nm (red). Preferential non-radiative decay (dashed black lines) from the excited $m_s = \pm 1$ spin states via the intermediate singlet states leads to spin polarization of the $m_s = 0$ ground state via excitation by 532 nm (green) laser excitation.

It has been well established that the negative charge state, NV^-, is comprised of six electrons (or two holes), which gives rise to a spin-1 system with C_{3V} point-defect

symmetry [142]. Considering the symmetry of the defect and the fact that there are four available atomic orbitals surrounding the vacancy, it can be shown that such a spin system possesses a triplet ground and excited state ($^3A_1$ and ^{3}E, respectively), and at least two additional singlet states ($^1A_1$ and ^{1}E, respectively). Figure 1.4 depicts the optical transitions and electronic states associated with the NV^- center.

The defect is optically identified by either its zero-phonon line (ZPL) at 637 nm between the ground and excited state spin-triplet [34, 35] or the much weaker ZPL at 1042 nm [108, 185] between the two intermediate singlet states. Each ZPL is accompanied by a broad phonon side band (PSB) which, given the Frank-Condon principle [186], arise from optical transitions including local lattice phonon modes. Examples of the NV fluorescence spectra in the visible and near-infrared (NIR) from References [187] and [185], respectively, are shown in Fig. 1.5.

A feature unique to NV^- spins is their ability to be initialized into the $m_s = 0$ ground state and read out via laser light excitation, a property which was observed as early as 1977 [30]. It is understood that the origin of this property is a preferential decay of the excited $m_s = \pm 1$ into the upper singlet state. Such an intersystem crossing is possible when two magnetic spin states that are close in energy and phonon modes, plus spin-orbit coupling, provide the required energy and angular momentum for a spin-flip [177, 178, 182]. The spin population in the upper singlet state, however, decays rather quickly ($\lesssim 1$ ns), and it does mostly non-radiatively into the metastable lower singlet state (~ 250 ns) [108], which preferentially couples to the $m_s = 0$ ground

state (indicated by dashed lines, Fig. 1.4). After a few cycles of laser light excitation, a significant amount of spin population is thus pumped into the $m_s = 0$ ground state, which enables the efficient polarization of the NV^- spin state. This in drastic contrast to the otherwise Boltzmann-distributed spin population which, at ambient temperature, leads to approximately equally populated ground-state spin states. A few experiments have quantified the degree of spin polarization, and reported values are 60 % [40] and 92 % [124] for single NVs, and 80 % for ensembles [175].

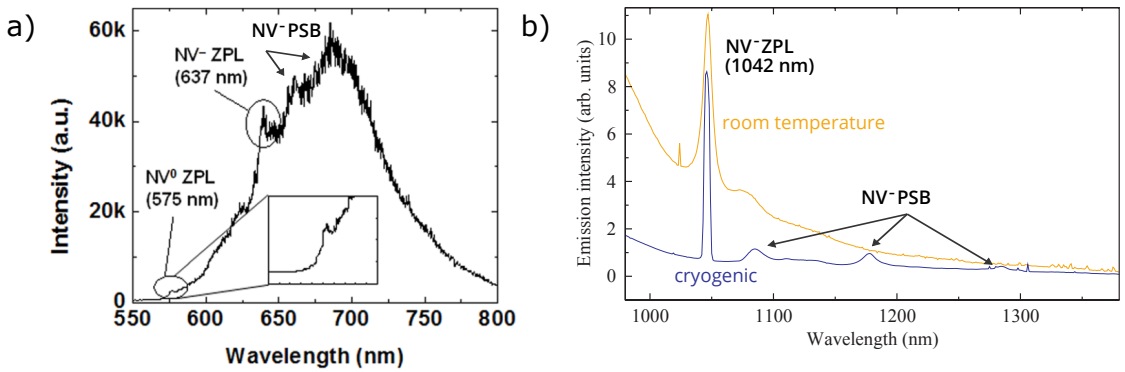

Figure 1.5: NV fluorescence spectrum – In the visible (a) and near-infrared (b) reproduced from Reference [187] and [185], respectively. The ZPL and PSB associated with both main NV^- optical transitions are labeled. For details see text.

Another important aspect of the enhanced branching ratio of $m_s = \pm 1$ into the upper singlet state is the spin-state-dependent fluorescence signal: The NV^- exhibits maximal fluorescence in the visible when in the $m_s = 0$ ground state, and it shows a reduced emission when in the $m_s = \pm 1$ state providing optical readout of ground-state spin population. Figure 1.6 depicts the time-resolved fluorescence intensity from each state for a single NV center reproduced from Reference [188]. The difference in

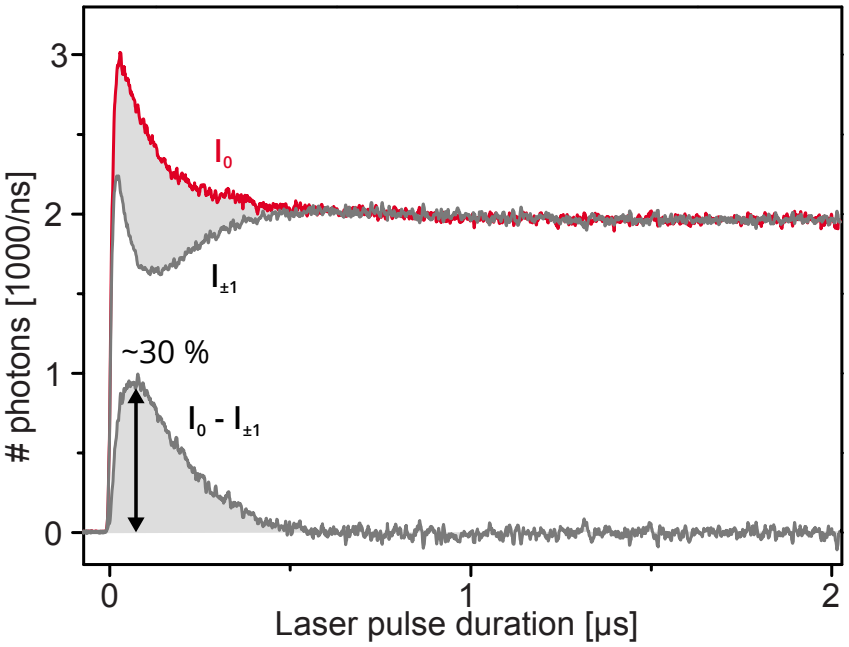

Figure 1.6: Time-resolved NV^- fluorescence – The fluorescence signals from the $m_s = 0$ and $m_s = \pm 1$ spin states are plotted as a function of laser pulse readout duration. The spin-state-dependent signal from individual NV^- centers leads to a measurable difference in fluorescence from which the spin state of the NV^- ground state is inferred. A maximal spin contrast of $C \sim 30\,\%$ is obtained by taking the difference of $m_s = 0$ and $m_s = \pm 1$ signals for short readout durations. For sensing experiments with single centers and ensembles, the readout duration is typically optimized to maximize the product $C\sqrt{I}$. Graph reproduced from Reference [188].

NV^- fluorescence from each state is quantified by the *measurement contrast* obtained when the $m_s = 0$ to the $m_s = \pm 1$ fluorescence is compared (lower curve, Fig. 1.6). The maximal contrast can be estimated from the difference in the experimentally determined lifetimes of the $m_s = 0$ and $m_s = \pm 1$ excited state sublevels, which are attributed to leakage into the upper singlet transition. For example, the experimentally determined single NV^- values of 12 ns ($m_s = 0$) and 7.8 ns ($m_s = \pm 1$) reported in Reference [176] yield an approximate contrast ratio of 35 %. This value is in good

agreement with contrast values observed in single NV experiments ($25-30\,\%$)[188]. For ensembles, this value is reduced and typically in the $1-10\,\%$ range [135, 189]. Several factors affect the readout contrast including MW and laser light power [190, 191], background fluorescence from off-axis NV^- classes and additional optically active defects in diamond (in particular NV^0 centers), and as uncontrolled charge state conversion from NV^- to NV^0. The detailed mechanisms of contrast reduction in ensembles measurements, however, are still to be investigated [172, 192].

Much research has been conducted to identify optimal laser source wavelengths for excitation of the NV^- spin state, although doubled Nd:YAG laser light ($\lambda = 532\,\text{nm}$) is most commonly employed [124, 144, 172, 180, 183, 193]. In Ch. 4 we show how excitation at wavelengths resonant with the ZPL at 637 nm (red) in combination with 594 nm (yellow) and 532 nm (green) is used to efficiently control the NV^- and NV^0 charge state and allows for an alternative readout scheme free of photon-shot-noise via charge state detection.

1.3.4 Ground-State Hamiltonian

The NV^- ground-state Hamiltonian is that of an electronic spin-1 system with axial symmetry [7] and given by (omitting nuclear Zeeman effects) [142]

$$H/h = \underbrace{D\,\mathbf{S}_z^2}_{\text{spin-spin}} + \underbrace{M_z\mathbf{S}_z^2 + M_x(\mathbf{S}_y^2-\mathbf{S}_x^2) + M_y(\mathbf{S}_x\mathbf{S}_y+\mathbf{S}_y\mathbf{S}_x)}_{\text{electric field/strain contributions}} + \underbrace{\frac{\gamma_{NV}}{2\pi}\mathbf{B}\cdot\mathbf{S}}_{\text{Zeeman}} + \underbrace{\mathbf{I}\cdot\hat{\mathbf{A}}\cdot\mathbf{S}}_{\text{hyperfine}} + \underbrace{P\mathbf{I}_z^2}_{\text{quadrupole}}\,, \tag{1.1}$$

where $D \approx 2.87\,\text{GHz}$ is the zero-field spin-spin splitting, $\{\mathbf{S}_x, \mathbf{S}_y, \mathbf{S}_z\} = \mathbf{S}$ are the dimensionless electronic spin-1 operators, $\{M_x, M_y, M_z\}$ collect strain and electric field

contributions to H [125, 126], $\gamma_{NV} \approx 2\pi \times 28\,\mathrm{GHz/T}$ is the NV gyromagnetic-ratio [142, Tab. 2], $\{B_x, B_y, B_z\} = \mathbf{B}$ are the local magnetic field components, $\hat{\mathbf{A}}$ is the magnetic hyperfine tensor, P is the experimentally determined quadrupole splitting parameter, and $\{\mathbf{I}_x, \mathbf{I}_y, \mathbf{I}_z\} = \mathbf{I}$ are the dimensionless nuclear spin operators. When a small magnetic field B_z is applied along the NV quantization axis $\frac{\gamma_{NV}}{2\pi} B_z \ll D$, $D \gg \{\frac{\gamma_{NV}}{2\pi} B_x, \frac{\gamma_{NV}}{2\pi} B_y, M_x, M_y, M_z\}$ and sets the largest energy scale. A common approximation is therefore to ignore terms $\propto \mathbf{S}_x, \mathbf{S}_y, \mathbf{I}_x$, and $\mathbf{I}_y$ to simplify the Hamiltonian. Equation 1.1 is then purely diagonal and the frequencies for the spin states $m_s = 0, \pm 1$ are given by

$$f_{\pm 1} \approx D + M_z + |m_I| P \pm (\frac{\gamma_{NV}}{2\pi} B_z + m_I A_z) \text{ and} \tag{1.2}$$

$$f_0 = |m_I| P, \tag{1.3}$$

where A_z is the on-axis hyperfine component. Note that in Eqn. 1.2 and 1.3 the quadropolar contribution $|m_I|P$ is typically omitted. Such a term leads to a constant energy shift of the $m_I = \pm 1$ nuclear spin states but does not effect the electronic spin transitions, which are given by the energy difference between f_{-1} (or f_{+1}) and f_0. In addition, for ^{15}N isotopes no quadropolar splitting exists and $P = 0$ [142].

In case of a natural abundance of nitrogen ($[^{14}\mathrm{N}] = 99.636\,\%$) with nuclear spin $I = 1$, hyperfine splitting $A_z \approx -2.2\,\mathrm{MHz}$ [142, see Tab. 1], and quadrupolar splitting $P \approx -5\,\mathrm{MHz}$ [142, see Tab. 1], the $^{14}\mathrm{NV}^-$ spin states become $|m_s = 0, \pm 1; m_I = 0, \pm 1\rangle$ and the resonance spectrum correspondingly exhibits up to six magnetic resonances. Figure 1.7 depicts a qualitative picture of the NV energy levels and expected energy spectrum. With a static magnetic field bias field B_z is applied,

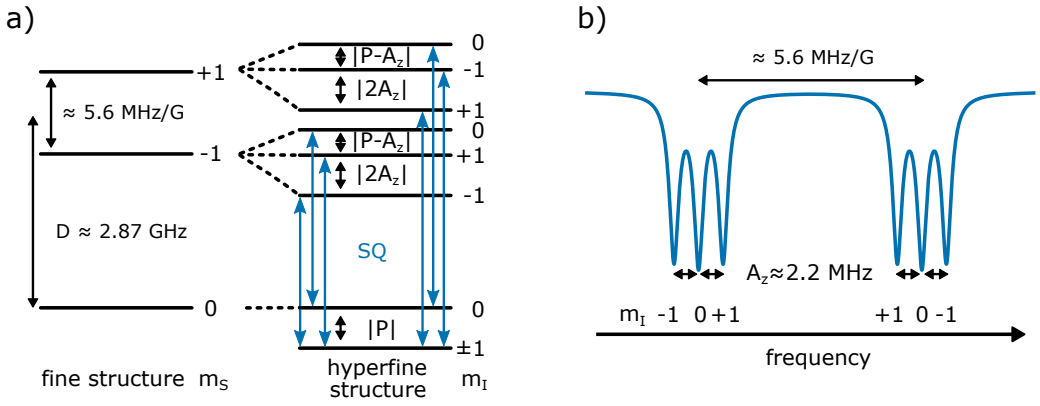

Figure 1.7: NV^- ground-state structure for the ^{14}N isotope – a) Level diagram for f_0 and $f_{\pm1}$ given by Eqn. 1.2 taking fine (m_S) and hyperfine structure (m_I) into account. The hyperfine parameter $A_z \approx -2.2\,\text{MHz}$ and quadropolar splitting $P \approx -5\,\text{MHz}$ are determined experimentally [142, see Tab. 1]. Nuclear Zeeman energies are typical to small to be experimentally relevant and are thus often ignored. Dipole-allowed transitions are indicated by blue arrows. b) Expected energy spectrum with transitions depicted as Lorentzians. The hyperfine splitting leads two a pair of hyperfine triplets for the two spin transitions $f_{-1} \leftrightarrow f_0$ and $f_{-+1} \leftrightarrow f_0$. Note that the quadrupolar splitting parameter P does not affect the electronic spin transitions, which are calculated by the energy difference between the respective energy levels.

the degeneracy of the $|0\rangle \leftrightarrow |+1\rangle$ and $|0\rangle \leftrightarrow |-1\rangle$ spin transition is lifted, which results in a pair of hyperfine triplets with spacing $|A_z| \approx 2.2\,\text{MHz}$ spectrally separated by $2 \times \frac{\gamma_{NV}}{2\pi} \approx 5.6\,\text{MHz/G}$. NV experiments are typically performed by working with either of the two hyperfine groups, that is the $|0\rangle \leftrightarrow |+1\rangle$ or $|0\rangle \leftrightarrow |-1\rangle$ electronic spin transition. Each transition approximates an effective two-level system and since Δm_s changes by 1, we refer to them as single quantum (SQ) transitions. By addressing both SQ transitions simultaneously, experiments can also be performed utilizing the $|-1\rangle \leftrightarrow |+1\rangle$ transition, here referred to as double quantum (DQ) since $\Delta m_s = 2$. The ability to manipulate the NV ground state in either the SQ or DQ basis provides great flexibility for spin manipulation and further details with specific applications

are discussed in Sec. 1.5 and Ch. 5. For a detailed analysis of the Hamiltonian in Eqn. 1.1 using perturbation theory that include effects of M_x, M_y, B_x, and B_y, see Sec. C.2.

1.4 Primary Pulse Sequences

In the previous section, we have discussed the optical and magnetic properties of the NV^- center. In this section, we introduce a set of control sequences that allow complex manipulation of the NV spin and sequential optical read out via laser light.

1.4.1 Electron Spin Resonance

The most basic form of NV spin manipulation is to apply a continuous MW signal resonant with either of the two SQ transitions. This type of spin manipulation is known as electron spin resonance (ESR), or alternatively, optically detected magnetic resonance (ODMR), as the NV fluorescence is employed for spin state readout (see Sec.1.3.3).

The general form of an ODMR sequence is shown in Fig. 1.8a. Application of 532 nm laser light is used to initialize the NV spin state into the $m_s = 0$ ground state (ignoring hyperfine splitting for simplicity) and the ODMR signal is plotted as a function of the applied MW frequency. When the continuous MW radiation is on-resonant with the either the $|0\rangle \leftrightarrow |-1\rangle$ or $|0\rangle \leftrightarrow |+1\rangle$ spin transition, the NV^- fluorescence reduces as the spin populations are redistributed between the ground-state spin states. The NV ODMR signal thus exhibits three resonances that are

attributed to a single electronic spin transition given the triplet hyperfine structure of the ground state; this is shown in Fig. 1.8b ("SIG"). However, when considering all four possible NV axes in diamond, two electronic spin transitions, and the triplet hyperfine structure, a full NV-diamond ODMR spectrum exhibits a total of up 24 peaks when an arbitrary magnetic field is applied. Such a spectrum is discussed in Sec. 1.6 and depicted in Fig. 1.17.

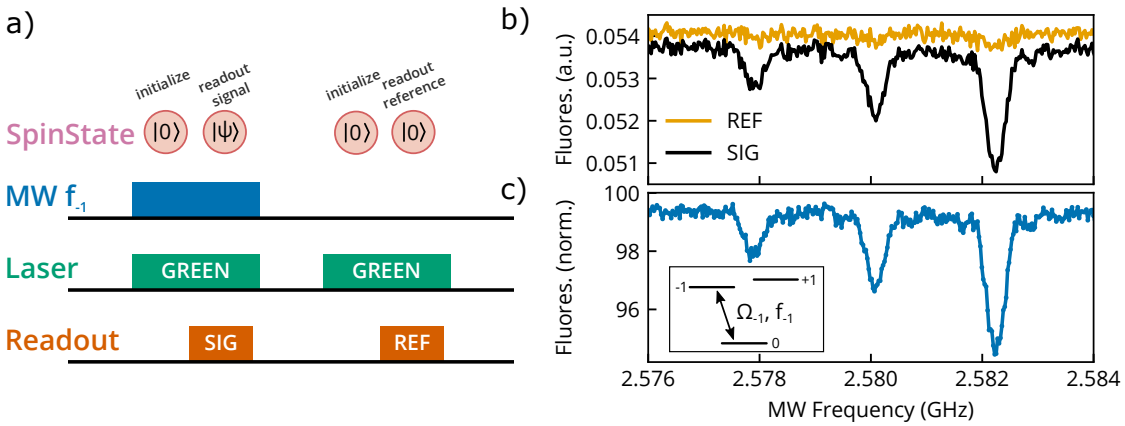

Figure 1.8: ESR sequence – (a) Applying continuous MW to either the $|0\rangle \leftrightarrow |-1\rangle$ or $|0\rangle \leftrightarrow |+1\rangle$ spin transition leads to a measurable difference in fluorescence signal when the MW radiation is on resonance with the electronic-hyperfine transitions (compare Fig. 1.6). (b) Fluorescence signal (SIG) and reference (REF) obtained as a function of MW frequency representative for an ensemble measurement. The data was taken with the setup described in Ch. 5 for Sample B (see Table 5.1). (c) Normalized fluorescence signal given by SIG/REF.

The obtained resonance signal can be referenced to the steady-state fluorescence measured with an identical sequence when no MW fields are applied ("REF", Fig. 1.8a and b). Laser light amplitude fluctuations are efficiently canceled and the signal is

expressed in normalized fluorescence units (see Fig. 1.8c) given by

$$\text{Fluorescence (norm.)} = \text{SIG/REF.} \tag{1.4}$$

The spin dynamics in an ESR sequence can be complex and exhibit unwanted linewidth narrowing and broadening, or contrast degradation may also occur. These effects are described by a rate equation model, which takes into account the lifetime of individual NV level, the laser light intensity and the MW drive strength [191, 194]. Employing a *pulsed* ESR scheme allows mitigation of some of the drawbacks encountered in ESR with continuous MW but requires calibration of the Rabi frequency, which is discussed next [194].

1.4.2 Rabi Nutation and Unitary Rotations

Applying continuous MW to either the $|0\rangle \leftrightarrow |+1\rangle$ or $|0\rangle \leftrightarrow |-1\rangle$ NV transition results in Rabi oscillations of the NV spin state and ODMR fluorescence signal. A typical Rabi sequence and measured Rabi signal is shown in Fig. 1.9. Similar to the ESR sequence, green laser light initializes the NV into the $m_s = 0$ ground state. Following initialization and picking the $|0\rangle \leftrightarrow |-1\rangle$ transition for example, resonant MW fields applied for a fixed period τ mix the $m_s = 0$ and -1 spin states. A short laser readout pulse collects the spin-population-dependent fluorescence, which is compared to a reference signal without any MW applied. By repeating the sequence for varying τ, a full Rabi curve is traced out. The resulting ODMR signal that exhibits coherent oscillation is shown in Fig. 1.9b.

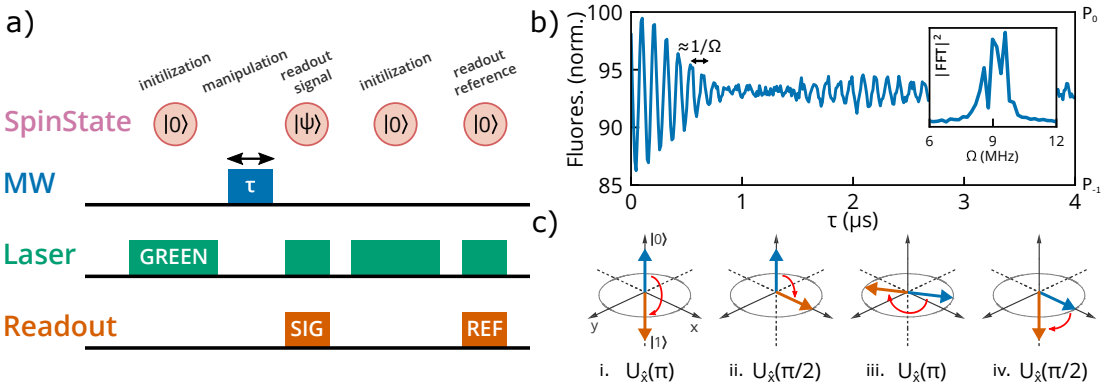

Figure 1.9: Rabi sequence – (a) Resonant MW fields are applied for a duration τ to either the $|0\rangle \leftrightarrow |-1\rangle$ or $|0\rangle \leftrightarrow |+1\rangle$ spin transition leading to oscillations of the NV fluorescence signal. (b) Normalized Rabi fluorescence signal as a function of MW pulse duration τ representative for a NV ensemble measurement. The data was taken with the setup described in Ch. 5 for Sample B (see Table 5.1). (c) Common spin manipulations explained using the Bloch sphere picture for varying initial spin states (blue arrows) and resulting final states (orange arrows). (i.) A π-pulse applied around $\hat{x}$ to the $|0\rangle$ state results in inversion of the spin population and yields $|-1\rangle$ (and vice versa). (ii.) A $\pi/2$-pulse applied around $\hat{x}$ to the $|0\rangle$ state results in the superposition state $\frac{1}{\sqrt{2}}(|0\rangle + |-1\rangle)$. (iii.) A π-pulse applied around $\hat{x}$ to the superposition state $\frac{1}{\sqrt{2}}(|0\rangle + e^{i\phi}|-1\rangle)$ results in a phase swap that yields the state $\frac{1}{\sqrt{2}}(|-1\rangle - e^{i\phi}|0\rangle)$. (iv.) A $\pi/2$-pulse applied around $\hat{x}$ to the superposition state $\frac{1}{\sqrt{2}}(|0\rangle + |-1\rangle)$ results in the state $|-1\rangle$.

For an idealized two-level system, the Rabi dynamics are described by the Hamiltonian (in the rotating frame, see Sec.A.1)

$$H_{rot}/h \approx -\delta|-1\rangle\langle -1| - \Omega(|0\rangle\langle -1| + |-1\rangle\langle 0|). \tag{1.5}$$

Here, δ is the detuning of the drive frequency from the $|0\rangle \leftrightarrow |-1\rangle$ spin transition and $\Omega \equiv \frac{\gamma_{NV}}{2\pi} B_1$ is the Rabi frequency for a given AC field B_1 applied *perpendicular* to the NV quantization axis. Solving the Schrödinger equation for the Hamiltonian in Eqn. 1.5, we find that for zero detuning ($\delta = 0$) the spin population in the $m_s = 0$

state, $P_{|0\rangle}$, changes sinusoidally with pulse duration τ and Rabi frequency Ω,

$$P_{|0\rangle} \propto \cos(2\pi\Omega\tau). \tag{1.6}$$

The evolution of $P_{|0\rangle}$ with applied on-resonant MW drive is evident by the oscillation of the ODMR signal in Fig. 1.9b, where a high fluorescence signal corresponds to maximal population in the $m_s = 0$ state ($P_{|0\rangle} \approx 1, P_{|-1\rangle} \approx 0$) and a minimal signal to maximal population in the $m_s = -1$ state ($P_{|0\rangle} \approx 0, P_{|-1\rangle} \approx 1$). It is important to note that it is the millisecond-long spin lifetime of the NV center ground state that allows for coherent manipulation of the spin state via MW fields and the sequential initialization and readout via laser light. Typical Rabi frequencies are $\sim 10\,\text{MHz}$ and correspond to MW pulse durations $\sim 100\,\text{ns}$. Typical laser pulses used for initialization are $\sim 1 - 10\,\mu\text{s}$, and typical readout times are $\sim 1\,\mu\text{s}$. All of these time scales are significantly shorter than the spin lifetime of the NV ground state ($\sim 1\,\text{ms}$).

In reality, the NV Rabi signal exhibits multiple Rabi frequencies that beat against each other. This is a consequence of the closely spaced hyperfine transitions that are inevitably driven off-resonantly with effective Rabi drive $\Omega_{eff} = \sqrt{\Omega^2 + \delta^2}$, where the detuning δ approximately equals the hyperfine splitting A_z. This can be readily seen by taking the Fourier transform of the plotted Rabi signal (Fig 1.9b inset), which displays three distinct effective Rabi frequencies. Moreover, the overall Rabi amplitude exhibits exponential-type decay as a manifestation of loss of polarization and decoherence of the NV quantum state over time. The exact decay shape of Rabi signals is beyond the scope of this section, but discussed for example in Reference [195] for a single NV and in Reference [196] for ensembles.

Unitary Evolution

With known Rabi frequency $\approx \Omega$ it is now possible to define a set of MW pulses to coherently control the NV spin state population. From Eqn. 1.6, it can be seen that after timing intervals $\tau_\pi \equiv 1/2\Omega$ the population is transfered from the $|0\rangle$ to the $|-1\rangle$ state and back, as evidenced by the oscillations of the ODMR Rabi signal. A MW pulse of duration τ_π ("π-pulse") subsequently describes the inversion of the spin population. This idea can be formulated more generally and it is convenient to describe the spin manipulation as arbitrary rotations of an initial spin state $|\psi\rangle$ on the Bloch sphere. The unitary rotation operator for an idealized spin$-1/2$ system and resonant driving ($\delta = 0$) is given by

$$\hat{U}_{\hat{n}}(\theta) \equiv \mathrm{e}^{i\theta\hat{n}\cdot\mathbf{S}} = \mathbf{I}\cos(\theta) + \hat{n}\cdot\mathbf{S}\sin(\theta), \tag{1.7}$$

where $\theta \equiv 2\pi\Omega\tau$ is the angle of rotation, $\mathbf{I}$ is the 2×2 identity matrix, $\hat{n} \in \{\hat{x}, \hat{y}, \hat{z}\}$ are the Cartesian unit vectors and $\mathbf{S} = \{\boldsymbol{\sigma}_x, \boldsymbol{\sigma}_y, \boldsymbol{\sigma}_z\}$ are the dimensionless Pauli matrices. It is then straightforward to show that $\hat{U}_{\hat{x}}(\pi)$ applied to the initial state $|0\rangle$ yields $|-1\rangle$ and vice versa, as one would expect from the Rabi signal. Additional common spin rotations used in NV experiments are shown in Fig. 1.9c and described in the caption. Coherent control of the NV spin states via rotations defined by Eqn. 1.7 and Fig. 1.9c are the building blocks for more advanced pulse sequences used in NV quantum information and quantum sensing applications. Pulse errors due to experimental imperfections must also be taken into account [197]. They enter in Eqn. 1.7 in two ways. First, imperfect pulse calibrations lead to errors in the

angle of rotation and $\theta \rightarrow \theta + \epsilon$, where $\epsilon \ll \theta$ is the rotation angle error. Second, rotations may not be perfect around a single axis, which leads to a tilt in the axis of rotation. For example, in the case of x-rotations with $\hat{x} = (1, 0, 0)$, then $\hat{x} \rightarrow (\sqrt{1 - n_y^2 - n_z^2}, n_y, n_z)$, where $n_y \ll 1$ and $n_z \ll 1$ describe the small tilt in the y- and z-direction, respectively. Although such tilt errors are typically small in experiments and dependent on hardware or calibration, pulse errors due to the nuclear hyperfine coupling ($m_I A_z$) become a relevant mechanism to be considered when many pulses are applied. For further discussion, see, for example, Reference [197]. We discuss protocols for DC and AC magnetic field quantum sensing in the following section.

1.4.3 Ramsey/Free Induction Decay Experiment

A pulsed Ramsey experiment, also known as free induction decay (FID) [135, 198, 199], is given by the sequence of pulses $\pi/2 - \tau - \pi/2$, where $\pi/2$ denotes MW pulses resonant with an NV transition of duration $\tau_{\pi/2} \equiv 1/4\Omega$ and τ is a free evolution interval. Without any prior knowledge of the exact details of the Ramsey sequence, intuition can be used from the unitary operator formalism introduced in the last section (Eqn. 1.7). The signal $S(\tau)_{Ramsey}$ of a Ramsey sequence is then calculated by

$$\begin{aligned} S_{\text{Ramsey}}(\tau) &= \|\langle 0|\hat{U}_{\hat{x}}(\pi/2)\hat{U}_{\hat{z}}(\tau)\hat{U}_{\hat{x}}(\pi/2)|0\rangle\|^2 \\ &= \tfrac{1}{2}[1 + \cos\phi(\tau)], \end{aligned} \tag{1.8}$$

or, alternatively,

$$\begin{aligned} S^{180^\circ}_{\text{Ramsey}}(\tau) &= \|\langle 0|\hat{U}_{-\hat{x}}(\pi/2)\hat{U}_{\hat{z}}(\tau)\hat{U}_{\hat{x}}(\pi/2)|0\rangle\|^2 \\ &= \tfrac{1}{2}[1 - \cos\phi(\tau)], \end{aligned} \tag{1.9}$$

.

Here, we have introduced the free evolution operator $\hat{U}_{\hat{z}}(\tau) \equiv \mathrm{e}^{i\phi(\tau)\boldsymbol{\sigma}_Z}$ which describes the precession of the spin on the Bloch sphere accumulating phase

$$\phi(\tau) = \gamma B_{DC} \tau \tag{1.10}$$

due to an external magnetic field B_{DC} *parallel* to the NV quantization axis during the time interval τ. The signal $S(\tau)_{Ramsey}$ thus oscillates at a frequency proportional to the applied field B_{DC} when the precession time τ is fixed (and vice versa). This is the foundation for sensing of DC magnetic fields using NV centers. In addition, the axis of rotation can be changed from $\hat{x}$ (Eqn. 1.8) to $-\hat{x}$ (Eqn. 1.9) in the last $\pi/2$ pulse to alter the phase of $S(\tau)_{Ramsey}$ by 180°. Similarly, we could use an axis of rotation around $\hat{x}$ and $\hat{y}$ (or $\hat{x}$ and $-\hat{y}$) in Eqn. 1.8 and 1.9, respectively, to obtain the sine signal of the phase and $S_{\mathrm{Ramsey}} \propto \sin\phi(\tau)$. The notion of being sensitive to either the cosine or sine and the accumulated phase ϕ is also referred to as cosine- and sine-magnetometry, respectively.

In experiments, each measurement is typically averaged over many runs, which results in an exponential-type decay of the mean Ramsey signal. This can be understood by taking the average of the signal $S(\tau)_{Ramsey}$, i.e., $S(\tau)_{Ramsey} \propto \langle \cos\delta\phi(\tau) \rangle$, where the noise of the accumulated phase $\delta\phi$ is a random variable. Applying the central limit theorem yields $S_{Ramsey} \propto \mathrm{e}^{-\langle \delta\phi^2 \rangle/2}$ and the Ramsey signal exhibits a Gaussian decay shape [200, 201]. This has been experimentally verified in single NV measurements, which show excellent agreement with the theory [49, 199]. In ensemble experiments, however, the Ramsey envelope exhibits simple exponential decay and highlights a fundamental difference between single-spin and many-spin experiments.

This difference is consistently observed throughout all NV measurements and is discussed in more detail in Ch. 2 and 6.

Figure 1.10 summarizes the NV Ramsey experiment. The general form of the experimental sequence (Fig. 1.10a) with initialization or readout via green laser light and manipulation with MW is similar to the ESR and Rabi sequences discussed in the last two sections. For fixed B_{DC} given by an applied bias field, the free evolution time τ between the $\pi/2$-pulses is swept and the ODMR fluorescence signal is plotted as a function of τ (Fig. 1.10b and c).

Double-Pulsed Scheme

Instead of providing a reference signal without any MW applied, as in the case of ESR and Rabi measurements, the Ramsey sequence is performed twice, and the phase of the last MW pulse is altered the second time. The total signal of such a *double-pulsed* Ramsey scheme [53] is then given by

$$\begin{aligned} S(\tau)_{\text{double-pulsed}} &= \frac{S(\tau)-S(\tau)^{180^\circ}}{S(\tau)+S(\tau)^{180^\circ}} \\ &= \cos\phi(\tau), \end{aligned} \tag{1.11}$$

and has a simple motivation: Laser noise amplitude fluctuations are efficiently canceled on a time scale T, where T is the spacing between laser readout pulses (resembling a lock-in scheme), while the SNR of the signal $S_{\text{Ramsey}}(\tau)$ increases by $\sqrt{2}\times$ when compared to the initial reference scheme discussed earlier (see Eqn. 1.4). Depending on the exact duration of τ between $\pi/2$-pulses and the length of readout/initialization pulses, the lock-in frequency $1/T$ can be as high as several hundreds

kHz. Figure 1.10b shows each individual Ramsey signal obtained (SIG1 and SIG2), exhibiting the 180° phase shift due to the change of the axis of rotation between the two Ramsey sequences. The combined final signal given by Eqn. 1.11 is depicted in Figure 1.10c and presented in units of contrast.

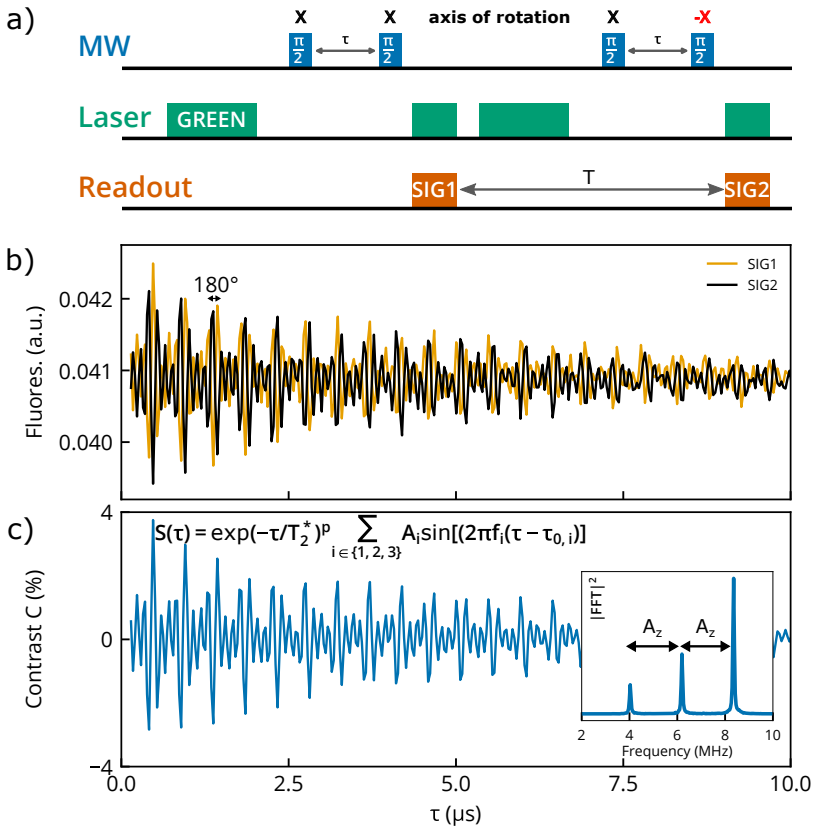

Figure 1.10: Ramsey sequence with double-pulse noise cancellation scheme – (a) A $\pi/2-\tau-\pi/2$ Ramsey protocol. (b) Individual Ramsey signals obtained through double-pulsed measurement (SIG1 and SIG2) representative for an ensemble measurement. By altering the phase of the final $\pi/2$ pulse from x to -x in (a), the Ramsey signals are phase shifted by 180 ° (compare Eqn. 1.8 and 1.9). The data was taken with the setup described in Ch. 5 for Sample B (see Table 5.1). (c) Normalized signal given by (SIG1-SIG2)/(SIG1+SIG2); Inset - FFT of Ramsey signal. The beat frequencies occur at $\delta + m_I Az$. When a finite drive detuning $\delta > A_z$ with the NV spin transitions is chosen, the beat frequencies are clearly separated. In the shown case, $\delta \approx 6\,\mathrm{MHz}$.

The measured Ramsey signals exhibits both the exponential-type decay and up to three sinusoidal signals beating against each other. Again, this is a consequence of the closely-spaced hyperfine transitions that are inevitably collectively addressed, a fact that was already mentioned in the Rabi experiment (Sec. 1.4.2). To distinguish the hyperfine beating frequencies, the applied MW field is slightly detuned from the exact NV resonances by a small amount δ resulting in three non-degenerate frequencies. It should also be noted that MW fields resonant with one of the hyperfine transitions would yield exactly two beat frequencies, or one if the center resonance is chosen. The beat frequencies are readily identified in the Fourier transform of the Ramsey signal (inset Fig. 1.10c), which reveals three peaks positioned at $\delta + m_I A_z$. When a detuning $\delta > A_z$ is chosen, the beat frequencies are clearly separated and spaced by the hyperfine splitting A_z.

In addition, the Ramsey envelope signal decays on a time-scale defined as T_2^* - the *inhomogeneous spin dephasing time*. Extending T_2^* and therefore prolonging the decay envelope is of crucial importance to improving the sensitivity for Ramsey-type DC magnetic field sensing. Mechanisms that limit T_2^* are discussed in more detail in Sec. 2.3.1 and this is also the focus of Ch. 5. Lastly, the measured Ramsey decay signal is well described by the analytical expression

$$S(\tau) = \exp(-\tau/T_2^*)^p \sum_{i\in\{1,2,3\}} A_i \sin[(2\pi f_i(\tau - \tau_0)], \tag{1.12}$$

where T_2^* is the characteristic decay time of the envelope, p is a phenomenological parameter, and A_i, f_i, and $\tau_{0,i}$ characterize the (up to) three hyperfine beat signals.

1.4.4 Ramsey DC Sensing

In Eqn. 1.8 and 1.9 we showed that for fixed free evolution time $\tau \equiv \tau_{meas}$, the fluorescence signal oscillates with a frequency proportional to the external magnetic field B_{DC}. Ramsey measurements thus provide a means to sense external magnetic fields by detecting a change in the accumulated phase of the NV sensor spin(s). Fig. 1.11 shows a typical NV Ramsey sensing sequence with applied calibration field B_{DC}. A typical sensing protocol is as follows:

i) trace out a Ramsey decay curve for fixed B_{DC} (Fig. 1.11b);

ii) fix the free evolution $\tau = \tau_{meas}$ that corresponds to a point of maximum sensitivity, so the sensitivity thereby scales with precession time τ_{meas} and contrast C_{meas} and is optimized when $\tau_{meas} \approx T_2^*$ (see below);

iii) repeat the Ramsey measurement at fixed τ_{meas} for different strengths of B_{DC} to trace out a magnetometry curve (Fig. 1.11c);

iv) select the region of maximum slope, $\max|\frac{\partial S}{\partial B}|$ (red lines, Fig. 1.10c), by fixing $B_{DC} \approx 0$; and

v) sense arbitrary fields by monitoring the change in measurement contrast using the calibration curve obtained in step iii).

The Ramsey signal for fixed τ_{meas}, indeed oscillates with a frequency proportional to B_{DC} and we have $S_{Ramsey}(B_{DC}) \propto \sin(\phi(B_{DC}))$ in sine magnetometry or $\propto \cos(\phi(B_{DC}))$ in cosine magnetometry. Sitting on any of the nodes of the magnetometry curve corresponding to maximum slopes $\max|\frac{\partial S}{\partial B}|$ (red lines, Fig. 1.10c), makes

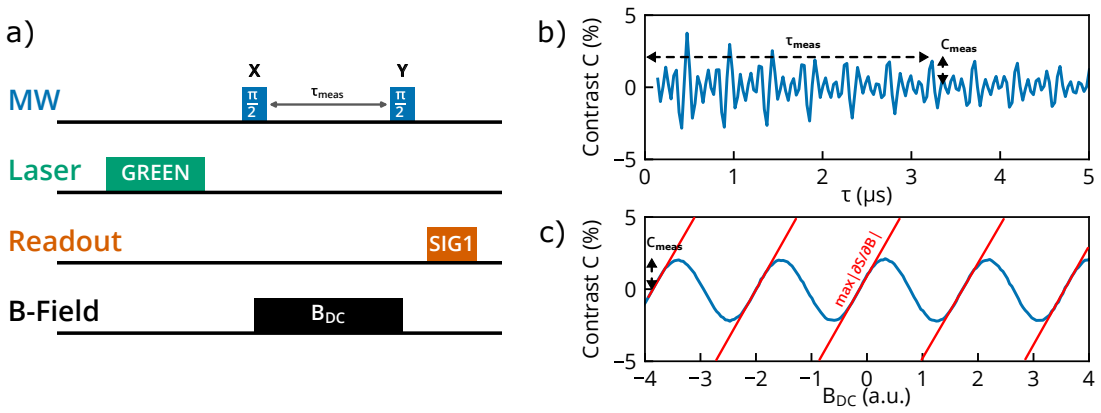

Figure 1.11: Ramsey sensing sequence – (a) Similar to Fig. 1.10 and by fixing B_{DC}, the normalized Ramsey signal in (b) is obtained. Note that the second half of the double-pulsed scheme is omitted for simplicity. (c) By fixing $\tau = \tau_{meas}$, however, and sweeping B_{DC}, a magnetometry curve is traced out. Red lines indicate the positions of maximal slope at which the Ramsey signal is maximally sensitive to the external fields that are to be sensed.

the Ramsey sequence maximally sensitive to changes in the magnetic fields B_{DC} that are to be sensed. Any change in B_{DC} is detected through a change in NV fluorescence or contrast signal, and the magnetic field strength can be extracted from the calibration curve obtained in step (iii). A drawback of such a Ramsey sensing scheme is the 2π phase ambiguity due to the sinusoidal nature of the signal and magnetic fields $B_{DC}(1 + m)$, where m is an integer number, whose values yield identical contrast values. However, such measurements are still useful for relative magnetic field sensing and noise spectroscopy.

Sensitivity Estimate

An important consideration in this protocol is the maximal magnetic sensitivity that can be obtained, which is derived in the following. Assuming a signal-to-noise ratio of unity, the minimum detectable magnetic field δB_{min} in a Ramsey measurement is

given by [41, 202]

$$\delta B_{min} \approx \frac{\delta S}{\max|\frac{\partial S}{\partial B}|}, \tag{1.13}$$

where the Ramsey signal in sine-magnetometry is

$$S = C_{meas}\sin(\gamma_{NV} B_{DC} \tau_{meas}).$$

Here, $C_{meas} \equiv C_0 \mathrm{e}^{-(\tau_{meas}/T_2^*)^p}$ is the measurement contrast at time τ_{meas} defined via the NV spin-state-dependent fluorescence visibility C_0 (see Eqn.1.4 and 1.11), γ_{NV} is the NV gyromagnetic ratio, B_{DC} is the magnetic field to be sensed, and τ_{meas} is the sensing time during which the NV sensor spins precess and accumulate phase. The term $\max|\frac{\partial S}{\partial B}|$ is the maximum slope of the Ramsey magnetometry signal,

$$\max|\frac{\partial S}{\partial B}| = C_{meas}\gamma_{NV}\tau_{meas}.$$

Assuming uncorrelated, Gaussian noise of the contrast signal with variance σ, the standard error of the contrast signal, $\delta S = \sigma(\tau_{meas})/\sqrt{n_{meas}}$, improves with the number of measurements n_{meas}. Including a dead time τ_D, which accounts for time spent during initialization of the NV ensemble and readout of the spin-state-dependent fluorescence during a single measurement, $n_{meas} = T/(\tau_{meas} + \tau_D)$ measurements are made over the total measurement time T. δB_{min} is then found to be

$$\delta B_{min} = \frac{\sigma\sqrt{\tau_{meas} + \tau_D}}{C_{meas}\gamma_{NV}\tau_{meas}\sqrt{T}},$$

and the sensitivity η is given by multiplying δB_{min} by the inverse bandwidth $\sqrt{T}$:

$$\eta = \delta B_{min}\sqrt{T} = \frac{\sigma\sqrt{\tau_{meas} + \tau_D}}{C_{meas}\gamma_{NV}\tau_{meas}}. \tag{1.14}$$

In the ideal case, neglecting state preparation and readout time, $\tau_D \ll \tau_{meas}$ and $\frac{\sqrt{\tau_{meas}+\tau_D}}{\tau_{meas}} \approx 1/\sqrt{\tau_{meas}}$. In this instance, the sensitivity becomes

$$\eta = \frac{\sigma}{C_{meas}\gamma_{NV}\sqrt{\tau_{meas}}}. \tag{1.15}$$

At this point we have not rigorously justified how to choose the optimal measurement time τ_{meas}, which enters in Eqn. 1.14 and 1.15 additionally via the measurement contrast $C_{meas}(\tau_{meas})$. Minimizing Eqn. 1.14 and 1.15 with respect to τ_{meas}, we find that in the ideal case (negligible overhead time, $\tau_D \ll \tau_{meas}$) the optimal precession interval is given by $\tau_{meas} = T_2^*/2$, while in the more realistic case with overhead ($\tau_D \gg \tau_{meas}$), $\tau_{meas} \approx T_2^*$.

Although this section has focused on DC sensing via Ramsey-type spectroscopy, many other sensing techniques exists. These include continuous [83, 101] and pulsed ESR sensing [194]. For each technique, a detailed sensitivity analysis should be made with consideration for MW and laser power and homogeneity requirements, bandwidth, and technical complexity. A comprehensive comparison is beyond the scope of this section but for example provided in Reference [86]. Nonetheless, given the straightforward experimental implementation, Ramsey sensing is expected to be a preferred DC sensing scheme. Furthermore, in Sec. 1.5 and Ch. 5, we show that Ramsey sensing in the $\{-1, +1\}$ ground-state sub-basis (so-called DQ Ramsey) can provide significant additional enhancements in magnetic sensitivity.

In ensemble magnetometry, additional improvements are obtained by noting that a magnetometer composed of N spins provides further enhancement in sensitivity

$\propto N^{-1/2}$. For example, taking a sensing volume of 1 mm^3 at an NV spin concentration of 1 ppm provides $N \sim 10^{14}$ spins. A challenge is then to optimize the product $(NT_2^*)^{1/2}$, since generally it is found that $T_2^* \propto 1/N$ and enhancements in sensor density are negated by a decrease in dephasing time T_2^*. This simplified picture does not consider experimental overhead time due to initialization and readout, laser and MW power requirements, or contrast degradation in high density samples into account but it is required for an extensive discussion of optimal sample characteristics in diamond sensing. Nonetheless, understanding limitations of T_2^* and increasing $(NT_2^*)^{1/2}$ in ensemble samples is at the forefront of developing ultra-high sensitivity bulk magnetometers and is discussed in more detail in Ch. 5.

1.4.5 Hahn Echo and Dynamical Decoupling

A spin Hahn echo measurement is given by the pulse sequence $\pi/2-\tau/2-\pi-\tau/2-\pi/2$, which differs from a Ramsey experiment only by a MW π-pulse applied halfway between the $\pi/2$-pulses [203]. Using the unitary operator formalism, it can be shown that the expected echo signal is identical to that of a Ramsey sequence (see Eqn. 1.8, 1.9, and 1.11), that is,

$$S_{echo}(\tau) = \cos(\phi), \tag{1.16}$$

but with an accumulated phase determined by

$$\phi(\tau) = \gamma_{NV} \left(\int_0^{\tau/2} B(\tau')d\tau' - \int_{\tau/2}^{\tau} B(\tau')d\tau' \right). \tag{1.17}$$

From Eqn. 1.17 it immediately follows that the echo sequence is *insensitive* to any static magnetic fields as the integral terms on the right-hand side are canceled. In contrast, this sequence is maximally sensitive to AC magnetic fields and noise components

at frequencies $f_{AC} \approx 1/\tau$, where τ is the sensing time of the protocol (see Fig.1.12a). Application of a π-pulse to the Ramsey sequence thus fundamentally changes the response of spin echo to magnetic fields when compared to Ramsey measurements. An alternative interpretation of the echo response can occur by noting that a π-pulse reverses the precession direction of our NV spin by swapping the spin populations in each basis state ($\{0, +1\}$ or $\{0, -1\}$) half-way through the measurement time. Given that the magnetic field remains constant throughout the measurement sequence, any phase $\phi(B_{DC})$ accumulated by the state $|-1\rangle$ (or $|+1\rangle$) during the first precession interval, is negated by the phase (with the opposing sign) accumulated during the second interval. Figure 1.12 shows a typical NV echo sequence and obtained signal.

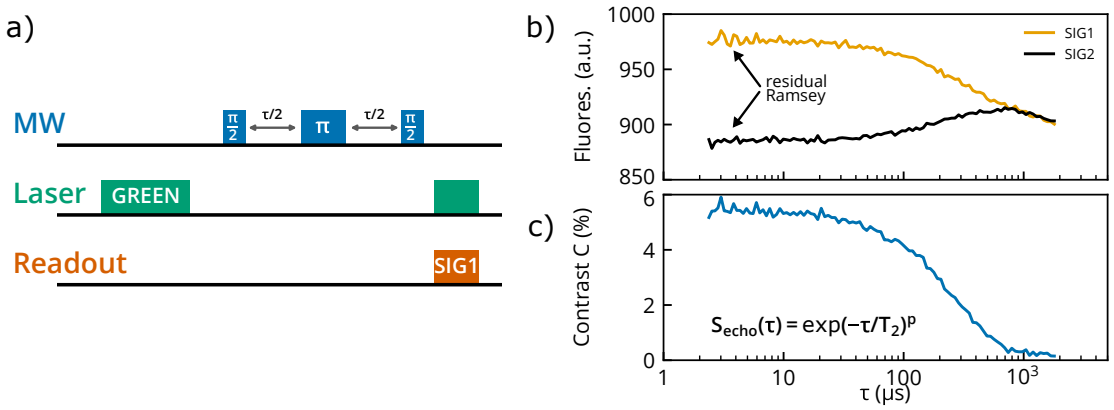

Figure 1.12: Hahn echo sequence – (a) A $\pi/2-\tau/2-\pi-\tau/2-\pi/2$ protocol representative for an ensemble measurement. Note that the second half of the double-pulsed scheme is omitted for simplicity (see Fig. 1.10). The data was taken with the setup described in Ch. 5 for Sample B (see Table 5.1). (b) Fluorescence signal (SIG1) and reference signal (SIG2) obtained via the sequence. The decay of SIG2 (and SIG1) at long precession times τ is due to spin-relaxation. Spin-relaxation effects are subtracted when (c) normalizing signal given by (SIG1-SIG2)/(SIG1+SIG2).

The echo curves (Fig. 1.12b and c) exhibit exponential-type decay, again a manifestation of the central limit theorem when averaging over many experimental iterations

$S_{echo}(\tau)$. The insensitivity of spin echo to static and slow varying magnetic fields also leads to a significantly prolonged decay time, denoted T_2; the *homogeneous spin dephasing time* [142] or *coherence time*. In a seminal study from 2009 it was shown that for single NV centers in ultra-pure, isotopically purified samples T_2 approaches the spin-lattice time of diamond ($T_2 \sim T_1 \sim$ ms) [123]. In ensemble samples, however, T_2 is typically limited by interactions with paramagnetic bath spins. A discussion of T_2 is provided in Sec. 2.3.2 and we experimentally study T_2 in Ch. 6.

Similar to the Rabi and Ramsey protocols, the finite detuning of the MW drive $\delta \approx A_z$ with the NV hyperfine spin states results in Ramsey-type oscillations on top of the Hahn echo decay signal [204]. These oscillations are suppressed when $\Omega/\delta \gg 1$. In addition, the residual Ramsey signal decays on a timescale T_2^* and when $T_2^* \ll T_2$, they will vanish quickly in the NV echo fluorescence signal, as shown in Fig. 1.12b.

Many extensions of spin echo have been investigated since its invention more than 60 years ago by Erwin Hahn [203]. Most importantly, by introducing an integer number n of equally spaced π-pulses to the sequence, the bandwidth is adjusted to n/T, given a total measurement time T [49, 197, 205, 206]. At the same time, the additional π-pulses alter the spectral response of the NV sensor to its surrounding environment, which leads to an increase of T_2. This technique, known as *dynamical decoupling*, allows the extension of T_2 to values that approach ~~to~~ the spin-lattice-relaxation time of diamond ($T_1 \sim 1$ ms at ambient temperature) for single [48, 49, 205] and ensemble samples [53, 189]. Generally, however, the coherence time improves

sublinearly with the number of pulses; i.e., $T_2 \propto n^{\lambda}$, where $\lambda < 1$ is a parameter that describes the efficacy of a pulse sequence to decouple a given bath noise spectrum. In Ch. 2 and 6, we show that λ for NV centers in a bath of electronic substitutional nitrogen spins (P1 centers) is $\lesssim 2/3$, which requires hundreds of decoupling pulses in specific cases to obtain a significant enhancement in T_2. Figure 1.13 summarizes the discussed pulse sequences so far and shows two important multi-pulse extensions to standard Ramsey and Hahn echo measurements.

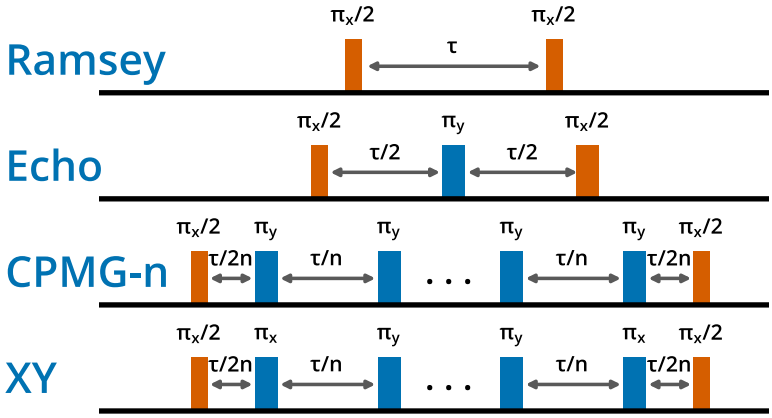

Figure 1.13: Common NV pulse sequences summarized – The Ramsey and Hahn echo protocol are compared to more advanced pulse sequences. CPMG is an extension of Hahn echo, where an even number of π-pulses are introduced[205]. XY is similar to CPMG but uses symmetric alteration of the axis of rotation between π-pulses (of the form x-x-y-x-y...y-x-y-x-x) to minimize the effect of pulse errors[197, 206].

1.5 $\{-1, +1\}$ Double Quantum Basis

All experimental protocols discussed so far were performed in either the $|0\rangle \leftrightarrow |+1\rangle$ or $|0\rangle \leftrightarrow |-1\rangle$ sub-basis of the NV^- ground state and approximate a spin$-1/2$ two-level system. In Sec. 1.3.4 we denoted the respective states $\{0, +1\}$ and $\{0, -1\}$ as single quantum (SQ) bases, since $\Delta m_s = 1$. In this section we highlight a few experimental differences when sensing in the $\{-1, +1\}$ sub-basis (DQ basis, $\Delta m_s = 2$) [41, 135, 202, 207, 208].

Several benefits can arise when sensing in the NV DQ basis, which takes advantage of the full spin-1 nature of the defect and employs the spin-1 basis states $\{0, -1, +1\}$. First, in the DQ basis, the NV gyromagnetic ratio is enhanced by a factor of two. Consequently, the phase accumulation due to external magnetic fields is doubled in Ramsey (see Eqn. 1.10), spin echo (see Eqn. 1.17), and related experiments when compared to SQ basis experiments. For a given precession time τ, this leads an increase in signal $\propto 2 \times \phi$ but also but also a sensing time (T_2^* or T_2) decreased twofold, which is a consequence of the enhanced gyromagnetic ratio in the DQ basis and increased susceptibility to magnetic noise. In this instance, the shot-noise limited sensitivity (Eqn. 1.15) improves by $\approx 2 \times \sqrt{1/2} = \sqrt{2}\times$. That said, much greater enhancements may be achieved in select cases, such as when the sensing time is limited by sources other than magnetic noise.

A DQ measurement probes the energy difference between the $m_s = +1$ and -1 states and hence is *immune* to perturbations (to first order) that shift the $m_s = -1$

and +1 spin states in common-mode. This can be seen from the NV ground state energy levels, which, in the simplified case, $D \gg \{\frac{\gamma_{NV}}{2\pi}B_x, \frac{\gamma_{NV}}{2\pi}B_y, M_x, M_y\}$ are given by (compare with Eqn. 1.2)

$$f_{\pm 1} \approx \underbrace{D + M_z}_{common-mode} \pm(\underbrace{\frac{\gamma_{NV}}{2\pi}B_z}_{differential} + m_i A_z). \tag{1.18}$$

By probing the energy difference, $\Delta f = f_{+1} - f_{-1}$, common-mode noise contributions, which enter via the D and M_z term, are largely suppressed, while magnetic noise contributions, entering via the B_z-dependence, double (consistent with a doubled gyromagnetic ratio).

It is the interplay between common-mode and differential terms in Eqn. 1.18 that dictate if the NV becomes more or less susceptible to a specific noise source when DQ is employed. For example, significant magnetic sensitivity enhancements can be obtained when the common-mode terms D and M_z in Eqn. 1.18 limit the magnetic sensitivity in a SQ basis measurements. The terms are suppressed in the DQ basis. This is indeed the case in ensemble measurement that utilize low nitrogen density samples. Indeed, in Ch. 5, we provide a detailed study of noise contributions in a [N] $\lesssim$ 0.05, 1, and 10 ppm sample, and this chapter offer the finding that in samples with [N] $\lesssim$ 1 ppm, crystal lattice strain fields ($\propto M_x, M_y, M_z$,) are the dominant noise mechanisms in DC sensing experiments when probed in the SQ basis. Measurements in the DQ basis are strain-insensitive when a magnetic bias field B_z is applied and therefore provide additional enhancements in magnetic field sensitivity beyond the factor $\sqrt{2}$. Similarly, the DQ basis can be employed for enhanced temperature sensing by making the measurement protocol twice as sensitive to the D parameter in

Eqn. 1.18 ($\frac{dD}{dT} \approx 74\,\mathrm{kHz/K}$ [108]) while canceling magnetic noise contributions [109].

1.5.1 Double Quantum Rabi

Although the experimental implementation of DQ measurements is straightforward, important differences exists for the sequences introduced in Sec. 1.4.1 - 1.4.5 when comparing SQ to DQ measurements. These differences become apparent in CW experiments in particular, and they are here discussed in the context of Rabi signals. In a SQ Rabi experiment (Sec.1.4.2), MW radiation resonant with $|0\rangle \leftrightarrow |+1\rangle$ (or $|0\rangle \leftrightarrow |-1\rangle$) transition result in a redistribution of the $\{0,+1\}$ (or $\{0,-1\}$) spin population and coherent oscillation of the NV fluorescence signal. An important notion is that MW fields cannot drive the $|-1\rangle \leftrightarrow |+1\rangle$ transition directly since the spin quantum Δm_s can only be changed by 1. The closest DQ analog to a SQ Rabi experiment is obtained by applying coherent MW drives simultaneously to the $|0\rangle \leftrightarrow |+1\rangle$ and $|0\rangle \leftrightarrow |-1\rangle$ transitions, and a typical DQ Rabi scheme is shown in Fig. 1.14.

For an idealized three-level system, the quantum dynamics with two Rabi drives Ω_{+1} and Ω_{-1} and detunings δ_{+1} and δ_{-1} are given by the Hamiltoniain (in the rotating frame)

$$H_{\mathrm{rot}}/h = -\delta_{+1}|+1\rangle\langle+1| - \delta_{-1}|-1\rangle\langle-1| - \frac{\Omega_{+1}}{\sqrt{2}}(|+1\rangle\langle 0| + |0\rangle\langle+1|) - \frac{\Omega_{-1}}{\sqrt{2}}(|-1\rangle\langle 0| + |0\rangle\langle-1|). \tag{1.19}$$

In this Hamiltonian, the MW field couples predominantly to the $|+1\rangle + |-1\rangle$ superposition state and by defining a bright and dark state basis, $|B\rangle = \frac{1}{\sqrt{2}}(|+1\rangle +$

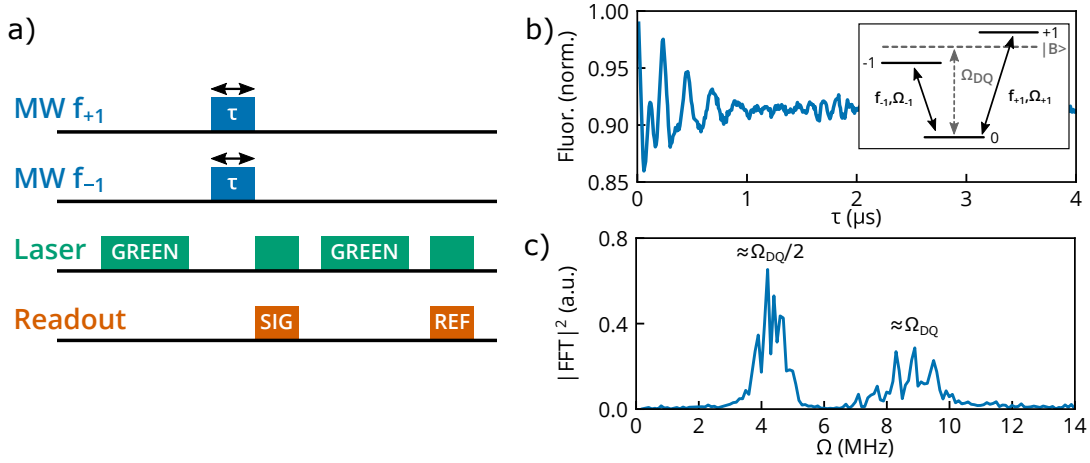

Figure 1.14: DQ Rabi protocol – (a) Schematic showing two Rabi drives $\Omega_{+1} \approx \Omega_{-1}$ applied to the SQ spin transitions and (b) resulting DQ Rabi oscillation representative for an ensemble measurement. Inset: level diagram with two-tone SQ drives and effective $\Omega_{DQ} = \sqrt{\Omega_{+1} + \Omega_{-1}}$ between the zero and bright state. (c) The Fourier transform of the Rabi signal exhibits the Rabi frequencies at $\Omega_{DQ} \approx \sqrt{2}\Omega_{SQ}$ and residual signals at $\approx \Omega_{DQ}/2$ with additional frequencies due to the hyperfine coupling A_z (see text for details). The data was taken with the setup described in Ch. 5 using Sample B (see Table 5.1).

$|-1\rangle$) and $|D\rangle = \frac{1}{\sqrt{2}}(|+1\rangle - |-1\rangle)$, respectively, Eqn. 1.19 can be recast to

$$H_{\text{rot}}/h = -\delta_{+1}|B\rangle\langle D| - \delta_{-1}|D\rangle\langle B| - \sqrt{\Omega_{+1} + \Omega_{-1}}(|B\rangle\langle 0| + |0\rangle\langle B|). \tag{1.20}$$

The Hamiltonian in Eqn. 1.20 is identical in form to the spin$-1/2$ single Rabi Hamiltonian given in Eqn. 1.5 and for zero detunings ($\delta_{+1} = \delta_{-1} = 0$) the spin population oscillates with enhanced DQ Rabi frequency $\Omega_{DQ} = \sqrt{\Omega_{+1}^2 + \Omega_{-1}^2}$ between the zero and bright state. When both Rabi drive frequencies are chosen to be equal, that is, $\Omega_{-1} \approx \Omega_{+1} \equiv \Omega_{SQ}$, the DQ Rabi frequency simply becomes $\Omega_{DQ} = \sqrt{2}\Omega_{SQ}$.

For finite detunings ($\delta_{+1} = \delta_{-1} \neq 0$), however, a residual population oscillates between the $m_s = 0$ and the dark state $|D\rangle$, adding Rabi frequencies at $\approx \Omega_{DQ}/2$ to

the signal. This leads to a rather complex Rabi beating in NV measurements and is shown in Fig. 1.14b. The Rabi frequency spectrum (Fig. 1.14c) thus exhibits multiple Rabi frequencies given the triplet hyperfine structure and two-tone Rabi drive. Nonetheless, since both fast and slow Rabi frequencies differ by $\approx 2\times$, an approximate DQ Rabi frequency Ω_{DQ} can be extracted from the measured Rabi signal and its Fourier transform. In Sec. A.1, we provide a detailed analysis of the DQ Rabi Hamiltonian described by Eqn.1.19 and its resulting signals for varying drives and detunings.

1.5.2 Double Quantum Ramsey

For pulsed experiments, the unitary operator formalism from Sec. 1.4.2 is easily adapted to the spin-1 system by replacing the Pauli matrices in Eqn. 1.7 with the dimensionless spin-1 operators and the 2×2 identity matrix with it 3×3 counter part. The signals for a Ramsey or echo sequence are then straightforwardly calculated and identical to the SQ case, where the accumulated phase ϕ_{DQ} is twice that of the SQ basis. It follows that the pulse sequences discussed in Sec. 1.4.2 - 1.4.5 can be equally employed by utilizing the spin-1 basis states $\{0, -1, +1\}$ and sensing is performed in the DQ $\{-1, +1\}$ sub-basis. We compare here the experimental difference when comparing SQ to DQ experiments.

First, in the SQ basis, the superposition state $\frac{1}{\sqrt{2}}(|0\rangle + |+1\rangle)$ (or $\frac{1}{\sqrt{2}}(|0\rangle + |-1\rangle)$ is used for sensing and obtained via application of a $\pi/2$-pulse of duration $\tau_{\pi/2} =$

$1/(4\Omega_{SQ})$ to the respective NV transition. We deployed the unitary rotation formalism to show that this is analog to a rotation of the $|0\rangle$ basis state by the angle $\theta = \pi/2$, i.e $\hat{U}_{\hat{x}}(\theta = \frac{\pi}{2})|0\rangle_{S=1/2}$. Similarly, the superposition state $\frac{1}{\sqrt{2}}(|+1\rangle + |-1\rangle|)$ that is relevant for DQ sensing (i.e., the previously-defined bright state $|B\rangle$) is obtained when the spin-1 $|0\rangle$ basis state is rotated by an angle $\theta = \pi/2$. This rotation is achieved experimentally by a full swap of the spin population from $|0\rangle$ to the bright state $|B\rangle$, which requires a DQ π-pulse of duration $\tau_\pi = 1/2\Omega_{DQ}$. A DQ Ramsey sequence thus consists of π-pulses in the bright-dark-state basis and not $\pi/2$-pulses as might be expected. Using $\Omega_{DQ} \approx \sqrt{2}\Omega_{SQ}$, the duration of the respective SQ pulses are found to be $\tau = 1/\sqrt{8}\Omega_{SQ}$, or $\sqrt{2}\times$ shorter than a π-pulse in the SQ basis.

In Fig. 1.15 we depict a typical DQ Ramsey protocol and resulting signal. Individual MW pulses applied to the $|0\rangle \leftrightarrow |+1\rangle$ and $|0\rangle \leftrightarrow |-1\rangle$ SQ transitions are labeled and portrayed along with the effective MW pulses that are relevant for manipulation of the spin-1 basis states (see Fig. 1.15a). The resulting DQ Ramsey signal (Fig. 1.15) is visually comparable to that of a SQ Ramsey sequence but oscillates at twice the hyperfine frequencies when finite and equal-magnitude detunings δ_{+1} and δ_{-1} with respect to $m_I = 0$ center resonances are chosen (see FFT Fig. 1.15c and inset).

Second, the detunings δ_{+1} and δ_{-1} must to be chosen with opposite sign, i.e, $\delta_{+1} = -\delta_{-1}$, to address the correct NV^- hyperfine states. This is readily seen in the inset of Fig. 1.15b, where the drive frequencies, $f_{+1} + \delta_{+1}$, $f_{-1} - \delta_{+1}$ and NV^- hyperfine states m_I are labeled. For arbitrary detunings, the DQ Ramsey signal beats

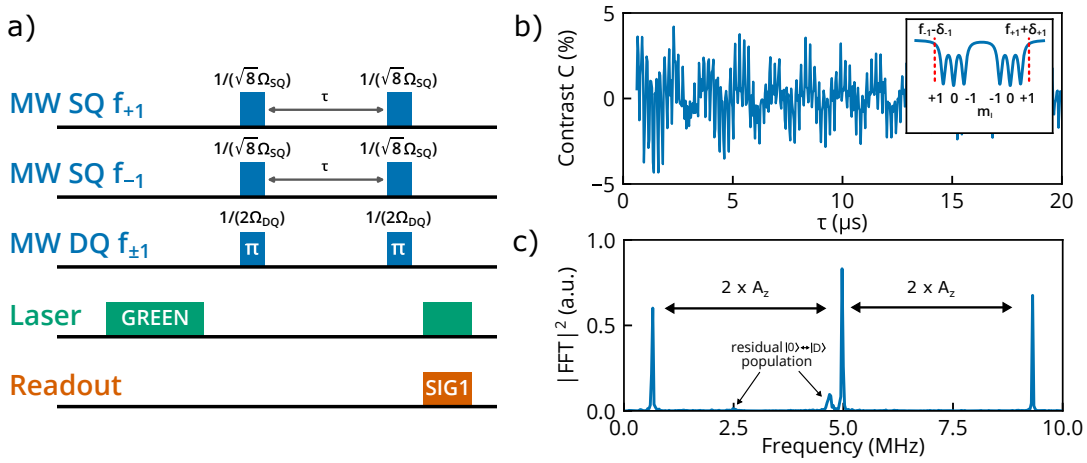

Figure 1.15: DQ Ramsey protocol – Sensing in the DQ basis $\{-1, +1\}$ requires a population swap from the spin-1 $|0\rangle$ state to the bright state $|B\rangle$ and is obtained via DQ π-pulses. Effective pulses for the DQ basis are obtained via manipulation of the SQ transitions. The data was taken with the setup described in Ch. 5 for Sample B (see Table 5.1). (b) DQ Ramsey signal and (c) Fourier transform, with resonances spaced by twice the hyperfine splitting. This is a manifestation of the doubled gyromagnetic ratio of the DQ basis. The data was taken with the setup described in Ch. 5 for Sample B (see Table 5.1).

at frequencies given by the difference between detunings and hyperfine splitting or it may exhibit additional beating at half of the precession frequency due to oscillation of population between the $|0\rangle$ and dark state $|D\rangle$. Pulse errors due to imperfect Rabi calibration and the finite detunings may also cause additional signals but are suppressed similarly to the SQ Rabi case when $\Omega_{DQ} \gg \delta_{\pm 1}$ (see Fig. 1.15c).

Third and lastly, we examine the axis of rotation in a double-pulsed DQ Ramsey. In Sec. 1.4.3, we have discussed the double-pulse scheme to allow for effective noise cancellation by measuring the Ramsey sequence twice. For the second Ramsey signal, however, we varied the axis of rotation for the last $\pi/2$-pulse from $\hat{x}$ (Eqn. 1.8) to $-\hat{x}$

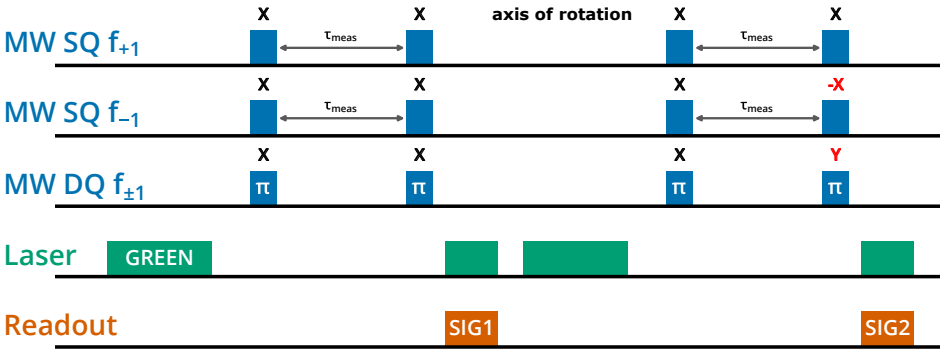

Figure 1.16: DQ Ramsey double-pulsed scheme for effective noise cancellation – The double-pulsed scheme for SQ Ramsey was explained in Sec. 1.4.3 and is adapted here to DQ Ramsey pulsed experiments. Note the change of axis of rotation for the last DQ π-pulse obtained by changing the axis of rotation of the SQ transition pulses. Similarly, the axis of rotation in the DQ basis can be manipulated for more advanced pulse sequences through control of the SQ transitions.

(Eqn. 1.9) to obtain a 180° phase-shifted signal, where the total signal was calculated via the visibility (SIG1 - SIG2)/(SIG1 + SIG2) $\propto \cos\phi$. A similar noise-canceling scheme can be deployed for DQ pulse experiments where the axis of rotation for the bright state $|B\rangle$ is determined through the axes of the SQ rotations. A resulting double-pulsed scheme for DQ Ramsey is shown in Fig. 1.16 and is calculated, for example, using the unitary operator formalism introduced in Eqn. 1.7, but adapted to the spin-1 system.

1.6 $^{14}NV^-$ and $^{15}NV^-$ Comparison

In Sec. 1.3.2 we have introduced the formation of NV^- centers either via growth or implantation of ^{14}N and ^{15}N isotopes. Experimentally, it can therefore be expected

that differences arise when working with $^{14}NV^-$ or $^{15}NV^-$ spins in NV applications. Most importantly, the spin multiplicity of the nitrogen-15 nuclear spin, $I = 1/2$, results in two different hyperfine spin states, $m_I = \pm 1/2$, and the corresponding NV^- ground-state energy spectrum thus exhibits two instead of three hyperfine transitions when compared to ^{14}N with $I = 1$ (see Eqn. 5.2). In addition, $^{15}NV^-$ spins exhibit a slightly increased hyperfine coupling $A_z \approx 3.1\,\text{MHz}$ [142, Tab. 1]. The change in the spin multiplicity and hyperfine coupling parameter is readily observed in NV applications when comparing $^{14}NV^-$ to $^{15}NV^-$ spins and discussed next.

1.6.1 Electron Spin Resonance

In Fig. 1.17 we compare a typical ensemble ESR frequency spectrum obtained for both NV^- isotope variants. The triplet hyperfine structure in the $^{14}NV^-$ case is reduced to a hyperfine doublet for $^{15}NV^-$ spins. In addition, the larger $^{15}NV^-$ hyperfine coupling results in increased spacing between individual hyperfine states. Note that in this figure we show the full NV ESR spectrum of the ensemble sample, and the spectrum exhibits four hyperfine resonance pairs, where each pair corresponds to the $|0\rangle \leftrightarrow |+1>$ and $|0\rangle \leftrightarrow |-1>$ spin transition aligned with one of four [111] diamond crystal axis.

1.6.2 Ramsey

The differences are also observable in Ramsey experiments and the SQ signals for both spin species are compared in Fig. 1.18. In both instances, the Ramsey signal exhibits a characteristic beating at frequencies $\delta + m_I A_z$ due to the finite detuning

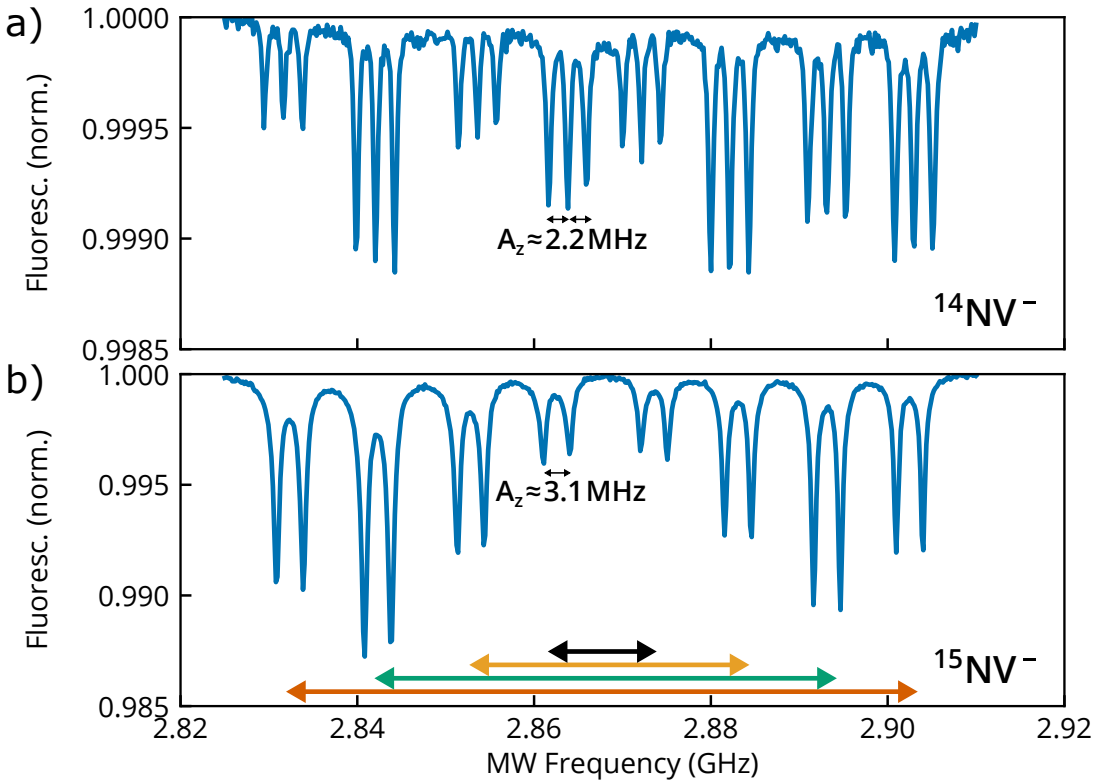

Figure 1.17: $^{14}NV^-$ and $^{15}NV^-$ ESR comparison – Full ESR spectrum for NV center ensembles with the ^{14}N (a) and the ^{15}N isotope. (b) The four resonance pairs indicated by the colored arrows correspond to the $|0\rangle \leftrightarrow |+1>$ and $|0\rangle \leftrightarrow |-1>$ electronic spin transitions for the four NV centers classes with quantization axes aligned along any of four [111] crystal directions. An arbitrary bias B-field direction was chosen. The difference in spin multiplicity and hyperfine coupling between the each isotope's nuclear spin modifies the NV ground-state energy spectrum given by Eqn. 1.2. The data in (a) was taken using Sample B (see Table 5.1), and in (b) using a $[^{12}C] = 99.999\,\%$ electronic-grade substrate, implanted with ^{15}N (14 keV, $2 \times 10^{12}\,cm^{-2}$). Both measurement were performed using the setup described in Reference [101]. Note that the contrast, linewidths, and distributions of the spin population in each hyperfine pair are dependent on sample properties and experimental details.

δ of the resonance drive frequency from the hyperfine resonances. In each case, a detuning $\delta > A_z$ was chosen to clearly separate the beat frequencies. The frequencies and hyperfine splittings are identified in the Fourier spectrum of the Ramsey signal

and are plotted in the insets of Fig. 1.18.

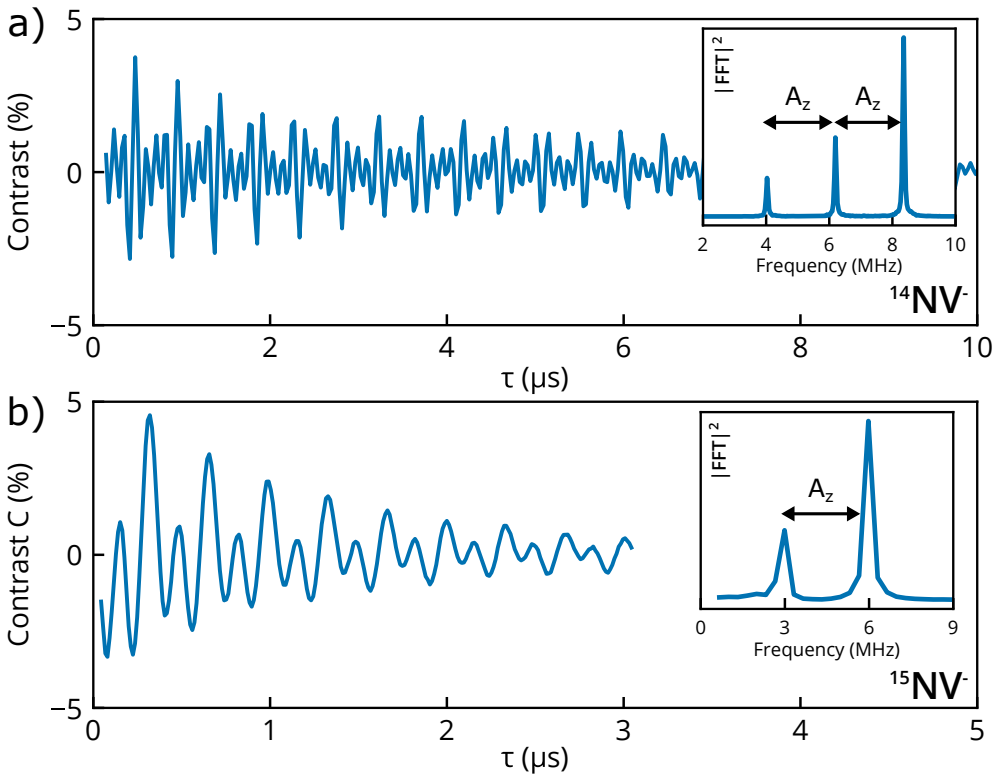

Figure 1.18: $^{14}NV^-$ and $^{15}NV^-$ Ramsey comparison – Ramsey signal for NV centers with the ^{14}N (a) and the ^{15}N isotope. (b) The difference in spin multiplicity and hyperfine splitting is readily observed in the Fourier-transformed Ramsey frequency spectrum (insets). Note that the decay time and measurement contrasts are dependent on sample properties. The data in (a) and (b) was taken with the setup described in Ch. 5 using Sample B and Sample C, respectively (see Table 5.1).

1.6.3 Echo/Electron-Spin-Echo-Envelope-Modulation

The most striking difference between $^{14}NV^-$ and $^{15}NV^-$ centers is apparent in a spin echo or dynamical decoupling sequence when a small off-axis magnetic field per-

pendicular to the NV quantization is present, as depicted in Fig 1.19. In the $^{15}NV^-$ case (Fig 1.19b), the Hahn echo signal exhibits *electron-spin-echo-envelope-modulation* (ESEEM) [14, 209–212]. This ESEEM results in a modulation of the $^{15}NV^-$ echo decay envelope at approximately the hyperfine frequency $A_z \approx 3.1\,\mathrm{MHz}$ and at a second frequency $f_L \approx \frac{\gamma_{^{15}N}}{2\pi} B_z$, which is proportional to the Larmor precession frequency of the ^{15}N nuclear spin in the applied bias field [213], where $\gamma_{^{15}N} = 2\pi \times 4.316\,\mathrm{MHz/T}$ is the nuclear gyromagnetic ratio of the ^{15}N.

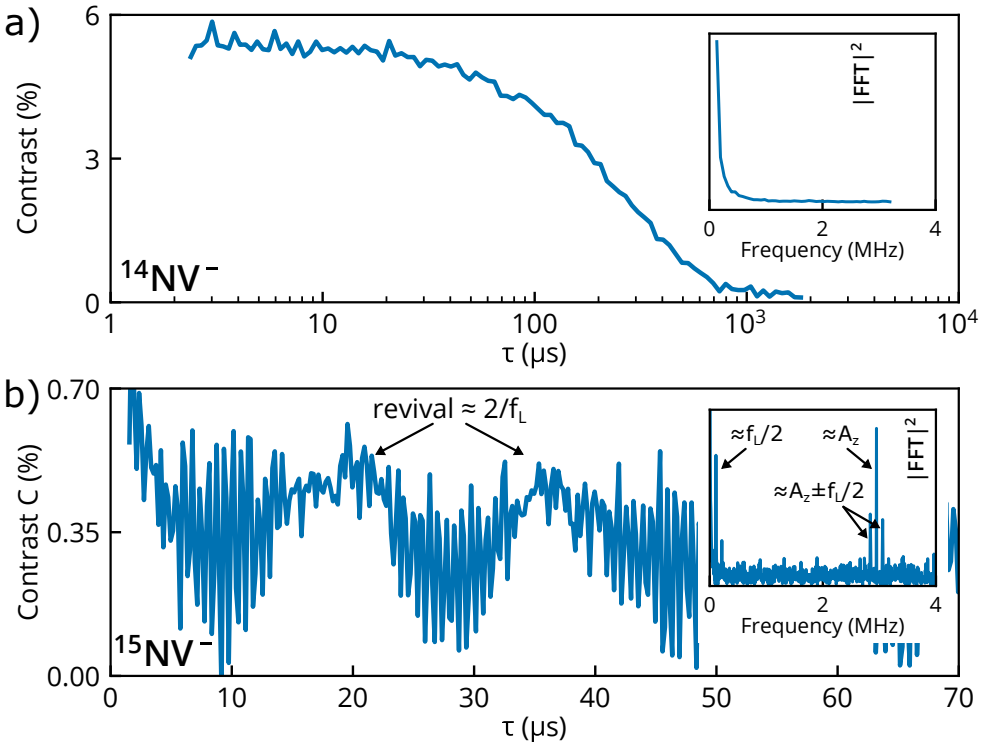

Figure 1.19: $^{14}NV^-$ and $^{15}NV^-$ spin echo comparison – Echo signal for NV centers with ^{14}N (a) and ^{15}N isotope (b). The absence of a quadropolar splitting in ^{15}N isotopes results in spin-echo-envelope-modulation (ESEEM) of the $^{15}NV^-$ decay envelope when a small magnetic field perpendicular to the NV quantization is present (for details see text). The data in (a) and (b) was taken with the setup described in Ch. 5 using Sample B and Sample C, respectively (see Table 5.1).

The absence of ESEEM in $^{14}NV^-$ centers (Fig 1.19a) highlights a fundamental difference in the NV ground state Hamiltonian for both nitrogen isotopes, which has discussed in Sec. 1.3.4. Specifically, the quadrupolar term PI_z^2 with quadropolar splitting parameter $P \approx -5\,\text{MHz}$ leads to a constant shift of the $m_I = \pm 1$ NV spin hyperfine states for ^{14}N isotopes. Although the quadropolar term has no effect on the NV electronic spin transitions, which are calculated by the difference in energy between the f_{-1} (or f_{+1}) and f_0 energy levels, it fixes the quantization of the ^{14}N nuclear spin along the quantization axis of the NV, irrespective of a small perpendicular magnetic field $\gamma_{^{15}N} B_\perp \ll P$. In other words, the large quadropolar splitting prevents the ^{14}N nuclear spin from Larmor precessing and explains the absence of ESEEM in $^{14}NV^-$ centers. For ^{15}N isotopes no quadropolar splitting exists, the quadropolar term vanishes and the ESEEM signal is visible in $^{15}NV^-$ centers. Similar ESEEM signals are observed for other nuclear spin species in diamond, particularly nuclear ^{13}C bath spins, and these are discussed in Sec. 2.6 [211, 214].

It is interesting to note that ESEEM is a coherent modulation of the echo envelope and AC magnetic field sensing could still be performed by sitting on any of the revival nodes of the signal that occur at multiples of $\approx 2/f_L$. The revivals and coherent modulation of the echo signal for $^{15}NV^-$ spins can be expressed by the analytical formula [209, 211, 212]

$$S_{\text{ESEEM}}(\tau) = A\text{e}^{-(\tau/T_2)^p}\left[1 - B\sin^2(\frac{2\pi f_1 \tau}{2})\sin^2(\frac{2\pi f_2 \tau}{2})\right], \tag{1.21}$$

where the first term describes the exponential-type decay of the signal envelope discussed in Sec. 1.4.5, A and B are constants, and $f_1 \approx A_z$, and $f_2 \approx f_L$ characterize the

sinusoidal modulation due to the hyperfine splitting and Larmor precession, respectively. With better magnetic field alignment of the bias field, the amplitude of the modulation is reduced and eventually disappears. In this instance, the $^{15}NV^-$ echo signal exhibits only exponential-type decay that is analogous to the $^{14}NV^-$ echo signal shown in Fig. 1.19a. In addition, the slow frequency modulation frequency given by $\approx f_L$ can be adjusted via the externally applied magnetic field and no modulation is observed when $f_L \ll 1/T_2$. Lastly, we note that the signals given in Eqn. 1.21 are derived for single center measurements, and since the average of many individual NV centers located at different lattice sites is taken for the ensemble signal, the single NV signal can only be considered as an approximation in ensemble measurements.

Chapter 2

Diamond Spin Bath

During diamond growth and NV center formation, a wide range of undesirable spin species may be incorporated into the diamond lattice [7, 169]. Paramagnetic defects interact with the NV spin state and result in a shortening of the NV spin coherence and lifetimes. Electronic impurities also act as dopants and can destabilize the charge state of NV centers. A thorough understanding of the diamond bath surrounding the NV spins is therefore of fundamental interest in NV research.

2.1 Introduction

Due to its high natural abundance and integral role in NV formation, substitutional nitrogen, the P1 center (N_S^0, S=1/2, 99.6 % ^{14}N natural abundance), is among the most important and comprehensibly studied spin defects in diamond [5–10]. Yet, nitrogen forms many other defect types including the ionized N_S^+ [169, 215], the

interstitial N_I nitrogen defect [169, 216], nitrogen clusters [169], nitrogen-vacancy-hydrogen (NVH) defects [217–219], and of course NV centers.

In diamonds with a natural abundance of ^{13}C isotopes ($I = 1/2$, 1.07 %), ^{13}C nuclear spins are the second relevant spin species to be considered due to their naturally high density. Over recent years, much has been learned about the ^{13}C spin bath and its contribution to NV decoherence [123, 190, 199, 211, 213, 214, 220–224]. Most importantly, by fabricating isotopically enriched ^{12}C samples ($[^{13}C] \ll 1.07\,\%$), interactions with ^{13}C bath spins can be largely eliminated, and purified samples are a preferred modality to date.

In addition to nitrogen and ^{13}C spins, vacancy-related defects are of fundamental interest in NV research [29, 146, 147, 169, 225–227]. Vacancies are introduced into the lattice during diamond growth as well as the irradiation step and they form many compound defects, including di- and multi-vacancy clusters. Although vacancies in diamond have been studied extensively, their crucial role in NV formation has lead to a recent increase in interest [146, 147, 227]. Lastly, at sufficiently high conversion efficiencies ($NV^-/N_S^0 \gg 1\,\%$), the bath dynamics are dominated by interactions between NV centers. Multiple studies have just begun to explore this high NV-density regime in detail [59, 228, 229].

In this chapter, we focus on the spin bath consisting of paramagnetic substitutional nitrogen spins, the P1 center, and ^{13}C nuclear spins. We first introduce

the physics of the P1 defect in in Sec. 2.2, then we describe its Jahn-Teller distortion and the origin of its resonance spectrum as measured through double-electron-electron-resonance (DEER) ESR. We then discuss the characteristic NV relaxation times associated with a bath of nitrogen spins (Sec. 2.3). In Sec. 2.4 we introduce an analytical model to describe the spin bath dynamics and we show validity with numerical simulations in Sec. 2.5. In Sec. 2.6 we provide a review of the ^{13}C nuclear spin bath characteristics. Lastly, three additional MW control techniques are introduced which, in combination with the spin control techniques introduced in Ch. 1, form a powerful set of tools to study the bath spins.

2.2 Nitrogen Spin bath

2.2.1 P1 Center

Naively, one might assume that a substitutional nitrogen atom in diamond forms four covalent bonds with its neighboring C-atoms and possesses a tetrahedral defect symmetry equivalent to that of diamond. In this configuration, the extra nitrogen valence electron could occupy any of the four anti-bonding orbitals along any of the [111] directions that are degenerate in energy. This degeneracy, however, gives rise to a Jahn-Teller distortion (see Sec. 2.2.2) and it has been found that the nitrogen atom does not occupy the carbon lattice site exactly, but is relaxed 10-40% away from any of the four neighboring carbon atoms [8, 9]. Consequently, the symmetry of the P1 center is reduced from tetrahedral to trigonal C_{3V}, such that the P1 center has the same symmetry as the NV^- center. This configuration is not stable by

any means and contrary to NV centers, and the P1 center constantly reorients itself with a reorientation rate determined by temperature, strain, quantum tunneling and external fields [8].

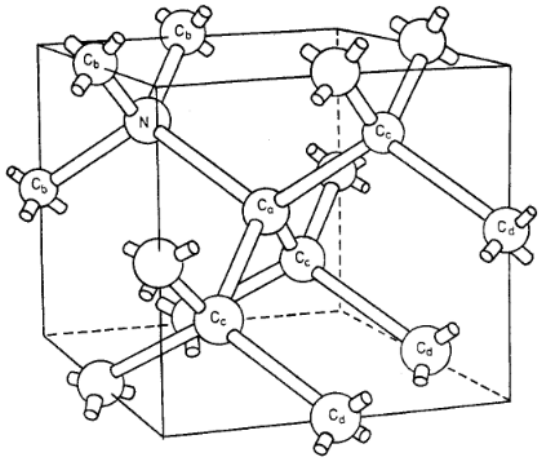

Figure 2.1: P_1 center schematic – Graph reproduced from Reference [7] - C_x correspond to the different neighboring carbon lattice sites. Equal letters describe atoms with equivalent dipolar-interaction strength.

2.2.2 Jahn-Teller Effect (JTE)

The Jahn-Teller effect (JTE) is a fundamental concept in molecular physics which has been studied in great detail for a wide range of systems [230]. In literature, especially regarding the NV center, the JTE effect is discussed as a *dynamic* process [136, 231], which refers to the fact that it is temperature activated. In this instance, local phonons (i.e., vibrons) interact with the electronic spin state of the central spin aiding the system to "relax" and lower its ground state energy. At cryogenic temperatures when the vibrionic degrees are frozen out, other effects may assist with this relaxation. This regime is referred to as the *static* Jahn-Teller regime.

An important notion is that the hyperfine coupling of the P1 center with its nuclear spin for both ^{14}N and ^{15}N isotopes is intimately related to the JTE. Fig. 2.2 shows a schematic of the P1 allowed magnetic dipole transitions when quadrupolar effects are neglected. When a magnetic field is applied to the diamond crystal, a single P1 center consisting of a ^{14}N isotope exhibits three ESR resonance dips corresponding to the three dipole-allowed transitions. The Jahn-Teller distortion, however, sets the quantization axis along any of the [111] crystal directions irrespective of the applied magnetic field and taking all four P1 orientations in diamond into account, the combined spectrum thus exhibits up to twelve resonances for ^{14}N. In case of ^{15}N, up to eight resonances are visible. When the magnetic field is aligned parallel to any of the [111] crystal axes relevant for NV experiments, the twelve (eight) spin resonances for ^{14}N (^{15}N) are partially degenerate.

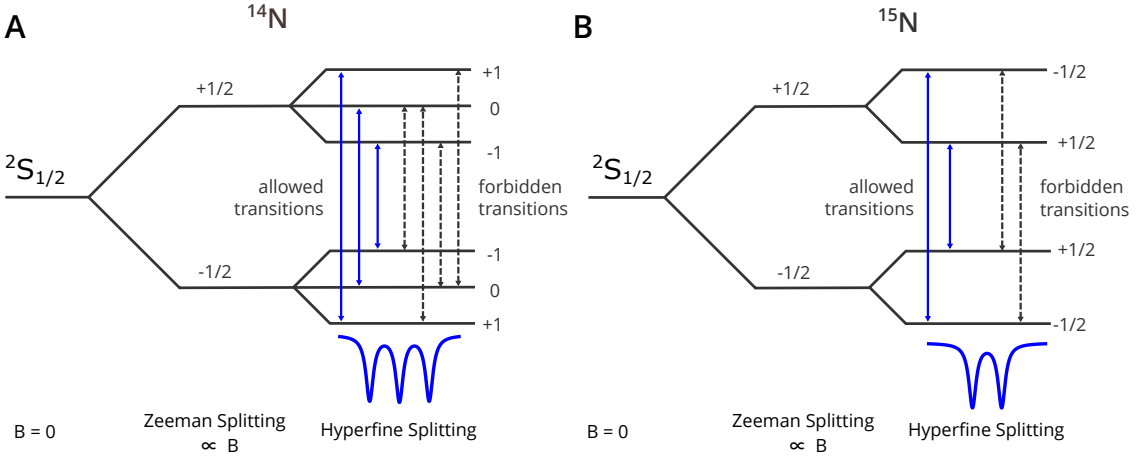

Figure 2.2: P1 center level structure – For the (a) ^{14}N and (b) ^{15}N isotope. Similar to the NV center, the difference in nuclear spin multiplicity modifies the energy levels. Allowed dipole-allowed transitions are shown in blue, solid lines. Forbidden transitions are shown as dashed lines. Note that quadropolar splitting is ignored.

Reorientation Rate

An remaining question has been the exact JTE reorientation rate at room temperature and is for example relevant for understanding NV decoherence. The rate has been studied in the low ($T \ll 280\,\mathrm{K}$) and high temperature regime ($T \gg 280\,\mathrm{K}$). The exact value at room temperature has not been determined experimentally, but is expected to be smaller than 35 kHz, a lower bound that was set by P1-linewidth measurements using ENDOR [6]. The rate is divided into the three temperature-dependent regimes [8, 9]:

i. A thermally activated regime (T $>$ 450 K),

ii. a tunneling regime (T $<$ 250 K), and

iii. an intermediate regime where thermal excitations and tunneling contribute to the reorientation.

The regimes are summarized in Fig. 2.3. In the thermally activated regime (i.), the reorientation rate may be described by an Arrhenius law,

$$\nu = \nu_0 \mathrm{e}^{-\frac{V}{k_b T}}, \tag{2.1}$$

where $\nu_0 \sim 4 \times 10^{12}\,1/\mathrm{s}$ is the bare reorientation rate at infinite temperature and $V = 0.76\,\mathrm{eV}$ is the activation energy. Both constants have been determined experimentally [7]. For temperatures below 250 K (ii.), the reorientation rate is well-described by a tunneling probability between two harmonic potential minima and is shown as a solid curve in Fig. 2.3 [8]. It is interesting to compare the estimated values for the room temperature reorientation rate (iii.) using both models and we find that

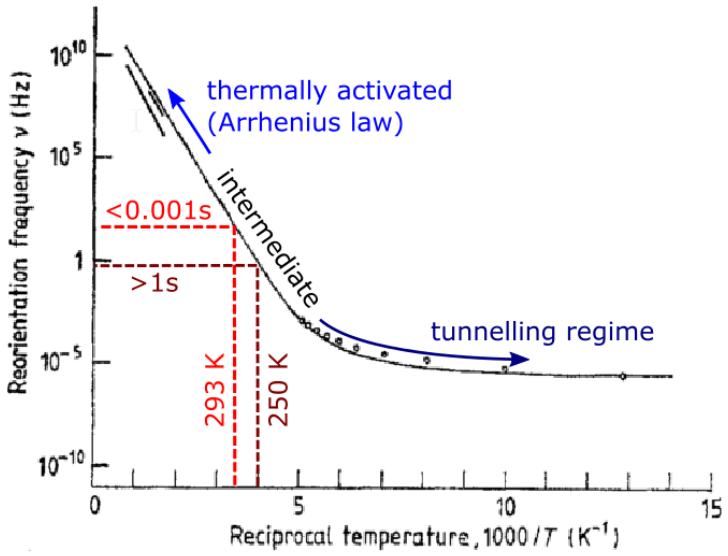

Figure 2.3: Jahn-Teller effect – Plot reproduced from References [9, p.37] and [8] with annotations: Circles and short lines at high temperature are experimental data. The cold-temperature simulations are extrapolated to room temperature. Reorientation rates at 250 and 293 K are labeled based on the extrapolated curve.

$\nu_{\text{Arrhenius}}(T = 293\,\text{K}) \sim 1\,\text{s}$; calculated using Eqn. 2.1, and

$\nu_{\text{tunneling}}(T = 293\,\text{K}) \sim 0.001\,\text{s}$; extrapolated from Fig. 2.3.

We find that both models give at best an order-of-magnitude estimate of the reorientation rate, but place it somewhere in the $0.001 - 1\,\text{s}$ range. The Jahn-Teller rate is thus close to the spin-relaxation time of diamond ($\sim$ ms). Further investigation is required. Recently, it was suggested that single NV centers may be employed to determine the P1 reorientation rate at intermediate temperatures $\lesssim 250\,\text{K}$ more precisely [232].

2.2.3 Hamiltonian

In this section we account for all the resonances in terms of Jahn-Teller, hyperfine, and quadrupolar splittings and present a full Hamiltonian calculation for the substitutional nitrogen defect. Such a resonance spectrum is for example obtained using paramagnetic resonance or alternatively the double-electron-electron-resonance (DEER) technique, which employs the NV center sensor for readout (see Sec. 2.7.1). In Fig. 2.4 we depict a typical ^{14}N and ^{15}N frequency spectrum measured via the DEER technique [177] and the observed resonance features are now discussed.

The relevant spin Hamiltonian for the substitutional nitrogen defect is given by [5–7, 10]

$$H_{\mathrm{P1}}/h = \underbrace{\mu_B/h\ \mathbf{B}\cdot\mathbf{g}\cdot\mathbf{S}}_{\text{electronic Zeeman}} + \underbrace{\mu_N/h\ \mathbf{B}\cdot\mathbf{I}}_{\text{nuclear Zeeman}} + \underbrace{\mathbf{S}\cdot\mathbf{A}\cdot\mathbf{I}}_{\text{hyperfine}} + \underbrace{\mathbf{I}\cdot\mathbf{Q}\cdot\mathbf{I}}_{\text{quadropolar}} \tag{2.2}$$

where μ_B is the Bohr magneton, h is Planck's constant, $\mathbf{B} = (B_x, B_y, B_z)$ are the magnetic field vector components, $\mathbf{g}$ is the electronic g-factor tensor, μ_N is the nuclear magneton, $\mathbf{S} = (\mathbf{S}_x, \mathbf{S}_y, \mathbf{S}_z)$ is the electronic spin vector, $\mathbf{A}$ is the hyperfine tensor, $\mathbf{I} = (\mathbf{I}_x, \mathbf{I}_y, \mathbf{I}_z)$ is the nuclear spin vector, and $\mathbf{Q}$ is the nuclear electric quadrupole tensor. This Hamiltonian can be simplified in the following way: First, we neglect the nuclear Zeeman energy since its contribution is negligible at magnetic fields used in this work ($\simeq 10\,\mathrm{mT}$). Second, the Jahn-Teller distortion defines a symmetry axis for the nitrogen defect along any of the [111]-crystal axis directions [8, 9]. Under this trigonal symmetry (as with NV centers), and by going into an appropriate coordinate system, tensors $\mathbf{g}$, $\mathbf{A}$, and $\mathbf{Q}$ are diagonal and defined by at most two parameters:

$$\mathbf{g} = \begin{pmatrix} g_\perp & 0 & 0 \\ 0 & g_\perp & 0 \\ 0 & 0 & g_\parallel \end{pmatrix}, \mathbf{A} = \begin{pmatrix} A_\perp & 0 & 0 \\ 0 & A_\perp & 0 \\ 0 & 0 & A_\parallel \end{pmatrix}, \text{ and } \mathbf{Q} = \begin{pmatrix} P_\perp & 0 & 0 \\ 0 & P_\perp & 0 \\ 0 & 0 & P_\parallel \end{pmatrix}. \quad (2.3)$$

Here, $g_\perp$, $g_\parallel$, $A_\perp$, $A_\parallel$, $P_\perp$, and $P_\parallel$ are the gyromagnetic, hyperfine, and quadrupolar on- and off-axis tensor components, respectively, in the principal coordinate system. Further simplifications can be made, by noting that the g-factor is isotropic [5], $g_\perp = g_\parallel \equiv g$, and that for exact axial symmetry the off-axis components of the quadrupole tensor, $P_\perp$, vanish [233]. Equation 2.2 may now be written as

$$H_{\mathrm{P1}}/h = g\mu_B/h \; B_z \; \mathbf{S}_z + A_\parallel \mathbf{S}_z \cdot \mathbf{I}_z + A_\perp(\mathbf{S}_x \cdot \mathbf{I}_x + \mathbf{S}_y \cdot \mathbf{I}_y) + P_{||}(\mathbf{I}_z^2), \quad (2.4)$$

where we dropped terms of the form $\mathbf{I}^3/3$ that lead to a constant energy shift, but do not affect the electronic spin transitions energies.

^{14}N Spectrum

The resulting calculated nitrogen frequency spectrum is compared with measurements in Fig. 2.4. The ^{14}N isotope has an electronic spin $S = 1/2$ and nuclear spin $I = 1$, leading to the six eigenstates $|m_S = \pm 1/2, m_I = 0, \pm 1\rangle$. The corresponding three dipole-allowed transitions ($\Delta m_S = \pm 1, \Delta m_I = 0$, solid arrows) are shown in Fig. 2.2a, along with the four first-order forbidden transitions ($\Delta m_S = \pm 1, \Delta m_I = \pm 1$, dashed arrows). The JTE effect sets a quantization axis along any of the four [111] crystallographic directions, irrespective of the applied magnetic field. Taking all JT

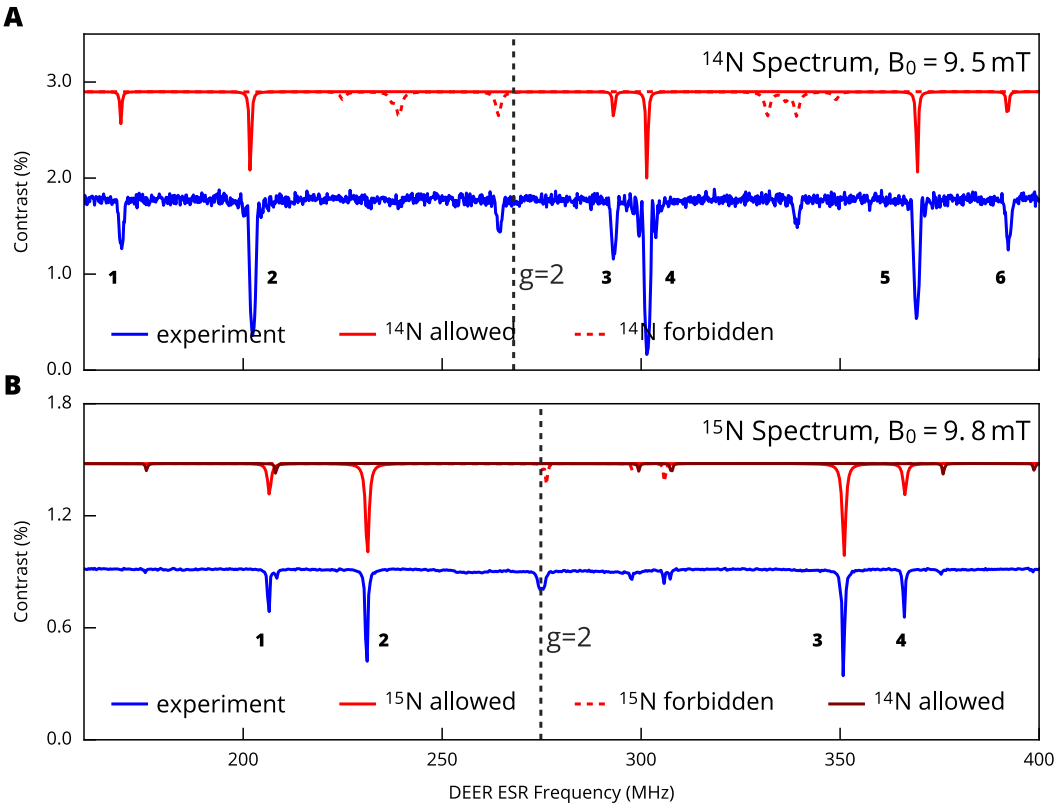

Figure 2.4: ^{14}N and ^{15}N ESR spectra taken with the NV DEER measurement protocol – (a) Simulated ^{14}N spectrum (red) and measured spectrum (blue) for a [N] = 0.75 ppm, ^{14}N sample. The dipole-allowed nitrogen hyperfine transitions are labeled 1 - 6. Smaller peaks are attributed to degenerate forbidden hyperfine transitions ($\Delta m_I \neq 0$) of the off-axis nitrogen orientations. The frequencies were simulated using Eqn. 2.4 and are plotted as Lorentzians with widths and amplitudes chosen to reflect the experimental data. The allowed hyperfine transitions have an approximate amplitude ratio of 1:3:1:3:3:1 (see main text). The Larmor frequency of an electronic spin without hyperfine shift ($g = 2$) is indicated as dashed black line. (b) Simulated spectrum (red) with measurements (blue) for a [N] = 10 ppm, ^{15}N sample. The ^{15}N dipole-allowed hyperfine transitions are labeled 1 - 4. Smaller peaks are attributed to forbidden ^{15}N hyperfine transitions and $g = 2$ dark spins. The spectrum of a small abundance of ^{14}N spins ($\approx 5\%$ of ^{15}N density) is visible as well. The data in (a) and (b) was taken with the setup described in Ch. 5 using Sample B and Sample C, respectively (see Table 5.1).

	^{14}N
g	2.0024[5]
$A_\perp, A_{\|\|}$	114 MHz, 81.3 MHz[5, 6, 10]
$P_{\|\|}$	-3.97 MHz[6]
	^{15}N
$A_{\|\|}$, $A_\perp$	-159.7 MHz, -113.83 MHz[10]
P	0 (since $I < 1$)

Table 2.1: Nitrogen defect parameters – Summary of defect parameters used to simulate the nitrogen resonance spectrum using Eqn. 2.4.

orientations into account, the full ^{14}N spin resonance spectrum displays a total of 12 dipole-allowed resonances. By aligning the magnetic field along any of the [111]-directions of the diamond crystal, the twelve transitions are partially degenerate and reduce to six visible resonances in an NV DEER measurement, with an amplitude ratio 1:3:1:3:3:1. We obtain the spectrum for the off-axis and degenerate JT orientations from Eqn. 2.4 by rotating the bias field by an angle $\theta = 109.471$ around either the x or y axis, where θ is the angle between any two crystallographic axes, i.e., taking $\mathbf{B} \rightarrow \mathbf{R}_{\text{x or y}}(\theta = 109.471^\circ) \cdot \mathbf{B}$.

In Fig. 2.4a, the simulated partially-degenerate spectrum for ^{14}N spins is shown together with experimental data from a [N] = 0.75 ppm sample. A magnetic field $B_z = 95.5\,\text{mT}$ was applied along one of the [111]-orientations. For the simulation the following parameters have been used: $g\mu_B/h \approx 2.8024 \times 10^4$ MHz/T, where

$g = 2.0024$ is the P1 electronic g-factor [5], $\mu_B = 9.274 \times 10^{-24}$ J/T is the Bohr magneton, $h = 6.626 \times 10^{-34}$ Js is Planck's constant, $A_{\|} = 114$ MHz, $A_{\perp} = 81.3$ MHz [5, 6, 10], and $P_{\|} = -3.97\,\text{MHz}$ [6]. The parameters are summarized in Tab. 2.1.

^{15}N Spectrum

The ^{15}N isotope has $S = 1/2$ and $I = 1/2$, leading to the four eigenstates $|m_S = \pm 1/2, m_I = \pm 1/2\rangle$. The corresponding two dipole-allowed transitions ($\Delta m_S = \pm 1, \Delta m_I = 0$, solid arrows) are shown in Fig. 2.2b, along with the two first-order forbidden transitions ($\Delta m_S = \pm 1, \Delta m_I = \pm 1$, dashed arrows). The experimental NV DEER spectrum for a sample with $[^{15}\text{N}] = 10\,\text{ppm}$ is shown in Fig. 2.4b, along with the simulated ^{15}N spectrum. For the ^{15}N simulation we used $B_0 = 9.8\,\text{mT}$, $A_{\|} = -159.7$ MHz, $A_{\perp} = -113.83$ MHz [10], and $P_{\|} = 0$ (since $I < 1$, compare Tab. 2.1). A small contribution due to residual ^{14}N spins in this ^{14}N sample is visible as well.

2.3 Relaxation Time Scales

To characterize the diamond spin bath, we consider the three characteristic NV center spin relaxation time scales T_2^* (inhomogenous dephasing), T_2 (homogeneous dephasing), and T_1 (spin-population decay) at ambient temperatures for varying nitrogen and ^{13}C spin concentrations. These time scales were introduced in Ch. 1 and can be determined experimentally employing ESR and pulsed measurements (see Sec. 1.4.1 - 1.5). In general it is found that $T_2^* \ll T_2 \ll T_1$, albeit T_2^* and T_2 may be significantly prolonged when quantum control techniques are employed for both NV center and

bath spins. A theoretical description of T_2^* and T_2 via a mean field approach is given in Sec. 2.4.1 and supported by simulations in Sec. 2.5. Detailed experimental results discussing limitations to T_2^* and T_2 values for NV centers in a bath of paramagnetic nitrogen spins are presented in Ch. 5 and 6.

2.3.1 Inhomogeneous Dephasing Time T_2^*

For single and ensemble measurements, the inhomogenous dephasing T_2^* is defined by the spin resonance linewidth measured in an ESR experiment (see Sec. 1.4.1). In these measurements, however, broadening due to the applied MW drives and laser light ought to be avoided [191, 194]. The linewidth is then limited by static and quasi-static bath noise sources that include dipolar interactions with paramagnetic bath spins, crystal lattice strain-fields, magnetic field gradients and expansion of the diamond lattice due to ambient temperature changes [135].

For single NV centers in ultra-pure diamond samples ([N] $\ll 1\,\mathrm{ppm}$, [^{13}C] $\ll 1.07\,\%$), T_2^* values in the $50 - 450\,\mu\mathrm{s}$ range have been reported [52, 202, 208, 234]. These high values are in drastic contrast to typical ensemble measurements $\lesssim 1\,\mu\mathrm{s}$ [71, 108, 146, 160]. For ensembles at low bath spin concentrations, T_2^* is typically limited by gradient fields intrinsic to the diamond or of the experimental apparatus. For single centers spatial inhomogeneities due to gradient fields are not relevant and a single NV T_2^* may therefore greatly exceed the ensemble value. In Fig. 2.5 we summarize reported T_2^* ensemble values for NV centers and related spin systems.

A distribution of single NV measurements in an ultra-pure diamond from Reference [234] is shown for comparison. At fractional sensor densities $\ll 1$, inhomogeneities including paramagnetic bath spins and strain-fields limit $T_{2\,\mathrm{ens}}^{*}$ to a value well-below the spin-spin interaction limit (red shaded area). This limit is estimated calculating the average dipolar coupling interaction strength between sensor spins given by $\gamma_{\mathrm{e-e}} = \frac{\mu_0}{4\pi} g^2 \mu_B^2 / \hbar \frac{1}{\langle r \rangle^3} \approx 2\pi \times 9 \cdot [f]\,\mathrm{GHz}$, where μ_0 is the vacuum permeability, g is the electron g-factor, μ_B is the Bohr magneton, $\hbar$ is the reduced Planck constant, and $\langle r \rangle$ is the average spacing between spins. A fractional sensor density of 1 corresponds to $10^{23}\mathrm{cm}^{-3}$ and at spin sensor densities approaching unity, spin-spin interaction thus places an upper bound on T_2^*.

2.3.2 Homogeneous Dephasing Time T_2

In a Hahn echo sequence, the NV spin is insensitive to static and low-frequency noise sources in the spin bath, which are efficiently canceled by inverting the spin precession direction via application of a π-pulse half-way through the free precession interval (see Sec. 1.4.5) [49, 53, 60, 189, 214, 235]. The increased susceptibility of the NV center to AC noise, but reduced susceptibility to static noise sources leads to a significantly prolonged decay time in Hahn echo experiments, when it is compared to Ramsey. Since in Ramsey measurements static noise dominates, we generally have $T_2 \gg T_2^*$ for both single and ensemble measurements.

For low nitrogen content, isotopically purified ^{12}C samples ([N] $\ll 1\,$ppm, [^{13}C] $\ll$

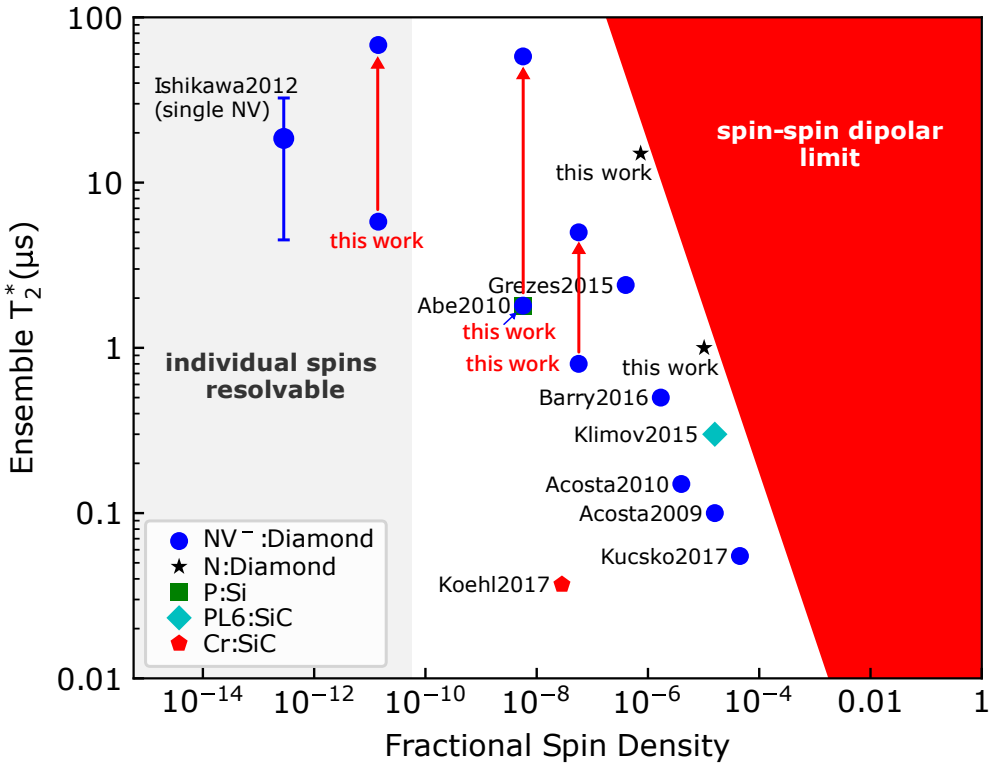

Figure 2.5: T_2^* survey for electronic solid-state spin ensembles as a function of density for NV centers and related systems (see legend) – Inhomogeneous dephasing due to paramagnetic bath spins, strain fields and other effects limit $T_{2\,ens}^*$ at low sensor densities $\ll 1$ (see text for details). At spin densities approaching unity, spin-spin interaction places an upper bound on the ensemble dephasing. The region in which individual, single spins are resolvable with confocal microscopy ($\sim 200\,\mathrm{nm}$ average spin distance) is shown in gray. T_2^* values determined for the nitrogen spins (P1 centers) are shown for reference as well (black stars, see Sec. C.5). Measurements by Ishikawa et al.[234] were performed on single NV centers and the error bar indicates the spread in measured T_2^* values. Red arrows indicate improvement from the bare T_2^* as measured in the NV SQ basis and increase when quantum control techniques are employed to suppress inhomogeneities (see Ch. 5). For references see [135].

1.07 %), T_2 approaches the spin-lattice relaxation time in diamond ($T_2 \sim T_1 \sim 1\,\mathrm{ms}$, see Sec. 2.3.3) [123]. However, when the diamond spin bath contains a relevant

concentration of paramagnetic spin species ($\gg 1\,\mathrm{ppb}$), T_2 scales approximately inversely with the concentration of bath spins and $1/T_2 \propto \frac{\mu_0}{4\pi}\gamma_{NV}\gamma_n\hbar[\mathrm{n}]$, where [n] is the bath spin density [3, 222, 236]. In Ch. 5 and 6, we study the dependence for both the ensemble T_2^* and T_2 as a function of nitrogen concentration over the range $[\mathrm{N}] = 0.01{-}300\,\mathrm{ppm}$ and extract the characteristic scalings $T_2^*(N) = 10.6{\pm}1.9\,\mu\mathrm{s}{\cdot}\mathrm{ppm}$ and $T_2(N) = 156 \pm 15\,\mu\mathrm{s}{\cdot}\mathrm{ppm}$.

It is important to note that the single and ensemble T_2 values extracted via Hahn echo measurement are of similar magnitude [201], since inhomogeneities including strain and magnetic field gradients are not relevant. This stands in contrast to Ramsey measurements where generally $T_{2\,\mathrm{single}}^* \neq T_{2\,\mathrm{ens}}^*$. For this reason, T_2 is also referred to as the *homogeneous dephasing time* [142]. Nonetheless, in T_2 measurements a difference between single and ensemble signal is observed and given by a change in stretched exponential parameter p, which is discussed in Sec. 2.4.1.

For a dynamical decoupling sequence, such as CPMG-n and XY-n (see Fig. 1.13), T_2 is enhanced proportionally to the applied number of π-pulses [53, 177, 197, 201, 237] and the Hahn echo T_2 time is replaced by

$$T_{2,n} = \left[1/(T_2 n^{\lambda}) + 1/T_{2,max}\right]^{-1}. \tag{2.5}$$

Here, $\lambda < 1$ is a spin-bath noise related parameter [49, 197, 201, 237] (see Sec. 6.4) and $T_{2,max} \approx T_1/2$ accounts for the coherence time limit imposed by the finite spin-lattice relaxation time T_1 [53].

2.3.3 Relaxation Time T_1

While T_2^* and T_2 are the characteristic time scales of decoherence in a spin system, T_1 characterizes the loss of spin population towards the Boltzmann distributed equilibrium. When spin population is lost, coherences are also inevitable destroyed and T_1 therefore imposes an upper limit on the maximal value of T_2^* and T_2. The limitations to T_1 in bulk diamond are separated into a spin-lattice-relaxation and cross-relaxation regime [53, 171, 228, 238–242].

In the low NV density regime, i.e., when interactions between individual NV centers can be neglected, T_1 is limited by spin-lattice relaxation. In this instance, collective crystal lattice phonon modes modify the orbital stats of the NV spin resulting in decay of spin population in the NV ground state towards the Boltzmann populations [142, 242]. For a spin-1/2 system, the relationship between T_2 and T_1 is well-established and given by $T_{2,max} \leq 2T_1$ [233]. For NV centers in bulk diamond, however, this limit has been reported to be $T_{2,max} \approx 0.5T_1$ [53] and was also confirmed in nano-diamonds [243], a discrepancy that remains unresolved to date. The room-temperature T_1 times in bulk diamond are typically in the $1 - 10\,\mathrm{ms}$ range and comparable for single centers [52] and ensembles [128, 239, 244]. A set of ensemble T_1 times is shown for example in Fig. 6.1b. Since lattice phonons are temperature activated, the T_1 time and thus T_{2max} are increased when working at cryogenic temperatures. In this instance, T_1 is prolonged by orders of magnitudes when $T \ll 280\,\mathrm{K}$ and values exceeding few seconds have been demonstrated [38, 53, 171, 238].

A second T_1 relaxation mechanism is introduced at high NV spin densities, when interactions between individual NV centers become relevant. In this regime, a single NV spin can relax via a flip-flop with a neighboring resonant spin. Population is then removed from the two-spin system via interactions with additional resonant centers, a process known as *cross-relaxation*. In this regime, T_1 is dependent on the NV density [228, 229, 241].

For NV centers within few nanometers from the diamond boundaries, surface effects also need to be taken into account. In this instance, the T_1 value is greatly reduced in comparison to bulk samples. For further discussion see Reference [106, 107].

2.4 Analytical Model of the Spin Bath Dynamics

A simplification of the description between the NV central spin and the spin bath is obtained via a mean field approach. In this picture, the NV-bath interaction is given by the semi-classical Hamiltonian [49, 245]

$$H_{\text{NV-bath}} = S_z B(t) \tag{2.6}$$

where $B(t)$ is a random noise process. $B(t)$ should be Gaussian with mean $\langle B(t) \rangle = 0$, Markovian, and stationary which is only full-filled by the Orenstein-Uhlenbeck stochastic noise process [246] and a derivation is motivated here.

2.4.1 Orenstein-Uhlenbeck Noise Process

The total accumulated phase of an NV center is generally described by

$$\phi = \gamma_{NV} \int dt f(t) B(t), \tag{2.7}$$

where γ_{NV} is the NV spin gyromagnetic ratio, $f(t)$ is the step-like filter function of our pulse sequence, and $B(t)$ is the magnetic field that the spin senses, including both external fields and fields originating from the spin bath surrounding the spin. The probability to find the NV in state $|0\rangle$ after time τ is given by

$$S(\tau) = \frac{1}{2}\left(1 + \langle \cos\phi \rangle\right) = \frac{1}{2}\left(1 + \Re[\langle e^{i\phi} \rangle]\right), \tag{2.8}$$

where $i\phi$ is a random variable drawn from a distribution. Note that Eqn. 2.8 is a more generalized version of the spin signals derived for Ramsey and Hahn echo in Sec. 1.4.3 and Sec. 1.4.5, respectively. In these sections, we described the action of the coherent MW pulses as unitary rotations applied to an idealized spin-1/2 system and derived the sinusoidal spin signal in the first part of Eqn. 2.8. The statistical average over the sinusoidal signal was motivated by an average over many experimental runs.

Considering we have a large number of impurity spins with different couplings to the NV center, we assume that the random fluctuating B-field due to the spin bath has a Gaussian distribution with zero mean, simply due to the central limit theorem. This makes the moment generating function $M_{i\phi}(1) = e^{-\langle \phi^2 \rangle/2}$, giving us

$$S(\tau) = \frac{1}{2}\left(1 + e^{-\langle \phi^2 \rangle/2}\right) = \frac{1}{2}\left(1 + e^{-\chi(\tau)}\right). \tag{2.9}$$

Here,

$$\chi(\tau) \equiv \int_0^\infty \frac{d\omega}{\pi} S_B(\omega) \frac{F(\omega\tau)}{\omega^2}, \tag{2.10}$$

where the classical B-field spectral noise density is

$$S_B = \gamma_{NV}^2 \int dt \mathrm{e}^{i\omega t} \langle B(t)B(0)\rangle, \tag{2.11}$$

and $2F(\omega\tau)/\omega^2$ is the Fourier transform of the filter function $f(t)$ squared. $F(\omega\tau)$ for the Ramsey, Hahn echo and CPMG-n sequence are summarized in Tab. 2.2.

Sequence	$F(\omega\tau)$
Ramsey	$2\sin^2(\frac{\omega\tau}{2})$
Hahn echo	$8\sin^4(\frac{\omega\tau}{4})$
CPMG-n (odd n)	$2\tan^2(\frac{\omega\tau}{2\omega\tau n+2})\sin^2(\frac{\omega\tau}{2})$
CPMG-n (even n)	$8\sin^4(\frac{\omega\tau}{4n})\sin^2(\frac{\omega\tau}{2})/\cos^2(\frac{\omega\tau}{2n})$

Table 2.2: Filter functions $F(\omega\tau)$ for a Ramsey, Hahn echo and CPMG-n sequence reproduced from Reference [235].

For a bath spin Larmor precessing at ω_L, the effective B-field at the central spin is given by $B_0\cos(\omega_L t)$. Let us assume this impurity spin couples to other bath spins over time scales characterized by τ_c (the bath correlation time) such that the coherent spin precession decays and the B-field at the central spin can be approximated by $B(t) = B_0\cos(\omega_L t)\mathrm{e}^{-t/\tau_c}$. Thus, the bath spectral density becomes

$$\begin{aligned} S_B(\omega) &= \gamma_{NV}^2 \int dt \mathrm{e}^{i\omega t}\langle B_0^2\rangle \cos(\omega_L t)\mathrm{e}^{-t/\tau_c} \\ &= \tau_c\gamma_{\mathrm{NV}}^2\langle B_0^2\rangle \left\{ \frac{1}{1+(\omega-\omega_L)^2\tau_c^2} + \frac{1}{1+(\omega+\omega_L)^2\tau_c^2} \right\}. \end{aligned} \tag{2.12}$$

In the short time (high frequency) limit, the bath spectral density function can be simplified to

$$S_B(\omega) \approx \gamma_{NV}^2\langle B_0^2\rangle\tau_c \frac{2}{1+((\omega-\omega_L)\tau_c)^2}. \tag{2.13}$$

This is equivalent to treating the spin bath as an Ornstein-Uhlenbeck stochastic process [177, 201, 246, 247]. In both cases, B_0 characterizes the total magnetic noise contributions to the central spin (in frequency units), and τ_c characterizes the spin bath interaction time-scales. Defining $\Delta^2\tau_c/\pi = 2\gamma_{NV}^2\langle B_0^2\rangle$ and setting $\omega_L = 0$, the Lorentzian spectral density given in Eqn. 2.13 takes the form

$$S(\omega, \Delta, \tau_c) = \frac{\Delta^2\tau_c}{\pi}\frac{1}{1+(\omega\tau_c)^2}, \tag{2.14}$$

which has an amplitude $\Delta^2\tau_c$ and HWHM of $1/\tau_c$.

2.4.2 Single Center Decay

Ramsey

For a Ramsey measurement, which was discussed in the first chapter, Sec. 1.4.3, the filter function is given by $F(\omega\tau) = 2\sin^2(\omega\tau/2)$ (see Tab. 2.2), leading to

$$\begin{aligned}\chi_{Ramsey}(\tau) &= \frac{1}{\pi}\int_0^\infty \frac{d\omega}{\omega^2}\frac{\Delta^2\tau_c}{\pi}\frac{1}{1+(\omega\tau_c)^2}2\sin^2(\omega\tau/2) \\ &= \Delta^2\tau_c^2\left(\frac{\tau}{\tau_c} - 1 + \mathrm{e}^{-\tau/\tau_c}\right).\end{aligned} \tag{2.15}$$

For short times, i.e., $\tau \ll \tau_c$ (but $\Delta\tau_c \gg 1$), χ is approximately given by

$$\chi_{Ramsey}(\tau) \approx \frac{1}{2}\Delta^2\tau^2,$$

Substituting this in Eqn. 2.9, we get

$$S_{\text{single}}^{\text{Ramsey}}(\tau) = \frac{1}{2}\left(1 + \mathrm{e}^{-(\tau/T_{2\,\text{single}}^*)^2}\right), \tag{2.16}$$

where

$$T_{2\,\text{single}}^* \equiv \sqrt{2}/\Delta. \tag{2.17}$$

We see that T_2^* for a single NV is solely determined by the NV-bath coupling Δ and intra-bath dynamics characterized by τ_c can be ignored at short timescales $\tau \ll \tau_c$, which is typically a good approximation for single NV experiments [49, 199]. Moreover, the Ramsey decay exhibits Gaussian decay, in agreement with the central limit theorem [200, 248, 249].

The Ramsey measurement can also be related to the spin resonance lineshape measured via an ESR sequence (see Sec. 1.4.1). While ESR measurements probe the frequency domain, Ramsey measurements probe dephasing in the time domain, and the ESR lineshape is obtained from a Fourier transform of the Ramsey signal. For single NV centers, the Fourier transform of the decay shape in Eqn. 2.16 gives a Gaussian lineshape,

$$S(f)^{\mathrm{ESR}}_{\mathrm{single}} = A\mathrm{e}^{-\frac{1}{2}\left(\frac{f}{\sigma}\right)^2} \tag{2.18}$$

and is characterized by the variance σ. Latter is related to $T^*_{2\,\mathrm{single}}$ by

$$T^*_{2\,\mathrm{single}} = \frac{\sqrt{2}}{2\pi\sigma} = \frac{2\sqrt{\ln 2}}{\pi\Gamma_{\mathrm{single}}}, \tag{2.19}$$

where $\Gamma_{\mathrm{single}} = 2\sqrt{2\ln 2}\sigma \approx 2.35\sigma$ is the full width at half max (FWHM) of the ESR lineshape and $\Delta = 2\pi\sigma$ [200, 250].

Hahn Echo

For a spin echo measurement, the filter function is $F(\omega\tau) = 8\sin^4(\omega\tau/4)$ (see Tab. 2.2 giving us

$$\begin{aligned}\chi_{\text{Echo}}(\tau) &= \frac{1}{\pi}\int \frac{d\omega}{\omega^2}\frac{\Delta^2\tau_c}{\pi}\frac{1}{1+(\omega\tau_c)^2}8\sin^4(\omega\tau/4) \\ &= \Delta^2\tau_c^2\left(\frac{\tau}{\tau_c} - 3 - \mathrm{e}^{-\tau/\tau_c} + 4\mathrm{e}^{-\tau/2\tau_c}\right). \end{aligned} \tag{2.20}$$

For short times, i.e., $\tau \ll \tau_c$ (but $\Delta\tau_c \gg 1$), χ is approximately given by

$$\chi_{\text{Echo}}(\tau) \approx \frac{\Delta^2}{12\tau_c}\tau^3. \tag{2.21}$$

Substituting this in Eqn. 2.9, we get

$$S^{Echo}_{\text{single}}(\tau) = \frac{1}{2}\left(1 + \mathrm{e}^{-(\tau/T_{2\text{single}})^3}\right), \tag{2.22}$$

and the Hahn echo signal has qubic decay shape. For $\tau \ll \tau_c$ we have $T_2 = \left(\frac{12\tau_c}{\Delta^2}\right)^{1/3}$, and the T_2 time is a function of both NV-bath coupling Δ and intra-bath coupling τ_c.

2.4.3 Ensemble Decay

The time dependences in a NV ensemble measurement become different if we average the signal from several NV centers at different lattice site with varying local environments.

Ramsey

The probability distribution function (PDF) relating a single NV value Δ_{single} and the ensemble value Δ_{ens} was given by [200]

$$P(\Delta_{\text{single}}) = \frac{\Delta_{\text{ens}}}{\Delta^2_{\text{single}}}\sqrt{\frac{2}{\pi}}\text{e}^{-\frac{1}{2}\left(\frac{\Delta_{\text{ens}}}{\Delta_{\text{single}}}\right)^2}. \tag{2.23}$$

Since the distribution in Eqn. 2.23 exhibits a heavy-tail $\propto 1/\Delta^2_{\text{singe}}$, a single NV value is only weakly determined by the ensemble value and one cannot be inferred easily from the other [200].

To obtain the T_2^* signal from an ensemble of NV centers, we average over various Δ_{single} giving us

$$S(\tau)^{\text{ens}}_{\text{Ramsey}} \propto \int_0^\infty P(\Delta_{\text{single}})\text{e}^{-(\tau/T_2^*)^2}d\Delta_{\text{single}}, \tag{2.24}$$

where from Eqn. 2.17 we know that $T^*_{2\,\text{single}} = \sqrt{2}/\Delta_{\text{single}}$. Integrating over Δ_{single} we obtain

$$S^{\text{ens}}_{\text{Ramsey}}(\tau) = \frac{1}{2}\left(1 + \text{e}^{-(\tau/T^*_{2,ens})}\right) \tag{2.25}$$

where

$$T^*_{2,ens} = 1/\Delta_{\text{ens}}. \tag{2.26}$$

Thus, measuring the Ramsey decay of an ensemble gives us the mean coupling strength between NV centers and the bath spins. In addition, the decay shape is simple exponential and different from the Gaussian decay observed in a single NV Ramsey measurement.

Similar to the single NV case, we can relate the ensemble Ramsey signal to the ensemble lineshape measured in an ESR sequence. The Fourier transform of Eqn. 2.25 gives a Lorentzian lineshape,

$$S(f)^{\mathrm{ESR}}_{\mathrm{ens}} = A\frac{1}{1+\left(\frac{f}{\delta}\right)^2} \tag{2.27}$$

where δ is the half width at half max (HWHM). δ and the $T^*_{2\,\mathrm{ens}}$ are related by

$$T^*_{2\,\mathrm{ens}} = \frac{1}{2\pi\delta} = \frac{1}{\pi\Gamma_{\mathrm{ens}}}, \tag{2.28}$$

and $\Gamma_{\mathrm{ens}} = 2\delta$ is the FWHM of the Lorentzian lineshape [200, 250].

Hahn echo

We now perform a similar analysis to get an expression for the ensemble-averaged $T_{2\mathrm{ens}}$. In this case, we need to take into account the bath dynamics. The PDF of $\tau_{\mathrm{c,single}}$ is approximated to be similar to that of Δ_{single} since both are determined by dipolar-interactions. We thus have

$$P(\tau_{\mathrm{c,single}}) = \frac{(1/\tau_{\mathrm{c,ens}})^2}{(1/\tau_{\mathrm{c,single}})}\sqrt{\frac{2}{\pi}}\mathrm{e}^{-\frac{1}{2}\left(\frac{1/\tau_{\mathrm{c,ens}}}{1/\tau_{\mathrm{c,single}}}\right)^2}. \tag{2.29}$$

First, we average over various Δ_{single} to get

$$S(\tau) \propto \int_0^\infty P(\Delta_{\mathrm{single}})\mathrm{e}^{-(\tau/T_2)^3}d\Delta = \mathrm{e}^{-\frac{\Delta_{\mathrm{ens}}\tau^{3/2}}{\sqrt{6\tau_{\mathrm{c}}}}}, \tag{2.30}$$

where $T_2 \approx \left(\frac{12\tau_{\mathrm{c,single}}}{\Delta^2_{\mathrm{single}}}\right)$ (see Eqn. 2.21). Integrating over the distribution of τ_c gives us

$$S(\tau) \propto \int_0^\infty P(\tau_{c,\mathrm{single}})\mathrm{e}^{-\frac{\Delta_{\mathrm{ens}}\tau^{3/2}}{\sqrt{6\tau_{\mathrm{c,single}}}}}d\tau_{c,\mathrm{single}} = \frac{\Delta^6_{\mathrm{ens}}\tau^9}{1769472\pi^2\tau^3_{\mathrm{c,ens}}}\mathbf{G}^{5,0}_{0,0}\left(\frac{\Delta^4_{\mathrm{e}}\tau^6}{18432\tau^2_{\mathrm{c,ens}}}|_{\{-\frac{3}{2},-\frac{5}{4},-1,-\frac{3}{4},0\}}\right), \tag{2.31}$$

where **G** is the Meijer-G function. For the wide range of experimental parameters $(\tau, \tau_{\mathrm{c,ens}}, \Delta_{\mathrm{ens}})$ under consideration, the Meijer-G function can be well-approximated by an exponential, giving us

$$S_{\mathrm{ens}}^{\mathrm{Echo}}(\tau) \approx \frac{1}{2}\left(1 + \mathrm{e}^{-(\tau/T_{2,ens})^{3/2}}\right), \tag{2.32}$$

where $T_{2,ens} = (9\tau_{\mathrm{c,ens}}/\Delta_{\mathrm{ens}}^2)^{1/3}$.

The stretched exponential parameter $p \approx 3/2$ of the decay signal in Eqn. 2.32 in an ensemble measurement is thus reduced by a factor 1/2 when compared to the single NV value ($p = 3$, see Eqn. 2.22); in analogy to the reduction of the Ramsey decay stretched exponential parameter when the single ($p = 2$, see Eqn. 2.16) to the ensemble measurement ($p = 1$, see Eqn. 2.25) is compared.

2.4.4 T_1 Decay

We discuss here for completeness the decay shapes observed in T_1 experiments, although a rigorous derivation is beyond the scope of this section. The T_1 decay shape in both single [52] and ensemble [171, 239, 244] measurements is of approximately simple exponential form when T_1 is limited by spin-lattice relaxation,

$$S(\tau)_{\text{lattice-relaxation}} = A\mathrm{e}^{-\tau/T_1}. \tag{2.33}$$

However, when T_1 is limited by cross-relaxation, T_1 is dependent on the NV spin density and the ensemble decay shape exhibits a square-root-type decay shape of the form [229, 241]

$$S(\tau)_{\text{cross-relaxation}} = A\mathrm{e}^{-(\tau/T_1)^{1/2}}. \tag{2.34}$$

The change in decay shape from simple exponential in Eqn. 2.33 to square-root-type in Eqn 2.34 is, again, attributed to the spatial averaging of many individual NV center signals and consistent with the change in stretched exponential parameter observed in T_2^* and T_2 measurements. In the intermediate regime, when both spin-lattice- and cross-relaxation contribute to T_1 decay, the decay is more generally described by a free stretched exponential parameter p and given by [251]

$$S(\tau)_{\text{intermediate-regime}} = A\mathrm{e}^{-(\tau/T_1)^p}, \tag{2.35}$$

where $0.5 < p < 1$ [228, 229, 241].

2.5 Numerical Spin Bath Simulation

In order to test the validity of our analytical theory explaining our measurement results, we numerical simulate the ensemble T_2^* and T_2 values in a bath of paramagnetic nitrogen spins. In the simulation, we place a single NV at the origin of a three-dimensional diamond lattice, and electronic nitrogen spins (N) are placed randomly around it. A typical *single* bath configuration is shown in Fig. 2.6.

The dipolar interaction Hamiltonian between two spins S_1 and S_2 is given by (see for example [250])

$$H_{\text{dip}}/\hbar = \frac{\mu_0}{4\pi}\frac{\gamma^2\hbar}{r^3}\left[\mathbf{S}_1\mathbf{S}_2 - 3\frac{(\mathbf{S}_1\cdot\mathbf{r})(\mathbf{S}_2\cdot\mathbf{r})}{r^2}\right], \tag{2.36}$$

where μ_0 is the vacuum permeability, $\gamma_1 = \gamma_2 = \gamma$ is the spin's gyromagnetic ratio, $\hbar$ is the Planck constant, and $\mathbf{r}$ is the vector connecting both spins (see Fig. 2.6a).

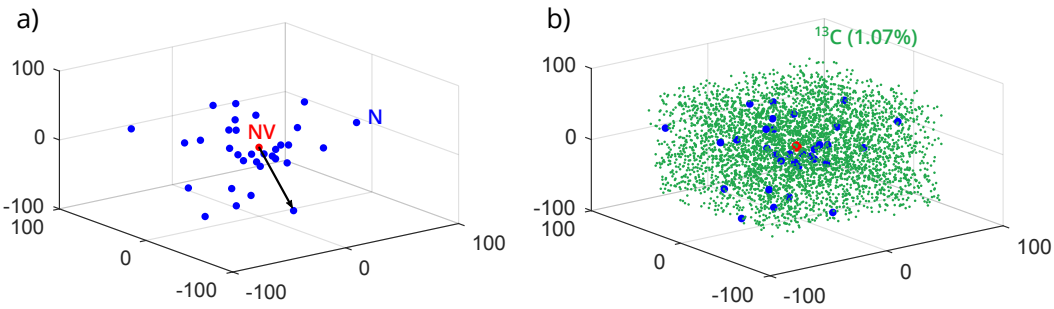

Figure 2.6: Spin bath simulation – a) Single bath configuration showing NV center (red) as central spin at the origin of the diamond lattice and P1 centers (blue) randomly placed around it. b) Spin bath including ^{13}C spins at 1.07 %.

Expanding the spin operators in spherical coordinates and keeping only the secular terms of the dipolar Hamiltonian, the relevant components are given by the S_zS_z interaction term

$$H_{\text{dip}}^{\text{zz}}/\hbar = \frac{\mu_0}{4\pi}\frac{\gamma^2\hbar}{r^3}S_{z,1}S_{z,2}(1-3\cos\theta), \tag{2.37}$$

and the flip-flop term

$$H_{\text{dip}}^{\text{flip-flop}}/\hbar = -\frac{1}{4}\frac{\mu_0}{4\pi}\frac{\gamma^2\hbar}{r^3}(1-3\cos\theta)(\mathbf{S}_{+,1}\mathbf{S}_{-,2}+\mathbf{S}_{-,2}\mathbf{S}_{+,1}), \tag{2.38}$$

where θ is the angle the vector connecting both spins makes with the applied bias field $B_0 \,||\, [111]$, and $\mathbf{S}_{\pm,1}$ and $\mathbf{S}_{\pm,2}$ are the spin raising and lowering operators. Although NV and nitrogen spins are both of electronic nature ($\gamma_{NV} \approx \gamma_N \approx 28\,\text{GHz/T}$), the large energy mismatch due to the zero-field splitting D in the NV ground state disallows spin-flip-flops between NV-N pairs (unlike spins). In this instance, the only interaction to be considered is the one of type S_zS_z (Eqn. 2.37). For pairwise interaction between nitrogen spins, however, the flip-flop interaction term is to be considered as well.

2.5.1 T_2^* Results

For a central NV spin, the second moment of the ESR linewidth $\Delta_{\text{single}} = 2\pi\sigma$ is calculated by [250, p. 122f]

$$\Delta_{\text{single}} = \sqrt{\sum_k A_k^2}, \tag{2.39}$$

where the sum runs over all NV-N spin pairs for a single bath configuration (see Fig. 2.6a). The Aks are determined through the S_zS_z interaction term of the dipolar Hamiltonian, that is,

$$A_k = \sqrt{\frac{1}{3}S(S+1)}\frac{\mu_0}{4\pi}\frac{\gamma^2\hbar}{r}(1-3b\cos\theta_k^2). \tag{2.40}$$

Here, $S = 1/2$ is spin value of the nitrogen bath spins, θ_k the angle of the vector from the origin to the k-th bath spin with the magnetic field axis ($\equiv$ quantization axis of the NV), r is the distance between the k-th bath spin and NV, and b is a geometrical factor accounting for the alignment of the B-field with respect to the crystal lattice axes. For the NV relevant case, $B_0 \,||\, [111]$, $b = 2/3$. Equation 2.40 is similar to the S_zS_z interaction term given in Eqn. 2.37 but does not contain any NV spin dependence as it gets traced out in the moment calculation (for details see Ch. III and IV in Reference [250]).

For a fixed nitrogen concentration, we simulate the distribution $P(\Delta_{\text{single}})$ by generating 10000 bath configurations and calculate in each case the second moment regarding Eqn. 2.40. The results for a spin bath consisting of [N] = 1 and 100 ppm are shown in Fig. 2.7. The simulated distributions are non-Gaussian and exhibit a heavy tail due to the long-range character of the dipolar interaction [200]. An ensem-

ble linewidth is thus only very weakly determined by a single NV measurement (and vice versa) but is extracted by fitting the simulated linewidths distributions to the analytical expression $P(\Delta_{\text{single}}) = A\frac{\Delta_{\text{ens}}}{(\Delta_{\text{single}})^2}\sqrt{\frac{2}{\pi}}\exp\left[-\frac{1}{2}\left(\frac{\Delta_{\text{ens}}}{\Delta_{\text{single}}}\right)^2\right]$ which was given in Sec. 2.4.3 and Reference [200]. Here, $\Delta_{\text{ens}} \equiv 2\pi\delta$ is decay rate of the ensemble Ramsey signal and δ the half-width of the Lorentzian ESR lineshape (see Eqn. 2.27).

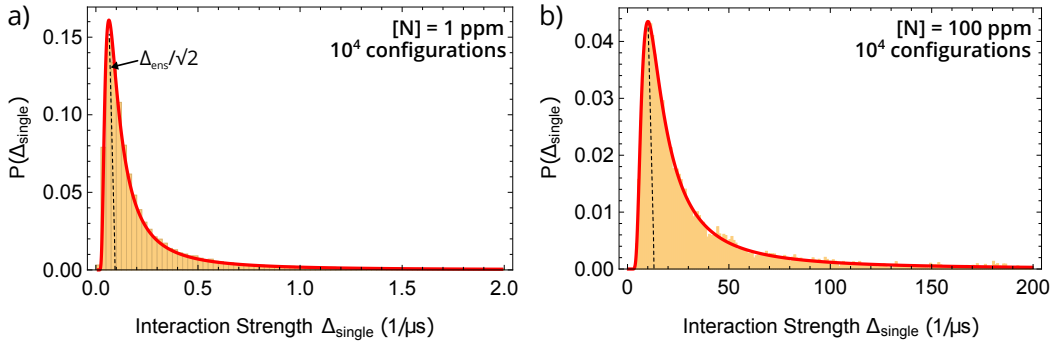

Figure 2.7: Simulation results of Δ_{singe} for a) [N] = 1 ppm and b) [N] = 100 ppm – The ensemble decay rate Δ_{ens} is extracted by fitting the analytical expression given in Eqn. 2.23 to the distribution of simulated values (red line).

We find that the analytical expression fits in all instances our simulations well. Moreover, the extracted ensemble linewidths and resulting $T^*_{2\,\text{ens}} = 1/(\Delta_{\text{ens}})$ are in good agreement with a set of measurements on nitrogen-rich diamonds. The results of the simulation and experiment are the focus of Ch. 6 and are depicted in Fig. 6.2.

2.5.2 T_2 Results

Similarly, we calculate the characteristic nitrogen bath interaction strength $1/\tau_c$ using Eqn. 2.38 by summing over all pair-wise interactions between nitrogen spins for each spin configuration. The second moment of a nitrogen spin is thereby calculated iden-

tically to that of given in Eqn. 2.39 and 2.40 but is $3/2\times$ larger due to an additional contribution of the dipolar flip-flop-term (Eqn. 2.38) to the second moment [250, p. 112f]. We also exclude from the second moment calculation all N-N pairs for which $A_k > \Delta_{ens}$ as those interactions are suppressed due to motional narrowing [49, 201, 233]. For the physical system in consideration, this corresponds to ignoring the P1 spin pairs that interact more strongly with each other than the NV center. These are typically pairs of spins close to each other but far from the NV center. As such, they would not contribute significantly to the decoherence of the NV center. The results for $1/\tau_c$ are shown in Fig 2.8.

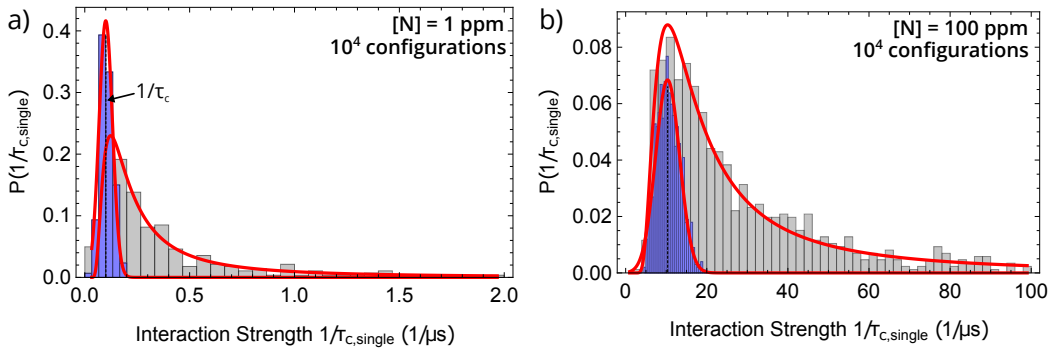

Figure 2.8: Simulation results of $1/\tau_{c,single}$ for a) [N] = 1 ppm and b) [N] = 100 ppm. The data in gray is the distribution $P(1/\tau_{c,single})$ simulated using second moment given Eqn. 2.39 and 2.40. The distribution in blue is a calculation with the terms $A_k > \Delta_{ens}$ dropped due to motional narrowing (see text). $1/\tau_c$ is extracted from a Gaussian fit to the blue distribution.

Without motional narrowing, the distribution $P(1/\tau_{c,single})$ (gray) has a same form as $P(\Delta_{\text{single}})$ but with a maximum shifted by $\approx 3/2$ to higher frequencies, as expected from the slightly larger prefactor in the second moment calculation. With motional narrowing (blue), however, the high frequencies in the tails are eliminated,

and the distribution $P(1/\tau_{c,single})$ is approximately of Gaussian form. The mean value of this distribution is extracted from a fit to a Gaussian line shape. The values extracted for the average N-N coupling $1/\tau_{c,ens}$ are found to be nearly identical to Δ_{ens} for a given [N].

To extract T_2 using the simulated values Δ_{ens} and $1/\tau_{c,ens}$ for a given nitrogen concentration, we employ the formalism developed in Sec. 2.4.1 and solve the integral equation in Eqn. 2.10 numerically for the Hahn echo [235, Tab. 1] filter function. The $T_{2,echo}$ value is extracted from a fit of the form $C_0 \exp[-(t/T_2)^p]$ to the numerically calculated signal

$$S_{\text{echo}}(\tau) = \mathrm{e}^{-\chi(\tau,\Delta,\tau_c)}. \tag{2.41}$$

We compare T_2^* and T_2 from simulation and experiment in Fig. 6.2 of Ch. 6. In general, we find excellent agreement between the simulated and measured ensemble T_2^* values, and good agreement for T_2.

2.6 ^{13}C Nuclear Spin Bath

The carbon spin bath in diamond has received a great deal of attention over the past 10 years, which has resulted in a vastly improved understanding [123, 190, 199, 211, 213, 214, 220–224]. Most importantly, by employing isotopically enriched ^{12}C diamond samples [123], the effects of the paramagnetic ^{13}C nuclear spins ($I = 1/2$, 1.07 % natural abundance) can be largely eliminated. Isotopically enriched diamond samples are therefore preferred for quantum applications and sensing. While a complete review of the ^{13}C spin bath is beyond the scope of this section, we will highlight

important aspects briefly.

The interaction of NV center spins with a bath of nuclear ^{13}C isotopes is determined through the anisotropic-dipolar and isotropic-Fermi-contact parts of the hyperfine Hamiltonian given by [7, 211, 213]

$$H_{\text{hyperfine}}/\hbar = \frac{\mu_0}{4\pi}\gamma_{NV}\gamma_I\hbar\left[\underbrace{-\frac{8\pi}{3}|\psi(0)|^2\mathbf{I}\cdot\mathbf{S}}_{\text{Fermi}} + \underbrace{\left(\frac{\mathbf{S}\cdot\mathbf{I}}{r^3} - 3\frac{(\mathbf{I}\cdot\mathbf{r})(\mathbf{S}\cdot\mathbf{r})}{r^5}\right)}_{\text{dipolar}}\right], \qquad (2.42)$$

where $\gamma_{NV} = 2\pi \times 28\,\text{GHz/T}$ and $\gamma_{^{13}C} = 2\pi \times 10.7\text{MHz/T}$ are the NV and ^{13}C spin gyromagnetic ratio, respectively, $\psi(0)$ is the NV wavefunction at the ^{13}C nucleus, $\mathbf{S}$ is the NV spin, $\mathbf{I}$ is the ^{13}C nuclear spin and $\mathbf{r}$ is the vector connecting both. The long-range nature of the dipolar interaction and short-range aspect of the contact interaction thereby lead to drastic different values for the characteristic NV-^{13}C interaction strengths, which we consider here. For ^{13}C spins at least several lattice sites away from the NV center, an order-of-magnitude estimate of the characteristic ^{13}C-NV coupling strength is obtained by calculating the average dipolar interaction $\gamma_{\text{NV}-^{13}\text{C}} \approx \frac{\mu_0}{4\pi}\gamma_{NV}\gamma_{^{13}C}\frac{1}{\langle r\rangle^3} \approx 2\pi \times 35 \cdot [^{13}\text{C}]\,\text{kHz}/\%$. Here, $\langle r\rangle = 0.55[^{13}\text{C}]^{-1/3}$ is the average spacing between bath spins as a function of ^{13}C density. In natural abundance samples with 1.07 % ^{13}C spins, $\langle r\rangle \approx 0.8\,\text{nm}$ (or about five lattice sites) yielding an estimated value of $\gamma_{\text{NV}-^{13}\text{C}} \approx 2\pi \times 35\,\text{kHz}$ and an ensemble $T_2^* = 1/\gamma_{\text{NV}-^{13}\text{C}} \approx 4\,\mu\text{s}$. This estimate for $\gamma_{\text{NV}-^{13}\text{C}}$ is about 4× smaller than the experimentally determined value (see Ch. 5) indicating that for natural abundance samples both dipolar- and contact-interaction are relevant. For ^{13}C spins even closer to the NV central spins, however, the hyperfine interaction is dominated by the contact term and coupling

strengths of $\approx 130\,\mathrm{MHz}$ for nearest neighbor and $\approx 20\,\mathrm{MHz}$ for next-nearest neighbor spins to the NV spin have been measured [190, 222]. The contact interaction of close-by spins thus vastly exceeds the contribution from purely dipolar interactions and qualitatively results in two different spin regimes when comparing low- and high density ^{13}C diamonds.

This change in characteristic energy scale is indeed observed in single NV measurements when the variation of T_2^*-values for different NV centers is compared [199]. Similarly, the transition from dipolar to contact interaction is observed in ensemble T_2^* measurements when T_2^* is plotted as a function of ^{13}C bath density [222]. While in the *dilute* density regime ($[^{13}\mathrm{C}] \ll 1\,\%$) the NV ensemble linewidth $1/T_2^*$ scales linearly with spin bath concentration, at high densities ($[^{13}\mathrm{C}] \gg 1\,\%$) a square-root dependence $\propto [^{13}\mathrm{C}]^{1/2}$ is measured [222]. This change in linewidth dependence is also observed for electronic phosphor donors in a bath of nuclear ^{29}Si spins [3] and agrees with theoretical calculations using the moment analysis of an ESR line [250, see Ch. III and IV]. In Fig. 2.9, we compare the ESR signal for a $[^{13}\mathrm{C}] = 1.1, 5$, and $50\,\%^{13}$C sample. The dipolar term of the hyperfine interaction leads to a broadening of the main NV ESR linewidths and additional discrete hyperfine splittings due to the Fermi contact part are introduced, which become visible at $[^{13}\mathrm{C}] = 5\,\%$. At higher densities, $[^{13}\mathrm{C}] \gg 1\,\%$, the ESR spectrum is dominated by these discrete splittings.

The effects of the paramagnetic ^{13}C bath spins are also easily observed in T_2 measurements. In these measurement, the ^{13}C nuclear spins collectively Larmor precess at the frequency $f_L \approx \gamma_{^{13}\mathrm{C}} B_0$ when a bias field B_0 is applied. As a result, the T_2

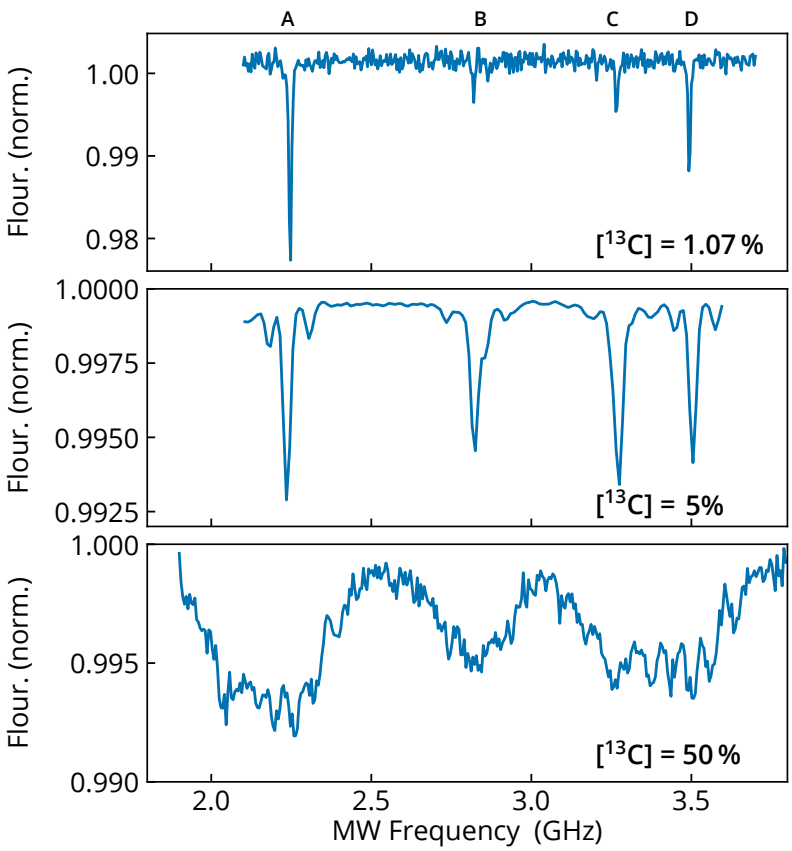

Figure 2.9: Full ESR spectrum of NV ensembles for three different ^{13}C concentrations – NV-related resonance peaks are labeled. A and D correspond to the on-axis NV orientations for which $B_0 \,||\, [111]$. Peaks B and C correspond to the partially degenerate three off-axis NV orientations. Additional resonances become visible at $[^{13}\mathrm{C}] = 5\,\%$ due to the strong contact interaction of ^{13}C spins within a few lattice sites of the NV center spins. At high ^{13}C densities, the ESR signal is dominated by this interaction and leads to strong linewidth broadening. All samples are electronic-grade substrates from Element Six with the given ^{13}C concentration. For each substrate, nitrogen has been implemented to create NV centers (^{14}N, 85 keV, $[\mathrm{N}] = 2 \times 10^{10}\,\mathrm{cm}^{-2}$). Measurements were performed using the setup described in Ch. 5.

decay envelope exhibits electron-spin-echo-envelope-modulation (ESEEM) as shown in Fig 2.10. We have discussed the ESEEM in the context of $^{15}\mathrm{NV}^-$ spins in Sec. 1.6.3

and the NV Hahn echo signal in a ^{13}C bath is similarly given by [209, 211, 213]

$$S_{\mathrm{ESEEM}}(\tau) = \prod_k A\mathrm{e}^{-(\tau/T_2)^p}\left[1 - B\sin^2(\frac{2\pi f_L\tau}{2})\sin^2(\frac{2\pi f_k\tau}{2})\right]. \tag{2.43}$$

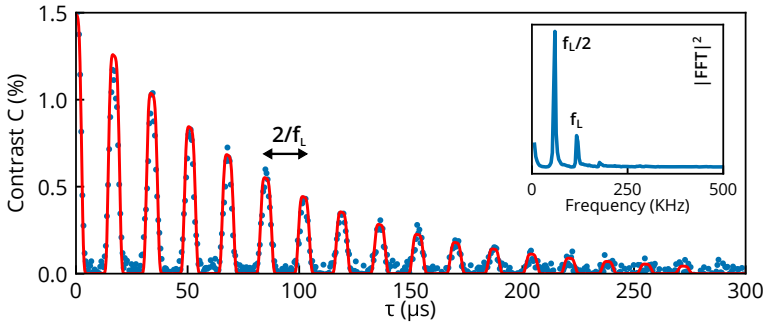

Figure 2.10: NV ensemble Hahn echo signal in a natural abundance ^{13}C sample – The collective Larmor precession of ^{13}C nuclear spins ($I = 1/2$) causes collapses and revivals of the decay envelope. Revivals occur at $\tau_{\mathrm{rev}} = 2/(\gamma_{^{13}\mathrm{C}}B_z)$, twice the Larmor precession period f_L. The ensemble signal is fit to Eqn. 2.44 and shown in red. Inset: FFT of NV signal with Larmor frequency labeled. The sample is a natural abundance electronic-grade substrate from Element Six. Nitrogen spins were implemented to create NV centers (^{14}N, 85 keV, [N] $= 2 \times 10^{10}\,\mathrm{cm}^{-2}$). Measurements were performed using the setup described in Ch. 5.

In the ^{13}C case, however, we obtain the NV signal by taking the product over all hyperfine coupling frequencies f_k due to the variation in interactions of the NV center with the ^{13}C bath spins, which are located randomly in the diamond lattice. The product over individual ESEEM signals is not required in the ^{15}NV$^-$ case where the strong hyperfine coupling of the NV with its ^{15}N nucleus dominates. In this instance, the frequencies were given by $f_k \approx A_z$.

By expanding the sine-functions in Eqn. 2.43 around the nodes $2\pi n$, Eqn. 2.43

can be approximated by [221]

$$S_{\mathrm{ESEEM}}(\tau) \approx A\mathrm{e}^{-(\tau/T_2)^p} \sum_{n\in\{0,1,2,\dots\}} \mathrm{e}^{-\left(\frac{\tau-n\cdot\tau_{\mathrm{rev}}}{\sigma_{\mathrm{rev}}}\right)^{p_{\mathrm{rev}}}} \tag{2.44}$$

and the signal exhibits collapses and revivals of approximately squared-Gaussian lineshape ($p_{\mathrm{rev}} = 4$) when $B_0 \gg f_k$, with centers that occur at integer multiples of $\tau_{rev} = 2/(\gamma_{^{13}\mathrm{C}} B_0)$ (twice the Larmor precession period). The stretched exponential parameters p and p_{rev} and modulation width σ_{rev} in Eqn. 2.44 are thereby dependent on the external magnetic field strength and magnetic field alignment as discussed for example in Reference [221] Sec. E. Lastly, the alignment of the bias B_0 with the NV quantization axis is paramount when working with natural abundance or enriched ^{13}C diamond samples and a strong dependence of T_2 on misalignment angle was reported [214, 220]. For a detailed theoretical description of these effects we refer to Reference [220], [223], and [221]. Lastly, the signals given in Eqn. 2.43 and 2.44 are derived for single center measurements. In an ensemble measurement, the average over many individual NV signals at different lattice sites is taken and the presented analytical descriptions of the T_2 signal can only be considered an approximation. For ensembles, we find that the ^{13}C ensemble ESEEM signal is well-fitted by Eqn. 2.44 with $p_{\mathrm{rev}} = 4$ in select cases. However, by leaving p_{rev} as a free parameter, we find that the revivals in the example of Fig. 2.10 are approximately Gaussian. The reduction of $p_{\mathrm{rev}} = 4$ to $p_{\mathrm{rev}} = 2$ for ensembles is thereby consistent with the changing decay shapes observed for T_2^*, T_2, and T_1 measurements when the ensemble signal is compared to that of a single NV.

2.7 Quantum Control of Bath Spins

In this section we introduce the primary pulse sequences which are employed to manipulate and control the bath spins in analogy to coherent control the NV spin introduced in Ch. 1. The ability to manipulate both the NV center and the bath spins separately provides a sophisticated mechanism, which allows to elucidate the intricate relationship between the NV sensor and its surrounding bath.

2.7.1 Double-Electron-Electron-Resonance

A typical pulsed double-electron-electron-resonance (DEER) protocol [127, 252, 253] utilizes the NV Hahn echo sequence and simultaneous radio frequency fields applied to the bath spins, as depicted in Fig. 2.11a [127, 252]. In that sense, the DEER protocol is an AC sensing experiment, which employs a regular NV spin echo sequence. The NV sensor is thereby made maximally sensitive to the spectral properties of the spin bath when the bath radiation field is resonant with a transition of the bath spins.

2.7.2 Pulsed DEER ESR

A straightforward application of the spin echo DEER protocol is pulsed DEER ESR, which provides a measurement of the bath spin frequency spectrum [49, 253]. It is a pulsed analog of the continuous field ESR sequence introduced for NV centers in Sec. 1.4.1 and obtained by fixing the NV Hahn echo precession time to $\tau \approx T_2$ (see Fig. 2.11a) maximizing the NV center's AC sensitivity. When a bath π-pulse (red, Fig. 2.11a) is resonant with a bath spin transition, the refocusing effect of NV's π-pulse is negated. Consequently, the NV fluorescence signal is modulated revealing an

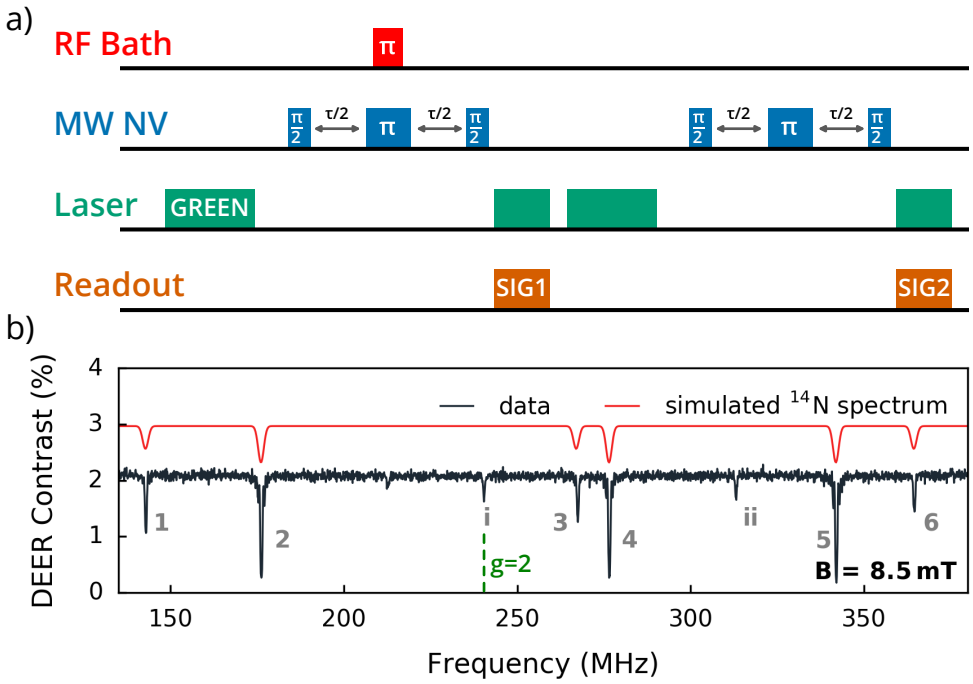

Figure 2.11: Double-electron-electron-resonance (DEER) protocol – a) A DEER sequence consists of a NV Hahn echo sensing scheme, with additional radiation fields applied simultaneously to the bath spins. b) Typical ESR spectrum obtained by a) when the NV precession time is fixed at $\tau \approx T_2$ maximizing AC sensitivity and the bath field frequency is swept (x-axis). When a bath π-pulse is resonant with a bath spin transition, the refocusing effect of the NV π-pulse is negated and an increase in NV decoherence is detected by a change in NV fluorescence contrast. Labels $1-6$ correspond to dipole-allowed ^{14}N bath spin transitions. Labels i and ii, show dipole-forbidden ^{14}N transitions. For details see Sec. 2.2.3. The position of a $g = 2$ free electron resonance is shown as green line. The data was taken with the setup described in Ch. 5 for Sample B (see Table 5.1).

enhanced NV decoherence induced by the group of resonantly addressed bath spins.

An example DEER ESR spectrum for substitutional nitrogen spins N_S^0 is shown in Fig. 2.11b, exhibiting six distinct resonances in case of ^{14}N when a magnetic field $B_z \sim 10\,\mathrm{mT}$ is applied along one of the [111] crystal directions. We have discussed the origin of this frequency spectrum earlier (see Sec 2.2.3) but highlight here that

the nitrogen resonance frequencies are distributed in the radio frequency regime ($\approx 100 - 600\,\mathrm{MHz}$) for typical bias magnetic fields $B_z \sim 10\,\mathrm{mT}$ and are different from the NV center resonances located in the microwave regime ($\approx 2 - 4\,\mathrm{GHz}$). Indeed, due to the absence of a zero-field splitting D, the N_S^0 frequencies are centered around the Larmor precession frequency of a single "$g = 2$" electronic spin given by $f_{L,\mathrm{e}} = \frac{\gamma_\mathrm{e}}{2\pi} B_z$, where $\gamma_\mathrm{e} \approx 28\,\mathrm{GHz/T}$ is gyromagnetic ratio of the free electron. The free electron resonance is depicted for reference as a green line in Fig. 2.11b. The ^{14}N spin transitions are not exactly located at the $g = 2$ resonance due to a hyperfine interaction $|A_z| \approx 100\,\mathrm{MHz}$ of the ^{14}N electron with its paramagnetic nuclear spin ($I = 1$), analogous to the hyperfine interaction of the NV center with its nitrogen nucleus ($|A_z| \approx 2.2\,\mathrm{MHz}$, see Sec. 1.3.4). For a more detailed discussion of the nitrogen frequency spectrum and Hamiltonian see Sec 2.2.3.

The spectral features measured via DEER ESR are thereby not only originating from nitrogen and electronic $g = 2$ spins, but reveal spin resonances for a wide range of electronic defects in diamond including vacancy clusters, vacancy-hydrogen defects and such, if they exists at spin concentrations comparable to or exceeding the NV concentration. Similar spectra can be obtained for nuclear spin species in electron-nuclear-double-resonance (ENDOR) experiments, but these measurements typically require magnetic fields $B_z \gtrsim 1\,\mathrm{T}$ due the $\sim 1000\times$ smaller gyromagnetic ratio of nuclei [9, 10, 252, 254]. Lastly, we note that the sequence in Fig. 2.11a can also be equally employed to detect Rabi oscillations of the bath spin species, by varying the amplitude or duration of the applied bath π-pulse [127] on-resonance with a nitrogen

spin transition. Through such a DEER Rabi measurement, the bath π-pulse for individual bath spin transitions is calibrated allowing for more advanced spin bath manipulations.

2.7.3 Spin-Echo-Double-Resonance

The DEER protocol can also be employed to measure individual contributions to NV decoherence caused by a select group of bath spins. In such spin-echo-double-electron-resonance (SEDOR) experiment [127], the NV free precession time τ (see Fig. 2.11a) is swept, as in a regular spin echo experiments. Without any resonant bath spin π-pulses, this sequence recovers the bare Hahn echo T_2 as discussed in Sec. 1.4.5 and 2.3.2. However, when one or multiple bath π-pulses are resonant with individual bath spin transitions, the NV signal exhibits an increased decoherence and a shortened decay time (denoted T_2^{SEDOR}) due to the individually addressed spin bath resonances. There is an interesting relationship between the decay times determined through SEDOR, the bare NV Ramsey T_2^* and bare Hahn echo T_2: For single NV centers, the SEDOR signal exhibits Gaussian decay ($p = 2$, consistent with a Gaussian Ramsey decay) and the NV decay times are related by [127]

$$1/T_{2\,\mathrm{single}}^* \approx \sqrt{\sum_i \left(1/T_{2,i}^{\mathrm{SEDOR}}\right)^2 + \left(1/T_2\right)^2}, \tag{2.45}$$

where $T_{2,i}^{\mathrm{SEDOR}}$ is the NV SEDOR decay time measured when the i-th spin bath transition is selectively addressed via a bath π-pulse. In the dipolar-limited regime, i.e., when the NV T_2^* is limited by dipolar interactions with a homogeneous bath of paramagnetic spins, as is the case for high density nitrogen samples, Eqn. 2.45 becomes an exact equality. Otherwise, an additional term $\left(1/T_{2,other}^*\right)^2$ is to be added

inside the square-root of Eqn. 2.45 to account for additional dephasing mechanisms not revealed by SEDOR (e.g., strain fields, nuclear bath spins, etc.). For ensemble samples, the SEDOR decay is of simple exponential form ($p = 1$, consistent with a simple exponential Ramsey decay) and Eqn. 2.45 is to be modified to

$$1/T^*_{2\,\mathrm{ens}} \approx \sum_i 1/T^{\mathrm{SEDOR}}_{2,i} + 1/T_2. \tag{2.46}$$

2.7.4 Ramsey-Double-Electron-Resonance

Similarly to AC sensing, a DC Ramsey sensing scheme can be deployed to reveal interactions of the NV with a set of bath spins. Here, we discuss two modalities: i) Continuous (CW) and ii) pulsed driving driving of the nitrogen bath spin to effectively decouple the NV-N bath coupling. A typical Ramsey-double-electron-resonance (RADOR) [127] sequence is shown in Fig. 2.12a. In CW driving, the bath spins are driven continuously such that they undergo many Rabi oscillations during the characteristic interaction time $1/\gamma_{NV-N}$, and thus the time-averaged NV-N dipolar interaction approaches zero. For pulsed driving, a single (or multi-frequency) π-pulse resonant with a single (or multiple) spin transition(s) in the bath is applied midway through the NV Ramsey free precession interval, to refocus bath-induced dephasing, in analogy to the refocusing π-pulse in a NV Hahn echo sequence. Fig. 2.12a illustrates both methods for a given RF field applied to the nitrogen bath spins with a Rabi frequency of Ω_N.

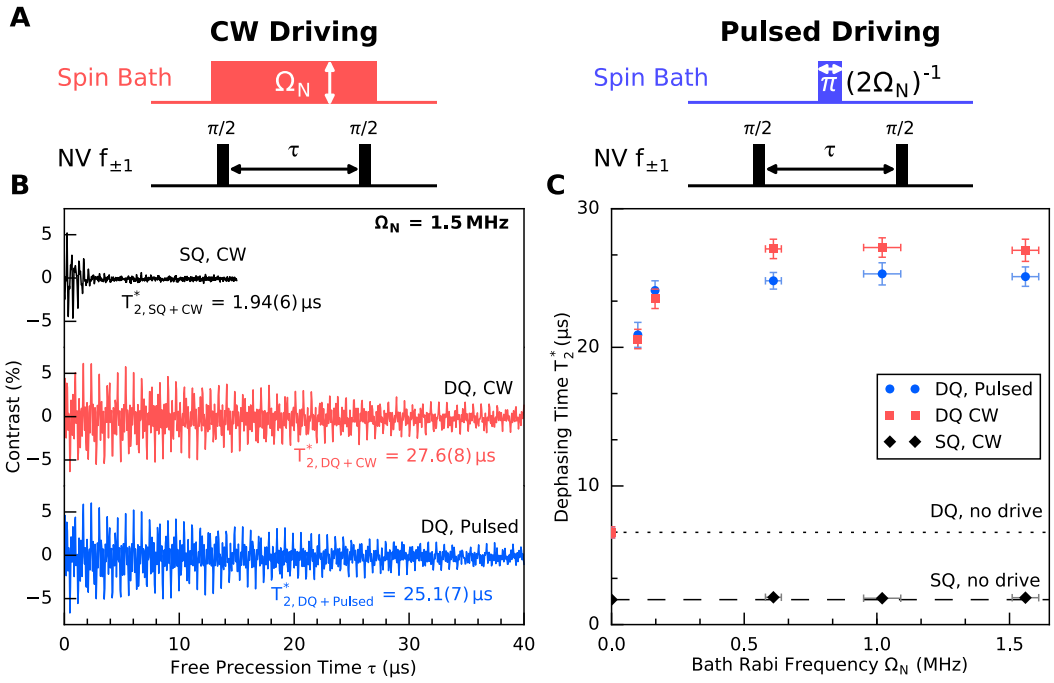

Figure 2.12: Ramsey-double-electron-resonance (RADOR) protocol – a) Illustrates the sequences used for CW (left) and pulsed (right) decoupling of the electronic nitrogen spin bath. For both methods, six distinct frequencies are used to resonantly address the nitrogen spin bath via an applied RF field with equal Rabi frequency Ω_N on each spin transition. In b) the Ramsey decay in the DQ basis for CW and pulsed driving are compared ($\Omega_N = 1.5\,\mathrm{MHz}$). The decay for CW driving in the SQ basis is included for reference and is limited by additional dephasing mechanisms (including strain and magnetic field gradients) independent of the bath drive. For details on DQ and spin bath driving see Ch. 5. c) Depicts T_2^* as a function of bath Rabi frequency for DQ CW (red squares) and DQ pulsed (blue circles) spin bath driving, with the SQ CW results (black diamonds) again included for reference. The finely (coarsely) dashed line indicates the T_2^* value in the DQ (SQ) basis without any drive field applied to the bath spins. The data was taken with the setup described in Ch. 5 for Sample B (see Table 5.1).

Chapter 3

Superresolution Optical Magnetic Imaging and Spectroscopy using Individual Electronic Spins in Diamond

3.1 Introduction

Nitrogen vacancy (NV) color centers, atomic-scale quantum defects embedded in diamond [142], are now the leading modality for nanoscale magnetic sensing, with wide-ranging applications in both the physical and life sciences. For example, single NV center probes have been used for imaging of magnetic vortices [255] and spin waves [256] in condensed matter systems, as well as for single proton magnetic resonance imaging (MRI) [73] and single protein NMR [77]. Ensembles of NV centers

have been used for noninvasive sensing of single neuron action potentials [83] and wide-field magnetic imaging of biological cells [80, 82] and geoscience samples [99]. Many envisioned applications of NV centers at the nanoscale, such as determining atomic arrangements in single biomolecules [73] or realizing selective strong coupling between individual spins [54] as a pathway to scalable quantum simulations [43], would benefit from a combination of superresolution imaging with high sensitivity magnetometry. NV mapping of magnetic fields with resolution below the diffraction limit has been realized by real-space techniques such as scanned magnetic tips [257] or diamond-AFM probes [258], as well as a Fourier (i.e., k-space) method employing pulsed magnetic field gradients [92]. Alternatively, far-field optical superresolution techniques have the advantages of being versatile, simple to integrate into standard NV-diamond microscopes, require no special fabrication, avoid strong magnetic field gradients that can adversely affect the sample to be probed [259], are compatible with a wide range of NV sensing techniques, and allow for fast switching between and selective addressing of multiple NV centers. Coordinate-stochastic superresolution imaging methods, namely STochastic Optical Reconstruction Microscopy (STORM) and Photo Activated Localization Microscopy (PALM), readily offer high parallelization in sparse samples, but are prone to artefacts at high emitter densities and have been implemented until now only for a few NV centers per diffraction limited volume[260, 261]. On the other hand, coordinate-deterministic superresolution methods provide targeted probing of individual NV spins with nanometric resolution [50, 262, 263], which is well suited for the purpose of coherent nanoscale AC magnetometry, where each NV acts as a local phase-controlled magnetometer probe.

Here, we demonstrate the capability of spin-RESOLFT (REversible Saturable OpticaL Fluorescence Transitions) as a coordinate-deterministic technique for combined far-field optical imaging and precision magnetometry. An earlier study showed how spin-RESOLFT provides coherent manipulation of NV spins with simultaneous superresolution imaging of NV position [264]. In the present study, we use spin-RESOLFT to map spatially varying magnetic fields at the nanoscale, including the NMR signal from external nuclear spins. Importantly, spin-RESOLFT does not require multi-wavelength excitation and high optical powers, as typically used with STimulated Emission Depletion (STED) [265] microscopy or Ground State Depletion (GSD) by metastable state pumping [266]. As shown below, we use spin-RESOLFT to optically resolve individual NV centers in a bulk diamond sample with a resolution of about 20 nm in the lateral (xy) directions, while exploiting the spin-state dependent optical properties (Fig. 3.1(a)) and long electronic spin coherence times of NV centers in bulk diamond for precision magnetic field sensing. Moreover, we show that the localization along the beam propagation (z) axis can be improved to sub-nanometer precision via combining spin-RESOLFT with NV NMR measurements from proton spins in a sample external to the diamond.

3.2 Experimental Setup

Our NV spin-RESOLFT magnetic microscope (Fig. 3.1(b) and (c)) is based on a standard NV-diamond confocal setup. Here, a Gaussian laser beam at 532 nm is used

to initialize and readout the NV centers while microwaves at 3 GHz are used to coherently manipulate the NV center ground state electronic spin (Fig. 3.1(a)). When electronically excited by green light absorption, the $m_s = 0$ spin state largely fluoresces in the red with no change to the spin state, whereas the $m_s = 1$ spin state has a significant probability to decay through a singlet state to the $m_s = 0$ spin state, which effectively reduces the $m_s = 1$ fluorescence rate and allows spin-state initialization into $m_s = 0$. For superresolved NV imaging and spin readout, we overlap a second 532 nm, Laguerre-Gaussian doughnut beam with an intensity zero at the center. Similar to other coordinate-targeted, deterministic superresolution techniques[50, 265, 266], the doughnut beam does not affect NV centers that are located in the dark doughnut center. However, NV centers that are slightly displaced from the dark center, i.e., closer to the doughnut crest, are repolarized by the laser light into the $m_s = 0$ state, and hence all NV spin-state information is erased (see Sec. 3.3).

3.3 Spin-RESOLFT Imaging

By first applying a π-pulse to switch all the NV centers into the spin state $m_s = 1$ and then using a selectively repolarizing green doughnut beam, we pump off-center NVs into the $m_s = 0$ ground-state. These off-center NV centers contribute a spatially broad 'background' fluorescence signal in addition to a spatially narrower fluorescence feature characteristic of superresolved NV centers in the center of the doughnut beam (green curve in Fig. 3.2(a). We determine the background from the off-center NVs by recording a confocal scan (blue curve in Fig. 3.2(a) immediately following the scan

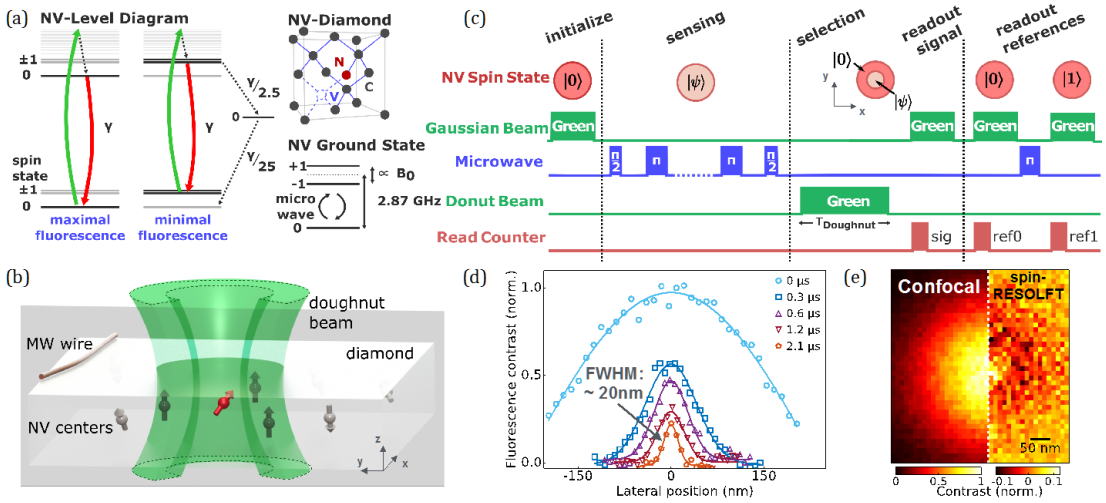

Figure 3.1: Spin-RESOLFT imaging of NV centers. (a) Energy levels and diamond lattice schematic for the negatively charged NV center in diamond, which has electronic spin $S = 1$. (b) The spin-RESOLFT experimental setup is an NV-diamond scanning confocal microscope augmented with a low power green doughnut beam. (c) Spin-RESOLFT experimental sequence for quantum sensing using NV centers in diamond, e.g., AC magnetometry with the dynamical decoupling pulse sequence shown. Spatially selective repolarisation via the pulsed green doughnut beam is inserted before the spin readout to interrogate only a specific NV center. Readout reference measurements allow calibration of photon count to spin state. (d) 1D spin-RESOLFT scans for a single NV center and different doughnut durations, with doughnut beam power of 700 µW. (e) 2D spin-RESOLFT image of the same NV as in (d) with similar resolution ≈ 35 nm but with a much lower doughnut beam power of 25 µW and longer duration of 50 µs. Comparison confocal data in (d) and (e) are normalized to the maximum photon counts. spin-RESOLFT profiles and images are determined by comparing the fluorescence after applying the doughnut (pulse sig) with confocal scans (pulse ref0) and normalized with respect to the maximum spin contrast (see Sec. 3.3).

acquired with the doughnut beam. By subtracting the two signals, we obtain the 1D spin-RESOLFT image, which displays a non-Gaussian intensity profile (Fig. 3.2(b)). In Fig. 3.1(d-e) and Fig. 3.3(a-b), the intensity profiles are normalized with different normalization procedures to allow for a straightforward graphical comparison. Confocal intensity profiles are normalized by the maximum photon counts: I = sig(x)/sig(0). spin-RESOLFT profiles are normalized by the maximum spin contrast (ref0 - ref1): C = (sig(x) - ref0(x)) / (ref0(0) + ref1(0)). The observed profile is strongly dependent on the degree of NV spin repolarization that occurs when the doughnut beam is applied, which is discussed below. We note that the intensity profiles in Fig. 3.1(d) were taken under conditions of short doughnut pulse duration, permitting us to approximate the linewidth as Gaussian.

spin-RESOLFT provides fast switching between emitters because it is a deterministic superresolution imaging technique, in contrast to STORM/PALM techniques that rely on the stochastic fluorescence behavior of emitters at low illumination powers. Thus, spin-RESOLFT allows one to arbitrarily and quickly choose an NV sensor of choice and acquire information about the magnetic field at a particular local position. Moreover, the dead time induced by the presence of the doughnut beam is negligible, as the doughnut pulse is shorter than typical sensing times. In the case of spin-RESOLFT magnetic imaging, the data acquisition time is determined by the finite fluorescence rate of NV centers as well as the scanning parameters used to obtain high-resolution images.

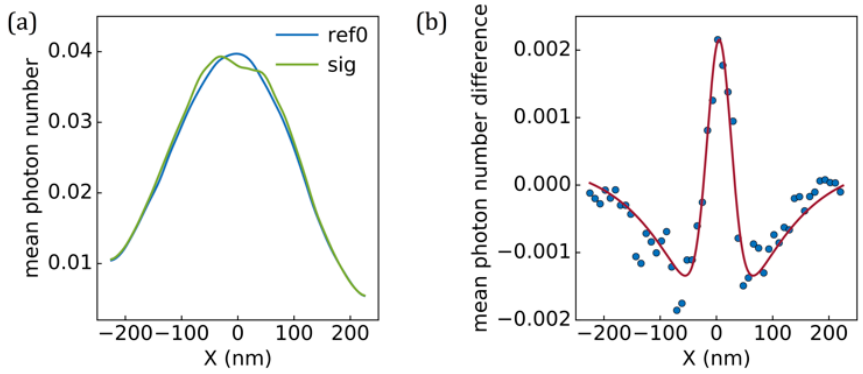

Figure 3.2: (a) Single NV fluorescence measurements as a function of relative position (1D) acquired for the spin-RESOLFT protocol: after the application of the doughnut beam (signal, green) and after a complete repolarization with a Gaussian beam (ref0, blue). A 2-pixel running average is applied to smooth shot-noise-limited intensity fluctuations. At certain positions, the NV spin repolarization occurring from doughnut beam illumination is more efficient, leading eventually to a stronger fluorescence signal. (b) 1D spin-RESOLFT NV image (blue dots) constructed by subtracting the fluorescence curves shown in a. Red curve is a numerical fit of data to a five level model (see next section).

In Fig. 3.3(b) of the main text, we show that two NV centers within the same diffraction-limited volume are distinguished by the spin-RESOLFT technique. From the correlated spin-RESOLFT image we extract the distance between the two NV centers to be $d = 105 \pm 16\,\text{nm}$. Due to a $\approx 20\,\text{nm}$ misalignment between the Gaussian readout and doughnut beams, the maximum fluorescence in the confocal image is not perfectly aligned with the axis formed by the two NV centers.

3.4 Results

We first demonstrated how spin-RESOLFT allows imaging of NV centers with sub-diffraction resolution given by [50] FWHM $\approx \lambda/[2\text{NA}(1 + \Gamma\tau_{doughnut})^{1/2}]$ in the ideal case. Here, NA= 1.45 is the numerical aperture of the objective, Γ is the optical

pump rate, and $\tau_{doughnut}$ is the duration for which the doughnut beam is applied during the spin-RESOLFT experimental sequence (see Fig. 3.1 (c)). Fig. 3.1(d) shows examples of one-dimensional scans of a single NV center imaged after applying the doughnut beam with power of 700 μW and for different durations, with the data fitted numerically using a five level model for the NV (see Sec. B.2). For a doughnut duration of 2.1 μs, we extract a 1D NV image with FWHM= 20 ± 2 nm, more than an order-of-magnitude improvement over confocal resolution. We note that the duration of the selective doughnut beam pulse (few microseconds) has minimal effect on the total sequence time (few hundred microseconds). Moreover by adjusting $\tau_{doughnut}$, sub-diffraction NV images can be attained with doughnut powers as low as 25 μW, ultimately limited by the relaxation time $T_1 \sim 1$ ms. Importantly, owing to the long lifetimes of the states harnessed for NV separation, the optical powers required for superresolution are several orders-of-magnitude lower than those required for STED [262, 266]. For example, Fig. 3.1(e) shows a comparison of two-dimensional images of the same single NV center acquired both without (left) and with (right) the doughnut beam (25 μW power) applied before readout. In practice, the maximum optical resolution is limited by a non-vanishing field intensity at the center of the doughnut mode due to beam shaping imperfections [265], aberrations induced by the sample, as well as thermal and vibrational instabilities of the apparatus (see Sec. B.1). Reference measurements are interleaved with spin-RESOLFT measurements to allow compensation for slow drifts in the apparatus.

Sample A used in Fig. 3.1(d), Fig. 3.1(e), Fig. 3.3 and Fig. 3.4 of is an ultra-

pure CVD diamond, isotopically engineered (99.99% 12C) with NV density of $\sim 3 \times 10^{12}\,\mathrm{cm}^{-3}$, NV orientation along two of four crystal axes, NV spin coherence time (T_2) approaching one millisecond, and NV spin lattice relaxation time T_1 of a few milliseconds. Sample B used for measurements shown in Fig. 3.5 is also an ultra-pure CVD sample, isotopically engineered (99.999 % ^{12}C) with shallow implanted NV centers 1 - 20 nm below the surface (^{14}N at 2.5 keV) at a density of $1.4 \times 10^{12}\,\mathrm{cm}^{-2}$, NV orientation along all four crystal axes, and NV $T_2 \sim 30\,\mu\mathrm{s}$. All measurements were made at room temperature. Both samples were created by Element Six.

Spin-RESOLFT allows us to manipulate and address individual NV centers within a diffraction limited volume. For example, Fig. 3.3(a) shows a confocal image of two NV centers that are separated by less than the diffraction limit and can therefore not be resolved by means of confocal microscopy. In comparison, when using spin-RESOLFT microscopy (Fig. 3.3(b)), the individual NVs are clearly distinguished and their positions are localized within an uncertainty of 5 nm. To demonstrate selective coherent measurements of NV spins using spin-RESOLFT, we begin with measuring the Hahn-echo coherence time (T_2) for each NV individually (Fig. 3.3(c)) by applying a $\pi/2 - \pi - \pi/2$ MW pulse sequence, followed by spin selective readout using the exact positions for NV_1 and NV_2 extracted from Fig. 3.3(b) (see Sec. 1.4.5). We find that although the two NVs are subject to a nominally similar spin bath in the diamond sample, the measured T_2 for each NV spin differs due to slight variations in the local environment. The NV ensemble spin coherence time measured in confocal mode is consistent with an average of the two individual NV T_2 values measured with

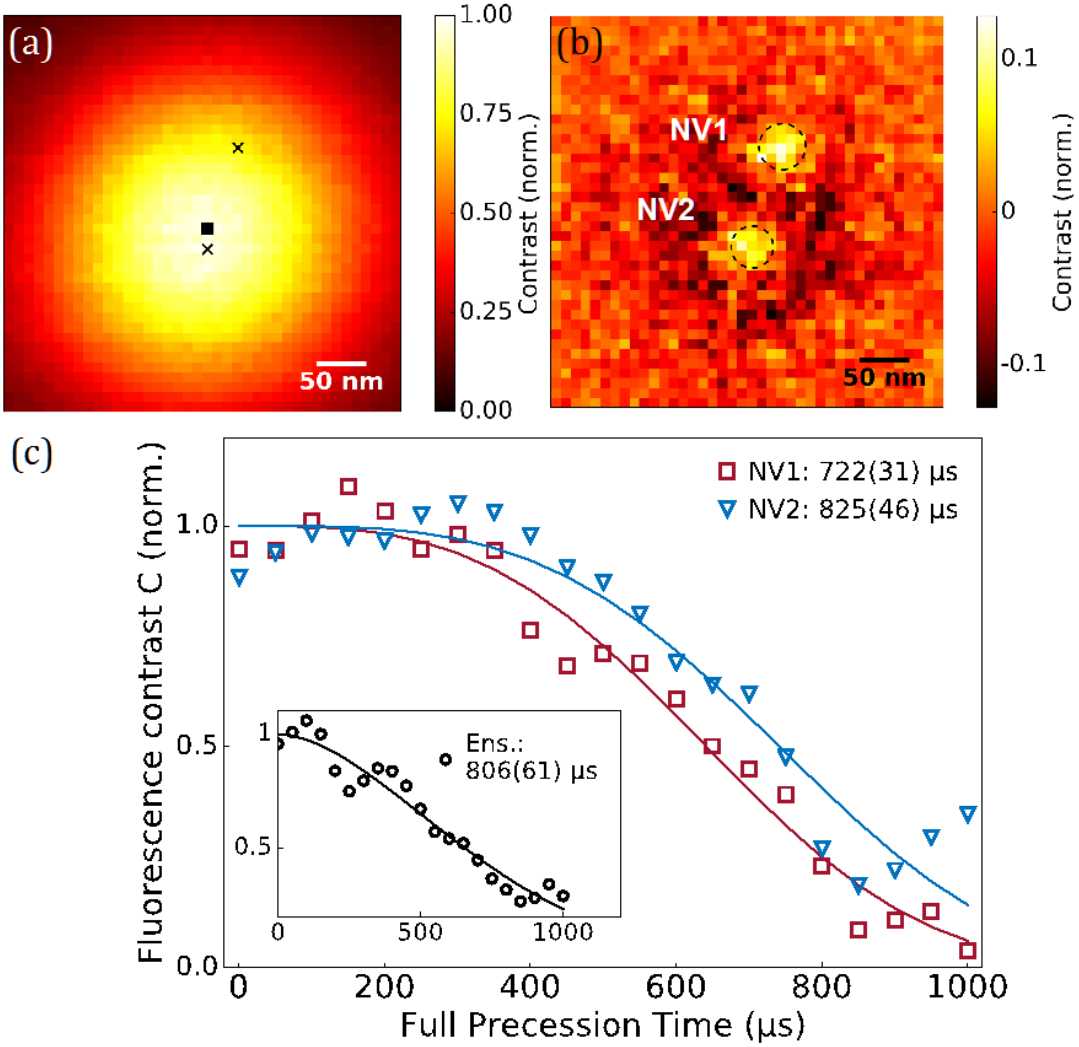

Figure 3.3: Spin coherence time measurement for two NV defects resolvable only via spin-RESOLFT. (a) 2D Confocal image of two unresolved NV centres with the same orientation of their spin quantization axes. Black crosses indicate the NV positions as extracted from the spin-RESOLFT image, the black square indicates the Gaussian green laser beam centre. (b) 2D spin-RESOLFT image of same field-of-view as in (a) (acquisition time of 9 s per pixel, 150 µW doughnut beam power with duration of 17 µs). A 50 nm FWHM is extracted using a numerical fit of a five-level model. (c) Selective NV spin coherence measurements and associated fits to a stretched exponential for the two NV centres shown in (a) and (b), using the same doughnut beam power and duration as in (b). Inset: spin coherence time determined for the ensemble of two NVs via a confocal measurement and associated fit. Shaded regions indicate 95% confidence interval extracted from the fits.

spin-RESOLFT, weighted by the fluorescence collected from each single NV center. Due to a slight systematic mismatch between the doughnut and the Gaussian beam centers, the black square does not lie exactly in the middle of the crosses indicating the NV positions and therefore the NV ensemble T_2 (inset Fig. 3.3(c)) is correspondingly closer to the T_2 of NV_2 as measured with spin-RESOLFT.

Next, we demonstrated the utility of spin-RESOLFT to deploy each NV within a confocal volume as a very-well-localized, point-like quantum sensor. First, we selectively measured the response of NV_1 and NV_2 to an externally and spatially varying AC applied magnetic field. We also performed ensemble measurements using confocal mode. The field is produced by an AC current that runs through a wire at a 10−micron distance (Fig. 3.4(a)). The resulting magnetic field gradient, $\Delta B/\Delta r \approx 1\,\mathrm{nT/nm}$, leads to a measurable difference in field strength for NV_1 and NV_2. In Fig. 3.4(b) we plot the measured coherence signal of NV_1 and NV_2, as well as the ensemble signal, obtained for different magnetic field strengths by incrementally varying the magnitude of the AC current through the wire. The observed oscillations in NV fluorescence contrast are characteristic for spin-based local magnetometry [220]. Note that the contrast in confocal mode is not necessarily the sum of the spin-RESOLFT contrast for NV_1 and NV_2, as the contrast with spin-RESOLFT depends on the doughnut beam power (Fig. 3.1(d)). At a fixed current $I_{AC} = 7\,\mathrm{mA}$ (Fig. 3.4(c) and (d)), we measured a magnetic field of $8.924 \pm 0.004\,\mu\mathrm{T}$ for NV_1 and $8.812 \pm 0.009\,\mu\mathrm{T}$ for NV_2, which is in good agreement with the expected magnetic field profile of the wire (see Sec. B.3). Doughnut beam imperfections typically reduce the

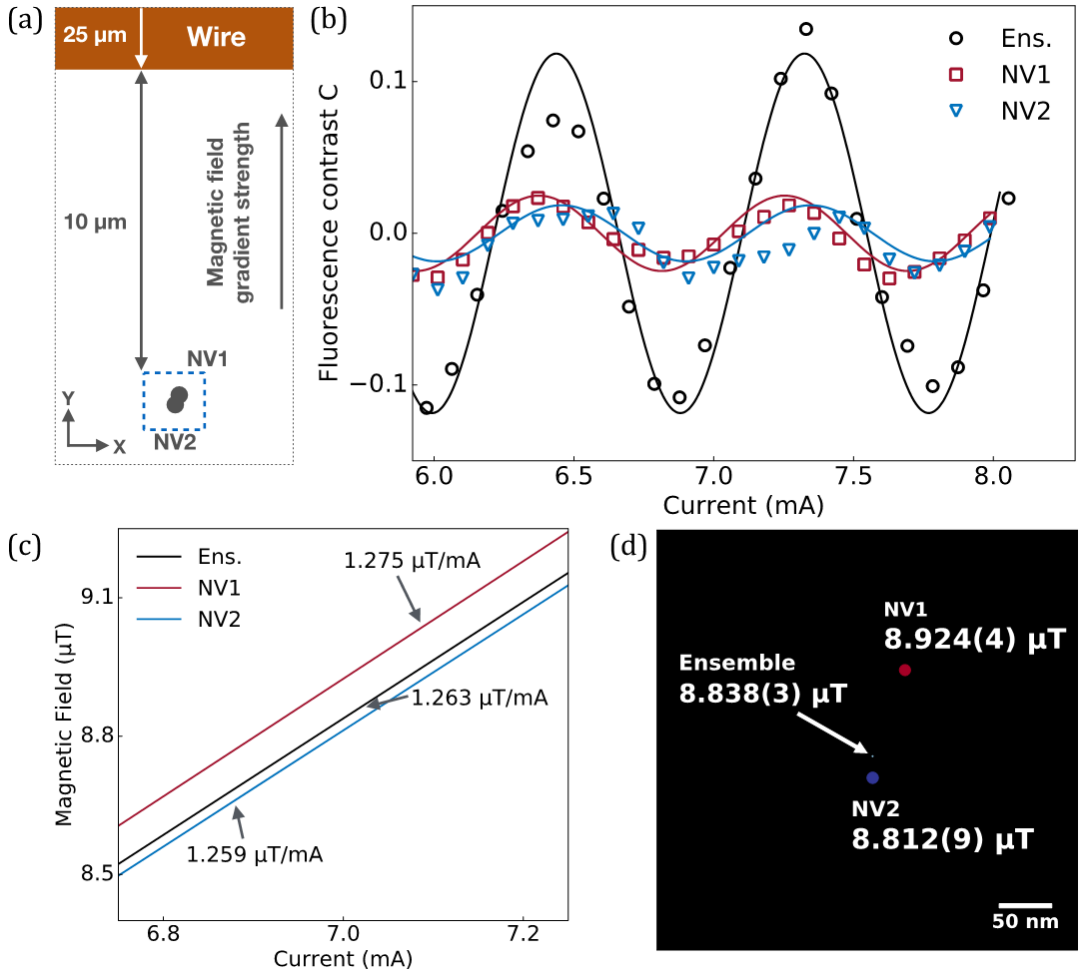

Figure 3.4: Superresolution magnetic field imaging for two NV centres via spin-RESOLFT. (a) Schematic of the AC current wire and two NV centers (same as in Fig. 3.3(b)). (b) spin-RESOLFT AC magnetometry measurements at $\nu_{AC} = 8.3\,\text{kHz}$ for each NV center individually and for the two NV ensemble in confocal mode. Also shown are fits of data to sinusoids with phase fixed to zero for no applied current. (c) AC magnetic field magnitude at $\nu_{AC} = 8.3\,\text{kHz}$ as a function of applied current, measured at the position of each NV center via spin-RESOLFT and for the two NV ensemble in confocal mode. (d) 2D-magnetic field map created by spin-RESOLFT (at two points) and confocal (one point) measurements at a fixed AC current 7 mA and $\nu_{AC} = 8.3\,\text{kHz}$. The size of the disc for each NV is given by the fit uncertainty (95 % confidence) of the 2D position from the superresolved NV imaging. For all spin-RESOLFT measurements in this figure, the same doughnut beam power and duration were used as in Fig. 3.3 (150 µW and 17 µs).

NV spin-state contrast, leading to a trade-off between spatial resolution and magnetic field sensitivity (see Sec. B.4). As with the NV spin coherence time measurements (Fig. 3.4), the magnitude of the AC magnetic field found in confocal mode depends systematically on the position of the Gaussian beam and is only a weighted average of the magnetic field magnitudes determined individually for NV1 and NV2 using spin-RESOLFT (Fig. 3.4(d)).

To show the applicability of NV spin-RESOLFT for nanoscale magnetic imaging and spectroscopy, we used a shallow NV center located approximately 3 nm below the diamond surface (see below), and simultaneously imaged the NV lateral position with sub-diffraction resolution of 50 nm while sensing the NMR signal from a statistically-polarized nanoscale sample of protons in immersion oil on the diamond surface. Shallow implanted NV centers are a promising modality for quantum computing[43], nanoscale magnetic resonance imaging [75] and single molecule detection [73] due to the strong dipolar and hyperfine interactions with electronic[258] and nuclear[267, 268] spin species located on the diamond surface. Adversely, surface effects tend to shorten the Hahn-echo T_2 of shallow NVs[105, 128], typically to tens of microseconds, which consequently leads to a reduction in magnetic field sensitivity. Thus we integrated spin-RESOLFT with an XY dynamic decoupling protocol to extend[49] the shallow NV T_2 and enable practical nanoscale NMR imaging (Fig. 3.5(a)).

3.5 Proton NMR Measurements

XY8-k pulse sequences are applied to a single shallow NV to measure the NMR signal produced by ~ 100 statistically-polarized protons spins in immersion oil placed on the diamond surface. These pulse sequences produce NV spin phase accumulation that is transferred to a spin state population difference by means of the last microwave $\pi/2$-pulse. The choice of the phase of this last pulse allows for projections onto each NV spin state $m_s = 0$ and $m_s = 1$, resulting in fluorescence measurements F_0 and F_1. Common-mode noise from laser fluctuations is suppressed by normalizing the fluorescence signals together in a fluorescence contrast $C = (F_0 - F_1)/(F_0 + F_1)$.

NV sensing of the magnetic field Fourier components at frequencies ν is realized by measuring the fluorescence contrast C over a range of free evolution times $\tau = \nu/2$. NV spin "background" decoherence is characterized by slow exponential decay of the fluorescence signal over hundreds of microseconds (Fig. 3.3(c) of the main text). This background decoherence is fit to a stretched exponential function and normalized out, leaving only the narrower proton-NMR-induced dip in NV signal contrast on top of a flat baseline, as shown in Fig. 3.4(b). The shape of this dip is determined by the magnetic field fluctuations produced by the dense ensemble of proton spins in the immersion oil on the diamond surface, as well as by the filter function corresponding to the XY8-k dynamical decoupling pulse sequence. The magnetic field signal has cubic dependence on the distance between the NV center and diamond surface ($B_{\mathrm{RMS}} \propto$

d_{NV}^{-3}), which can be then estimated by fitting the dip with the following formula:

$$C(\tau) = \exp\left(-\frac{2}{\pi}^2 \gamma_e^2 B_{RMS}^2 K(N\tau)\right). \tag{3.1}$$

Here B_{RMS} is the RMS magnetic field signal produced at the Larmor frequency by the proton spins, $K(N\tau)$ is a functional that depends on the pulse sequence and the nuclear spin coherence time, and N is the number of pulses, which are separated by the NV spin free precession time τ. A thorough derivation of this formula as well as the description of the functional $K(N\tau)$ is presented by Pham et al.[163].

The XY-8k dynamic decoupling protocol creates a coherent superposition of the NV $m_s = 0$ and $m_s = 1$ spin states, and then alternates this spin coherence between free evolution (of duration τ) and π phase flips, before converting the total accumulated phase into an NV spin state population that is measured optically (Fig. 3.4(b)). We find that spin-RESOLFT can be combined with dynamical decoupling sequences to increase the NV coherence time to at least 100 µs while providing superresolution. Moreover, the NV spin phase accumulation is strongly perturbed when a frequency component of the external magnetic field matches twice the free evolution period $\tau = \nu_B/2$. Thus we observed a spectrally narrow dip in the NV coherence signal (Fig. 3.4(c)) at the proton spin Larmor precession frequency $\nu_p = (\gamma_p 2)B_0 \approx 1.2$ MHz, which is indicative of an NMR signal from statistically-polarized proton spins in the immersion oil on the diamond surface [25]. Here, γ_p is the proton spin gyromagnetic ratio and $B_0 = 28.2$ mT is the applied static magnetic field. Importantly, we find that the spin-RESOLFT and confocal mode NMR measurements are consistent: e.g., application of a 10 µs long doughnut beam pulse of 30 µW average power does not

deteriorate the proton NMR signal, while allowing for far-field optical spin readout of a sub-diffraction sized area with a lateral diameter of around 50 ± 5 nm. Furthermore, by fitting the NV NMR data the analytical model given by Eqn. 3.1, we determined the depth of the NV quantum sensor below the diamond surface to be 3.0 ± 0.3 nm [163].

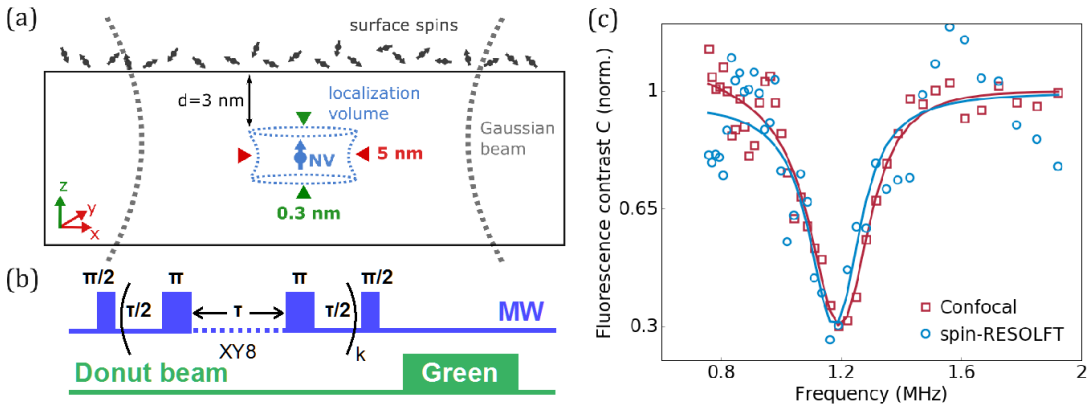

Figure 3.5: NV spin-RESOLFT sensing of proton NMR. (a) Schematic showing nanometer-scale localization volume of a shallow NV. (b) XY8-k dynamical decoupling pulse sequence used for NMR proton sensing with sub-diffraction resolution. (c) Example use of an XY8-4 sequence for spin-RESOLFT (blue) and confocal (red) NV NMR spectroscopy of proton spins in immersion oil on the diamond surface without degradation of the measured NMR proton linewidth (with doughnut beam power of 30 μW and duration of 10 μs). Fits to an analytical model (red and blue curves) determine the NV depth to be 3.0 ± 0.3 nm [163].

3.6 Discussion

In conclusion, we used spin-RESOLFT to selectively image and coherently manipulate two NV centers within a confocal volume, with no corrupting effect on NV spin coherence, enabling sensitive nanoscale magnetic imaging and spectroscopy. By combining this technique with spin sensing via dynamical decoupling sequences applied

to shallow NVs, we demonstrated the utility of spin-RESOLFT for nano-NMR. In comparison to other NV-diamond approaches for nanoscale magnetic imaging, such as scanning probe [257] and Fourier techniques using strong pulsed field gradients [92], spin-RESOLFT is technically straightforward, as it is all-optical and can be realized via extension of a confocal microscope. In future work we will extend spin-RESOLFT to many NVs within a diffraction-limited spot, allowing a diverse range of nanoscale magnetic imaging applications in both the physical and life sciences. We also anticipate that spin-RESOLFT will enable precise determination of the distance between two NV qubits, as well as their coherent manipulation. For a separation of 20 nm, the spin-spin vectorial interaction between individual NV centers (~ 10 kHz) is larger than their typical decoherence rate (~ 1 kHz), fulfilling a fundamental requirement for many quantum information protocols [54, 269]. Furthermore, low-power superresolution imaging techniques such as spin-RESOLFT can be critical for many applications, e.g., those that require cryogenic temperatures or shallow NV centers or for light-sensitive biological samples, as high optical power can cause heating as well as surface and sample deterioration. Finally, we expect that spin-RESOLFT can be straightforwardly extended to other NV-based sensing modalities, including temperature[108], electric field[103], and charge state[104] detection with nanoscale optical resolution.

Chapter 4

Improved Quantum Sensing with a Single Solid-state Spin via Spin-to-Charge Conversion

4.1 Introduction

Quantum defects in solids are emerging as the sensors of choice for detecting micrometre to nanometre phenomena in a wide range of systems in both the physical and life sciences. The Nitrogen-Vacancy (NV) color center in diamond is a prime example of such a solid-state quantum defect, combining long-lived electronic spin coherence with the ability to prepare and read out the spin state optically [41]. For example, NV centers have been used for high-spatial resolution sensing of magnetic fields in cell biology [80], bioassays [82], neuroscience [83], nanoscale NMR [72, 75, 270], and condensed matter physics [256, 271–273]. An important figure of merit for

this system is the spin readout noise per shot, specifying the accuracy with which the final state of the electron spin evolution can be measured in a single measurement attempt (shot). Current room temperature NV experiments rely on a spin-dependent fluorescence signal that is restricted to a short detection window (∼250 ns), after which the spin is optically pumped into the $m_s = 0$ state, such that the spin-state-dependent fluorescence contrast is typically limited to $\sim 25\%$ for a single NV center [41]. Recently, a new NV spin readout technique based on spin-to-charge conversion (SCC) that overcomes this limitation for NV centers was demonstrated in diamond nanobeams [124], in which the single NV fluorescence is enhanced by an order of magnitude compared to NV centers in bulk diamond. A similar protocol has also been demonstrated using high-intensity, near-infrared laser pulses and single NV centers under solid immersion lenses to achieve a spin-to-charge mapping via selective ionization of the singlet manifold [274]. Here, we show that SCC readout provides an order of magnitude improvement in single NV spin readout noise per shot in bulk diamond, without any influence of the charge state preparation on the NV spin coherence time. We then use SCC readout to demonstrate an improvement in single NV AC magnetometry sensitivity of about a factor of five, which is also about five times above the spin projection noise limit, similar to previous results for a single NV in nanobeams [124].

The conventional mechanism for room temperature optical readout of the NV electron spin (spin-1) is based on a spin-dependent intersystem crossing from the optical excited state into a manifold of optically dark singlet states. Under excitation

with 532nm light, an NV center initially in $m_s = 1$ is shelved into the metastable singlet level with about a 50% probability [178] and remains dark under subsequent excitation during the singlet state lifetime; whereas an NV center initially in $m_s = 0$ will continue to cycle and scatter photons during this readout time. These spin-state-dependent pathways induce repolarization of an NV center to the $m_s = 0$ ground state and constrain the detection window duration to ∼250 ns at room temperature. Consequently, the fluorescence collected from a single NV center in bulk diamond is limited to about 0.022 photons per readout with a low contrast (Fig. 4.1(a)). Thus, effective readout of the NV spin state can only be achieved statistically after many averages. Standard approaches to overcome this limitation involve using macroscopic ensembles of NVs [84, 90, 188] or photonically enhanced diamond nanostructures [275–277], in order to boost the fluorescence signal from the NV centers. Such techniques have their limitations, namely reduced spatial resolution and coherence time in the case of ensemble measurements, or limited sensing area and scalability in the case of photonic nanostructures. Therefore, techniques for improved readout of single NV centers in bulk diamond are of great interest.

4.2 Spin-to-Charge State Conversion Mechanism

A complementary approach is to develop readout techniques that transfer the spin state to more robust degrees of freedom than the relatively short-lived singlet. One such technique involves the transfer of spin information to the NV nuclear spin, which can subsequently be repetitively read out multiple times through the NV electronic spin [47]. This technique is capable of approaching the spin-projection noise limit,

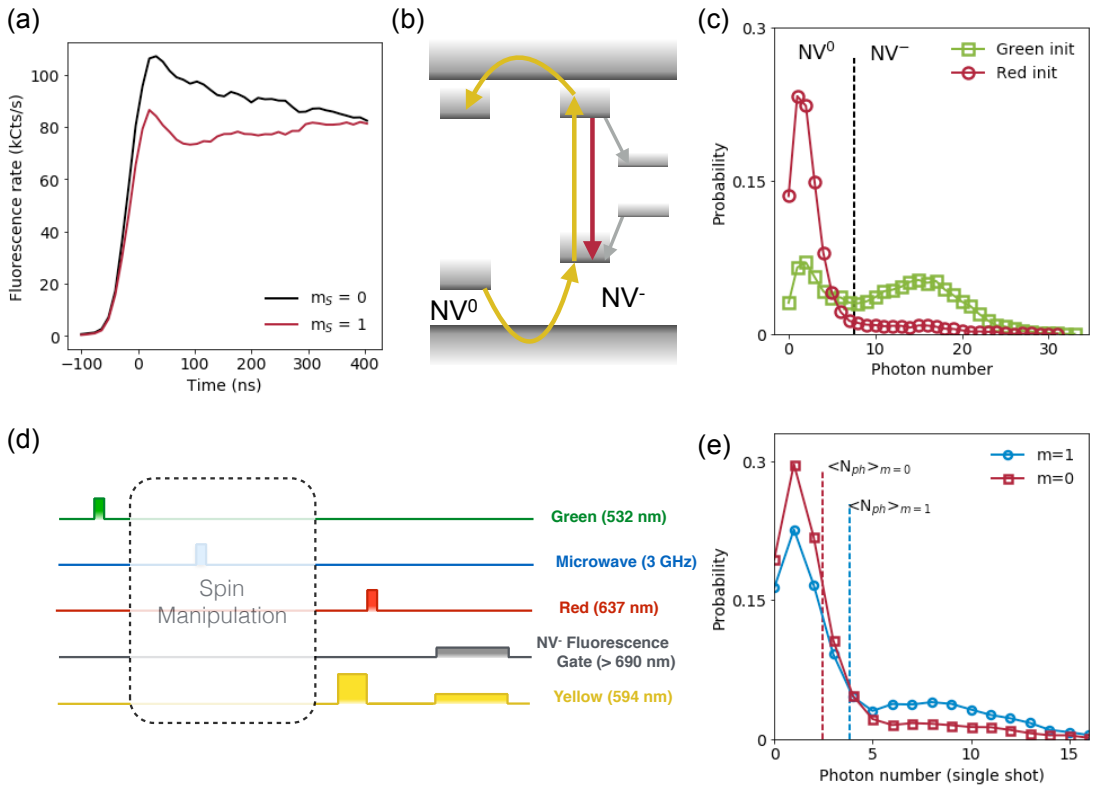

Figure 4.1: (a) Spin-state-dependent transients in the fluorescence of a NV center allowing for spin readout. (b) Energy levels of the neutral and negatively charged NV center. The NV^- electron spin can be polarized via decays through singlet states. A laser beam at a wavelength of 594nm only excites NV^-, leaving NV^0 dark, but it can also ionize NV^- to NV^0 (and induce recombination from NV^0 to NV^-). However, these processes are suppressed at low power, enabling high fidelity charge state readout. (c) Initialization of the charge state can be done with a green (532 nm) laser beam to prepare the negative charge state with a 70% probability. A red beam (637 nm) efficiently ionizes the NV center from NV^- to NV^0. (d) General sequence for NV quantum sensing. (e) The photon number distribution shows the efficiency of the spin-to-charge conversion (SCC) technique for a bulk NV. The dashed lines indicate the mean values of each distribution and show a spin readout contrast of 36%.

but has the disadvantage of requiring strong magnetic fields to split the nuclear spin levels, limiting its applicability. The present work deploys a spin-to-charge conversion (SCC) mechanism [124] that works by transferring the spin state to the charge state

of the NV, followed by a high-fidelity charge state measurement. This method has the advantage of being able to reach spin readout noise levels as low as twice the spin projection noise level, while being fully optical and easily incorporated in a confocal microscope and potentially with ensembles of NV centers.

The experimental setup is a confocal microscope adapted for NV spin-state measurements via both the SCC and conventional fluorescence techniques. Three laser beams (at 532, 594, and 637 nm) are coupled into single mode optical fibers to improve their spatial mode, and are then combined together with dichroic mirrors. A DPSS laser is used together with an acousto-optic modulator (AOM) to generate the green (532 nm) laser pulse. The protective yellow (594 nm) laser pulse and charge readout are both made with the same laser (HeNe 1.5mW) and AOM. To switch quickly from a relatively high yellow laser power (500 μW) for the protective step to a low power (5 μW) for the charge-state readout, two RF control signals are generated with voltage-controlled oscillators and controlled with RF switches. The red (637 nm) ionizing optical pulses are generated with a diode laser (HL63133DG, Thorlabs, 170 mW CW at 637 nm). The optical pulses are controlled with a pulse generator (AVO-2L-C-GL2, Avtech, 500 ps rise time, 2A), resulting in square pulse widths between 4 and 30 ns. The three laser beams are focused on a single NV in bulk diamond with a 1.45 NA, oil-immersion objective. The NV fluorescence ($\sim$90 kcounts/s) is collected through the same objective and then detected with an avalanche photodiode. A 150 μm pinhole restricts the longitudinal point-spread function to 500 nm and avoids out-of-focus background fluorescence from other NV centers.

NV centers are found mainly in two charge configurations [142], NV^0 and NV^- (Fig. 4.1(b)), which can be switched via a photo-ionization process [266]. Moreover, the NV center charge state can be read out in a single shot with a laser beam at 594nm, which efficiently excites NV^- but only weakly NV^0, producing a high fluorescence contrast between the two charge states [179, 180, 278] (Fig. 4.1(c)). For high readout fidelity, photo-ionization must be suppressed during readout, requiring low laser powers (as low as a few microwatts) and long readout times (from tens of microseconds to few milliseconds, depending on the desired single shot charge state readout fidelity). To switch between the charge states, a green laser beam (532 nm) initializes the charge state of the NV center preferentially to NV^- with 70% probability; while a 10-nanosecond pulse of red light (637 nm) almost ideally ionizes the NV center from NV^- to NV^0 via a two-step process that occurs between the NV center ground state and the conduction band.

The ionization process under 637nm illumination can be made spin-state-dependent by first shelving one spin state into the metastable singlet level, for which ionization is suppressed. In particular, the $m_s = 1$ population can be protected from ionization by first transferring it with a 594nm, 50ns-long pulse into the singlet state before ionizing the remaining triplet state population (mainly $m_s = 0$) with an intense 637nm pulse. The 637nm light does not excite the singlet state, so the ionization process is blocked for $m_s = 1$, and the NV remains in the negative charge state. We implement this spin-to-charge conversion with the sequence depicted in figure 4.1(d). We plot the

photon number distributions in figure 4.1(e) for the two cases where the NV center is prepared in $m_s = 0$ (no microwave pulse) and $m_s = 1$ (microwave π pulse), illustrating our SCC efficiency. As expected, $m_s = 0$ is converted almost entirely to NV^0, while $m_s = 1$ remains in NV^- to a large degree. From the mean values of the two distributions ($\langle N_{ph}\rangle_{m=0} = 2.4$ and $\langle N_{ph}\rangle_{m=1} = 3.8$), we extract a spin-state contrast of 36%, which is larger than for the conventional (singlet-state) readout scheme (by about a factor of 1.5x) due to the fact that the ionization occurs when the population of the singlet state is maximum. More importantly, the robustness of the charge states allows for the collection of an arbitrary number of photons in a single shot (typically, about 5 photons in a 1 ms time window). This increased photon number largely eliminates the contribution of photon shot noise in the measurement, limiting the SCC method to spin-projection noise and conversion noise during the spin-to-charge mapping.

We define the spin readout noise per shot σ_R as the ratio between the measured spin noise and the spin projection noise $\sigma_{SPN} = \sqrt{p_0(1-p_0)}$, where p_0 is the probability of detecting one projection, e.g., $m_s = 0$, of our effective two-level spin system. The spin readout noise can be estimated directly from the collected photon distribution for each class of spin. In the case of SCC readout, a perfect mapping would link the spin state $m_s = 0$ and $m_s = 1$ to the neutral charge state NV^0 and negatively charged state NV^-, respectively. We define errors ϵ_0 and ϵ_1 to be the probabilities that the detected charge state deviates from such a perfect mapping. Then we can recast the spin readout noise per shot expressed in [124] as $\sigma_R = \sqrt{1-(\epsilon_0-\epsilon_1)^2}/(1-(\epsilon_0+\epsilon_1))$.

These errors can be straightforwardly estimated from figure 4.1(e) by choosing a threshold (here equal to 5 photons) that distinguishes the charge states from each other as depicted in figure 4.1(c). In the experiments reported here, we typically obtain $\epsilon_0 \approx 0.14$ and $\epsilon_1 \approx 0.69$, which results in $\sigma_R \approx 5$. For comparison, conventional NV spin-state readout is limited by photon shot noise [41, 124]. The spin readout noise per shot consequently becomes $\sigma_R \simeq 2(V\sqrt{n})^{-1} \approx 54$, where $n \approx 0.022$ is the average mean photon number per detection window and V$\approx$ 25% is the contrast for single NV confocal detection (Fig. 4.1(a)).

4.3 Application to Magnetic Sensing

As a proof of concept of the performance of the SCC method for quantum sensing, we use the single NV center as a nanoscale AC magnetic field sensor. Oscillating magnetic fields can be probed by applying a synchronized Hahn-echo sequence. During the period τ, the NV center's quantum state evolves under the influence of the AC magnetic field as well as environmental noise. This evolution is manifested by a phase accumulation that is converted into an optically-readable spin state population difference. Because of the noise environment, such phase accumulation is limited to the characteristic coherence time T_2. For a single NV, T_2 can approach one millisecond [49, 189] via the implementation of dynamical decoupling sequences that act as filter functions to suppress the effects of noise fluctuations.

In the absence of an applied AC magnetic field, the single NV coherence time

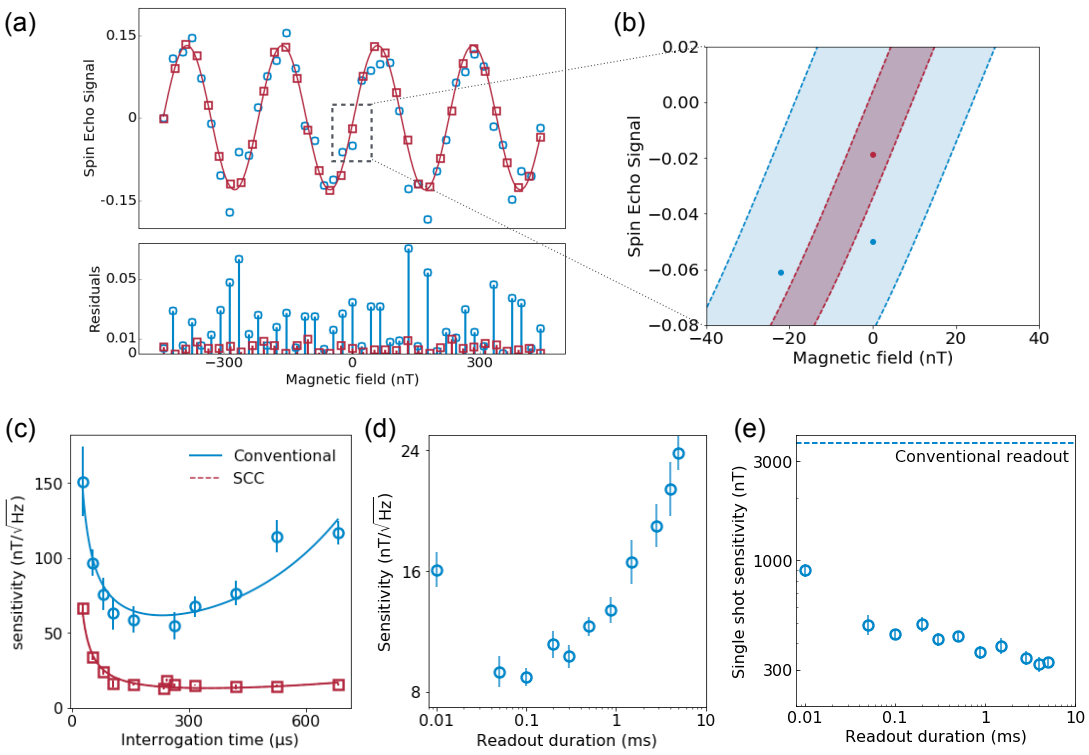

Figure 4.2: (a) Examples of measured normalized NV fluorescence signals as a function of AC field magnitude using a Hahn-echo sequence with the conventional (blue) or SCC (red) readout techniques. The interrogation time is set to match the AC magnetic field frequency of 4 kHz. The total duration of the data acquisition (1 h) is the same for both curves, showing improved sensitivity for the SCC scheme, as indicated by reduced residuals. (b) Zoom showing the improved sensitivity, from 45(12) nT/$\sqrt{\text{Hz}}$ for the conventional readout technique to 9(1) nT/$\sqrt{\text{Hz}}$ for the SCC technique, at the most sensitive operating point (around zero AC magnetic field amplitude). (c) Measured magnetic field sensitivity as a function of interrogation time. The straight lines are fits using Eq. (1) fixing $T_2 = 465$ μs as independently measured. The SCC scheme is even more advantageous than the conventional readout technique at long interrogation time, where single, efficient readouts are superior to multiple repetitions of the readout protocol. (d) Optimization of the SCC techniques magnetic field sensitivity by tuning the readout duration to limit the inactive time. Here we adapted the readout power for each readout duration to maximize the charge state readout fidelity. (e) Smallest magnetic field amplitude measurable with the SCC technique (i.e., with a signal-to-noise ratio of 1) for a single realization of the magnetometry sequence.

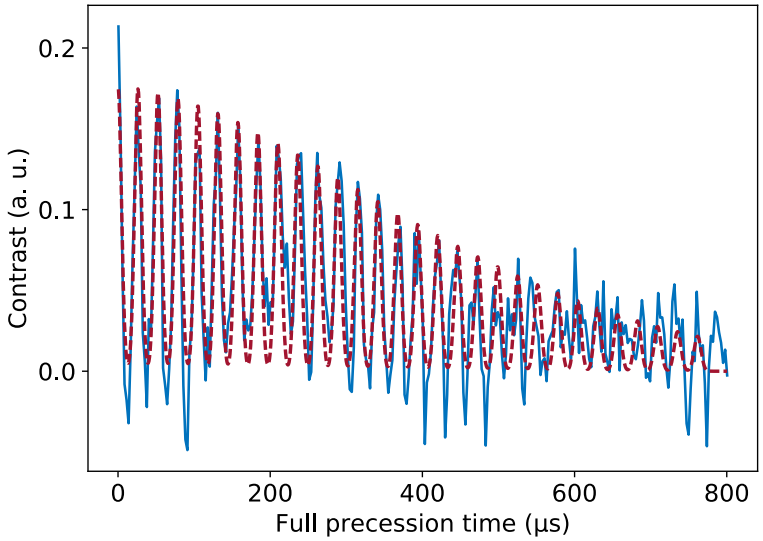

Figure 4.3: Coherence decay of the NV center measured with a Hahn-echo sequence.

T_2 can be measured using the same Hahn-echo sequence as described in the main text. As we vary the free evolution time τ, we find that the superposition of $m_s = 0$ and 1 decays to an incoherent state in a time $T_2 = 461.5$ μs. Due to the presence of ^{13}C atoms in the diamond lattice (at the natural abundance of 1.1%), the coherence of the NV center is modulated by revivals that occur at multiples of the Larmor precession time $t_{rev} = 26.28$ μs. AC magnetometry can only be done at evolution times that corresponds to the different revivals. Consequently, the optimal experimental sensitivity is achieved for $\tau_{opt} = 223.34$ μs $\simeq T_2/2$.

We drive the NV center's electronic spin into a superposition of $m_s = 0$ and $m_s = 1$ that acquires a relative phase scaling linearly with the magnetic field amplitude $\phi = \frac{2\mu_B}{\pi\hbar} B\tau = \alpha B\tau$ [257, 279]. This measurement protocol results in a rotation of the

Bloch vector in the equatorial plane, which is observed as a sinusoidal oscillation of the NV fluorescence signal with AC magnetic field amplitude, as the phase is transferred to a population difference (fig. 4.2(a)). Figure 4.2(b) is a zoom around the point of zero AC magnetic field amplitude, where the NV magnetometer sensitivity $\eta(\tau)$ is maximum, which we estimate by [41]:

$$\eta(\tau) = \sigma_R \frac{\mathrm{e}^{\left(\frac{\tau}{T_2}\right)^p}}{\alpha\sqrt{\tau}} \sqrt{\frac{t_{\mathrm{init}} + \tau + t_{\mathrm{ro}}}{\tau}}. \tag{4.1}$$

Here, σ_R is the spin readout noise per shot, normalized to the spin projection noise, α is the scaling factor between the phase acquired and the field measured, and p is an exponent containing information related to the spin bath [53]. $\sqrt{(t_{\mathrm{init}} + \tau + t_{\mathrm{ro}})/\tau}$ is a time penalty, where the initialization time and the readout time are denoted respectively t_{init} and t_{ro}. For our demonstration experiment, we find an improvement of a factor 5 in AC magnetic field sensitivity of the SCC method, 9(1) nT/$\sqrt{\mathrm{Hz}}$, over the conventional readout technique, 45(12) nT/$\sqrt{\mathrm{Hz}}$.

We next investigate the sensitivity improvement provided by the SCC scheme for different evolution times τ. Increasing this time results in a stronger integrated readout signal, but is only favorable up to the point where spin decoherence reduces the measurement contrast. According to equation (4.1), there is an optimum of sensitivity at $\tau = T_2/2 = 232$ μs for the conventional readout scheme (for which the initialization and readout time are negligible and p $\approx$ 1), as is clearly visible in figure 4.2(c). The SCC technique performs noticeably better than conventional readout over a wide range of evolution times between 50 μs to 700 μs. As τ increases and becomes significantly longer than the readout time, the gain must approach its max-

imum value, $\sigma_R^{\mathrm{SCC}}/\sigma_R^{\mathrm{stand.}}$. At the other extreme, we expect that short spin readout times will prevail when τ is short since they allow for fast repetition of quantum sensing sequences. We find that this regime is not reached yet at evolution times as short as 50 μs, where the sensitivity improvement is still in favor of the SCC technique by a factor of two (fig. 4.2(c)). From the parameters of each fit, we determine that the spin readout noise per shot σ_R for conventional readout is $\sigma_R^{\mathrm{conven.}} \approx 60$ and $\sigma_R^{\mathrm{SCC}} \approx 5$ for SCC readout, confirming the values reported above. Interestingly, the fitted p parameter in (1) is different for the two readouts ($p_{\mathrm{SCC}} = 1.01$ and $p_{\mathrm{conven.}} = 1.33$), so that the sensitivity improvement is not yet saturated for 700 μs evolution time. Moreover, we note that AC magnetic field sensitivity at high frequency can be improved by dynamical decoupling sequences, which both move the filter function's central frequency to higher values (allowing long accumulation times even for fast oscillating fields), and extend the coherence time.

Since the time penalty term in (1) becomes significant only for a readout time comparable to or longer than the interrogation time, the SCC sensitivity improvement can be optimized by increasing the readout time (and consequently decreasing σ_R) while keeping the time penalty negligible. We demonstrate this explicitly in figure 4.2(d) by measuring the sensitivity for different readout durations. At the evolution time where the sensitivity is optimal for conventional readout, we measure an SCC sensitivity of 9(1) $\mathrm{nT}/\sqrt{\mathrm{Hz}}$ for $t_{\mathrm{ro}} = 40$ μs. On the other hand, the duty cycle of quantum sensors can also be limited by an external parameter, e.g., the repetition rate of the recorded events. In such scenarios, the correct figure of merit is the single shot

magnetic field sensitivity. In particular, one can take full benefit of long readout time windows of a few milliseconds to improve the performance of the spin readout and consequently of NV magnetometers using the SCC technique. For example, as shown in Figure 4.2(e), we realize a magnetic field amplitude uncertainty of 307(29) nT in a single SCC measurement with a 5 ms readout time, for which the photon shot noise is nearly totally suppressed. This uncertainty is an order of magnitude smaller than with conventional NV spin readout.

The 30 μs-long green initialization leaves the NV center in its neutral charge state one third of the time, allowing for a substantial improvement in the SCC technique performance by detecting aberrant initializations prior to the coherent microwave manipulation. This protocol can be performed with charge-state readout capability with either a 'try till success' polarization technique or by post-selecting on the initial charge state being NV^-. Although the former offers the best sensitivity, it also requires fast readout electronics to compute the result of the first charge state readout. We implemented the latter by reading out the charge state of the NV center with a 10 ms long yellow readout pulse. The duration is chosen to limit ionization during this step, although some remains in practice, as one can see that the spin readout noise per shot increases to about 8. In figure 4.4(a), we plot the distribution of photons obtained from the first readout gate (blue curve). The post-selection is conditioned on having acquired a number of photons during the first charge state readout pulse that is strictly higher than a certain threshold (6 photons in figure 4.4(a), filled blue area). Because we mainly reject sequences where the NV center is in NV^0,

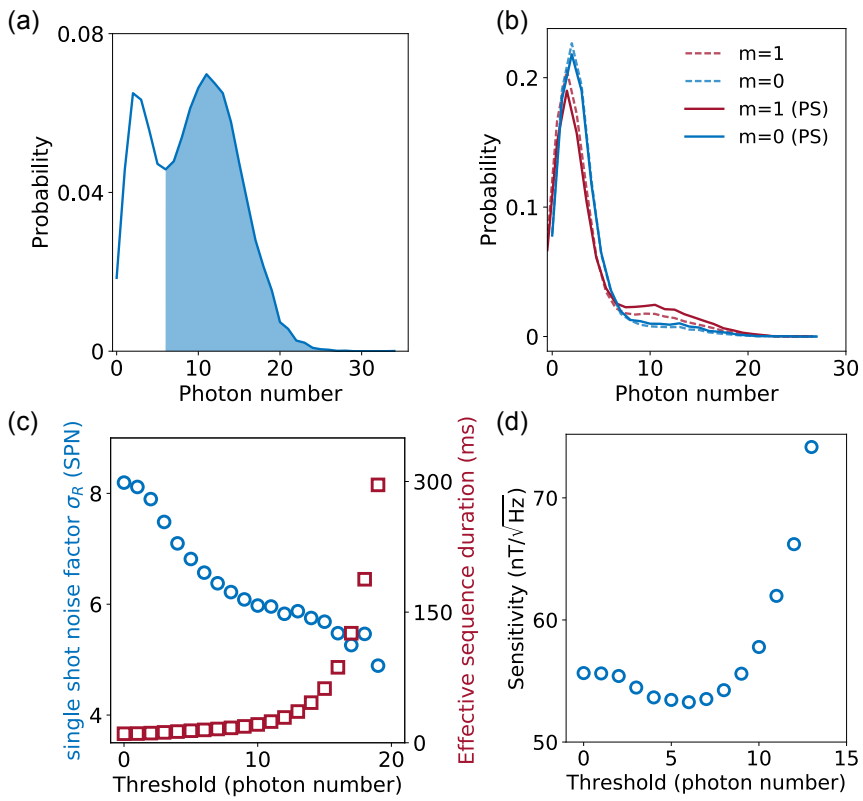

Figure 4.4: Post-selection enhancement of SCC technique. (a) Photon distribution recorded in an initial charge readout pulse prior to microwave manipulation. The distribution of all sequences (solid line) shows that a significant fraction of events is executed on the neutral charge state and can be discarded to keep mainly results obtained with NV^- (filled area). (b) Photon distributions after post-selecting for NV^- (solid lines) have greater distinguishability than the distributions for all events (dashed lines). The Kolmogorov-Smirnov test gives a distinguishability of 0.12 against 0.08 for no post-selection. (c) Spin readout noise per shot as a function of threshold, and effective sequence time. Eliminating initial NV^0 events improves the efficiency of SCC mapping at the cost of increasing the sequence duration. (d) AC magnetic field sensitivity for different thresholds, showing a 5% improvement in sensitivity by post-selecting for the initial NV charge state. The length of both charge-state readout windows (20 ms in total) limits the absolute sensitivity to 53(16) $\mathrm{nT}/\sqrt{\mathrm{Hz}}$. Alternatively, very short time windows that would allow for the detection a single photon would be enough to determine the charge state of the NV center.

the distinguishability between the spin states is enhanced (Fig. 4.4(b)). To further demonstrate the improvement due to post-selection, we measure the readout noise for various thresholds. We see in figure 4.4(c) that σ_R decreases faster at low threshold because we remove measurements where the NV center could not be used to sense any magnetic fields. After a threshold that corresponds to the visual limit between NV^0 and NV^-, the slope becomes less steep as we discard good measurements. In parallel, we estimate the cost of rejecting measurements by computing an effective sequence time. The sensitivity can be improved if σ_R decreases faster than the square root of the effective sequence time increases (eq. (4.1)). We show that this is indeed the case for thresholds smaller than 6 photons per readout pulse, with an improvement of about 5% (Fig. 4.4(d)), limited mainly by the long duration of the first charge state readout.

4.4 Charge State Readout of Shallow NV Centers

Shallow implanted NV centers are a promising modality for nanoscale magnetic resonance imaging and single molecule detection due to the strong dipolar and hyperfine interactions with electronic and nuclear spin species located on the diamond surface [**Shushkov2014a**, 267, 268]. Adversely, surface effects tend to shorten the coherence time of shallow NVs, typically to tens of microseconds, and could also potentially modify their charge state dynamics. We show in figure 4.5 that we see no change in the charge state dynamics of shallow NV centers; and also that they can still be read out with high fidelity. We plot in figure 4.5(a) a typical time trace of the observed fluorescence, under constant 594nm light illumination, from a single NV center

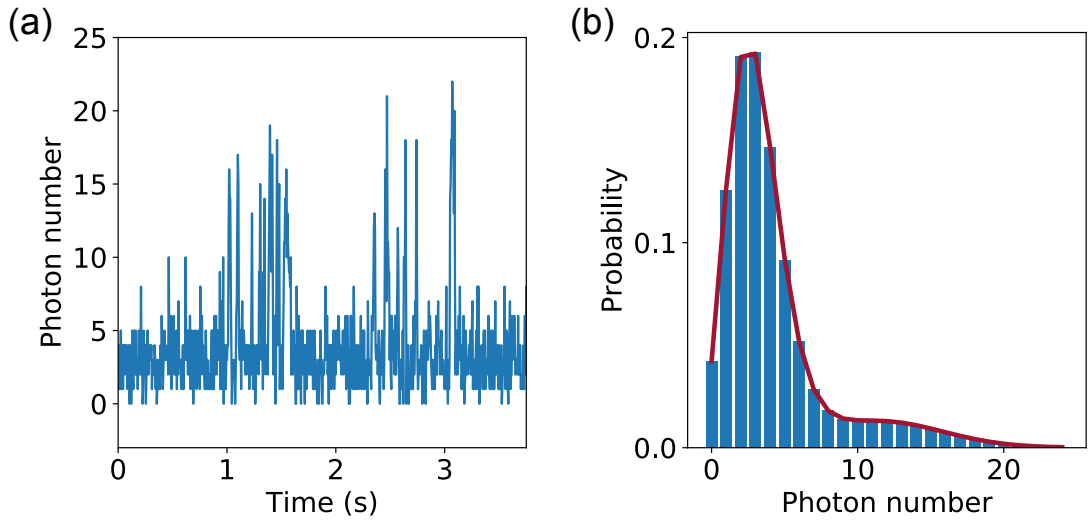

Figure 4.5: (a) An example of time traces of a shallow NV center's fluorescence under 594nm light illumination, revealing charge state jumps. (b) Photon number distribution displaying two levels of fluorescence. The red line is a numerical fit based on the master equation that describes the behaviour of the charge state under a 594nm light illumination [124].

implanted 3nm below the surface (measured by a nanoscale NMR technique [163]) exhibiting the expected behaviour: i.e. ionization and recombination between charge state NV^0 (low fluorescence level) and NV^- (high fluorescence level).

The histogram of such time traces is plotted in figure 4.5(b) and displays two peaks associated with these two levels of fluorescence. We perform a numerical fit based on the master equation that describes the behaviour of the charge state under a 594nm light illumination [124] and extract the fluorescence rates $\gamma_0 = 200$ Hz and $\gamma_- = 1.3$ kHz, the ionization rate $g_0 = 45$ Hz, and the recombination rate $g_- = 6$ Hz for an excitation power of 280 μW. These rates are very similar to those measured with NV centers in bulk diamond and indicate that the SCC readout will provide a similar improvement with shallow NV centers as that reported in the main text for

deep NVs.

4.5 Conclusion

In this work, we show that the spin-to-charge conversion technique, together with single-shot charge-state readout, provides about a factor of five improvement in AC magnetic field sensitivity for a single NV center in bulk diamond. This readout scheme is not only beneficial to AC magnetometry but also to any kind of quantum sensing measurement that benefits from long coherence time, such as T_2-limited thermometry [81] or ancilla-assisted DC magnetometry [280]. Furthermore, for typical NV spin dephasing times observed in isotopically purified 12C samples with low Nitrogen concentration ($T_2^* \approx 50$ μs) [281], SCC readout should be applicable to Ramsey-like DC magnetometry with a two-fold sensitivity improvement. Moreover, SCC readout is well suited to detecting pulsed magnetic fields, for example those created by neuron action potentials with typical pulse timescales of milliseconds and delays between pulses of 10-100 milliseconds [83]. In such cases, it is not necessary to optimize the duty cycle of the sensor and one can take advantage of dead times to increase the fidelity of the readout. In particular, SCC sensitivity is expected to improve by an order of magnitude compared to conventional readout, down to $\sim$300 nT for a single realization of the experimental protocol. Finally, because the neutral charge state is a dark state, the SCC readout scheme is also well suited for NV ensemble measurements and superresolution techniques [50, 143], which both suffer from background fluorescence. Indeed, off-axis NV centers are not affected by the microwave pulses and are consequently ionized during the spin to charge mapping.

Chapter 5

Order of Magnitude Improvement in T_2^* in Solid-State Spin Ensembles via Quantum Control

5.1 Introduction

Solid-state electronic spins, including defects in silicon carbide [15–19], phosphorus spins in silicon [3, 4], and silicon-vacancy [11, 14, 17] and nitrogen-vacancy (NV) centers[142] in diamond, have garnered increasing relevance for quantum science and sensing experiments. In particular, NV centers in diamond have been extensively studied and deployed in diverse applications facilitated by their long coherence times[123, 214] at ambient temperature and addressable optical and magnetic transitions[142]. Many applications utilize macroscopic NV spin ensembles for high-sensitivity DC magnetic field sensing [79, 83] and wide-field DC magnetic imaging [80, 82, 93, 95, 101], includ-

ing measurements of single-neuron action potentials[83], paleomagnetism[100, 101], and current flow in graphene[93].

For NV-ensembles, the DC magnetic field sensitivity is typically limited by dephasing of the NV sensor spins. In such instances, spin interactions with an inhomogeneous environment (see Fig. 5.1a) limit the experimental sensing time to $T_2^* \lesssim 1\,\mu$s[66, 71, 83, 108]. Hahn echo and dynamical decoupling protocols can restore the NV ensemble phase coherence by isolating the NV sensor spins from environmental noise and, in principle, permit sensing times approaching the spin lattice relaxation ($T_1 \sim$ ms)[49, 53]. However, these protocols restrict sensing to AC signals within a narrow bandwidth. For this reason, the development of high sensitivity, broadband magnetometers requires new approaches to extend T_2^* while retaining the ability to measure DC signals.

Several mechanisms contribute to NV spin ensemble dephasing in bulk diamond. In particular, the formation of negatively-charged NV centers ($S = 1$) requires the incorporation of nitrogen into the diamond lattice. As a result, paramagnetic substitutional nitrogen impurities (P1 centers, $S = 1/2$)[5–7] typically persist at densities similar to or exceeding the NV concentration. In addition, strain is well-known to affect the diamond crystal [133, 134], but the exact contribution of strain gradients to NV dephasing has not been quantified rigorously and varies throughout a sample. Furthermore, the interrogation of large NV ensembles requires the design of homogeneous magnetic bias fields to minimize magnetic field gradients across the detection

volume.

In this work, we combine double quantum (DQ) coherence magnetometry [202, 207] with spin bath control [127, 243] to mitigate the dominant sources of NV spin ensemble dephasing and extend T_2^*. In the DQ basis, noise sources that shift the $|\pm 1\rangle$ states in common-mode (i.e., strain inhomogeneities and temperature fluctuations) are suppressed by probing the energy difference between the $|+1\rangle$ and $|-1\rangle$ sublevels. In addition, the NV DQ spin coherence accumulates phase due to an external magnetic field at twice the rate of traditional single quantum (SQ) coherence magnetometry, in which the $|0\rangle$ and $|+1\rangle$ (or $|-1\rangle$) sublevels are probed. Thus, DQ magnetometry provides enhanced sensitivity to target magnetic field signals while also making the spin coherence twice as sensitive to magnetic noise, including interactions with the paramagnetic spin bath. We therefore use resonant radiofrequency control to decouple the nitrogen bath spins from the NV sensors. By employing both DQ magnetometry and spin bath control, we elucidate and effectively eliminate the dominate sources of NV ensemble dephasing, realizing up to a 16× extension of the ensemble T_2^* in diamond. We also demonstrate the compatibility of our techniques with Ramsey-based DC sensing. Our results should enable broadband DC sensing using NV spin ensembles with measurement times approaching those used in AC sensing; and may aid in the fabrication of optimized samples for a wide range of solid-state sensor species.

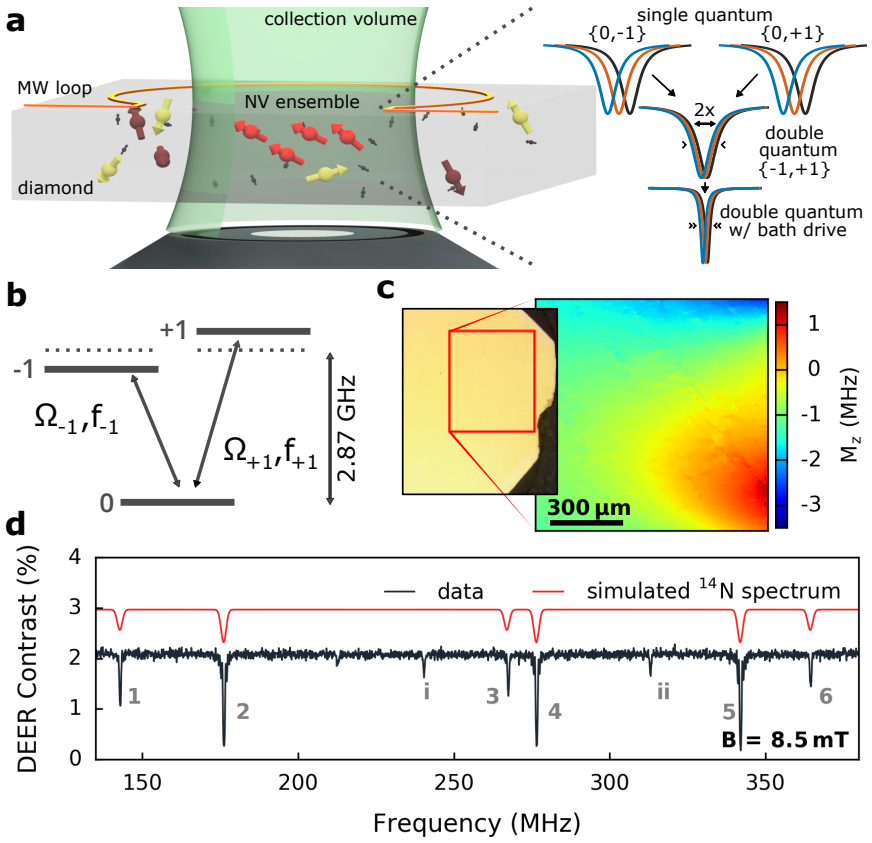

Figure 5.1: (a) The inhomogeneously broadened electron spin resonance (ESR) linewidth of nitrogen-vacancy (NV) ensembles is a complex function of the local environment within the diamond sample, including a diverse bath of electronic and nuclear spins. Inset: Schematics of NV ensemble ESR spectra in the single quantum and double quantum bases, and for double quantum with spin-bath drive. (b) Spin-1 ground state of the NV center. (c) Imaging of the longitudinal strain component M_z of one NV class across a 1-mm^2 field of view for Sample B. An optical microscope image of the diamond surface (left) is included for reference with a red box outlining the field of view shown in the NV strain image. (d) Double electron-electron resonance (DEER) ESR spectrum of Sample B, showing six nitrogen groups $(1-6)$ attributed to ^{14}N electronic spins with an external field $B_0 = 8.5\,\mathrm{mT}$ aligned along a [111]-crystallographic axis (see main text). Linewidths are Fourier-broadened. The peaks labeled *i* and *ii* correspond to dipole-forbidden transitions of the ^{14}N electronic spins ($\Delta m_I \neq 0$, see Sec. C.5). The simulated spectrum using the full nitrogen Hamiltonian is shown in red, with linewidth and amplitudes chosen to resemble experiment.

5.1.1 Double Quantum Magnetometry

The enhanced sensitivity to magnetic fields and insensitivity to common-mode noise sources in the DQ basis can be understood by considering the spin-1 ground-state Hamiltonian for NV centers as given by (neglecting hyperfine interaction) [125, 142],

$$H/h = D\,\mathbf{S}_z^2 + \frac{\gamma_{NV}}{2\pi}\mathbf{B}\cdot\mathbf{S} + M_z\mathbf{S}_z^2 + M_x(\mathbf{S}_y^2 - \mathbf{S}_x^2) + M_y(\mathbf{S}_x\mathbf{S}_y + \mathbf{S}_y\mathbf{S}_x), \tag{5.1}$$

where $D \approx 2.87\,\mathrm{GHz}$ is the zero-field spin-spin splitting, $\mathbf{S} = \{\mathbf{S}_x, \mathbf{S}_y, \mathbf{S}_z\}$ are the dimensionless spin-1 operators, $\mathbf{B} = \{B_x, B_y, B_z\}$ are the local magnetic field components, $\gamma_{NV}/2\pi \approx 28\,\mathrm{GHz/T}$ is the NV gyromagnetic ratio, and $\{M_x, M_y, M_z\}$ describe the strain and electric field contributions to H. Ignoring terms $\propto \mathbf{S}_x$, $\mathbf{S}_y$ due to the large zero-field splitting D, the transition frequencies $f_{\pm1}$ (see Fig. 5.1b) are

$$f_{\pm1} \approx D + M_z \pm \frac{\gamma_{NV}}{2\pi}B_z. \tag{5.2}$$

On-axis strain fields ($\propto M_z$) as well as temperature fluctuations ($\frac{\partial D}{\partial T} = -74\,\mathrm{kHz/K}$) [108, 109] shift the $f_{\pm1}$ transitions linearly, and thus their effects on DQ magnetometry are to first order suppressed. In addition, a pertubative analysis of the Hamiltonian in Eqn. 5.1 (see Supplement C.2) shows that the effects of off-axis strain fields ($\propto M_x, M_y$) on DQ magnetometry are mitigated by a factor $\frac{\sqrt{M_x^2+M_y^2}}{\gamma_{NV}B_z/\pi}$ when a bias magnetic field B_z is applied along z. Similarly, the effects of off-axis magnetic fields ($\propto B_x, B_y$) on DQ magnetometry are suppressed due to the large zero-field splitting D, and are also largely common-mode. Working in the DQ basis at moderate bias fields ($B_z \gtrsim 1\,\mathrm{mT}$) can therefore lead to an enhancement in T_2^* for NV ensembles if strain inhomogeneities, small off-axis magnetic field gradients ($B_x, B_y \ll D$), or temperature fluctuations are significant mechanisms of inhomogeneous dephasing. This

result should be contrasted with single NV measurements in which T_2^* and T_2 in the DQ basis were found to be approximately half the values in the SQ basis[202, 207]. Since spatial inhomogeneities are not relevant for single centers, the twice higher dephasing rate was attributed to enhanced sensitivity to magnetic noise from the paramagnetic spin bath.

For example, using vector magnetic microscopy (VMM) [101], we mapped the on-axis strain component M_z in a $1\,\mathrm{mm}^2$-region for one of our NV ensemble diamond samples ($[N] = 0.75\,\mathrm{ppm}$, Sample B) to quantify the length-scale and magnitude of strain inhomogeneity (Fig. 5.1c). From this analysis, we estimate a length-normalized strain gradient $M_z/L \approx 2.8\,\mathrm{kHz}/\mu\mathrm{m}$, which, as we show below, is in good agreement with the observed SQ T_2^* in our samples.

5.1.2 Spin Bath Control

To mitigate dephasing due to the spin bath, we drive the bath electronic spins [127, 243] using resonant radiofrequency (RF) radiation. In Fig. 5.1d, we display the spin resonance spectrum of a nitrogen-rich diamond sample ($[N] = 0.75\,\mathrm{ppm}$, Sample B), recorded via the NV double electron-electron resonance (DEER) technique [233] in the frequency range 100 - 500 MHz (see Sec. 2.2). The data reveal 6 distinct spectral peaks attributed to ^{14}N substitutional nitrogen defects in the diamond lattice. The resonance peaks have an approximate amplitude ratio of 1:3:1:3:3:1 resulting from the four crystallographic Jahn-Teller orientations of the nitrogen defects at two possible angles with respect to an applied bias magnetic field ($B_z = 8.5\,\mathrm{mT}$, aligned along

[111]-axis), as well as 3 hyperfine states [8, 9, 282]. Additional smaller peaks *i* and *ii* are attributed to dipole-forbidden nitrogen spin transitions and other electronic dark spins in the diamond[161].

In pulsed spin bath driving [127], a multi-frequency RF π-pulse is applied to each of the bath spin resonances midway through the NV Ramsey sequence, decoupling the bath from the NV sensor spins in analogy to a refocusing π-pulse in a spin echo sequence [49]. Alternatively, the bath spins can be driven continuously (CW) [127, 243]. In this case, the Rabi drive strength Ω_{Bath} at each bath spin resonance frequency must significantly exceed the characteristic coupling strength γ between the bath spins and NV centers, i.e., $\Omega_{Bath}/\gamma \gg 1$, to achieve effective decoupling. Under this condition, the baths spins undergo many Rabi oscillations during the characteristic dipolar interaction time $1/\gamma$. As a result, the average dipolar-interaction with the bath is motionally narrowed [233, 250] and the NV dephasing time increases.

5.2 Results

We studied three unirradiated diamond samples with varying nitrogen concentrations (see Table 5.1). Samples A ($[N] \lesssim 0.05\,\text{ppm}$) and B ($[N] = 0.75\,\text{ppm}$) each consist of a ^{14}N-doped, $\approx 100\,\mu\text{m}$-thick CVD layer (99.99% ^{12}C) deposited on top of a diamond substrate. Sample C ($[N] = 10\,\text{ppm}$) possesses a $40\,\mu\text{m}$-thick, ^{15}N-doped CVD layer (99.95% ^{12}C). For all three samples, the nitrogen-limited inhomogenous dephasing times are estimated from the average dipolar interaction strength between electronic

spins (see Methods) giving $T^*_{2,\text{NV-N}} \approx 350\,\mu\text{s}$, $23\,\mu\text{s}$, and $2\,\mu\text{s}$ for Samples A, B, and C, respectively. Analysis and measurements suggest that the ^{13}C limit to T_2^* is $\approx 100\,\mu\text{s}$ for Samples A and B, and $\approx 20\,\mu\text{s}$ for Sample C (see Methods). For all samples, the N-to-NV conversion efficiency is $\lesssim 1\%$ and therefore contributions from NV-NV dipolar interactions to T_2^* can be neglected.

T_2^* values in the SQ and DQ bases, denoted $T^*_{2,SQ}$ and $T^*_{2,DQ}$ from here on, were measured by performing either a single- or two-tone $\pi/2 - \pi/2$ Ramsey sequence (see inset Fig. 5.2). In both instances, the observed Ramsey signal exhibits a characteristic exponential decay envelope that is modulated by the frequency detunings of the applied NV drive(s) from the NV hyperfine transitions. The data is fit to the expression $\mathrm{e}^{-(\tau/T_2^*)^p} \sum_i \cos(2\pi f_i(\tau - \tau_{0,i}))$, where free parameters in the fit are T_2^*, p, time-offsets $\tau_{0,i}$, and (up to) three frequencies f_i from the NV hyperfine splittings. The stretched exponential parameter p is a phenomenological description of the decay envelope, which depends on the specific noise sources in the spin bath as well as the distribution of individual resonance lines within the NV ensemble. In the limit of a purely magnetic-noise-limited spin bath, the ensemble decay envelope exhibits exponential decay ($p = 1$) [200, 221], whereas Gaussian decay ($p = 2$) suggests gradient-limited ensemble dephasing.

Sample	[N] (ppm)	^{13}C (%)	[NV] (cm^{-3})	T_2^{meas} (μs)	$T_{2,SQ}^{*,meas}$ (μs)	$T_{2,DQ}^{*,meas}$ (μs)	$T_{2,NV-N}^{*,est}$ (μs)	$T_{2,NV-^{13}C}^{*,est}$ (μs)	$T_{2,NV-(^{13}C+N)}^{*,est}$ (μs)	dM_z^{meas}/dL (MHz/μm)
A	$\lesssim 0.05$	0.01	$\sim 3 \times 10^{12}$	$\gtrsim 630$	$5-12$	34(2)	350	100	78	n/a
B	0.75	0.01	$\sim 10^{14}$	$250-300$	$1-10$	6.9(5)	23	100	19	0.0028
C	10	0.05	$\sim 6 \times 10^{15}$	15-18	$0.3-1.2$	0.60(2)	2	20	2	n/a

Table 5.1: Characteristics of Samples A, B, and C. $T_2^{*,est}$ values are calculated using the estimated contributions of ^{13}C and nitrogen spins as described in the main text and methods. Reasonable agreement is found between the estimated $T_{2,NV-(13C+N)}^{*,est}$ and twice the measured $T_{2,DQ}^{*,meas}$, consistent with the twice faster dephasing in the DQ basis. Values listed with a $\sim$ symbol are order-of-magnitude estimates. For all samples, $[NV] \ll [N]$ and NV contributions to T_2^* can be neglected ($1\,\text{ppm} = 1.76 \times 10^{17}\,\text{cm}^{-3}$).

5.2.1 Strain Dominated Dephasing (Sample A: Low Nitrogen Regime)

Experiments on Sample A ([N] $\lesssim 0.05\,\text{ppm}$, ^{14}N) probed the low nitrogen density regime. In different regions of this diamond, the measured SQ Ramsey dephasing time varies between $T^*_{2,SQ} \simeq 5 - 12\,\mu\text{s}$, with $1 < p < 2$. Strikingly, even the longest measured $T^*_{2,SQ}$ is $\sim 30\times$ shorter than the calculated $T^*_{2,NV-N}$ given by the nitrogen concentration of the sample ($\gtrsim 350\,\mu\text{s}$, see Table 5.1) and $\sim 10\times$ smaller than the expected limit due to 0.01% ^{13}C spins ($\simeq 100\,\mu s$). This discrepancy indicates that dipolar broadening due to paramagnetic spins is not the dominant NV dephasing mechanism. Indeed, the spatial variation in $T^*_{2,SQ}$ and low concentration of nitrogen and ^{13}C spins suggests that crystal lattice strain inhomogeneity is the main source of NV ensemble dephasing in this sample. For the measured NV ensemble volume ($\sim 10^4\,\mu\text{m}^3$) and the reference strain gradient (Fig. 5.1c), we estimate a strain gradient limited dephasing time of $\sim 6\,\mu\text{s}$, in reasonable agreement with the observed $T^*_{2,SQ}$.

Measurements in the DQ basis at moderate bias magnetic fields are to first order strain-insensitive, and therefore provide a means to eliminate the contribution of strain to NV spin ensemble dephasing. Fig. 5.2 shows data for T_2^* in both the SQ and DQ bases for an example region of Sample A with SQ dephasing time $T^*_{2,SQ} = 5.8(2)\,\mu\text{s}$ and $p = 1.7(2)$. For these measurements, a small 2.2 mT bias field was applied parallel to one NV axis (misalignment angle $< 3°$) to lift the $|\pm 1>$ degeneracy, and the magnet geometry was optimized to reduce magnetic field gradients over the sensing volume (see Supplement C.4). In the DQ basis, we find

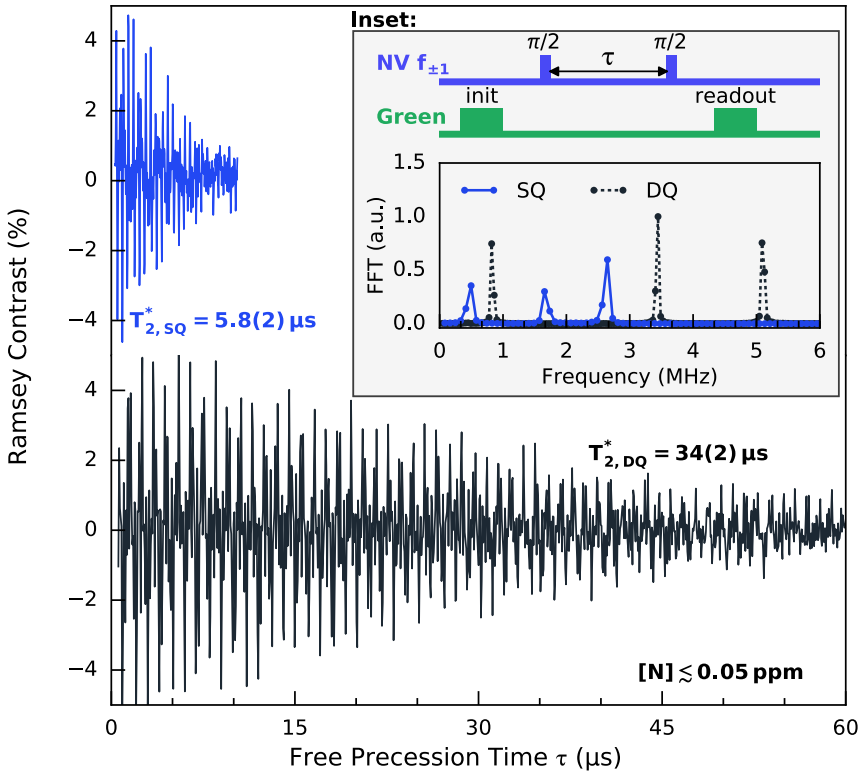

Figure 5.2: Ramsey measurements for Sample A ($[N] \lesssim 0.05$ ppm) at an applied bias magnetic field of $B_0 = 2.2\,\mathrm{mT}$. Comparison of time-domain data and resulting fit values for T_2^* for the single quantum (SQ) basis on the $\{0, +1\}$ transition (blue, upper); and the double quantum (DQ) basis on the $\{+1, -1\}$ transition (black, lower). Upper inset: Illustration of DQ Ramsey protocol with two-tone MW pulses. For SQ measurements, a single-tone MW pulse is applied instead. Lower inset: Discrete Fourier transform of the SQ (solid blue) and DQ (dashed black) Ramsey measurements with a MW drive detuned 0.4 MHz from the $\{0, +1\}$ transition. NV sensor spins accumulate phase twice as fast in the DQ basis as in the SQ basis.

$T^*_{2,DQ} = 34(2)\mu s$ with $p = 1.0(1)$, which is a $\sim 6\times$ improvement over the measured T_2^* in the SQ basis. Similar T_2^* improvements in the DQ basis were observed in other regions of this diamond. Our results suggest that in the low nitrogen density regime, dipolar interactions with the nuclear spin bath are the primary decoherence mechanism when DQ basis measurements are employed to remove strain and temperature effects. Specifically, the measured $T^*_{2,DQ}$ and p values in Sample A are consistent with the combined effect of NV dipolar interactions with (i) the 0.01 % concentration of ^{13}C nuclear spins ($T^*_{2,N-13C}/2 \simeq 50\,\mu s$) and (ii) residual nitrogen spins $[N] \sim 0.05\,$ppm; with an estimated net effect of $T^*_{2,DQ} \simeq 39\,\mu s$. Diamond samples with greater isotopic purity (^{12}C$>$ 99.99%) would likely yield further enhancements in $T^*_{2,DQ}$.

5.2.2 Strain and Dipolar-Dominated Dephasing (Sample B: Intermediate Nitrogen Density Regime)

Although Sample B ($[N] = 0.75\,$ppm, ^{14}N) contains more than an order of magnitude higher nitrogen spin concentration than Sample A ($[N] \lesssim 0.05\,$ppm), we observed SQ Ramsey dephasing times $T^*_{2,SQ} \simeq 1 - 10\,\mu s$ in different regions of Sample B, which are similar to the results from Sample A. We conclude that strain inhomogeneities continue to be a significant contributor to NV spin ensemble dephasing in Sample B. Comparative measurements of T_2^* in both the SQ and DQ bases yield a more moderate increase in $T^*_{2,DQ}$ for Sample B than for Sample A. Example Ramsey measurements of Sample B are displayed in Fig. 5.3, showing $T^*_{2,SQ} = 1.80(6)\,\mu s$ in the SQ basis increasing to $T^*_{2,DQ} = 6.9(5)\,\mu s$ in the DQ basis, a $\sim 4\times$ extension. The observed $T^*_{2,DQ}$ in Sample B approaches the expected limit set by dipolar coupling of NV spins

to residual nitrogen spins in the diamond ($T^*_{2,N-NV}/2 \simeq 12\,\mu s$), but is still well below the expected limit due to 0.01 % ^{13}C nuclear spins ($\simeq 50\,\mu s$).

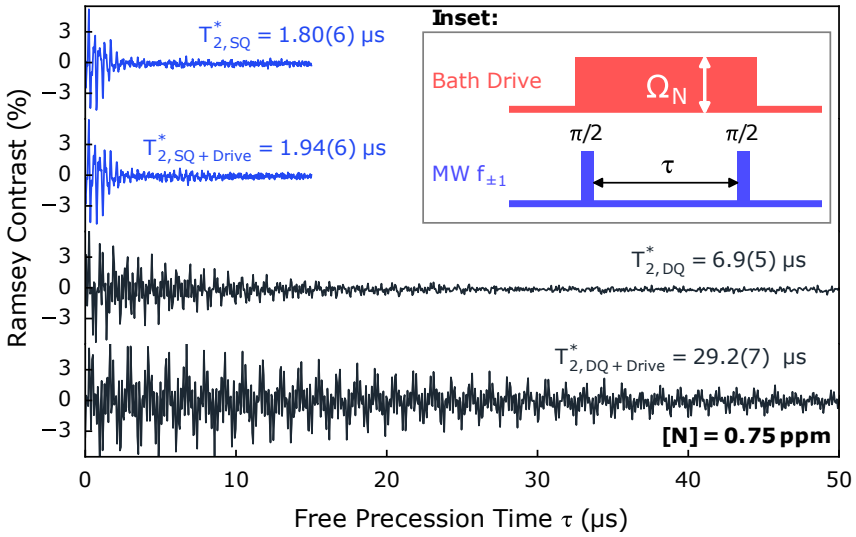

Figure 5.3: Ramsey measurements for Sample B (($[N] = 0.75$ ppm) at an applied bias magnetic field of $B_0 = 8.5\,\mathrm{mT}$. Comparison of time-domain data and resulting fit values for T_2^* for the single quantum (SQ) basis on the $\{0, +1\}$ transition (1$^{\mathrm{st}}$ from top); the SQ basis with spin-bath drive (2$^{\mathrm{nd}}$ from top); the DQ basis with no drive (3$^{\mathrm{rd}}$ from top); and the DQ basis with spin-bath drive (4$^{\mathrm{th}}$ from top). There is a 16.2× improvement of T_2^* in the DQ basis with spin-bath drive compared to SQ with no drive. Inset: Two-tone NV Ramsey protocol with spin-bath bath drive applied to nitrogen spins.

Measuring NV Ramsey decay in both the SQ and DQ bases while driving the nitrogen spins, either via continuous or pulsed RF fields[127, 243], is effective in isolating the electronic spin bath contribution to NV ensemble dephasing. With continuous drive fields of Rabi frequency $\Omega_N = 2\,\mathrm{MHz}$ applied to nitrogen spin resonances $1-6$, *i*, and *ii* (see Fig. 5.1d), we find that $T^*_{2,SQ+Drive} = 1.9(6)\,\mu s$, which only marginally exceeds $T^*_{2,SQ} = 1.80(6)\,\mu s$. This result is consistent with NV ensemble SQ dephasing being dominated by strain gradients in Sample B, rendering spin bath control

ineffective in the SQ basis. In contrast, DQ Ramsey measurements exhibit a significant additional increase in T_2^* when the bath drive is applied, improving from $T^*_{2,DQ} = 6.9(5)\,\mu$s to $T^*_{2,DQ+Drive} = 29.2(7)\,\mu$s. This $\sim 16\times$ improvement over $T^*_{2,SQ}$ confirms that, for Sample B, NV dipolar interactions with the nitrogen spin bath are the dominant mechanism of NV ensemble dephasing in the DQ basis without bath drive. Note that the Sample B dephasing time with DQ + spin bath drive is only slightly below that of Sample A with DQ alone ($\approx 34\,\mu$s). We attribute this T_2^* limit in Sample B primarily to NV dipolar interactions with 0.01% ^{13}C nuclear spins; with an additional small contribution from magnetic field gradients over the detection volume ($\sim 10^4\,\mu\text{m}^3$) due to the four times larger applied bias field ($B_0 = 8.5\,\text{mT}$), relative to Sample A, which was used in Sample B to resolve the nitrogen ESR spectral features. Similar extensions of T_2^* were obtained using pulsed driving of the nitrogen bath spins (see Sec. 2.12).

We also characterized the efficacy of CW spin bath driving for increasing T_2^* in both the SQ and DQ bases (see Fig. 5.4a). While $T^*_{2,SQ}$ remains approximately constant with varying Rabi drive frequency Ω_N, $T^*_{2,DQ}$ exhibits an initial, rapid increase and saturates at $T^*_{2,DQ} \approx 27\,\mu$s for $\Omega_N \gtrsim 1\,\text{MHz}$ (only resonances $1-6$ are driven here). To explain the observed trend, we introduce a model that distinguishes between (i) NV ensemble dephasing due to nitrogen bath spins, which depends upon bath drive strength Ω_N, and (ii) dephasing from drive-independent sources (including strain and ^{13}C spins):

$$1/T_2^* = 1/T^*_{2,NV-N}(\Omega_N) + 1/T^*_{2,other}. \tag{5.3}$$

In the motional narrowing regime ($\Omega_N \ll \gamma_{NV-N}$), $T^*_{2,NV-N}$ is expected to be $\propto \Omega_N/\gamma^2_{N-NV}$ [233, 250], where γ_{NV-N} is the average NV-N dipolar interaction strength. Our data is well described by the functional form (see Methods):

$$T^*_{2,NV-N}(\Omega_N) = \frac{1}{\gamma_{NV-N}}\left(\frac{\Omega_{N,eff}}{\gamma_{NV-N}} + \frac{1}{\Delta m}\right), \tag{5.4}$$

where $\Delta m = 1(2)$ is the change in spin quantum number in the SQ (DQ) basis, and $\Omega_{N,eff} = \Omega_N \frac{\Omega_N^2}{\Omega_N^2+(\Delta_N/2)^2}$ accounts for inefficient driving of the nitrogen spin resonances due to imperfect overlap and finite detuning Δ_N of the drive fields when weak drive fields are deployed ($\Omega_N \ll \Delta_N$). Using the NV-N dipolar estimate for Sample B, $\gamma_{NV-N} \approx 2\pi \times 7\,\text{kHz}$, $\Delta_N \approx 100\,\text{kHz}$ extracted from DEER ESR measurements (Suppl. C.5), and a saturation value of $T^*_{2,other} \approx 27\,\mu\text{s}$, we combine Eqns. 5.3 and 5.4 and plot the calculated T_2^* as a function of Ω_N in Fig. 5.4a (black, dashed line). The good agreement between the model and our data in the DQ basis suggests that Eqns. 5.3 and 5.4 capture the dependence of T_2^* on drive field magnitude (i.e., Rabi frequency). Alternatively, we fit the model to the DQ data (red, solid line) and extract $\gamma^{fit}_{NV-N} = 2\pi \times 9.2(2)\text{kHz}$ and $\Delta^{fit}_N = 140(11)\,\text{kHz}$, in reasonable agreement with our estimated parameters. In summary, the results from Sample B show that spin bath driving in the DQ basis suppresses inhomogeneous NV ensemble dephasing due to both interactions with the nitrogen spin bath and strain-gradients. Similar to Sample A, further enhancement in T_2^* could be achieved with improved isotopic purity, as well as reduced magnetic-gradients due to the applied magnetic bias field.

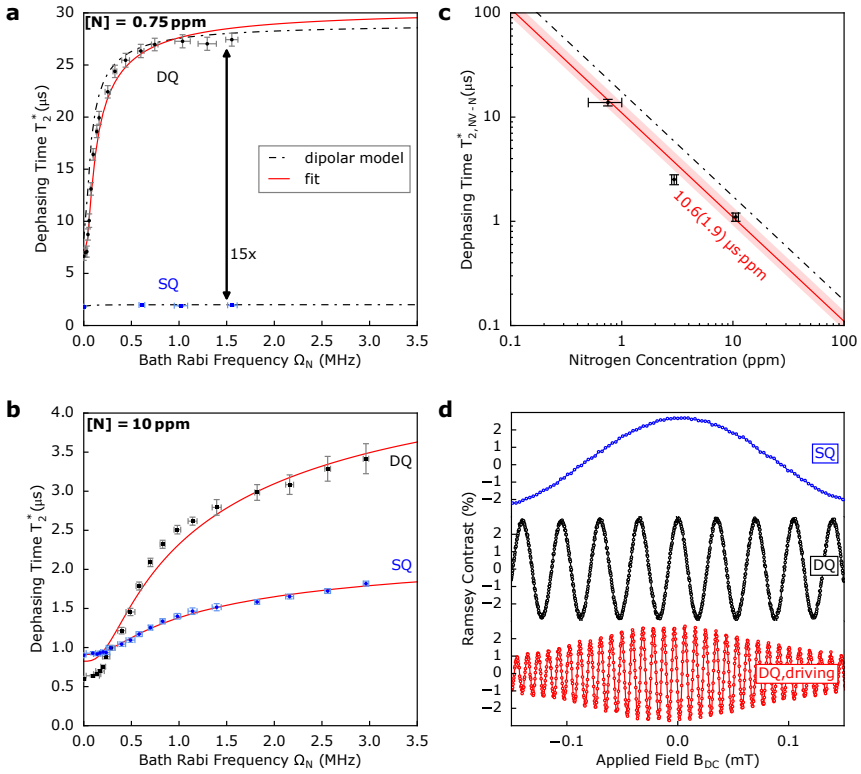

Figure 5.4: (a) Ramsey measurements of T_2^* in the single quantum (SQ, blue) and double quantum (DQ, black) bases for different spin-bath drive strengths (Rabi frequencies) for Sample B ([N] = 0.75 ppm) at $B_0 = 8.5\,\mathrm{mT}$. Black dashed line is calculated from a model of NV spins with dipolar interactions with a multi-component spin bath (Eqn. 5.3). Red solid line is a fit of the model to the T_2^* data (see main text for details). (b) Same as (a) but for Sample C ([N] = 10 ppm) and $B_0 = 10.3\,\mathrm{mT}$. (c) Measured $T^*_{2,N-NV} \equiv 2 \times T^*_{2,DQ}$ as a function of nitrogen concentration for Samples B, C, D, and E. The black, dashed line is the dipolar-interaction-estimated dependence of T_2^* on nitrogen concentration (see Methods). Red line is a fit to the data of $1/T_2^* = A_{NV-N}[N]$, yielding $A_{N-NV} = 2\pi \times 15(1.2)\,\mathrm{kHz/ppm}$ ($10.6(1.9)\,\mu\mathrm{s}\cdot\mathrm{ppm}$). The shaded region indicates the two standard deviation uncertainty in the fit value for A_{N-NV}. (d) Measured Ramsey DC magnetometry signal $S \propto C\sin(\phi(\tau))$ for Sample B, in the SQ and DQ bases, as well as the DQ basis with spin-bath drive (see main text for details). There is a 36× faster oscillation in the DQ basis with spin-bath drive compared to SQ with no drive. This greatly enhanced DC magnetic field sensitivity is a direct result of the extended T_2^*, with sensitivity enhancement given by $2 \times \sqrt{\tau_{DQ+Drive}/\tau_{SQ}}$ at equal contrast. The slight decrease in observed contrast in the DQ + drive case for $|B_{DC}| > 0.05\,\mathrm{mT}$ is due to the change in Zeeman energies of the nitrogen spins with applied test field B_{DC}, which was not corrected for in these measurements.

5.2.3 Dipolar-Dominated Dephasing (Sample C: High Nitrogen Density Regime)

Spin bath driving results for Sample C ([[N] = 10 ppm, ^{15}N) are shown in Fig. 5.4b. At this high nitrogen density, interactions with the nitrogen bath dominate NV ensemble dephasing, and $T^*_{2,SQ}$ and $T^*_{2,DQ}$ both exhibit a clear dependence on spin bath drive strength Ω_N. With no drive ($\Omega_N = 0$), we measured $T^*_{2,DQ} \approx T^*_{2,SQ}/2$, in agreement with dephasing dominated by a paramagnetic spin environment and the twice higher dephasing rate in the DQ basis[202, 207, 283]. Note that this result is in contrast to the observed DQ basis enhancement of T_2^* for the lower nitrogen density samples (Fig. 5.2 and 5.3). Nonetheless, we find that T_2^* in Sample C increases more rapidly as a function of spin bath drive amplitude in the DQ basis than in the SQ basis, such that $T^*_{2,DQ}$ surpasses $T^*_{2,SQ}$ with sufficient spin bath drive strength. We attribute the T_2^*-limit in the SQ basis ($\simeq 1.8\,\mu$s) to strain inhomogeneities in this sample, whereas the longest observed T_2^* in the DQ basis ($\simeq 3.4\,\mu$s) is in agreement with dephasing due to the 0.05% ^{13}C and 0.5 ppm residual ^{14}N spin impurities that were incorporated during growth of this sample (see Supplement Fig. C.4).

5.2.4 Ramsey Sensing

The sensing duration of ensemble-based DC sensing protocols is ultimately restricted by the inhomogeneous dephasing time T_2^*. We demonstrated the compatibility of the presented methods with Ramsey-type DC sensing by measuring a tunable static magnetic field of amplitude B_{DC}. Fig. 5.4d compares the accumulated phase for SQ, DQ,

and DQ plus spin bath drive measurements for Sample B. Sweeping B_{DC} leads to a characteristic observed oscillation of the Ramsey signal $S \propto C\sin(\phi)$, where C is the measurement contrast and $\phi = \Delta m \times \gamma_{NV} B_{DC} \tau$ is the accumulated phase during the free precession interval $\tau \approx T_2^*$. Choosing $\tau_{SQ} = 1.308\,\mu s$ and $\tau_{DQ+Drive} = 23.99\,\mu s$ (see Suppl. C.6), we found a 36.3(1.9)× faster oscillation period (at equal measurement contrast) when DQ and spin bath driving are both employed, compared to a SQ measurement. This enhancement in phase accumulation agrees very well with the expected improvement ($2 \times \tau_{DQ+Drive}/\tau_{SQ} = 36.7$).

Finally, having demonstrated that dephasing of NV ensembles in the DQ basis is predominantly limited by interactions with the nitrogen spin bath for Samples B and C, we plot the measured $T^*_{2,NV-N} \equiv 2 \times T^*_{2,DQ}$ versus the nitrogen concentration $[N]$ in Fig. 5.4c. To our knowledge, the dependence of the NV ensemble T_2^* on $[N]$ has not previously been experimentally reported. To improve the range of [N] coverage, we include DQ data for additional diamond Samples D ([N] = 3 ppm) and E ([N] = 48 ppm). Fitting the data to the function $1/T^*_{2,NV-N} = A_N \cdot [N]$ (red, solid line), we find the characteristic NV/nitrogen interaction strength for NV ensembles to be $A_N = 2\pi \times 15(2.8)\,\mathrm{kHz/ppm}$ [$10.6(2.0)\,\mu\mathrm{s} \cdot \mathrm{ppm}$]. This value is about 1.6× larger than the dipolar-estimate $\gamma_{\mathrm{e-e}} = 2\pi \times 9.1\,\mathrm{kHz/ppm}$ that is otherwise used in the present work (black, dashed line).

5.3 Discussion

We identified the dominant spin dephasing mechanisms for bulk NV ensembles in diamond and demonstrated that the combination of DQ magnetometry and spin bath driving can greatly extend T_2^*. For example, in Sample B we found that these quantum control techniques, when combined, provide a 16.2× improvement in T_2^*. Operation in the DQ basis protects against common-mode inhomogeneities and enables an extension of T_2^* for samples with $[N] \lesssim 1\,\text{ppm}$. In such samples, strain inhomogeneities are found to be the main causes of NV ensemble spin dephasing. In samples with higher N concentration, spin bath driving in combination with DQ sensing allows further increase of the NV ensemble T_2^* by decoupling paramagnetic nitrogen and other electronic dark spins from the NV spins. Our results suggest that quantum control techniques may allow the NV ensemble T_2^* to approach and even surpass the Hahn echo coherence time T_2. Note that spin bath driving has already been used to enhance the NV ensemble T_2 in Hahn echo, dynamical decoupling [49, 189], and spectral decomposition experimental protocols[128].

Furthermore, we showed that the combination of DQ magnetometry and spin bath driving is compatible with DC Ramsey magnetic field sensing. The relative increase in photon-shot-noise-limited sensitivity (neglecting experimental overhead time) is quantified by $2 \times \sqrt{\zeta}$, where the factor of two accounts for the enhanced gyromagnetic ratio in the DQ basis and $\zeta \equiv T_{2,DQ}^*/T_{2,SQ}^*$ is the ratio of maximally achieved T_2^* in the DQ basis (with spin bath drive when advantageous) and non-driven T_2^* in the SQ basis. For Samples A, B, and C, we find $2 \times \sqrt{\zeta} = 5.2\times$, $8.1\times$, and $3.9\times$,

respectively. In practice, increasing T_2^* also decreases the fractional overhead time associated with NV optical initialization and readout, resulting in even greater DC magnetic field sensitivity improvements (see Suppl. C.6). We expect that our quantum control techniques will remain effective when integrated with other approaches to optimize NV ensemble magnetic field sensitivity, such as high laser power and good N-NV conversion efficiency[86]. In such samples, conversion efficiencies of $1 - 30\%$ are obtained[108] and therefore T_2^* is likely limited by the paramagnetic nitrogen bath.

There are multiple avenues to further improve NV ensemble T_2^* and DC sensitivity, beyond the gains demonstrated in this work. First, the ^{13}C limitation to T_2^*, observed for all samples, can be mitigated via improved isotopic purity ($[^{12}\mathrm{C}] > 99.99\,\%$); or possibly through driving of the nuclear spin bath [284]. Second, more efficient RF delivery would enable faster spin bath driving (larger Rabi drive frequency Ω_N), which will be critical for decoupling denser nitrogen baths and thereby extending $T_2^* \propto \Omega_N/\gamma_{NV-N}^2 \propto \Omega_N[N]^2$ (see Eqn. 5.4). Third, short ensemble T_2^* times have so far prevented effective utilization of more exotic readout techniques, e.g., involving quantum logic [47, 51, 270] or spin-to-charge-conversion [124]. Such methods offer greatly improved NV spin-state readout fidelity but introduce substantial overhead time, typically requiring tens to hundreds of microseconds per readout operation. The NV ensemble dephasing times demonstrated in this work ($T_2^* \gtrsim 20\,\mu\mathrm{s}$) may allow for effective application of these readout schemes, which only offer sensitivity improvements when the sequence sensing time (set by T_2^* for DC sensing) is comparable to the added overhead time[86]. In summary, DQ magnetometry in combination with

spin bath driving allows for order of magnitude enhancement of the NV ensemble T_2^* in diamond, providing a clear path to ultra-high sensitivity DC magnetometry with NV ensemble coherence times approaching T_2.

5.4 Materials & Methods

Experimental methods

A custom-built, wide-field microscope collected the spin-dependent fluorescence from an NV ensemble onto an avalanche photodiode. Optical initialization and readout of the NV ensemble was accomplished via 532 nm continuous-wave (CW) laser light focused through the same objective used for fluorescence collection (Fig. 5.1a). The detection volume was given by the 532 nm beam excitation at the surface (diameter$\approx$ 20 μm) and sample thickness (100 μm for Samples A and B, 40 μm for Sample C). A static magnetic bias field was applied to split the $|-1\rangle$ and $|+1\rangle$ degeneracy in the NV ground state using two permanent samarium cobalt ring magnets in a Helmholtz-type configuration, with the generated field aligned along one [111] crystallographic axis of the diamond ($\equiv \hat{z}$). The magnet geometry was optimized using the Radia software package [285] to minimize field gradients over the detection volume (see Supplement C.4). A planar waveguide fabricated onto a glass substrate delivered $2 - 3.5$ GHz microwave radiation for coherent control of the NV ensemble spin states. To manipulate the nitrogen spin resonances (see Fig. 5.1d), a 1 mm-diameter copper loop was positioned above the diamond sample to apply $100 - 600$ MHz radiofrequency (RF) signals, synthesized from up to eight individual signal generators. Pulsed mea-

surements on the NV and nitrogen spins were performed using a computer-controlled pulse generator and microwave switches.

Strain contribution to T_2^*

The on-axis strain component M_z in Sample B was mapped across a 1×1 mm area using a separate widefield imager of NV spin-state-dependent fluorescence. A bias field B_0 ∼1.5 mT was applied to split the spin resonances from the four NV orientations. Measurements were performed following the vector magnetic microscopy (VMM) technique[101]. Eqn. 5.1 in the main text was used to analyze the measured NV resonance frequencies from each camera pixel (ignoring M_x and M_y terms as small perturbations, see Supplement C.2). This procedure yielded the average B_x, B_y, and B_z magnetic field components, as well as the M_z on-axis strain components for all four NV orientations in each camera pixel, corresponding to 2.42μm×2.42 μm transverse resolution on the diamond sample. Figure 5.1c of the main text shows the resulting map of the on-axis strain inhomogeneity M_z in Sample B for the NV orientation interrogated in this work. This map indicates an approximate strain gradient of 2.8 kHz/μm across the field of view. This estimated strain gradient was used for all samples, while recognizing the likely variation between samples and within different regions of a sample. Across a 20-μm diameter spot, the measured strain inhomogeneity corresponds to a T_2^* limit of ≈ 6 μs, which compares well with the measured variation in $T_{2,SQ}^*$ for Samples A and B (see Table 1). Note that the contributions to M_z can be microscopic (e.g., due to nearby charge defects) or macroscopic

(e.g., due to crystal defects with size $> 10\,\mu$m). In addition, the VMM technique integrates over macroscopic gradients along the beam excitation path, which for the present experiments were perpendicular to the diamond sample surface through the NV layer. Consequently, the strain gradient estimate shown in Fig. 5.1c is a measure of M_z gradients in-plane within the NV layer, and strain gradients across the NV layer thickness are not resolvable in this measurement.

Spin Bath Driving Model

The spin bath driving model for NV ensemble dephasing, used for Samples B and C (Eqn. 5.4) is:

$$T^*_{2,NV-N}(\Omega_N) = \frac{1}{\gamma_{NV-N}}(\frac{\Omega_{N,eff}}{\gamma_{NV-N}} + \frac{1}{\Delta m}).$$

This expression is a linear function of the form $ax + b$, with $a = 1/\gamma^2_{NV-N}$ and $x = \Omega_{N,eff}$ describing the motional narrowing regime, and $b = 1/(\Delta m \times \gamma_{NV-N})$ describing the static broadening of the NV ensemble spin resonance due to dipolar interactions with nitrogen bath spins. The model is derived with the following physical premises: In the absence of any spin bath drive ($\Omega_N = 0$), the NV ensemble dephasing time is limited by dipolar interactions with the nitrogen spin bath and $T^*_{2,NV-N} = 1/(\Delta m \times \gamma_{NV-N})$, where $\Delta m = 1$ (2) for the SQ (DQ) basis. This premise still holds in the high strain gradient samples, where strain is accounted for by $T^*_{2,other}$ in Eqn. 5.3. For a spin bath drive $\Omega_N > \gamma_{NV-N}$, $T^*_{2,NV-N}$ is linearly dependent on the drive frequency Ω_N, and quadratically dependent on γ_{NV-N}: i.e., $T^*_{2,NV-N} \propto \Omega_N/\gamma^2_{NV-N}$. This result is derived in the context of motional narrowing [233, 250]. However,

for a weak spin bath drive, $0 < \Omega_N \lesssim \gamma_{NV-N}$, the dependence of $T^*_{2,NV-N}$ on Ω_N becomes sublinear as nitrogen bath spins, which have a finite ensemble linewidth, are driven off-resonantly and less efficiently. To account for this effect and the small detuning between nitrogen spin resonances (see Suppl. C.5), an effective Rabi drive is introduced, $\Omega_{eff} = \Omega_N^2/(\Omega_N^2 + (\Delta_N/2)^2)$, which replaces Ω_N in the spin bath driving model (i.e., $\Omega_{eff} \to \Omega_N$ for $\Omega_N \gg \Delta_N$). This model is in excellent agreement with the data for Sample B. For Sample C, the model agrees reasonable well with measurements, but deviates from the motional narrowing case at drive frequencies $\Omega_N \approx \gamma_{NV-N}$. In this regime, the motional narrowing condition $\Omega_N/\gamma_{NV-N} \gg 1$ is not fulfilled and the measured Ramsey data exhibit multi-exponential decay. To nonetheless enable for a qualitative comparison with Sample B, in these instances the stretched exponential parameter is restricted to $p \geq 1$ when extracting T_2^*. A more complete driving model should take the changes of the spin bath dynamics at Rabi drive frequencies $\Omega_N \approx \gamma_{NV-N}$ into account.

Inhomogeneous dephasing due to the spin bath

The NV ensemble T_2^* as a function of nitrogen concentration is estimated from the average dipolar coupling between electronic nitrogen spins, which is given by $\gamma_{\mathrm{e-e}} = a \times \frac{\mu_0}{4\pi} g^2 \mu_B^2/\hbar \frac{1}{\langle r \rangle^3} \approx 2\pi \times 9.1 \cdot [N]\,\mathrm{kHz/ppm}$, where μ_0 is the vacuum permeability, g is the electron g-factor, μ_B is the Bohr magneton, $\hbar$ is the reduced Planck constant, $\langle r \rangle = 0.55[N]^{-1/3}$ is the average spacing between electronic nitrogen spins as a function of density $[N]$ (in parts-per-million) within diamond, and a is a factor of order unity collecting additional factors that need to be considered in the dipolar

estimate such as the $\cos^2$ dependence and line shape of the ensemble. A sample with $[N] = 1\,\text{ppm}$ has an estimated $T^*_{2,NV-N} \approx 1/(2\pi \times 9.1\,\text{kHz}) = 17.5\,\mu\text{s}$. Similarly, Table 5.1 gives the estimates $T^*_{2,NV-N}$ for Samples A, B, and C.

Uncertainties in nitrogen concentration $[N]$ used in Fig. 5.4c are estimated by considering: the values reported by the manufacturer (Element Six Inc.); fluorescence measurements in a confocal microscope (Sample A); and Hahn echo T_2 measurements using the calibration value $T_2(N) \simeq 157\,\mu\text{s}\cdot\text{ppm}$ reported in Ch. 6 (Samples B and C). For Sample B, Element Six reports $[N] = 1\,\text{ppm}$, whereas the measured $T_2 = 300\,\mu\text{s}$ suggests $N = 0.5\,\text{ppm}$. The average value is thus used: $N = 0.75 \pm 0.25\,\text{ppm}$.

To estimate the ^{13}C nuclear spin bath contribution to NV ensemble dephasing, T_2^* is measured for a low-nitrogen, natural isotopic abundance sample (98.93% ^{12}C) (see Supplement C.3 for details). In the dilute regime, where $[^{13}C] \lesssim 1.1\%$, $1/T_2^*$ is expected to be linearly dependent on the ^{13}C concentration [3, 250]. Thus the T_2^* measurement from a natural abundance sample provides a means to estimate the ^{13}C contribution in the isotopically enriched samples used in the present study. The ^{13}C-dependent decoherence rate per unit percentage concentration is found to be $A_{13C} \lesssim 2\pi \times 160\,\text{kHz}/\%$ ($\gtrsim 1\,\mu\text{s}\cdot\%$), indicating limits on NV ensemble dephasing of $T^*_{2,\text{NV-}^{13}\text{C}} \simeq 100\,\mu\text{s}$, $100\,\mu\text{s}$, and $20\,\mu\text{s}$ for Samples A, B, and C, respectively.

Measurement Contrast

The NV measurement contrast (Fig. 5.2, 5.3, and 5.4d) is determined by comparing the fluorescence from the NV ensemble in the $|0\rangle$ state (maximal fluorescence) relative to the $|+1\rangle$ or $|-1\rangle$ state (minimal fluorescence)[142] and is defined as visibility $C = \frac{max-min}{max+min}$. The DEER (Fig. 5.1d) and DC magnetometry contrast (Fig. 5.4d) is calculated in the same fashion but is reduced by $\approx 1/e$ since the best phase sensitivity in those measurements is obtained at $\tau \approx T_2$ and $\tau \approx T_2^*$, respectively (see Suppl. C.5). For noise rejection, most pulse sequences in this work use a back-to-back double measurement scheme[163], where the accumulated NV ensemble phase signal is first projected onto the $|0\rangle$ state and then $|+1\rangle$ (or $|-1\rangle$) state. The contrast for a single measurement is then defined as the visibility of both sequences.

Chapter 6

Quantum Coherence of Solid-State NV Center Spins in Diamond

6.1 Introduction

Solid-state electronic spins have garnered increasing relevance as building blocks in a wide range of quantum science experiments. Recently, ultra high-sensitivity quantum sensing experiments have been enabled by utilizing macroscopic NV spin ensembles in diamond[83, 85, 87] employing the center's well-known capabilities to be manipulated via coherent microwaves, initialized and read out via laser light, and a millisecond-long spin lifetime at ambient conditions. Most importantly, ensemble experiments benefit from an improved signal-to-noise ratio $\propto N^{1/2}$, where N is the number of sensor spins of the detector.

A major challenge in such experiments, however, is the reduction of ensemble

coherence due to dipolar interactions with excess nuclear and electronic spin species, i.e., the *spin bath* (see Fig. 6.1b). For example, the formation of negatively-charged NV^- centers ($S = 1$) requires the incorporation of nitrogen into the diamond lattice, and as a result, paramagnetic substitutional nitrogen impurities (P1 centers, $S = 1/2$)[5–7] persist at densities similar to or exceeding the NV concentration. An important figure of merit to be optimized for sensing applications is then the product $(N\tau)^{1/2}$, rather than N alone, where τ is the accessible sensing time of the quantum measurement. A thorough understanding of decoherence mechanisms limiting τ as a function of bath density parameters is therefore essential.

In this letter, we characterize the NV ensemble Hahn echo and CPMG coherence time in diamond samples with nitrogen bath densities changing by four orders of magnitude. We combine our experimental results with that of a related study[135] and numerical simulations and show good agreement with theory. Our results are an essential stepping stone for developing diamond host samples in next-generation spin-defect-based quantum applications.

6.2 Experimental Details

Our study comprises 19 natural abundance diamond samples ($[^{13}C] = 1.07\,\%$, "^{13}C-samples") and four isotopically enriched samples ($[^{13}C] \lesssim 0.05\,\%$, "^{12}C-samples") manufactured by Element Six and Apollo Diamond[1] with total nitrogen concen-

[1] now Scio Diamond Technology Corporation

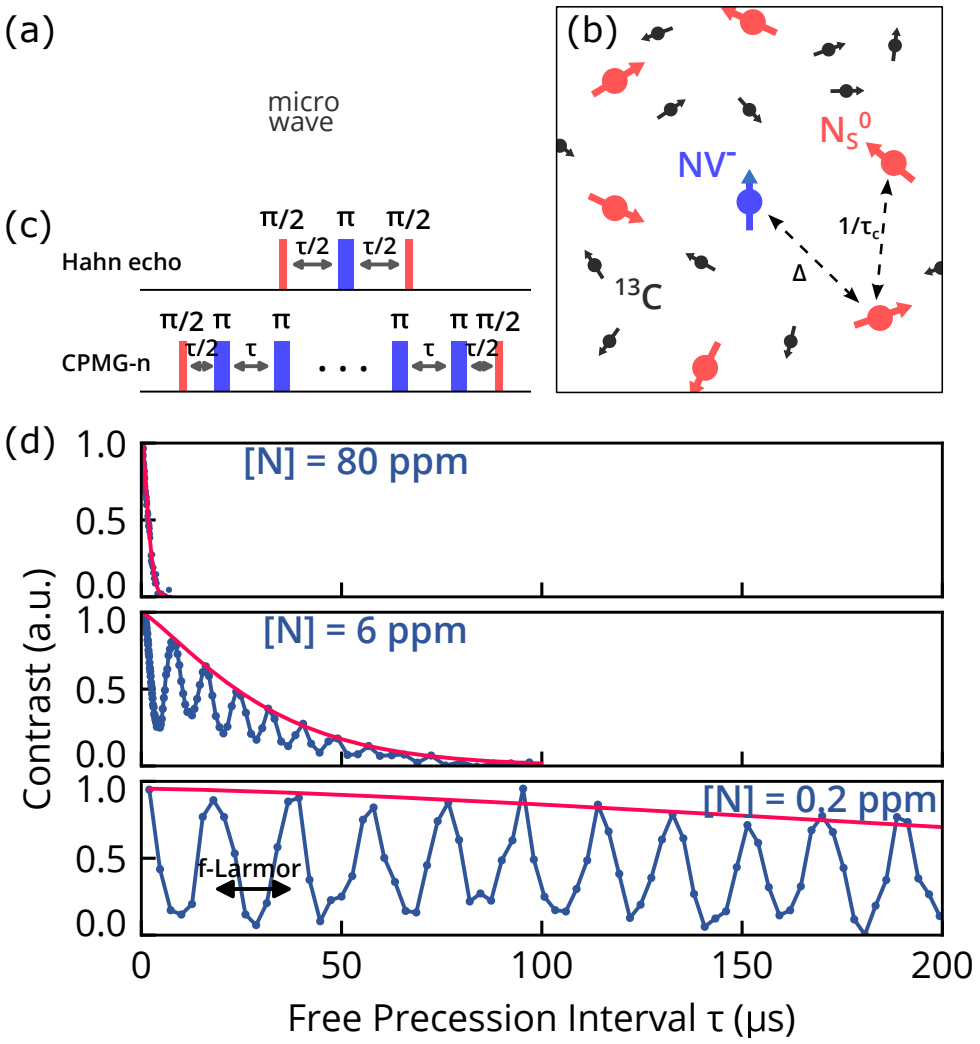

Figure 6.1: a) NV defect and ground-state energy level structure. b) Schematic of bath interaction in NV diamond showing NV^- approximated as central spin, substitutional nitrogen N_S^0 (P1 center, $S = 1/2$) and ^{13}C nuclear spin ($I = 1/2$). c) Hahn echo and CPMG dynamical decoupling protocol. d) Hahn coherence data for an [N] = 0.2, 6 and 80 ppm diamond sample typical for the set of measurements; the modulation of the echo signal in the low [N] samples is due to Larmor-precession of the ^{13}C nuclear spins due to the applied external magnetic field visible in ^{13}C natural abundance samples.

trations in the range [N] $= 0.01 - 300$ ppm. Samples with nitrogen spin densities [N]$\lesssim 100$ ppm were manufactured using chemical vapor deposition (CVD, for a review, see [164]) and consist of bulk diamond plates, as well as CVD thin-layers samples

grown on top of diamond substrates. Two of the samples were grown using the high-pressure-high-temperature (HPHT) method [24, 167–170] and cover the range [N] $\gtrsim 100\,\mathrm{ppm}$.

The total nitrogen concentration [N] is determined multi-fold. 1) For the majority of samples, the manufacturers provided either detailed spin concentrations extracted via UV-VIs, FTIR, or secondary ion mass spectroscopy (SIMS), or approximate spin concentrations. 2) In select cases, the NV concentration was measured through confocal microscopy and the nitrogen concentration is calculated using a fixed NV-to-N conversion efficiency of $\approx 0.3\,\%$ for Element Six and $\approx 1\,\%$ for Apollo Diamond samples [286]. 3) Alternatively, samples were sent out to a third party (EAG Laboratories) to perform SIMS. The uncertainties in [N] are calculated from the mean and variation in concentration values provided by the different methods. If only one method was available, the uncertainty is given by the range of possible conversion efficiency values reported in the literature (confocal method) or assuming a $50\,\%$ error on SIMS measurements. Note that in samples with a significant amount of nitrogen-unrelated charge traps (e.g., vacancies), a fraction of substitutional nitrogen spins N_S^0 is ionized to N_S^+ defects[215]. The total nitrogen concentration as measured through SIMS is given by $[\mathrm{N}] = [N_S^0] + [N_S^+]$, where typically $[N_S^+] \lesssim [N_S^0]$. The contribution to decoherence due the additional charge traps of concentration $\approx [N_S^+]$ is accounted for by $50\,\%$ error margin [N].

NV Hahn echo [203] and CPMG dynamical decoupling measurements[49] (see

Fig. 6.1c) are performed using a confocal or a wide field microscope. In both setups, 532 nm laser light is applied for optical initialization and readout of the NV spin polarization. In addition, a static magnetic field B_0 is aligned along one of the [111] crystal directions (misalignment angle $\leq 3°$) to single out 1 of the 4 possible NV orientations and lift the $|\pm 1\rangle$ degeneracy of the NV ground state (see Fig. 6.1a). Pulsed microwaves (MW) resonant with the $|0\rangle \rightarrow |-1\rangle$ single quantum transition (or $|0\rangle \rightarrow |+1\rangle$) are deployed to coherently manipulate the NV spin state.

6.3 Hahn Echo

In Fig. 6.1d we depict three Hahn echo curves typical for our set of diamond samples for a [N] = 0.2, 6, and 80 ppm sample, respectively. The data show the characteristic exponential-type decay associated with decoherence due to a dipolar-coupled system [49, 201]. In addition, the [N] = 0.2 and 6 ppm samples exhibit periodic modulation of the spin echo signal (ESEEM) owing to the Larmor precession of the ^{13}C nuclear spin bath at frequency $f_{Larmor} = \frac{\gamma_{13C}}{2\pi} B_0$, given the ^{13}C nuclear gyromagnetic ratio $\gamma_{13C} = 2\pi \times 10.07\,\mathrm{MHz/T}$[209, 211, 214]. To clearly separate the overall decay envelope from the Larmor signal, the bias field B_0 is adjusted between $2 - 30\,\mathrm{mT}$ to tune the Larmor precession frequency such that $f_{Larmor} \gg 1/T_2$ (low nitrogen regime) or $f_{Larmor} \ll 1/T_2$ (high nitrogen regime) for each natural abundance ^{13}C-sample. The ^{12}C-samples did not exhibit any modulation of the coherence signal irrespective of the applied magnetic field strength for the given range. For all samples, the coherence envelope was subsequently fitted to the form $C_0 \exp -(t/T_2)^p$ (red solid line, Fig. 6.1d) to extract the coherence time T_2, contrast C_0, and stretched exponential parameter

p[49, 201]. For clarity, we differentiate throughout the manuscript the generalized coherence time obtained in an n-pulse CPMG sequence (n being even integer) by $T_{2,n}$ and the decay time obtained through Hahn echo as $T_{2,echo}$ ($\equiv T_{2,n=1}$).

In Fig. 6.2a we summarize the NV Hahn echo T_2 values measured for each sample as a function of total nitrogen concentration [N], with two regimes discernible. At nitrogen concentrations $[N] \gtrsim 0.5\,\text{ppm}$ (high nitrogen regime), $T_{2,echo}$ exhibits a linear dependence on the nitrogen concentration, indicating that interactions with the nitrogen bath spins are the dominant source of decoherence. This linear scaling is consistent with studies in comparable crystalline systems [3, 204, 222, 236] and expected for dilute dipolar-coupled spin systems[250]. In such instances, $1/T_2$ is proportional to the bath density, i.e. $1/T_2 = A\, n_{bath}$, where n_{bath} is the density of nitrogen spins ($\approx [N]$) and A is the decoherence rate per unit density. At concentrations [N] $\lesssim 0.5\,\text{ppm}$ (low nitrogen regime), however, T_2 saturates at $\approx 600\,\mu\text{s}$, for both isotopically purified and natural abundance samples. In addition, we plot the stretched exponent p in the inset of Fig. 6.2a. The extracted p-values with an average value $p_{\text{avg}} \approx 1.5$ are in stark contrast to the cubic decay ($p = 3$) found for single centers[49, 201] (see discussion below).

We now analyze $T_{2,echo}$ in more detail. First, we fit the data to the form

$$1/T_2(N) \approx A_N[N] + 1/T_{2,other}, \tag{6.1}$$

where A_N is the nitrogen-dominated decoherence rate per unit density, $T_{2,other}$ collects decoherence mechanisms independent of nitrogen-concentration, and the "≈"-

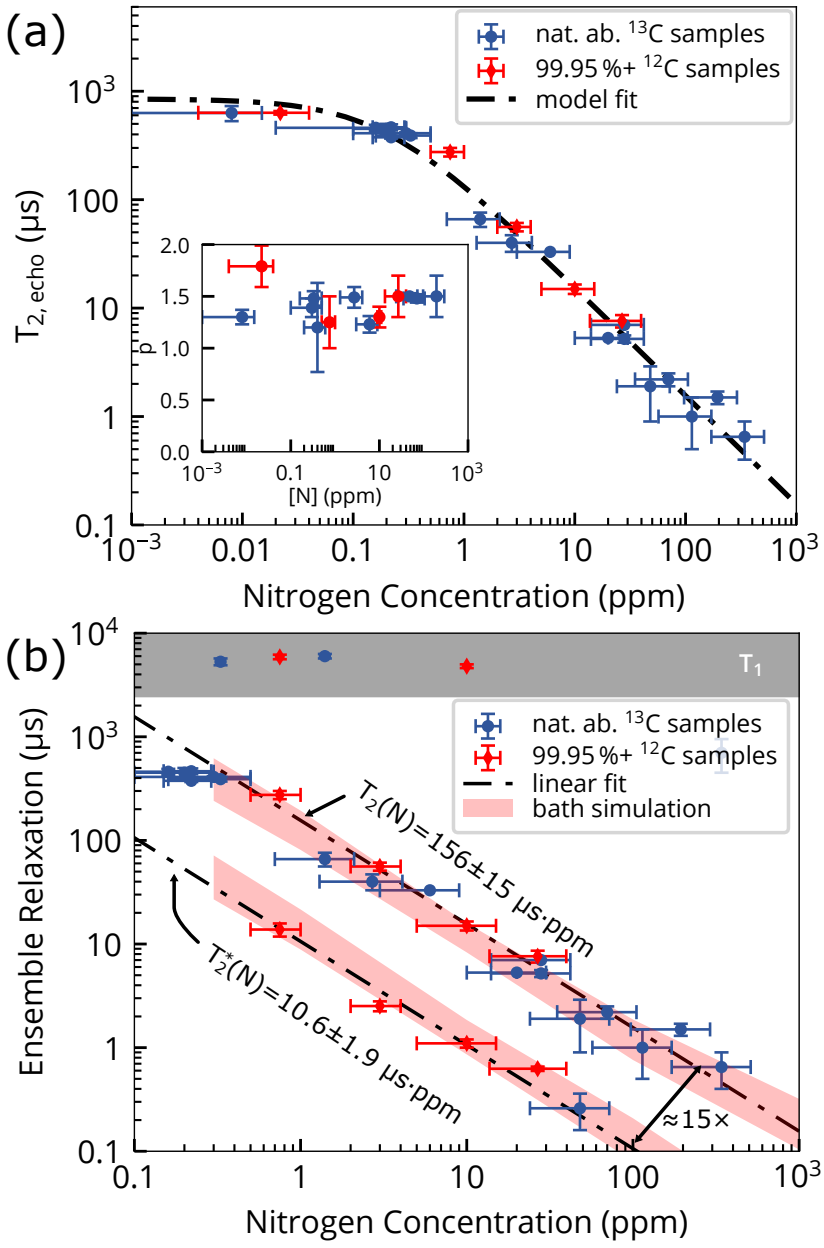

Figure 6.2: NV relaxation as a function of nitrogen concentration – a) Ensemble NV Hahn echo T_2 as a function of [N]; the black dashed line is a fit to Eqn. 6.1, Inset: stretched exponential parameter p extracted from measurements b) Ensemble T_2^*, T_2 and T_1 relaxation as a function of total nitrogen concentration [N]; red bands indicate 16/84% confidence intervals for parameters extracted from spin bath simulation; T_2^* values and scaling are reproduced from Ref. [135]

sign indicates that this model assumes that the relaxation rates add linearly. From the fit (black dashed line in Fig. 6.2a) we extract $A_N = 2\pi \times (1.0 \pm 0.1)\,\mathrm{kHz/ppm}$ $(156 \pm 15\,\mu\mathrm{s}\cdot\mathrm{ppm})$ and $T_{2,other} = 850 \pm 198\,\mu\mathrm{s}$. To support that A_N is indeed the intrinsic decoherence rate due to nitrogen bath spins, we performed numerical simulations of the bath dynamics and extract the inhomogeneous depasing time $T_2^*(N)$ and $T_{2,echo}(N)$.

In the simulation, the action of the nitrogen bath is modeled as a stochastic, Orenstein-Uhlenbeck (O-U) noise process [247, 287, 288]. In the context of NVs, the O-U process was first applied to single centers in dense type-1b samples[195] but has seen wide-ranging application since then [49, 106, 128, 130, 196, 197]. Most importantly, the dynamics in bulk diamond are described by a Lorentzian spectral density $S(\omega) = \frac{\Delta\tau_c}{\pi}\frac{1}{1+(\omega\tau_c)^2}$[245], where Δ is the mean coupling between ensemble sensor and bath spins (NV-N) and τ_c is the correlation time of the bath, which is related to intra-bath dynamics of the nitrogen spins (N-N)[49, 197, 201]. For single NV measurements, typically $\tau_c \gg 1/\Delta$ and also $\tau_c \gg T_{2,echo}$ and the intra-bath coupling N-N is much slower than the NV-bath coupling (NV-N) [49, 197]. In ensemble measurement, however, τ_c approaches the mean coupling between nitrogen bath spins and $\tau_{\mathrm{c,ens}} \approx 1/\Delta_{\mathrm{ens}}$[128]. This drastic difference between single and many spin measurements is a consequence of spatial averaging the signals from many individual NVs located at random lattice site with varying local spin bath environments when interrogating ensembles. Δ_{ens} and $\tau_{c,ens}$ are extracted from the numerical simulation by generating for a given nitrogen concentration P1-bath configurations with the NV

placed at the origin of the diamond lattice (central spin model). For each spin bath configuration Δ_{single} and $\tau_{\text{c,single}}$ are calculated using the secular components of the dipolar interaction Hamiltonian[250] for all NV-N and N-N spin pairs. The ensemble averages Δ_{ens} and $\tau_{\text{c,ens}}$ are extracted from the distributions $P(\Delta_{single})$ and $P(\tau_{c,single})$ which are generatred from 10000 bath configurations.

Bath simulation results of the NV ensemble relaxation as a function of [N] are shown in Fig. 6.2b (red bands). The nitrogen-dependent scaling of the inhomogenous ensemble dephasing time $T_2^*(N) \equiv 1/\Delta_{\text{ens}}(N)$ was recently determined experimentally in a related study to be $T_2^*(N) = 10.9 \pm 1.9\,\mu\text{s}\cdot\text{ppm}$ [135] and is plotted together with the experimentally determined $T_{2,echo}(N)$ result from this paper (black, dashed lines). As the data shows, we find good agreement between simulation and experiment for $T_2^*(N)$ and $T_{2,echo}(N)$ and conclude that for both natural abundance ^{13}C- and enriched ^{12}C-samples i) the O-U model describes the loss of coherence due to nitrogen bath spins sufficiently well, ii) A_n is indeed the experimentally determined decoherence rate due to nitrogen bath spins iii) the role of the ^{13}C bath is negligible if nitrogen is the dominant source of decoherence. At this point it is interesting to take the ratio $T_{2,echo}(N)/T_2^*(N)$ and we find that $T_{2,echo}(N)$ exceeds $T_2^*(N)$ by $\sim 15\times$ (14.7 ± 0.2). To our knowledge, this ratio has never been determined experimentally for NV centers and a straightforward application of the results is the calibration of bulk substitutional nitrogen spin concentrations through NV coherence measurements. Measurements of $T_{2,echo}$ should be particularly well-suited for nitrogen calibrations and advantageous over standard T_2^* (or linewidth) measurement schemes,

which may exhibit a shortened T_2^* due to power broadening [191, 194], strain inhomogeneities and magnetic field gradients throughout the crystal[135].

6.4 CPMG

We next perform n-pulse CPMG measurements on a select subset of samples to enhance T_2 and extract additional information about the spin bath. In a CPMG sequence the NV sensor spins are periodically flipped via application of π-pulses, effectively reducing the response to the paramagnetic spin noise environment. Typical $T_{2,n}$ data for the [N] = 0.2, 6, and 80 ppm samples are shown in Fig. 6.3a. In all instances, $T_{2,n}$ exhibits a characteristic power-law scaling with number of decoupling pulses n, i.e. $T_{2,n} \propto n^{\lambda_{\text{eff}}}$, where λ_{eff} is a phenomenological parameter describing the CPMG decoupling efficacy for a given spectral noise density $S(\omega)$[197, 201, 235]. For a Lorentzian spectral density used in our case to effectively describe the bath of nitrogen spins it can be shown that $\lambda_{eff} = 2/3$ [49, 197, 201, 235] and $T_{2,echo}$ increases sublinearly with number of pulses n. To extract λ_{eff}, we fit the $T_{2,n}$ data for each sample to the functional form $1/T_{2,n} = 1/(T_{2,echo} \cdot n^{\lambda_{\text{eff}}}) + 1/T_{2,max}$, where $T_{2,max} \approx T_1/2$ accounts for the NV coherence time limit imposed by spin-lattice relaxation[53]. For the subset of samples we extract $\lambda_{eff} \approx 0.5 - 2/3$ in reasonable agreement with a Lorentzian spectral density, albeit the slightly reduced λ_{eff} values measured for some samples are an indication that additional contributions to $T_{2,n}$ may need to be considered.

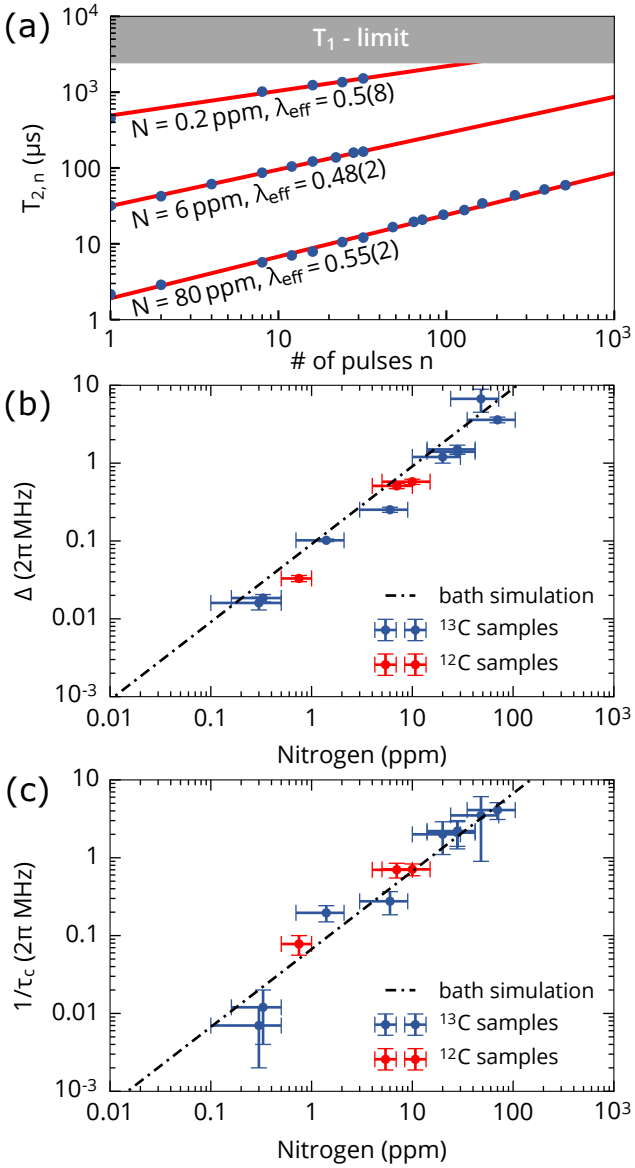

Figure 6.3: CPMG results – a) $T_{2,n}$ as a function of decoupling pulses n for $N = 0.2$, 6, and 80 ppm sample. Due to the T_1-limit (≈ 2.5 ms) the decoupling efficiency $\propto n^{\lambda_{eff}}$ decreases with increasing initial Hahn Echo $T_{2,echo}$ time. b) b) Δ and c) $1/\tau_c$ as a function of nitrogen concentration extracted from experiment.

Spectral decomposition of the CPMG coherence data[128, 289] provides a means to probe and study the spectral density $S(\omega)$ of the spin bath as a function of spin

impurity concentration. In principle, no a priori-information about the exact nature of the spectral source signal is necessary. However, for natural abundance ^{13}C samples that exhibit spin echo envelope modulation (see Fig. 6.1d) a direction deconvolution method of the coherence signal $C(t)$ as it was used in Ref. [53] cannot be straightforwardly applied. We therefore deploy a forward-fitting routine that only relies on $T_{2,n}$ obtained through CPMG measurements (see Fig. 6.3a) to extract Δ_{ens}, $\tau_{\mathrm{c,ens}}$, and $T_{2,\mathrm{max}}$. The spectral decomposition results are shown in Fig. 6.3b and c, respectively, together with the range of values determined from the spin bath simulations (red). We plot additionally in Fig. 6.3b and c the experimentally determined value $1/T_2^*(N)$ (black, dotted line). We find good agreement between Δ_{ens} extracted from spectral decomposition, bath simulation, and experiment.

6.5 Ensemble Decay Exponent

We now discuss the observed decay shape in Hahn echo ensemble experiments, which are characterized by the parameter p. For single NV measurements, the exponential-type decay shapes for Ramsey, Hahn Echo, and T_1 measurements have been well-determined through spin-resonance experiments in nitrogen-rich diamonds, showing excellent agreement with theory (see Tab. 6.1, column 2 and 3). Taking the single NV decay in Hahn echo experiments (qubic, $p = 3$), we find a striking difference in our ensemble measurements where $p \approx 1.5$. We explain this discrepancy with an ensemble averaging effect, when the qubic decay signal from individual centers with slightly varying spin environments and decay rates is integrated over many random lattice sites. In Ref. [196] it was shown that such a statistical average also funda-

Table 6.1: Decay shapes of single NV vs. NV ensemble measurements in a bath of dipolar-coupled spins.

Experiment	p single	Ref. exp./theo.	p ens.	Ref. exp./theo.
Hahn echo T_2	3	[49]/[201]	3/2	this work
Ramsey T_2^*	2	[49]/[201]	1	[135] / [196]
T_1 (cross-relax.)	-	-	1/2	[228] / [241],[229]
T_1 (spin-lattice relax.)	1	[52]	1	[171],[239]

mentally changes the NV Ramsey decay shape, which exhibits Gaussian decay for single NVs ($p = 2$)[49] but simple exponential decay for ensembles ($p = 1$)[135]. The NV ensemble linewidth as measured through ESR thus has a Lorentzian shape, in accordance with an earlier moment analysis of magnetic resonance linewidths derived for nuclear spin ensembles[250].

Recently, several studies independently reported a square-root decay shape ($p = 1/2$) of the ensemble T_1 spin lifetime in high NV density samples[228, 229, 241]. In these samples, the spin-lifetime was limited by cross-relaxation due to the strongly interacting bath of NV^- spins, rather than spin-lattice relaxation (i.e., phononic decay), which exhibits simple exponential decay ($p = 1$)[171, 238, 239]. The square-root dependence of T_1 was found to be explained, as well, to be an ensemble averaging effect obtained when integrating the simple exponential decay with spatially varying decay rates over the distribution of spins in the ensemble[229, 241]. This situation is comparable to ours, and $T_{2,echo}$ is the sum of many individual decays with de-

cay rates limited by interactions with an inhomogenous paramagnetic nitrogen spin bath. Using a similar approach than Ref. [200] (see Sec. 2.4.3), we find that the Hahn Echo decay for ensembles $\propto e^{-(t/T_{2,echo})^{3/2}}$, in agreement with our experimentally determined values ($p \approx 1.5$). We conclude that the ensemble decay shapes for Hahn echo, Ramsey, and T_1 are consistently explained by integrating the single NV signals over the distribution of decay rates in the ensemble. The results are summarized in Tab. 6.1 (column 4). The non-integer p-value is thereby also consistent with numerical simulations of the OU-process for different regimes of Δ and τ_c. In the first regime, we find that when the bath dynamics are slow compared to the intra-bath coupling, i.e., when $\tau_c \gg 1/\Delta$, the stretched exponential parameter p approaches 3, as it is the case for single NV measurements in nitrogen-rich diamonds[49, 197]. In the opposite regime, however, when $\tau_c \ll 1/\Delta$ (the motional narrowing regime) the simulation shows that p approaches 1. For the ensemble samples studied in this work, we are exactly in the intermediate regime, $\tau_c \approx 1/\Delta$, and the ensemble p exhibit non-integer values with an average of $\approx 3/2$.

6.6 Conclusion

In conclusion, we studied coherence of NV ensembles as a function of nitrogen concentration and extracted the scaling $T_{2,N} = 156 \pm 15\,\mu s \cdot ppm$. Combining this results with that of a related study on T_2^*, we found that the spin bath dynamics are well-described by an Orenstein-Uhlenbeck process and achieve good agreement with numerical bath simulations. Also, we analyzed the non-integer decay shape in ensemble Hahn echo measurements and find it explained by a statistical average over

many single NV signals, in analogy to the decay shapes observed in Ramsey and T_1 ensemble experiments.

Chapter 7

Conclusion & Outlook

In Ch. 1, we discussed NV applications, relevant NV physics and the primary pulse sequences used for manipulation of the NV ground state. Specifically, we showed how Ramsey and Hahn-echo-type pulse sequence are employed for sensing applications. In these applications, the active sensing time is limited by the inhomogeneous dephasing time T_2^* (Ramsey), homogeneous dephasing time T_2 (Hahn echo), and spin-lattice relaxation T_1 (CPMG-n, when a large number of pulses n are applied). We also provided a comparison between NV centers with ^{14}N and ^{15}N isotope and discussed the differences in Hahn echo and CPMG signals due to the absence of quadropolar splitting in ^{15}N.

In Ch. 2, we reviewed properties of the spin bath with a focus on nitrogen and ^{13}C bath spins, two spin species most relevant in NV applications. We introduced a set of pulse sequences to probe bath dynamics that extend the set of pulse sequences introduced in Ch. 1. We also gave a description of the bath dynamics using a mean

field approach and showed that the experimentally determined decay shapes for single and ensemble measurements are correctly predicted by this theory. Using the mean field approach, we presented a numerical spin bath simulation for the nitrogen bath and found good agreement between simulated and experimentally determined T_2^* and T_2 values.

In Ch. 3 the spin-RESOLFT technique was introduced. The technique allows selective imaging and coherently manipulation of NV centers within a confocal volume with spatial resolutions of approximately 20 nm, well-below the optical diffraction limit ($\sim$ 250 nm). By combining spin-RESOLFT with spin sensing via dynamical decoupling sequences applied to shallow NVs, we demonstrated the utility of spin-RESOLFT for nano-NMR. The spin-RESOLFT method can be straightforwardly extended to other NV-based sensing modalities, including temperature [108], electric field [103], and charge state [104] detection with nanoscale optical resolution.

In Ch. 4, we showed that the spin-to-charge conversion (SCC) technique, together with single-shot charge-state readout, provides $\sim 5\times$ improvements in AC magnetic field sensitivity for a single NV center in bulk diamond. The SCC readout scheme can be used for a wide range of NV sensing scheme. Most importantly, extending the SCC technique to ensemble measurements may provide significant gains these samples.

In Ch. 5 we studied the limitations to T_2^* in ensemble samples. We identi-

fied the dominant spin dephasing mechanisms for bulk NV ensembles in diamond and demonstrated that the combination of DQ magnetometry and spin bath driving could greatly extend T_2^*. When crystal lattice strain-fields are the dominant source of dephasing, working in the NVs $\{-1, +1\}$ DQ provides substantial enhancement in T_2^*. In samples with higher N concentration, spin bath driving in combination with DQ sensing allows further increase of the NV ensemble T_2^* by decoupling paramagnetic nitrogen and other electronic dark spins from the NV spins. The results indicate that T_2^* in ensemble samples can be significantly enhanced such that $T_{2\,\mathrm{ens}}^* \approx T_{2\,\mathrm{single}}^*$ eliminating inhomogeneous dephasing mechanisms which effect ensemble but not single NV centers. It is interesting to combine the DQ technique/spin bath driving with another method in the future. For example, short ensemble T_2^* times have so far prevented effective utilization of more exotic readout techniques, e.g., involving quantum logic [47, 51, 270] or the SCC technique discussed in Ch. 4 [124]. Such methods offer greatly improved NV spin-state readout fidelity but introduce substantial overhead time, typically requiring tens to hundreds of microseconds per readout operation.

In Ch. 6, we studied coherence of NV ensembles as a function of nitrogen concentration and extracted the scaling $T_{2,N} = 156 \pm 15\,\mu\mathrm{s} \cdot \mathrm{ppm}$. Combining this results with that of a related study on T_2^*, we found that the spin bath dynamics are well-described by a mean field approach and achieve good agreement with numerical bath simulations. Also, we presented a coherent picture of the variation in ensemble decays observed for ensemble when compared to single NVs. The decay shapes were already summarized in Ch. 2.

Appendix A

Single and Double Quantum Rabi Signals

A.1 Derivation of Rabi Oscillation for Three-Level System

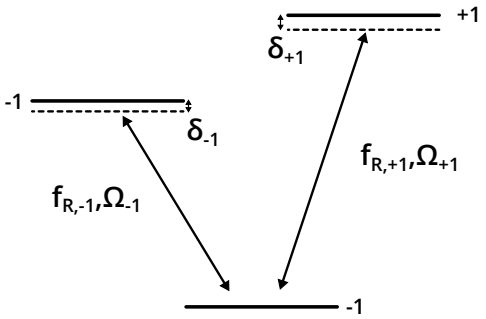

Figure A.1: Three-level scheme with double Rabi drive

For an idealized spin-1 three-level system with resonance transitions frequencies

f_{-1} and f_{+1} and two applied MW drives characterized by the amplitudes Ω_{-1} and Ω_{+1} and frequencies $f_{R,+1}$ and $f_{R,-1}$ (see Fig. A.1) the Hamiltonian is given by [202, 207]

$$\begin{aligned} H/h =& f_{-1}|-1\rangle\langle -1| + f_{+1}|+1\rangle\langle +1| + \\ & \Omega_{+1}\cos(2\pi f_{R,+1}t)[|-1\rangle\langle 0| + |0\rangle\langle -1|] + \\ & \Omega_{-1}\cos(2\pi f_{R,-1}t)[|+1\rangle\langle 0| + |0\rangle\langle +1|]. \end{aligned} \tag{A.1}$$

A.2 Bright and Dark State Basis

To simplify the problem it is convenient to express the Hamiltonian in the bright/dark state basis $\{0, B, D\}$, where

$$|B\rangle = \frac{\Omega_{+1}|+1\rangle + \Omega_{-1}|-1\rangle}{\sqrt{\Omega_{+1}^2 + \Omega_{-1}^2}}, \text{ and} \tag{A.2}$$

$$|D\rangle = \frac{\Omega_{+1}|+1\rangle - \Omega_{-1}|-1\rangle}{\sqrt{\Omega_{+1}^2 + \Omega_{-1}^2}}. \tag{A.3}$$

The motivation becomes clear when rewriting Eqn. A.1, which yields

$$H_{\text{rot}}/h = -\delta_{+1}|B\rangle\langle D| - \delta_{-1}|D\rangle\langle B| - \sqrt{\Omega_{+1}^2 + \Omega_{-1}^2}(|B\rangle\langle 0| + |0\rangle\langle B|). \tag{A.4}$$

This Hamiltonian has a similar form to that of a spin$-1/2$ system with finite detuning driven at the effective Rabi frequency $\sqrt{\Omega_{-1}^2 + \Omega_{+1}^2}$. At zero detuning, we thus reduce the three-level dynamics to that of a two-level system.

Case 1: Zero Detunings

For zero detuning, the Hamiltonian in Eqn. A.4 is of identical form to that of a spin$-1/2$ system. Qualitatively, we therefore expect the population in the $m_s = 0$

spin state to oscillate at Rabi frequency $\Omega_{DQ} = \sqrt{\Omega_{+1}^2 + \Omega_{-1}^2}$ between the zero and bright state. Interestingly, this consideration is independent of the exact values for Ω_{+1} and Ω_{-1}. For cases $\Omega_{+1} \neq \Omega_{-1}$, the dressed bright and dark state (Eqn. A.2 and A.3) are simply rescaled. In the case $\Omega_{+1} = \Omega_{-1} \equiv \Omega_{SQ}$, further simplifications can made and give $|B\rangle = \frac{1}{\sqrt{2}}(|+1\rangle + |1\rangle)$, $|D\rangle = \frac{1}{\sqrt{2}}(|+1\rangle - |1\rangle)$, and the enhanced Rabi frequency becomes $\sqrt{\Omega_{+1}^2 + \Omega_{+1}^2} = \sqrt{2}\Omega_{SQ}$. In the main text of Sec. 1.5 and Ch. 5, the bright state is the state relevant used for sensing due to the twice faster phase accumulation ($m_s = +1$ and $m_s = -1$ both accumulate phase). The $\{-1, +1\}$ sub-basis of the NV spin-1 system was therefore denoted DQ basis and the enhanced Rabi frequency between the $|0\rangle$ and bright state $|B\rangle$ the DQ Rabi frequency given by $\Omega_{DQ} = \sqrt{2}\Omega_{SQ}$.

Case 2: Finite Detunings, $\Omega_{+1} = \Omega_{-1}$, $\delta_{+1} = \delta - 1$

For finite single-photon detunings, the dynamics of the dark state need to be taken into account and Eqn. A.4 can then be solved for example numerically. We simulate the dynamics in the bright/dark state basis in Fig. A.2 for zero two-photon detuning $\Delta = \delta_{+1} - \delta_{-1} = 0$, with $\delta_{+1} = \delta_{+1} = 2.2\,\text{MHz}$ and Rabi frequencies $\Omega_{DQ}/\sqrt{2} = \Omega_{+1} = \Omega_{-1} = 5\,\text{MHz}$. Starting out with the initial population in the $m_s = 0$ state, then $P_0 = 1$, we find that that the population oscillates between the $|0\rangle$ and bright state $|B\rangle$ at frequency $\approx \Omega_{DQ}$, while additional population oscillates between the $|0\rangle$ and dark state at frequencies $\approx \Omega_{DQ}/2$. This causes a beating of the overall $m_s = 0$ state population signal (P_0) . The slight mismatch between observed and applied Rabi is thereby given by the finite detunings: As in the two-level Rabi case, the finite

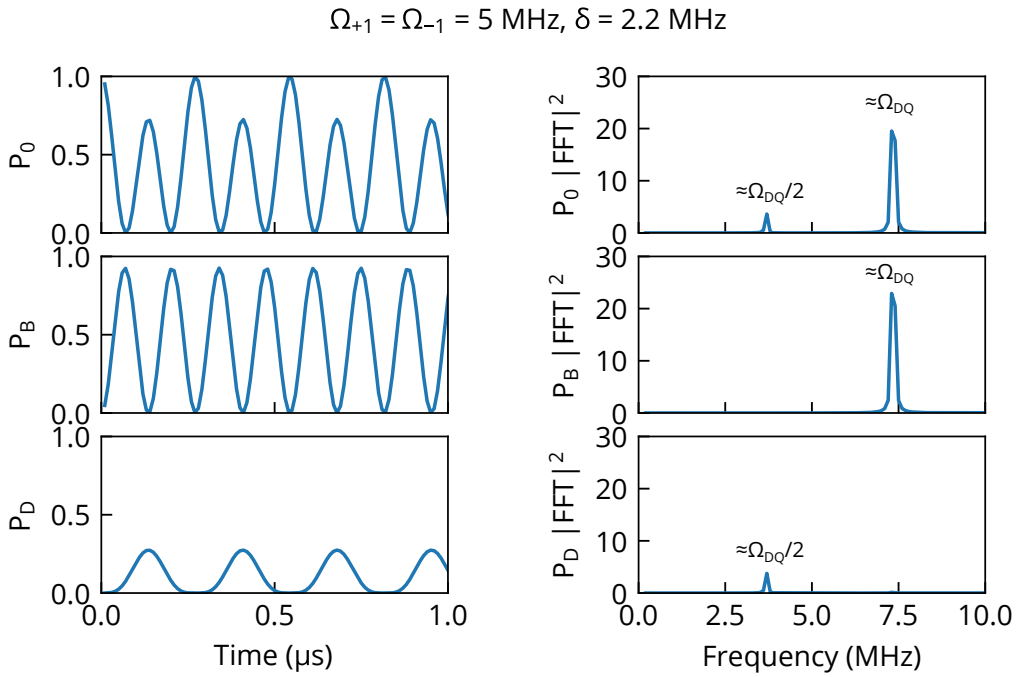

Figure A.2: Simulated DQ Rabi in bright/dark state picture for finite detunings – Left column shows the populations in the $|0\rangle$, $|B\rangle$, and $|D\rangle$ state. Right column shows FFT of the respective populations. The bright state population oscillates with enhanced DQ Rabi frequency $\Omega_{DQ} \approx \sqrt{\Omega_{+1}^2 + \Omega_{-1}^2} = \sqrt{2}\Omega_{SQ}$. The dark state population oscillates at frequency $\approx \Omega_{DQ}/2$ resulting in a beating of the $m_s = 0$ state population (P_0).

$\delta_{\pm 1}$ leads to an increased effective Rabi $\Omega_{DQ}^{\text{eff}} = \sqrt{\Omega_{DQ}^2 + \delta_{\pm 1}^2}$.

A.3 Comparing Experiment with Simulation

The experimental NV Rabi signals are well explained by dynamics of a three-level system with two-tone Rabi drive, discussed in the previous sections, taking the hyperfine splitting $A_z = \pm 12.2\,\text{MHz}$ into account. The relevant NV ground-state Hamiltonian with two-tone Rabi drive (neglecting strain and off-axis magnetic field terms

M_x, M_y, M_z and B_x, By, respectively) is given by

$$H/h = D\mathbf{S}_z^2 + \frac{\gamma_{NV}}{2\pi} B_z \mathbf{S}_z + A_{||}\mathbf{I}_z\mathbf{S}_z + [\Omega_{+1}\cos(2\pi f_{R,+1}t) + \Omega_{-1}\cos(2\pi f_{R,-1}t)]\mathbf{S}_x. \quad \text{(A.5)}$$

The two Rabi drives are characterized by the amplitudes $\Omega_{+1} = \frac{\gamma}{2\pi}B_{+1}$ and $\Omega_{-1} = \frac{\gamma}{2\pi}B_{-1}$ at frequencies $f_{R,+1}$ and $f_{R,-1}$, respectively. To simulate the Rabi signal we solve the Schrödinger equation $i\hbar\frac{d}{d\tau}\psi(\tau) = H\psi(\tau)$ for the Hamiltonian in Eqn. A.5 with Eigenstates $|m_s = 0, \pm 1, m_i = 0, \pm 1\rangle$. The population for the $m_s = 0$ state is then given by $\alpha_0(\tau) \approx \mathrm{e}^{-\tau/\tau'}|\langle\psi(\tau)|0\rangle|^2$ where we have included an exponential decay with time constant $\tau' \approx 1\,\mu\mathrm{s}$ to reflect the decay of the experimental Rabi signal in the ensemble [196, 200]. The calculations are performed using the numerical solver in Mathematica.

We first simulate the Rabi signal with single-tone drive (SQ Rabi, $\Omega_{+1} = 0$) as a function of detuning $\delta = D - \frac{\gamma}{2\pi}B_z - f_{R,-1}$ at fixed $B_z = 10\,\mathrm{mT}$ by sweeping $f_{R,-1}$ and comparing the Fourier transformed Rabi frequency spectra. As shown in Fig. A.3, there is good agreement between the experimental determined spectra and the simulation. The NV's triplet hyperfine structure leads to three hyperbole resonance shapes in the Rabi spectra. The hyperboles are a consequence of the enhanced effective Rabi frequency for non-zero detuning given by $\Omega_{\mathrm{e}ff,-1} = \sqrt{\Omega_{-1}^2 + \delta^2}$ for each of the hyperfine resonances, while the Rabi contrast decreases as $\Omega_{-1}/(\Omega_{-1}^2 + \delta^2)$. The results emphasize that the hyperfine structure of the NV leads to multiple visible Rabi frequencies when on-resonant with th $m_s = 0$ hyperfine transitions as it was discussed in Sec. 1.4.2, exhibiting up to three frequencies in the Rabi spectrum.

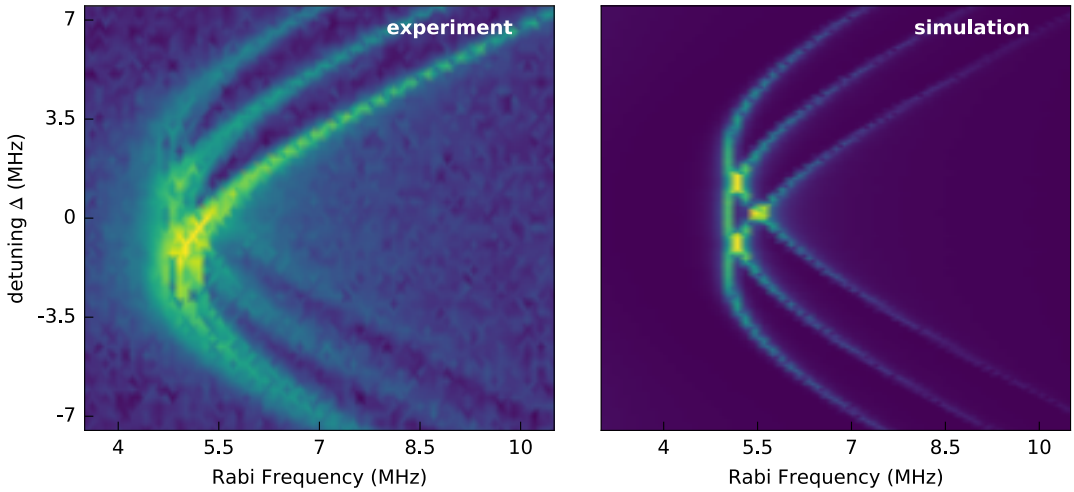

Figure A.3: Fourier transformed SQ Rabi signal plotted as a function of detuning$\Delta = D - \frac{\gamma}{2\pi}B_z - -f_1$ with f_1 being swept from -7.5 to $7.5\,\mathrm{MHz}$. The parameters used in Eqn. A.5 are $D = 2.87\,\mathrm{GHz}$, $\Omega_1 = 5\,\mathrm{Mhz}$, $\Omega_2 = 0$, $B_z = 10\,\mathrm{mT}$.

Similarly to the single-tone drive, we simulated the Rabi spectrum for two-tone drive (DQ Rabi, $B_{-1} = B_{+1} \neq 0$) and compare the Rabi spectra with experimental results for different detuning Δ. For the simulation, frequency f_{+1} is fixed at $f_{+1} = D - \frac{\gamma}{2\pi}B_z$ (on-resonance) and f_{-1} is swept across the second resonance with detuning $\Delta = D + \frac{\gamma}{2\pi}B_z - f_{-1}$. Figure A.4 compares the simulated Rabi spectra as a function of detuning with the experiment. Similarly, we find the hyperbole-type shapes appearing at Rabi frequencies $\approx \Omega_{DQ}$ and $\approx \Omega_{DQ}/2$ as expected from our analysis of the three-level system discussed earlier.

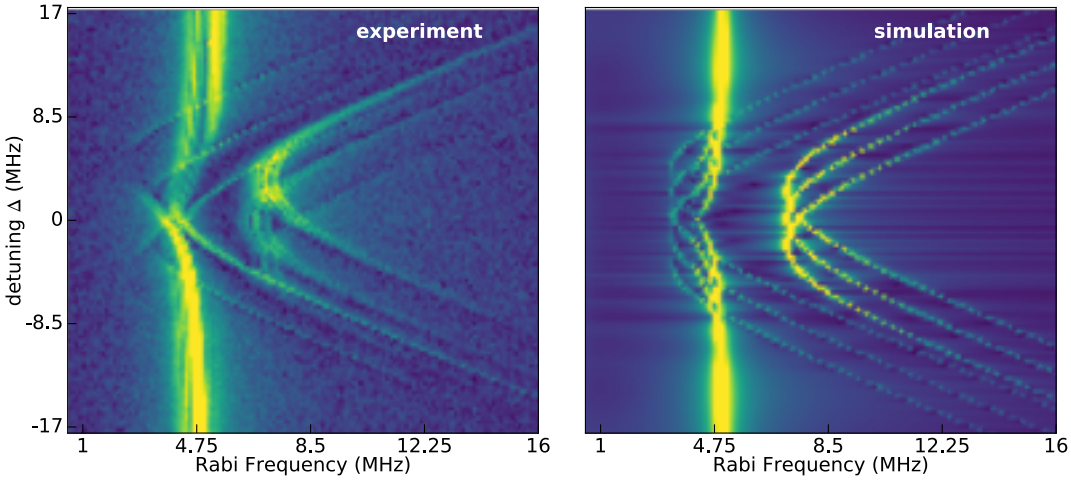

Figure A.4: Fourier transformed DQ Rabi signal – Measured NV Rabi spectrum in the DQ basis (left) and simulation (right) as a function of detuning $\Delta = D + \frac{\gamma}{2\pi}B_z - f_2$. The parameters used are $D = 2.87\,\mathrm{GHz}$, $\Omega_1 = \Omega_2 = 5\,\mathrm{Mhz}$, $B_z \approx 10\,\mathrm{mT}$, $f_1 = D - \frac{\gamma}{2\pi}$ and f_2 is swept from -17.5 to 17.5 MHz. From the simulation we find that even at $\Delta = 0$ the DQ Rabi spectrum exhibits up to four Rabi frequencies and comprises of off-resonant driven hyperfine transitions and a SQ Rabi contribution.

Appendix B

Superresolution Optical Magnetic Imaging and Spectroscopy using Individual Electronic Spins in Diamond - Supplement

B.1 NV Position Drift and Fluctuations

Because of separated optical paths, the spin-RESOLFT experimental setup is sensitive to the relative motion of the Gaussian beam, doughnut beam, and confocal PSF, over the typical timescale of a complete experiment (minutes to hours). In particular, a single realization of a spin-RESOLFT experimental sequence requires $\sim 20\,\mu s$, yielding ~ 0.02 collected photons. The sequence is repeated $\sim 20,000$ times for each imaging pixel to suppress photon shot noise to $5\,\%$. Thus, a full 1D scan of $\sim 400\,nm$

(100 pixels) across an NV center ideally takes $\sim 40\,\mathrm{s}$. However, due to overhead from data recording and display, such a single 1D scan actually requires $\sim 2\,\mathrm{min}$. In addition, between each scan the position of the NV center is recorded, and then the optical illumination is adjusted to place the NV back into the middle of the scan window. The tracking procedure consists of discrete probing of the fluorescence spatial distribution in the neighborhood of the NV center to determine the position of its maximum value. It is followed by 1D confocal scans in both lateral directions that are fitted with Gaussians to obtain the NV center position with a precision of about 5 nm. For the single NV spin-RESOLFT datasets plotted in Fig. 3.1(d) of the main text, the entire 1D scan is repeated and then averaged six times, leading to a total acquisition time of about 12 min. In the case of multiple NV imaging (Fig. 3.3 and 3.4 of main text), the tracking is done by taking a single nearby NV as reference. The reference NV is positioned about 1 µm away from the pair of NV centers, as shown in Fig. B.1. In the more general case of a wide field-of-view image, optical reflection from a golden nanoparticle attached on the surface of the diamond is used as a reference point.

During long acquisition times, the position of an NV center shows a strong correlation with laboratory temperature fluctuations, as shown in Fig. B.2. Due to thermal expansion of the objective holder, we observed drifts of the reference NV by approximately 500 nm. These drifts were minimized by using insulating enclosures in which the temperature fluctuates by not more than 0.1 °C over the course of a measurement. Nonetheless, such diminished drifts as well as table vibrations during

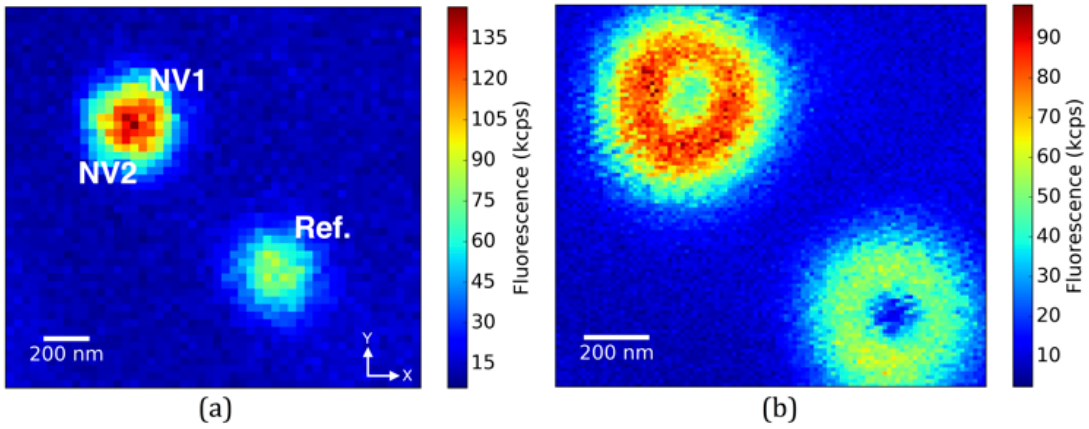

Figure B.1: Measured 2D images of a pair of proximal NV centers and a reference NV center (a) confocal scan; (b) green doughnut beam scan.

a line scan can still result in observable broadening of the PSF of the spin-RESOLFT microscope. 2D scans, which are usually acquired over 10 hours, are affected even more severely. Fig. B.2(b) displays the relative displacement of the NV center used in Fig. 3.1(d) of the main text after each line scan. From this trace, we identify a motion along the direction of the scan with a standard deviation of 11 nm.

B.2 NV Spin Repolarization

Due to the spin-dependent intersystem-crossing through its singlet states, NV centers preferentially decay into the $m_s = 0$ ground state under green illumination. This results in strong spin polarization after several excitation cycles. In spin-RESOLFT, the role of spin polarization is two-fold: preparing the initial NV state in $m_s = 0$ for sensing using a Gaussian beam, and repolarizing the NV center into $m_s = 0$ for superresolution imaging using the doughnut beam. As mentioned in the Ch. 3 and shown in the inset of Fig. 3.2 and 3.3, the fluorescence point-spread function (PSF)

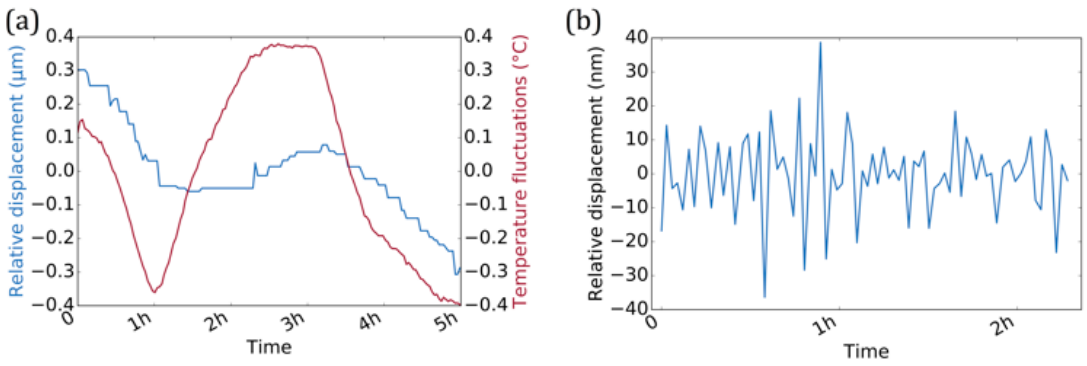

Figure B.2: Measured relative 1D position of an example NV center and the laboratory temperature during a 5 hour-long confocal scan. – (a) A 1D NV fluorescence intensity profile takes about 1 minute after which the temperature and the NV center position are recorded. The laboratory temperature oscillates with a period of about 1 hour and induces a correlated drifts of the NV center position $\sim$ 500 nm. (b) Stabilization of the laboratory temperature to a peak-to-peak variation of 0.1 °C allows data acquisition for two hours during which time the NV position is stable with a standard deviation of 11 nm.

displays a non-trivial shape that is the result of non-linear NV repolarization. To model the NV polarization dynamics, we use the five-level system shown in Fig. B.3.

The system of rate equations that governs the NV state populations under optical excitation can be formulated as

$$\frac{1}{\gamma}\frac{dn_1}{dt} = -I(t)\sigma \cdot n_1 + n_1 + a_5 1 n_5, \tag{B.1}$$

$$\frac{1}{\gamma}\frac{dn_2}{dt} = -I(t)\sigma \cdot n_2 + n_2 + a_5 2 n_5, \tag{B.2}$$

$$\frac{1}{\gamma}\frac{dn_3}{dt} = I(t)\sigma \cdot n_1 - n_3 - a_3 5 n_3, \tag{B.3}$$

$$\frac{1}{\gamma}\frac{dn_4}{dt} = I(t)\sigma \cdot n_2 - n_4 - a_4 5 n_4, \tag{B.4}$$

$$\frac{1}{\gamma}\frac{dn_5}{dt} = a_3 5 n_3 + a_4 5 n_4 - a_5 1 n_5 - a_5 2 n_5. \tag{B.5}$$

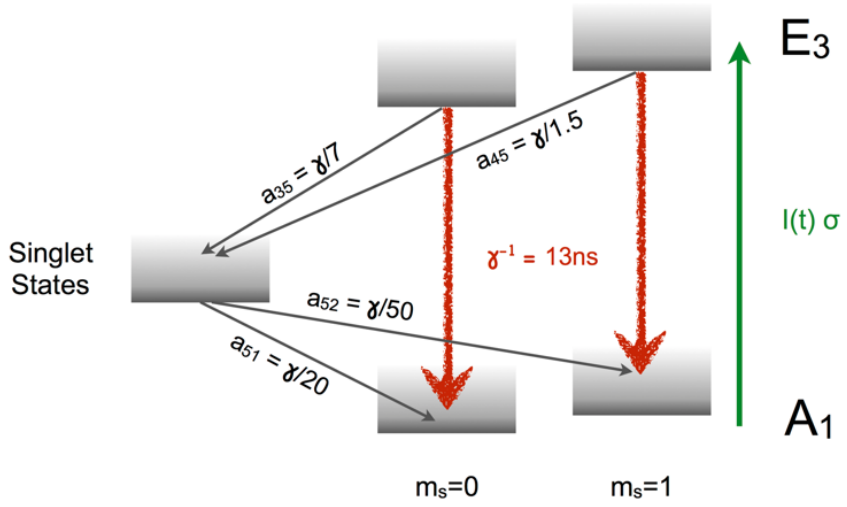

Figure B.3: NV level structure and decay rates. The populations are denoted by n_i, where i refers to the following levels: 1 for $m_s = 0$ ground state, 2 for $m_s = -1$ ground state, 3 for $m_s = 0$ excited state, 4 for $m_s = -1$ excited state and 5 for the singlet states. The decay rates a_{ij} between levels are indexed by the initial level i and the final level j. All rates are given relative to the primary fluorescence decay rate γ. The singlet states are represented as a single state for the sake of simplicity, and we use previously measured room temperature rates [178]

Here σ represents the cross-section of the primary NV electronic transition for a 532 nm laser beam pulse of intensity $I(t)$. Fig. B.4 shows the $m_s = 0$ ground state population after applying a square pulse starting at $t = 0$ on an unpolarized NV center with equal initial spin state population. We see that the degree of repolarization depends on both the intensity and duration of the excitation pulse. In particular, a higher degree of polarization is achieved with a long and weak green pulse (5 ms at 5 % of the saturation intensity). Moreover, for a fixed pulse duration, we find that the repolarization is non-linear in optical intensity, resulting in a strong effect on the PSF of the spin-RESOLFT microscope image determined by the spatial intensity distribution of the doughnut beam.

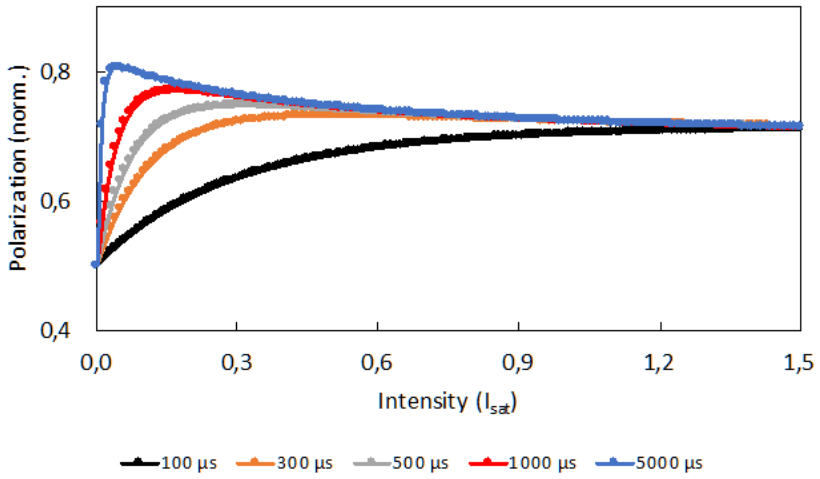

Figure B.4: Simulation of the dependence of the NV spin polarization on green excitation beam intensity. The degree of polarization displays a non-linear behaviour with light excitation. Short pulses of about 100 µs provide at most 70 % polarization, due to non-zero decay rates from the singlet state to both the ground state sublevels. Longer pulses provide a higher degree of polarization but restrict the intensity to a fraction of the saturation intensity. The highest resolution is obtained for durations where the slope near the doughnut center is steeper, which leads to strong non-linear behaviour, a degradation of the spin polarization far from the doughnut center and a non-trivial PSF profile.

Indeed, the doughnut intensity profile can be approximated near the center as

$$I(r) = I_0 \left[\left(\frac{r}{r_0} \right)^2 + \epsilon \right] \mathrm{e}^{-\left(\frac{r}{r_0}\right)^2} \tag{B.6}$$

where I_0 is the peak intensity, r_0 is the doughnut radius, and ϵ is the relative residual intensity in the doughnut center. Using this intensity profile as input to the system of equations in B.1, we plot the one-dimensional spin-RESOLFT PSF in Fig. B.5 for two different values of $\epsilon = 0.1\%$ and $\epsilon = 2\,\%$. As the intensity increases quadratically along the doughnut profile, the degree of NV polarization is convolved with the behavior displayed in Fig. B.4.

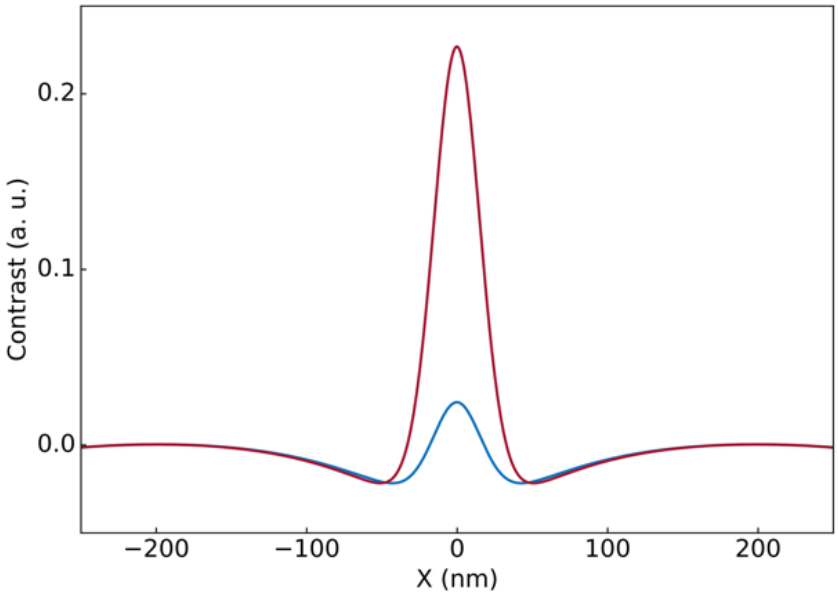

Figure B.5: Simulated spin-RESOLFT PSF for two different residual intensities in the center of the green doughnut beam: $\epsilon = 0.1\,\%$ (red) and $\epsilon = 2\,\%$ (blue).

Higher resolution is achieved for combinations of long durations and weak powers, which display strong repolarization. However, for a particular finite position in the doughnut profile, the intensity reaches the value where the repolarization is maximum before decreasing back to the steady value of 70%, which leads to negative contrast and non-Gaussian wings in the spin-RESOLFT PSF. Negative contrast should be understood as a polarization that is greater than the reference case of repolarization with a long or strong pulse. Doughnut imperfections, which lead to a non-zero intensity ϵI_0 in the doughnut beam center, tend to reduce the state dependent fluorescence contrast, but do not affect the shape of the intensity profile. We use the numerical solution to Eqn. B.1 to extract the resolutions reported in Fig. 3.1(d), 3.1(e), and 3.3(b) in the main text.

B.3 AC Magnetic Field Gradient

To create an AC magnetic field gradient, which results in a measurable difference in magnetic field strength at the position of NV_1 and NV_2 as used for the results in Fig. 3.4 of the main text, we drive an AC current $I_{AC} = 7\,\text{mA}$ at $8.3\,\text{kHz}$ through a copper wire (type Alfa Aesar, diameter $25\,\mu\text{m}$) that is $\sim 10\,\mu\text{m}$ from the NVs. The same wire also carries the microwaves for coherent NV spin manipulation.

To simulate the observed magnetic field dependence, we devised a simple model that takes the projection of the applied AC fields onto the NV axis into account. In our geometry, the wire is parallel to the horizontal axis of Figs. 3.3(b) and 3.4(d) (here, the y-direction), whereas the z-direction corresponds to the normal of the diamond's top surface and the x-direction completes the orthonormal reference frame. The NV center axis is determined by its polar θ and azithumal ϕ angles, as commonly defined. In this system of coordinates, NV_1 and NV_2 are directed along the x-direction ($\phi = 0°$) while making an angle with the z-axis of $\theta = 54.7°$. Moreover, the magnetic field lines form loops in the plane perpendicular to the wire. In AC magnetometry, the NV center is sensitive to the component of the magnetic field that is parallel to the NV axis, namely

$$B_{||}(\vec{r}) = B_{\text{wire}}(\vec{r}) \cdot NV(\vec{r}) \tag{B.7}$$

$$= \frac{\mu_0}{2\pi} \frac{I}{x^2 + z^2} (z \sin\phi \cos\theta + x \cos\phi) \tag{B.8}$$

In Fig. B.6, we simulate this magnetic field component for different positions along the x direction, with the center of the wire fixed at the origin and the NV

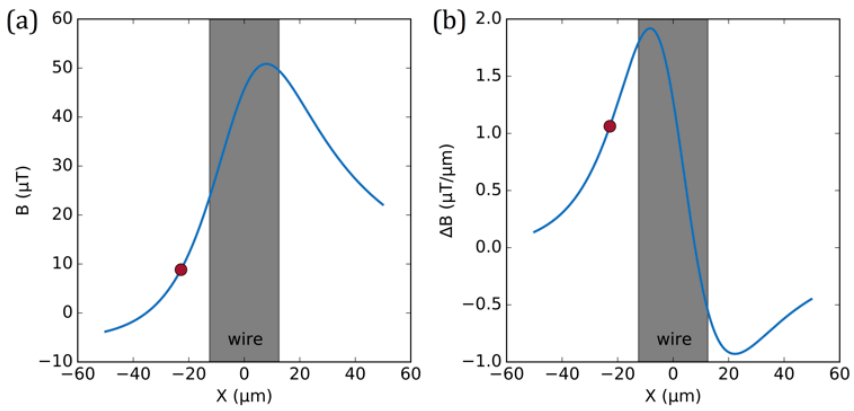

Figure B.6: Magnetic field strength and (b) gradient extracted from a model that takes into account the distance from the wire and the orientation of the NV center axis. At a horizontal distance of 10 μm from the wire, the measured magnetic field strength of 9 μT and (b) measured gradient of 1 nT/nm are in good agreement with the experimental values reported in the main text.

center's depth is chosen to be at $z = 12.5 + 7.5\,\mu\text{m} = 20\,\mu\text{m}$ under the wire. When the NV center is at $x = -10\,\mu\text{m}$ from the wire's edge, we find the calculated field along the NV center axis to be 9 μT, which is in good agreement with the experimental values we measure and report in the main text. Moreover, we plot the magnetic field gradient expected from this model as function of the x position in Fig. B.6(b). The value of the magnetic field gradient of about 1 nT/nm is also in good agreement with the gradient experimentally measured with the pair of NV centers (NV_1 and NV_2) separated by 105 nm.

$$B_{\perp}(\vec{r}) = B_{\text{wire}}(\vec{r}) - B_{\text{wire}}(\vec{r}) \cdot NV(\vec{r}) \tag{B.9}$$

Using the same experimental conditions as described above, we calculate a Rabi frequency of 5.5 MHz for a current of 30 mA. This is also in a good agreement with the measured Rabi frequency for this MW current in our setup (Fig. B.7).

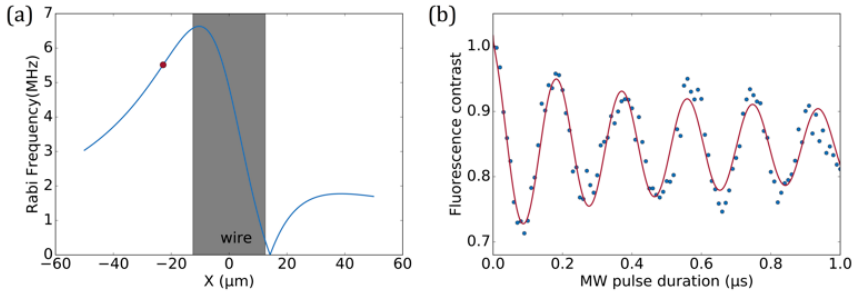

Figure B.7: Calculated NV Rabi frequency as a function of the NV center horizontal position – (a) This spatial behavior is calculated from a model that takes into account the distance between the wire and the NV center as well as the NV orientation. The red dot corresponds to the position of the two NV centers used in the main text (NV_1 and NV_2). (b) Measured NV Rabi oscillations (blue dots) and a fit to an exponentially damped sinusoid (red curve). The extracted Rabi frequency of 5.5 MHz is a good agreement with the model calculation.

B.4 AC Magnetic Field Sensitivity

The magnetic field sensitivity in a Hahn-Echo pulse sequence has the following expression [41]:

$$\eta = \frac{1}{\gamma_{NV}\frac{1}{C\mathrm{e}^{-\tau/T_2}}}\frac{\sqrt{\tau_R+\tau_I+\tau}}{\tau} \tag{B.10}$$

where γ_{NV} is the NV gyromagnetic ratio, C is the maximum spin contrast achievable in spin-RESOLFT imaging at a specified resolution, t_I, and t_R are the initialization and readout time, respectively. Because of experimental imperfections such as non-zero intensity at the doughnut center, the NV spin-state contrast decreases as we apply longer a doughnut laser beam to reach sub-diffraction resolution, which results in a degradation of the magnetic field sensitivity. For example, in the case of Fig. 3.4(b), we obtain a sensitivity of $\sim 60\,\mathrm{nT}/\sqrt{\mathrm{Hz}}$ in confocal mode with a single NV, and $\sim 250\,\mathrm{nT}/\sqrt{\mathrm{Hz}}$ with spin-RESOLFT for 50 nm spatial resolution as the contrast drops by a factor of about 4 from $\sim 10\,\%$ to $\sim 2.5\,\%$.

Appendix C

Order of Magnitude Improvement in T_2^* in Solid-State Spin Ensembles via Quantum Control - Supplement

C.1 Setup

C.2 NV Hamiltonian in Single and Double Quantum Bases

In this section we discuss the influence of strain and magnetic fields in the single quantum (SQ) and double quantum (DQ) bases by considering several limiting cases. We first discuss how common-mode noise sources, i.e., sources that shift the NV $|-1\rangle$ and $|+1\rangle$ energy levels in-phase and with equal magnitude, are suppressed

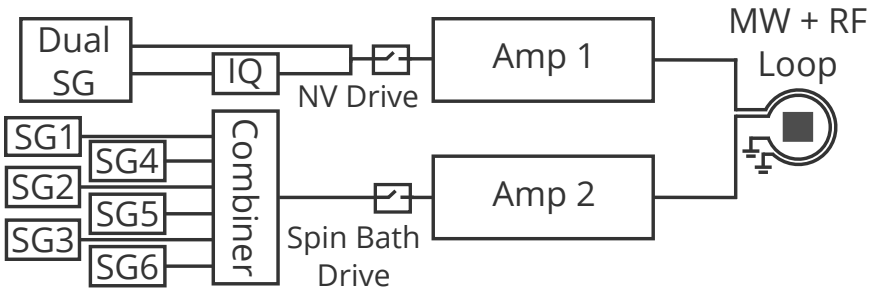

Figure C.1: Microwave generation and delivery schematic. For NV spin state control: Single and two-tone signals are generated using a dual channel Windfreak Technology Synth HD signal generator. One channel includes a Marki IQ-1545 mixer to manipulate the relative phase between both channels. A single Minicircuits ZASWA-2-50DR+ switch is used to generate the NV control pulses before amplification with a Minicircuits ZHL-16W-43 amplifer. The NV control fields are delivered to the diamond sample using a fabricated microwave waveguide (diameter 500 μm). For spin bath control: Up to eight single channel Windfreak Technology Synth NV signal generators are combined before passing through a switch and a Minicircuits ZHL-100W-52 100 W amplifier. The amplified field is delivered via a grounded cooper loop (1 mm diameter).

in the DQ basis. We then discuss how off-NV-axis strain fields are suppressed even by moderate bias magnetic fields. Lastly, we discuss the effect of off-axis B-fields on the NV spin-state energy levels and T_2^*. We begin with the negatively-charged NV ground electronic state electronic spin ($S = 1$) Hamiltonian, which is given by [142] (neglecting hyperfine interactions):

$$\mathbf{H}/h = D\mathbf{S}_z^2 + \frac{\gamma_{NV}}{2\pi}(B_x\mathbf{S}_x + B_y\mathbf{S}_y + B_z\mathbf{S}_z) + M_z\mathbf{S}_z^2 + M_x(\mathbf{S}_y^2 - \mathbf{S}_x^2) + M_y(\mathbf{S}_x\mathbf{S}_y + \mathbf{S}_y\mathbf{S}_x), \tag{C.1}$$

where $D \approx 2.87\,\text{GHz}$ is the NV zero-field splitting due to spin-spin interactions, $\{B_x, B_y, B_z\}$ are the magnetic field components, $\{M_x, M_y, M_z\}$ collect strain and electric field components, $\{\mathbf{S}_x, \mathbf{S}_y, \mathbf{S}_z\}$ are the dimensionless spin-1 operators, and

$\frac{g\mu_B}{h} = \frac{\gamma_{NV}}{2\pi} \approx 28.04\,\text{GHz/T}$ is the NV gyromagnetic ratio. Using $M_\perp \equiv -(M_x + iM_y)$, $B_\perp \equiv \frac{1}{\sqrt{2}}(B_x + iB_y)$, and the standard definitions for the spin operators $\{\mathbf{S}_x, \mathbf{S}_y, \mathbf{S}_z\}$, Eqn. C.1 reads in matrix form:

$$\mathbf{H}/h = \begin{pmatrix} D + M_z + \frac{\gamma_{NV}}{2\pi}B_z & \frac{\gamma_{NV}}{2\pi}B_\perp^* & M_\perp \\ \frac{\gamma_{NV}}{2\pi}B_\perp & 0 & \frac{\gamma_{NV}}{2\pi}B_\perp^* \\ M_\perp^* & \frac{\gamma_{NV}}{2\pi}B_\perp & D + M_z - \frac{\gamma_{NV}}{2\pi}B_z \end{pmatrix}. \tag{C.2}$$

Case 1: Zero Strain, Zero Off-Axis Magnetic Field

For zero strain/electric field ($\{M_x, M_y, M_z\} = 0$) and zero off-axis magnetic field ($B_\perp = 0$), the Hamiltonian in Eqn. C.2 is diagonal:

$$\mathbf{H}_0/h = \begin{pmatrix} D + \frac{\gamma_{NV}}{2\pi}B_z & 0 & 0 \\ 0 & 0 & 0 \\ 0 & 0 & D - \frac{\gamma_{NV}}{2\pi}B_z \end{pmatrix}, \tag{C.3}$$

and the energy levels are given by the zero-field splitting D and Zeeman energies $\pm\frac{\gamma_{NV}}{2\pi}B_z$,

$$E_{|\pm 1,0\rangle}/h = \{D \pm \frac{\gamma_{NV}}{2\pi}B_z, 0\}, \tag{C.4}$$

where $|\pm 1, 0\rangle$ are the Zeeman eigenstates

$$|+1\rangle = \begin{pmatrix} 1 \\ 0 \\ 0 \end{pmatrix}, |-1\rangle = \begin{pmatrix} 0 \\ 0 \\ 1 \end{pmatrix}, \text{and } |0\rangle = \begin{pmatrix} 0 \\ 1 \\ 0 \end{pmatrix}. \tag{C.5}$$

NV spin ensemble measurements in the DQ basis, for which the difference between the $f_{-1} = E_{|0\rangle\rightarrow|-1>}$ and $f_{+1} = E_{|0\rangle\rightarrow|+1>}$ transitions is probed (see Fig. 5.1b), are to first-order insensitive to inhomogeneities and fluctuations in D (e.g., due to drift in

temperature), and other common-mode noise sources. However, DQ measurements are twice as sensitive to magnetic fields along B_z. The DQ basis therefore provides both enhanced magnetic field sensitivity and protection against common-mode noise sources (for higher order effects see, e.g., the Supplement of Ref. [202]).

Case 2: Non-zero Strain, Zero Off-Axis Magnetic Field

For non-zero strain/electric field components, but negligible off-axis magnetic fields ($B_\perp \approx 0$), the energy eigenvalues of the NV Hamiltonian (Eqn. C.2) for the $|\pm 1\rangle$ states become

$$E_{|\pm 1\rangle}/h = D + M_z \pm \sqrt{(\frac{\gamma_{NV}}{2\pi}B_z)^2 + ||M_\perp||^2} \tag{C.6}$$

$$\approx D + M_z \pm \left[\frac{\gamma_{NV}}{2\pi}B_z + \frac{||M_\perp||^2}{2\frac{\gamma_{NV}}{2\pi}B_z} + \mathcal{O}\left(\frac{(||M_\perp||^4}{B_z^2}\right)\right]. \tag{C.7}$$

From Eqn. C.7 it follows that off-axis strain ($\propto ||M_\perp||$) is suppressed by moderate on-axis bias fields by a factor $\frac{||M_\perp||}{\gamma_{NV}B_z/\pi}$, as noted in the main text. Reported values for $||M_\perp||$ are $\sim 10\,\text{kHz}$ [202] and $\sim 100\,\text{kHz}$ [133] for single NV centers in bulk diamond, and $\sim 7\,\text{MHz}$ in nano-diamonds [133]. Fig. 5.1c in the main text shows that the measured on-axis strain M_z in Sample B varies between $2-3\,\text{MHz}$ (see Methods for details).

Case 3: Non-Zero Off-Axis Magnetic Field

For non-zero off-axis magnetic field ($B_\perp \neq 0$) we find the energy values for the NV Hamiltonian (Eqn. C.1) by treating $B_\perp$ as a small perturbation, with perturbation Hamiltonian $\mathbf{V} \equiv \mathbf{H} - \mathbf{H}_0$. To simplify the analysis we set $M_{||} = M_\perp = 0$. Using time-

independent perturbation theory (TIPT, see for example Ref. [290]), the corrected energy levels are then given by $E_{|\pm1,0\rangle} \approx E^{(0)}_{|\pm1,0\rangle} + E^{(1)}_{|\pm1,0\rangle} + E^{(2)}_{|\pm1,0\rangle} + \dots$, where $E^{(0)}_{|\pm1,0\rangle}$ are the bare Zeeman energies as given in Eqn. C.4 and $E^{(k)}_{|\pm1,0\rangle}$ for $k > 0$ are the k-th order corrections. The energy corrections at first and second order are:

$$E^{(1)}_{|\pm1,0\rangle} = \langle \pm1, 0|\mathbf{V}|\pm1, 0\rangle = 0, \tag{C.8}$$

and

$$E^{(2)}_{|\pm1\rangle} = \frac{\|\langle \mp1|\mathbf{V}|\pm1\rangle\|^2}{E_{|\pm1\rangle} - E_{|\mp1\rangle}} + \frac{\|\langle 0|\mathbf{V}|\pm1\rangle\|^2}{E_{|\pm1\rangle}} = \frac{\|\frac{\gamma_{NV}}{2\pi}B_\perp\|^2}{D \pm \frac{\gamma_{NV}}{2\pi}B_z} \approx \frac{\|\frac{\gamma_{NV}}{2\pi}B_\perp\|^2}{D}, \tag{C.9}$$

$$E^{(2)}_{|0\rangle} = \frac{\|\langle +1|\mathbf{V}|0\rangle\|^2}{-E_{|+1\rangle}} + \frac{\|\langle -1|\mathbf{V}|0\rangle\|^2}{-E_{|-1\rangle}} = -\left(\frac{\|\frac{\gamma_{NV}}{2\pi}B_\perp\|^2}{D + \frac{\gamma_{NV}}{2\pi}B_z} + \frac{\|\frac{\gamma_{NV}}{2\pi}B_\perp\|^2}{D - \frac{\gamma_{NV}}{2\pi}B_z}\right) \approx -\frac{2\|\frac{\gamma_{NV}}{2\pi}B_\perp\|^2}{D}, \tag{C.10}$$

where we have used in the last two lines the fact that $\frac{\gamma_{NV}}{2\pi}B_z \ll D$ in our experiments. The new transition frequencies for $E_{|0\rangle\to|\pm1\rangle}$ are then found to be

$$f_{\pm1} \approx D + \frac{3\|\frac{\gamma_{NV}}{2\pi}B_\perp\|^2}{D} \pm \frac{\gamma_{NV}}{2\pi}B_z. \tag{C.11}$$

From Eqn. C.11 it follows that energy level shifts due to perpendicular magnetic fields are mitigated by the large zero-field splitting D; and are further suppressed in the DQ basis, as they add (approximately) in common-mode. At moderate bias fields, $B_z = 2 - 20\,\mathrm{mT}$, and typical misalignment angles of $\theta \sim 3^\circ$ (or better), we estimate a frequency shift of $0.1 - 1\,\mathrm{kHz}$ in the SQ basis.

C.3 ^{13}C Contribution to T_2^*

In the dilute ^{13}C limit ($n_{13C} \lesssim 1.1\,\%$, where n_{13C} is the ^{13}C spin concentration in percent), the NV-^{13}C contact-interaction can be neglected and thus the NV ensemble

ESR linewidth is expected to be linearly-dependent on the ^{13}C concentration[3, 86, 250], i.e., $1/T^*_{2,\text{NV-13C}} = A_{\text{NV-13C}} \cdot n_{13\text{C}}$. An NV spin ensemble T_2^* measurement on a natural abundance sample with $n_{13\text{C}} = 1.07\,\%$ therefore provides a reasonable lower-bound estimate for $A_{\text{NV-13C}}$ from which the ^{13}C contribution in our diamond samples can be calculated. Fig. C.2 shows a DQ Ramsey measurement of a natural ^{13}C abundance sample. Via a fit to the Ramsey data in the time domain, we extract $T^*_{2,DQ} = 445(30)\,\text{ns}$ and $p = 1.0(1)$. After correcting for the small contribution of 0.4 ppm nitrogen spins in the sample using the calibration found in Fig. 5.4c of the main text, we calculate $A_{^{13}\text{C}} \approx 2\pi \times 160\,\text{kHz}/\%$ ($1/A_{^{13}\text{C}} \approx 1\,\mu\text{s} \cdot \%$) from which we determine the NV-^{13}C limits given in Table 1 and the main text of the paper.

C.4 Magnetic Field Gradient Contribution to T_2^*

The wide-field NV-diamond microscope employs a custom-built samarium-cobalt (SmCo) magnet geometry designed to apply a homogeneous external field B_0 parallel to NVs oriented along the [111] diamond crystallographic axis. The field strength can be varied between 2 to 20 mT (Fig. C.3a). SmCo was chosen for its low reversible temperature coefficient (-0.03 $\%/K$). Calculations performed using the Radia software package [285] enabled the optimization of the geometry to minimize B_0 gradients across the NV fluorescence collection volume. This collection volume is approximately cylindrical, with a measured diameter of $\approx 20\,\mu\text{m}$ and a length determined by the NV layer thickness along the z-axis ($40 - 100\,\mu\text{m}$, depending on the diamond sample, see descriptions in the main text).

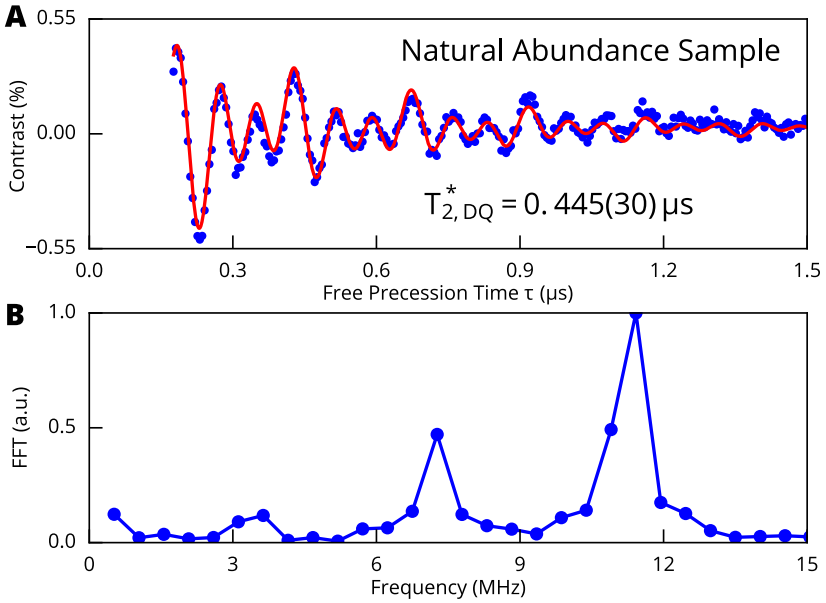

Figure C.2: NV Ramsey measurement for natural isotope abundance diamond sample. (a) DQ Ramsey measurement on a natural abundance sample ($[N] \simeq 0.4\,\text{ppm}$, $[^{13}C] = 1.07\,\%$) yields $T^*_{2,DQ} = 0.445(30)\,\mu\text{s}$. (b) Fourier transform of Ramsey signal showing the enhanced precession in the DQ basis. A frequency detuning from the center hyperfine state of 3.65 MHz was chosen in this measurement; by sensing in the DQ basis, the detuning from each hyperfine state has acquired a factor of two.

To calculate the expected B_0 field strength along the target NV orientation, the dimensions and properties of the magnets were used as Radia input, as well as an estimated 3° misalignment angle of the magnetic field with the NV axis. We find good agreement between the calculated field strength and values extracted from NV ESR measurements in Sample B, over a few millimeter lengthscale. The simulation results and measured values are plotted together in Fig. C.3b. The z-direction gradient is reduced compared to the gradient in the xy-plane due to a high degree of symmetry along the z-axis for the magnet geometry.

Using data and simulation, we calculate that the B_0 gradient at 8.5 mT induces an NV ensemble ESR linewidth broadening of less than 0.1 kHz across the collection volume of Sample B. This corresponds to a T_2^*-limit on the order of 1 ms. However, due to interaction of the bias magnetic with nearby materials and the displacement of the collection volume from the magnetic field saddle point, the experimentally realized gradient for Sample B was found to contribute an NV ESR linewidth broadening ≈ 1 kHz (implying a T_2^*-limit $\approx 320\,\mu$s), which constitutes a small but non-negligible contribution to the T_2^* values measured in this work. Ramsey measurements for Sample A were taken at a four times smaller bias field; we estimate therefore $\approx 4\times$ better magnetic field homogeneity. For Sample C, with a layer thickness of 40 μm, the contribution of the magnetic field gradient at 10 mT to T_2^* was similar to that of Sample B.

C.5 NV and Nitrogen Spin Resonance Linewidth Measurements

The NV and nitrogen (P1) ensemble spin resonance linewidths are determined using pulsed-ESR and pulsed-DEER NV spectral measurements, respectively, as shown in Fig. C.4. Low Rabi drive strength and consequently long π-pulse durations can be used to avoid Fourier power broadening [194]. We find that nitrogen spin resonance spectra are typically narrower than for NV ensembles in the SQ basis, due to the effects of strain gradients in diamond on NV zero-field splittings.

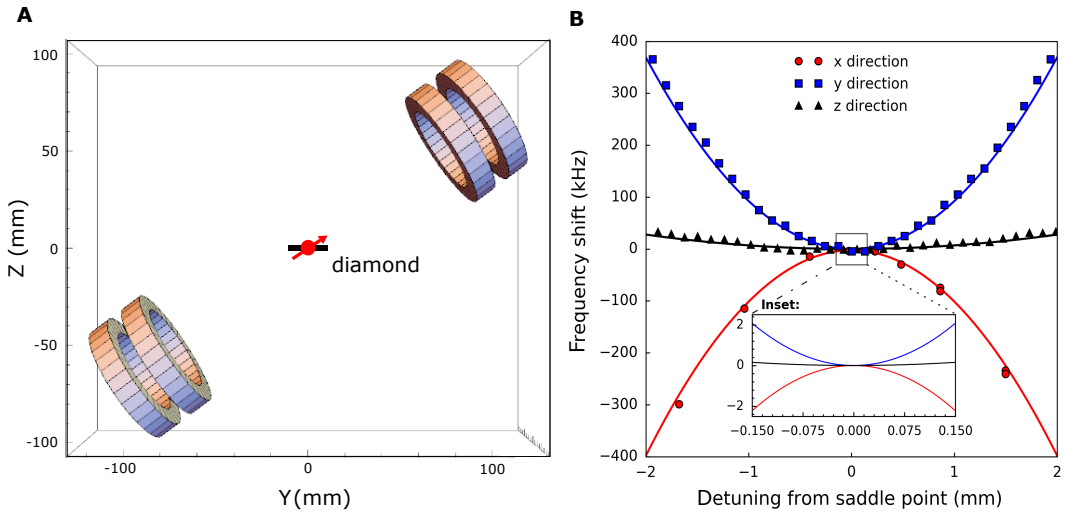

Figure C.3: Design of homogeneous magnetic bias field. (a) Magnet geometry used to apply an external B_0 field along one NV orientation within the diamond crystal (typically [111]) as modeled using Radia[285]. Red arrow depicts the NV orientation class interrogated in these experiments; black rectangle represents diamond sample approximately to scale. (b) Magnets are translated along three axes to measure the B_0 field strength (shift in ESR transition frequency) as a function of detuning from the origin (x,y,z =0) where the origin is defined as the center of the collection volume. Solid lines depict Radia simulation results while plotted points correspond to measured values. Inset: Zoomed-in view for length scale relevant for NV fluorescence collection volumes used in this work.

For the spin bath driving model described in the main text, we are interested in the natural (i.e., non-power-boadened) linewidth Δ_N of spin resonances corresponding to, for example, ^{14}N groups $1-6$ (see Fig. 5.2b in main text and Fig. C.4a in Supplement). In Ref. [49] it was reported that the different ^{14}N groups have approximately equal linewidth, i.e., that $\Delta_{N,i} \approx \Delta_N$. However, we find that the bias field B_z being only slightly misaligned ($\sim$1 degree) from one of the [111] crystal axes causes the three degenerate spin resonances to be imperfectly overlapped, leading to a larger effective linewidth.

In Fig. C.4b and c we compare the NV pulsed-DEER linewidths of ^{14}N group 1 (a single resonance) with that of group 5 (three overlapped resonances) for different π_{bath}-pulse durations. At short π_{bath}-pulse durations (high MW powers), the linewidths are power broadened due to the applied microwave field, such that the measured linewidth is a convolution of the natural linewidth and the inverse duration of the π_{bath}-pulse [194]. At long π_{bath}-pulse durations, however, the measured linewidth approaches its natural (Lorentzian) linewidth $\Gamma = 1/\pi T^*_{2,N}$. At the longest π_{bath}-pulse durations used in this work, we find that group 1 consists of a narrow, approximately 25 kHz-wide peak. In contrast, group 5 reveals two peaks, consisting of two overlapped ^{14}N transitions and one detuned transition, which is attributed to imperfect magnetic field alignment. The splitting between the two peaks in group 5 ≈ 100 kHz, which we use as the effective ^{14}N linewidth Δ_N in Eqn. 4 of the main text, and which is consistent with the value extracted from fitting the spin-bath driving model to the data (see Fig. 5.4a, $\Delta_{N,fit} \approx 140$ kHz).

In Fig. C.4d we compare the measured NV and ^{14}N group 1 ensemble linewidths for Sample B as a function of π-pulse duration. For both species the linewidth narrows at long π-pulse durations, as discussed above, reaching non-power-broadened (natural) values. The natural NV linewidth is found to be significantly larger (13×) than the natural ^{14}N linewidth of 20.6(1.2) kHz. This order-of-magnitude difference is a manifestation of the strong strain field gradients in this sample: pulsed ESR measurements of the NV ensemble linewidth (see Fig. C.4a) are performed in the SQ

$\{0, +1\}$ or $\{0, -1\}$ sub-basis, and are therefore strain gradient limited. In contrast, nitrogen defects in diamond have $S = 1/2$, and thus do not couple to electric fields or strain gradients. As a consistency check, note that NV ensemble Ramsey measurements in Sample B, made in the DQ basis (with no spin-bath driving), yield a strain-independent dephasing time $T^*_{2,DQ} = 6.9(5)\,\mu$s. This dephasing time, presumably limited by the nitrogen spin bath, implies a ^{14}N spin resonance linewidth given by $\frac{1}{2} \times 1/\pi T^*_{2,DQ} = 23(2)\,$kHz, which is in reasonable agreement with our pulsed-DEER measurements of the natural ^{14}N linewidth. Similar consistency is found for measurements of the NV and ^{15}N ensemble spin resonance linewidths in Sample C, as shown in Fig. C.4e. Such agreement across multiple samples is further evidence that the DQ T_2^* value for NV ensembles is limited by the surrounding nitrogen spin bath, as discussed in the main text. Note that for our samples $[NV] \ll [N]$ and we can therefore ignore the back action of NVs onto nitrogen spins in the DEER readout. For denser NV samples, however, this back action has to be taken into account [204].

C.6 DC Magnetometry with DQ and Spin-Bath Drive

Assuming a signal-to-noise ratio of unity, the minimum detectable magnetic field δB_{min} in a Ramsey measurement is given by [86, 202]

$$\delta B_{min} \approx \frac{\delta S}{\max|\frac{\partial S}{\partial B}|}, \tag{C.12}$$

where the Ramsey signal S is

$$S = C\sin(\gamma_{NV} B_{DC} \tau). \tag{C.13}$$

Here, C is the measurement contrast defined via the NV spin-state-dependent fluorescence visibility (see Methods), γ_{NV} is the NV gyromagnetic ratio, B_{DC} is the magnetic field to be sensed, and τ is the sensing time during which the NV sensor spins accumulate phase. The term $\max|\frac{\partial S}{\partial B}|$ is the maximum slope of the Ramsey signal:

$$\max|\frac{\partial S}{\partial B}| = C\gamma_{NV}\tau. \tag{C.14}$$

Assuming uncorrelated, Gaussian noise, $\delta S = \sigma(t)/\sqrt{n_{meas}}$ is the standard error of the contrast signal, which improves with number of measurements n_{meas}. Including a dead time τ_D that accounts for time spent during initialization of the NV ensemble and readout of the spin-state-dependent fluorescence during a single measurement, $n_{meas} = T/(\tau + \tau_D)$ measurements are made over the total measurement time T. δB_{min} is then found to be

$$\delta B_{min} = \frac{\sigma\sqrt{\tau + \tau_D}}{C\gamma_{NV}\tau\sqrt{T}}, \tag{C.15}$$

and the sensitivity is given by multiplying δB_{min} by the bandwidth $\sqrt{T}$ and including a factor $\Delta m = 1(2)$ for the SQ (DQ) basis:

$$\eta = \frac{\delta B_{min}\sqrt{T}}{\Delta m} = \frac{\sigma\sqrt{\tau + \tau_D}}{\Delta m \times C\gamma_{NV}\tau}. \tag{C.16}$$

Note that in the ideal case, $\tau_D \ll \tau$, we have $\frac{\sqrt{\tau+\tau_D}}{\tau} \approx 1/\sqrt{\tau}$ and the sensitivity η scales $\propto \tau^{-1/2}$. The optimal sensing time in our Ramsey experiment is then $\tau_{opt} = T_2^*/2$. However, in the more realistic case, $t_D \sim \tau$, the improvement of η with increasing τ approaches a linear scaling and $\eta \propto \tau^{-1}$ for $t_D \gg \tau$. The optimal sensing time then becomes $\tau_{opt} \approx T_2^*$. Consequently, the measured increase in sensitivity may exceed the enhancement estimated from the idealized case without overhead time.

With Eqn. C.16 we calculate and compare the sensitivities for the three measurement modalities (SQ, DQ, and DQ + spin-bath drive) applied to Sample B. Using $C \approx 0.026$, which remains constant for the three schemes (see Fig.C.5a), sensing times $\tau_{SQ} = 1.308\,\mu s$, $\tau_{DQ} = 6.436\,\mu s$, and $\tau_{DQ+Drive} = 23.99\,\mu s$, standard deviations $\sigma_{SQ} = 0.0321$, $\sigma_{DQ} = 0.0324$, and $\sigma_{DQ+Drive} = 0.0325$ calculated from 1 s of data, fixed sequence duration of $\tau + \tau_D = 70\,\mu s$, and $\gamma_{NV} = 2\pi \times 28\,\mathrm{GHz/T}$, the estimated sensitivities for the SQ, DQ and DQ+Drive measurement schemes are $\eta = 70.7$, 6.65, and $1.97\,\mathrm{nT}/\sqrt{\mathrm{Hz}}$, respectively. In summary, we obtain an $10\times$ improvement in DC magnetic field sensitivity in the DQ basis, relative to the conventional SQ basis, and a $35\times$ improvement using the DQ basis with spin bath drive. Note that this enhancement greatly exceeds the expected improvement when no dead time is present ($\tau_D \ll \tau$) and is attributed to the approximately linear increase in sensitivity with sensing time τ. Lastly, we plot the Allan deviation for the three schemes in Fig. C.5b showing a $t^{-1/2}$ scaling for a measurement time of $\approx 1\,s$ and the indicated enhancements in sensitivity.

C.7 Detailed Sample Information

Table C.1: Detailed information for Samples A - E. Values with $\sim$ symbol are order-of-magnitude estimates. For all samples, $[NV] \ll [N]$ and NV contributions to T_2^* can be neglected ($1\,\mathrm{ppm} = 1.76 \times 10^{17}\,\mathrm{cm}^{-3}$).

Sample	[N] (ppm)	^{13}C (%)	[NV] (cm^{-3})	T_2^{meas} (µs)	$T_{2,SQ}^{*,meas}$ (µs)	$T_{2,DQ}^{*,meas}$ (µs)	$T_{2,NV-N}^{*,est}$ (µs)	$T_{2,NV-13C}^{*,est}$ (µs)	$T_{2,NV-(13C+N)}^{*,est}$ (µs)	dM_z^{meas}/dL (MHz/µm)
A	$\lesssim 0.05$	0.01	$\sim 3 \times 10^{12}$	$\gtrsim 630$	$5-12$	34	350	100	78	n/a
B	0.75	0.01	$\sim 10^{14}$	$250-300$	$1-10$	14	23	100	19	0.0028
C	10	0.05	$\sim 6 \times 10^{15}$	15-18	$0.3-1.2$	0.6	2	20	2	n/a
D	3	< 0.01	$\sim 5 \times 10^{15}$	53	0.4	1.3	6	100	> 6	n/a
E	48	1.1	$\sim 1 \times 10^{17}$	1.8	0.07	0.12	0.3	1	0.2	n/a

Table C.2: NV spin ensemble dephasing mechanisms for Sample A Individual contributions to dephasing are determined using the estimated/calibrated values described in the main text and Methods (column 2). The data show good agreement between calculated and measured total dephasing times $T^*_{2,SQ}$ and $T^*_{2,DQ}$ (last two rows).

Channel	Magnitude	Dephasing		Method
		$1/\mu$s	μs	
strain	0.0028 MHz/μm	0.190	5	estimate
^{14}N	0.05 ppm	0.0029	348	dipolar estimate
^{13}C	0.01%	0.01	100	calibration
B-field gradient @ 20 G	0.000056 MHz/G	0.00112	893	estimate
total SQ		0.2035	4.9	$5-12\,\mu$s (measured)
total DQ $\times 2$ (no strain)		0.014	71	68 μs (measured)

Table C.3: NV spin ensemble dephasing mechanisms for Sample B Similar to Sample A. Additionally, spin echo double-electron resonance (SEDOR) measurements were performed to estimate dephasing contributions from individual nitrogen resonance lines (for details see Ref. [127]).

Channel	Magnitude	Dephasing		Method
		$1/\mu s$	μs	
strain	0.0028 MHz/μm	0.190	5	estimate
^{14}N (allowed)		0.056	18	SEDOR
^{14}N (forbidden)		0.0047	214	SEDOR
^{13}C	0.01%	0.01	100	calibration
B-field gradient @ 85 G	0.000056 MHz/G	0.00474	210	estimate
total SQ		0.265	3.8	$1-10\,\mu s$ (measured)
total DQ ×2 (no strain)		0.076	13.1	13.8 μs (measured)

Table C.4: NV spin ensemble dephasing mechanisms for Sample C Similar to Sample A and B.

Channel	Magnitude	Dephasing		Method
		$1/\mu s$	μs	
strain	0.0028 MHz/μm	0.140	7	estimate
^{15}N (allowed)		0.59	2	SEDOR
^{15}N (forbidden)		0.15	7	SEDOR
^{14}N (5% of N15)		0.0391	26	estimated
^{13}C	0.05%	0.05	20	calibrated
B-field gradient @ 100 G	0.000022 MHz/G	0.0022	446	estimate
total SQ		1.01	1.0	$0.3 - 1.2\,\mu s$ (measured)
total DQ ×2 (no strain)		0.87	1.1	1.2 μs (measured)

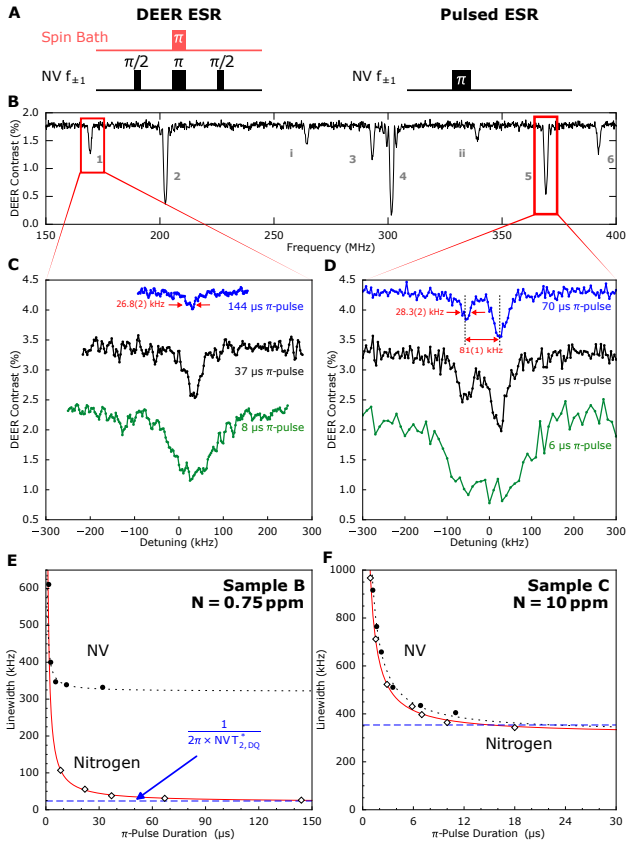

Figure C.4: Comparison of nitrogen and NV spin resonance linewidths. (a) Pulsed DEER (left) and pulsed ESR sequence (right) used for spin resonance measurements of the nitrogen and NV spins, respectively. (b) DEER spectrum including all six nitrogen transitions and two forbidden transitions in Sample B. (c) DEER spectra of a single nitrogen transition are shown for three different bath π-pulse durations. A minimum measured linewidth of 26.8(2) kHz was recorded using a 144 μs π-pulse. (d) DEER spectra for a group containing three nearly degenerate off-axis nitrogen transitions. When bath π-pulses of 70 μs and 35 μs are used, two features are resolved corresponding to a single nitrogen transition detuned by 81 kHz from two nearly overlapped transitions. (e) Comparison of the NV ESR linewidth (black dots) and the DEER linewidth for a single nitrogen transition (diamonds) as a function of π-pulse duration for Sample B ([N] = 0.75 ppm). The fine, black dashed line and red solid lines correspond to fits of the NV and nitrogen spin resonance linewidths to the functional form $a/x + b$, where b is the saturation linewidth. The coarse, blue dashed line indicates the expected linewidth from the measured NV T_2^* in the DQ basis (assuming a Lorentzian linewidth). (f) Same as (e) but for Sample C ([N] = 10 ppm).

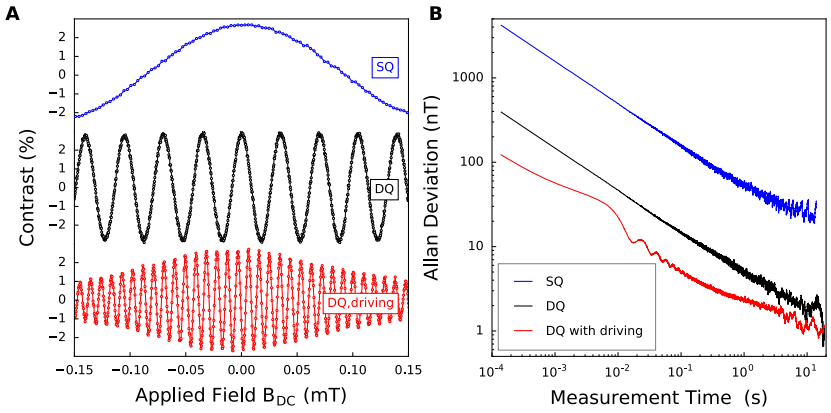

Figure C.5: DC magnetic field sensing and Allan deviation. (a) DC magnetometry curves for SQ, DQ, and DQ with spin-bath driving in Sample B, produced by sweeping the magnitude of a coil-generated applied magnetic field (in addition to the fixed bias field) while the free precession interval τ is set to $\tau_{SQ} = 1.308\,\mu$s (blue, top), $\tau_{DQ} = 6.436\,\mu$s (black, middle), and $\tau_{DQ,drive} = 23.990\,\mu s$ (red, bottom). (b) Allan deviation using the same fixed τ values from (a) for measurements using SQ (blue), DQ (black), and DQ with driving (red). The external field strength was tuned to sit on a zero crossing of the respective DC magnetometry curves in (a) for sine magnetometry.

Appendix D

Quantum Coherence of Solid-State NV center spins in Diamond - Supplement

D.1 Experimental Setup

All measurement were performed with either a wide-field or confocal microscope. In the wide-field microscope, the spin-dependent NV ensemble fluorescence was collected onto an avalanche photodiode (Hamamatsu C10508-01). Optical initialization and readout of the NV ensemble were accomplished via 532 nm continuous-wave (CW) laser light (Coherent Verdi G) focused through the same objective (Nikon CFI Plan Apo 20x/0.75 WD 1.5 Air) used for fluorescence collection. For pulsed operation, the laser light was modulated using an acousto-optic modulator (Isomet M1133-aQ80L).

The detection volume was given by the 532 nm beam excitation at the surface

(diameter $\approx 20\,\mu m$) and sample thickness. The static magnetic bias field applied to split the $|-1\rangle$ and $|+1\rangle$ degeneracy in the NV ground state was provided using two permanent samarium cobalt ring magnets in a Helmholtz-type configuration. The generated field was aligned along one [111] crystallographic axis of the diamond ($\equiv \hat{z}$) to single out one of the single quantum NV transitions. Microwaves (MW) in the $2-3.5\,GHz$ were applied via a planar waveguide fabricated onto a glass substrate and sourced from a SynthHD 54 MHz - 13.6 GHz microwave generator (Windfreak Technologies). The pulsed Hahn echo and CPMG measurements on the NV were performed using a computer-controlled pulse generator (Pulseblaster ESR PRO 500) and microwave switches (Minicircuit ZASWA-2-50DR+). Phase control for individual MW pulses was provided using a double-balanced IQ mixer (Marki IQ-1545).

Confocal measurements were based on a standard NV-diamond confocal setup. Here, a Gaussian laser beam at 532 nm (Coherent Compass 315ML) was used to initialize and readout the NV centers. The fluorescence was collected via a high NA objective (Nikon CFI PLAN APO LAMBDA 100X OIL) onto a single-photon counting APD (Perkin Elmer). Microwaves were similarly applied as in the wide-field case using a SynthNV 34 MHz - 4.4 GHz RF signal generator source (Windfreak Technologies). Magnetic fields were applied from a half-inch neodymium cylinder magnet using an automated magnetic field alignment procedure (see Suppl. **[VanderSar2015]**) and provided magnetic field alignment angles $< 3°$.

D.2 CPMG-n $T_{2,N}$ Scaling

When the bath noise possesses a Lorentzian spectral density, $\lambda_{\text{eff}} = 2/3$ and $T_{2,n}$ extends sublinearly with the number of decoupling pulses n[49, 197, 201, 235]. In Fig. D.1 we summarize the λ_{eff}-values extracted for the subset of samples, when fitting the CPMG data to the functional form

$$T_{2,n} = T_{2,\text{echo}} \cdot n^{\lambda_{\text{eff}}}. \tag{D.1}$$

The plot indicates an increase in λ_{eff} with increasing nitrogen density and λ_{eff} approaches the theoretical value of 2/3 when [N] $\gtrsim 100\,\text{ppm}$. At lower nitrogen concentrations ([N] $\ll 100\,\text{ppm}$), however, λ_{eff} decreases with decreases [N]. We attribute the observed trend and deviation from the theoretical value of 2/3 to the increasing contribution of spin-lattice relaxation T_1 at low nitrogen concentrations. Since in low [N] samples with high initial $T_{2,echo}$ spin-relaxation becomes a relevant decoherence mechanism, CPMG is rendered less efficient and the enhancement of $T_{2,n}$ over $T_{2,echo}$ for increasing pulse numbers n remains small ($\lambda_{eff} \to 0$). In this instance, the coherence time obtained through CPMG is also limited by spin-lattice relaxation and Eqn. D.1 is to be modified yielding

$$T_{2,n} = 1/(T_{2,\text{echo}} \cdot n^{\lambda_{\text{eff}}}) + 1/T_{2,max})^{-1}, \tag{D.2}$$

which was given in the main text.

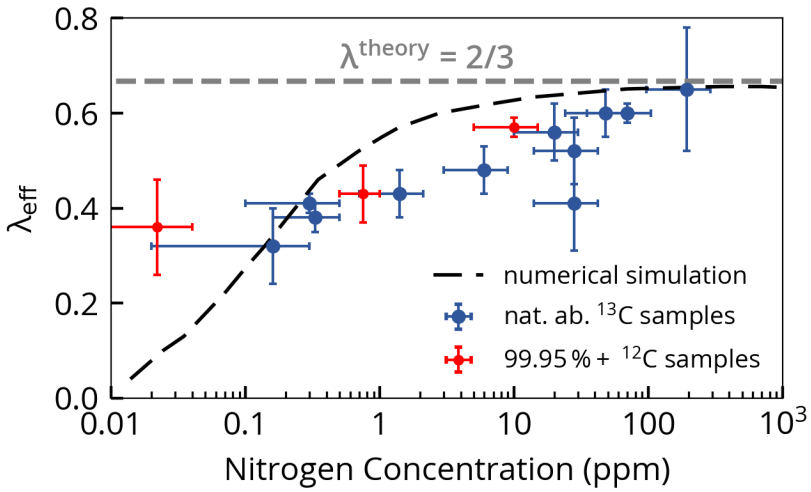

Figure D.1: Effective decoupling parameter λ_{eff} as a function of nitrogen concentration extracted from Eqn. D.2 fitted to the CPMG $T_{2,n}$ data. In the high nitrogen limit, for which $T_{2,echo} \ll T_1$, λ_{eff} approaches the theoretical value of 2/3.

D.3 Forward Fitting Routine

To extract Δ_{ens} and $\tau_{\text{c,ens}}$ depicted in Fig. 6.3 of the main text, we employ a forward-fitting routine that only relies on $T_{2,n}$ obtained through CPMG measurements (see Fig. 6.3a). In this routine, we numerically minimize the functional

$$\sum_n \| \left[T_{2,n}^{\text{meas}} - T_{2,n}(\Delta_{\text{ens}}, \tau_{\text{c,ens}}, T_{2,\text{max}}) \right] \|$$

and extract Δ_{ens}, $\tau_{\text{c,ens}}$ and $T_{2,\text{max}}$, where $T_{2,n}^{\text{meas}}$ is the experimentally determined coherence time for a given n (see Fig. 6.3a) and $T_{2,n}(\Delta_{\text{ens}}, \tau_{\text{c,ens}}, T_{2,\text{max}})$ is the calculated value for a spin bath with Lorentzian spectral density using Eqn. 2.10. Results for the [N] = 0.2, 6, and 80 ppm sample are shown in Fig. D.1. There is generally good agreement with the best-guess forward-fit (black, dashes line) and the experimental data. The fit of to Eqn. D.2 to the data (red, solid line) is shown for reference as well.

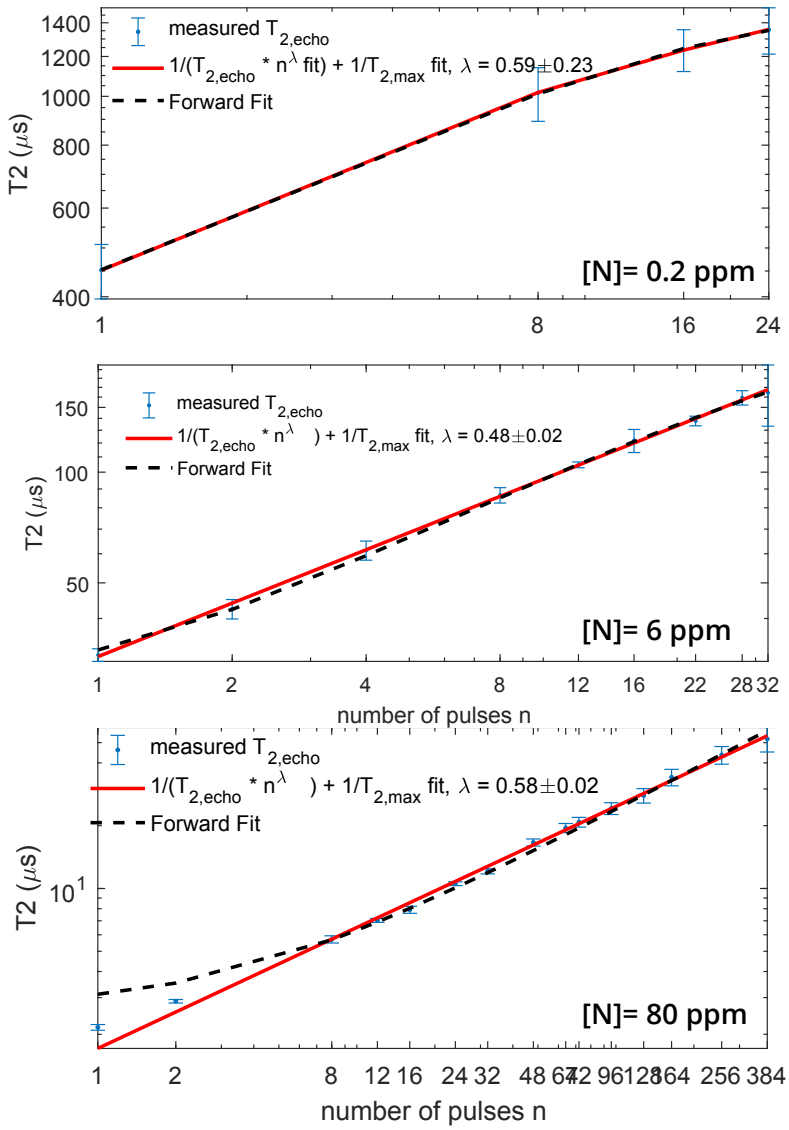

Figure D.2: $T_{2,n}$ data for the [N] = 0.2, 6, and 80 ppm sample. Red line is a fit to Eqn. D.2 from which λ_{eff} is extracted. Black, dashed line is best-guess from the forward-fitting routine (see text) from which Δ_{ens}, $\tau_{\text{c,ens}}$ and $T_{2,\text{max}}$ are extracted.

Bibliography

[1]G. Feher, and E. A. Gere, "Electron Spin Resonance Experiments on Donors in Silicon. II. Electron Spin Relaxation Effects", Physical Review **114**, 1245–1256 (1959) 10.1103/PhysRev.114.1245.

[2]W. M. Witzel, M. S. Carroll, A. Morello,. Cywiński, and S. Das Sarma, "Electron Spin Decoherence in Isotope-Enriched Silicon", Physical Review Letters **105**, 187602 (2010) 10.1103/PhysRevLett.105.187602.

[3]E. Abe, A. M. Tyryshkin, S. Tojo, J. J. L. Morton, W. M. Witzel, A. Fujimoto, J. W. Ager, E. E. Haller, J. Isoya, S. A. Lyon, M. L. W. Thewalt, and K. M. Itoh, "Electron spin coherence of phosphorus donors in silicon: Effect of environmental nuclei", Physical Review B **82**, 121201 (2010) 10.1103/PhysRevB.82.121201.

[4]A. M. Tyryshkin, S. Tojo, J. J. L. Morton, H. Riemann, N. V. Abrosimov, P. Becker, H.-J. Pohl, T. Schenkel, M. L. W. Thewalt, K. M. Itoh, and S. a. Lyon, "Electron spin coherence exceeding seconds in high-purity silicon", Nature Materials **11**, 143–147 (2011) 10.1038/nmat3182.

[5]W. V. Smith, P. P. Sorokin, I. L. Gelles, and G. J. Lasher, "Electron-spin resonance of nitrogen donors in diamond", Physical Review **115**, 1546–1552 (1959) 10.1103/PhysRev.115.1546.

[6]R. J. Cook, and D. H. Whiffen, "Electron Nuclear Double Resonance Study of a Nitrogen Centre in Diamond", Proceedings of the Royal Society A: Mathematical, Physical and Engineering Sciences **295**, 99–106 (1966) 10.1098/rspa.1966.0228.

[7]J. H. N. Loubser, and J. A. v. Wyk, "Electron spin resonance in the study of diamond", Reports on Progress in Physics **41**, 1201–1248 (1978) 10.1088/0034-4885/41/8/002.

[8]C. A. J. Ammerlaan, and E. A. Burgemeister, "Reorientation of Nitrogen in Type-Ib Diamond by Thermal Excitation and Tunneling", Physical Review Letters **47**, 954–957 (1981) 10.1103/PhysRevLett.47.954.

[9]G. Davies, "The Jahn-Teller effect and vibronic coupling at deep levels in diamond", Reports on Progress in Physics **44**, 787–830 (1981) 10.1088/0034-4885/44/7/003.

[10]A Cox, M. E. Newton, and J. M. Baker, "13 C, 14 N and 15 N ENDOR measurements on the single substitutional nitrogen centre (P1) in diamond", Journal of Physics: Condensed Matter **6**, 551–563 (1994) 10.1088/0953-8984/6/2/025.

[11]C. Hepp, T. Müller, V. Waselowski, J. N. Becker, B. Pingault, H. Sternschulte, D. Steinmüller-Nethl, A. Gali, J. R. Maze, M. Atatüre, and C. Becher, "Electronic structure of the silicon vacancy color center in diamond", Physical Review Letters **112**, 1–5 (2014) 10.1103/PhysRevLett.112.036405.

[12]J. N. Becker, J. Görlitz, C. Arend, M. Markham, and C. Becher, "Ultrafast, all-optical coherent control of single silicon vacancy colour centres in diamond", **2**, 1–6 (2016) 10.1038/ncomms13512.

[13]A. Sipahigil, R. E. Evans, D. D. Sukachev, M. J. Burek, J. Borregaard, M. K. Bhaskar, C. T. Nguyen, J. L. Pacheco, H. A. Atikian, C. Meuwly, R. M. Camacho, F. Jelezko, E. Bielejec, H. Park, M. Lončar, and M. D. Lukin, "An integrated diamond nanophotonics platform for quantum-optical networks", Science **354**, 847–850 (2016) 10.1126/science.aah6875.

[14]B. C. Rose, D. Huang, Z.-h. Zhang, A. M. Tyryshkin, S. Sangtawesin, S. Srinivasan, L. Loudin, M. L. Markham, A. M. Edmonds, D. J. Twitchen, S. A. Lyon, and N. P. de Leon, "Observation of an environmentally insensitive solid state spin defect in diamond", arXiv preprint **03** (2017).

[15]P. V. Klimov, A. L. Falk, D. J. Christle, V. V. Dobrovitski, and D. D. Awschalom, "Quantum entanglement at ambient conditions in a macroscopic solid-state spin ensemble", Science Advances **1**, e1501015–e1501015 (2015) 10.1126/sciadv.1501015.

[16]M. Widmann, S.-Y. Lee, T. Rendler, N. T. Son, H. Fedder, S. Paik, L.-P. Yang, N. Zhao, S. Yang, I. Booker, A. Denisenko, M. Jamali, S. A. Momenzadeh, I. Gerhardt, T. Ohshima, A. Gali, E. Janzén, and J. Wrachtrup, "Coherent control of single spins in silicon carbide at room temperature", Nature Materials **14**, 164–168 (2014) 10.1038/nmat4145.

[17]F. J. Heremans, C. G. Yale, and D. D. Awschalom, "Control of Spin Defects in Wide-Bandgap Semiconductors for Quantum Technologies", Proceedings of the IEEE **104**, 2009–2023 (2016) 10.1109/JPROC.2016.2561274.

[18]W. F. Koehl, B. Diler, S. J. Whiteley, A. Bourassa, N. T. Son, E. Janzén, and D. D. Awschalom, "Resonant optical spectroscopy and coherent control of Cr4+ spin ensembles in SiC and GaN", Physical Review B **95**, 035207 (2017) 10.1103/PhysRevB.95.035207.

[19]S. A. Tarasenko, A. V. Poshakinskiy, D Simin, V. A. Soltamov, E. N. Mokhov, P. G. Baranov, V. Dyakonov, and G. V. Astakhov, "Spin and Optical Properties of Silicon Vacancies in Silicon Carbide A Review", physica status solidi (b) **255**, 1700258 (2018) 10.1002/pssb.201700258.

[20]D. J. Christle, P. V. Klimov, C. F. de las Casas, K. Szász, V. Ivády, V. Jokubavicius, J. Ul Hassan, M. Syväjärvi, W. F. Koehl, T. Ohshima, N. T. Son, E. Janzén,. Gali, and D. D. Awschalom, "Isolated Spin Qubits in SiC with a High-Fidelity Infrared Spin-to-Photon Interface", Physical Review X **7**, 021046 (2017) 10.1103/PhysRevX.7.021046.

[21]H. Seo, A. L. Falk, P. V. Klimov, K. C. Miao, G. Galli, and D. D. Awschalom, "Quantum decoherence dynamics of divacancy spins in silicon carbide", Nature Communications **7**, 12935 (2016) 10.1038/ncomms12935.

[22]K. Benzid, a. Chetoui, M. Maamache, P. Turek, and J. Tribollet, "Intrinsic decoherence and Rabi oscillation damping of Mn 2+ and Co 2+ electron spin qubits in bulk ZnO", Epl **104**, 47005 (2013) 10.1209/0295-5075/104/47005.

[23]R. E. George, J. P. Edwards, and A. Ardavan, "Coherent spin control by electrical manipulation of the magnetic anisotropy", Physical Review Letters **110**, 1–5 (2013) 10.1103/PhysRevLett.110.027601.

[24]F. P. Bundy, H. T. Hall, H. M. Strong, and R. H. Wentorf, "Man-Made Diamonds", Nature **176**, 51–55 (1955) 10.1038/176051a0.

[25]L. du Preez, "Electron paramagnetic resonance and optical investigations of defect centres in diamond", PhD thesis (University of the Witwatersrand, Johannesburg, 1965).

[26]C. D. Clark, and C. A. Norris, "Photoluminescence associated with the 1.673, 1.944 and 2.498 eV centres in diamond", Journal of Physics C: Solid State Physics **4**, 2223–2229 (1971) 10.1088/0022-3719/4/14/036.

[27]G Davies, "Vibronic spectra in diamond", Journal of Physics C: Solid State Physics **7**, 3797–3809 (1974) 10.1088/0022-3719/7/20/019.

[28]G. Davies, and M. F. Hamer, "Optical Studies of the 1.945 eV Vibronic Band in Diamond", Proceedings of the Royal Society A: Mathematical, Physical and Engineering Sciences **348**, 285–298 (1976) 10.1098/rspa.1976.0039.

[29]G. Davies, "Charge states of the vacancy in diamond", Nature **269**, 498–500 (1977) 10.1038/269498a0.

[30]J. Loubser, and J. Van Wyk, "Optical spin-polarisation in a triplet state in irradiated and annealed type 1b diamonds", Diamond Research, 11–14 (1977).

[31]A. T. Collins, M. F. Thomaz, and M. I. B. Jorge, "Luminescence decay time of the 1.945 eV centre in type Ib diamond", Journal of Physics C: Solid State Physics **16**, 2177–2181 (1983) 10.1088/0022-3719/16/11/020.

[32]R. T. Harley, M. J. Henderson, and R. M. Macfarlane, "Persistent spectral hole burning of colour centres in diamond", Journal of Physics C: Solid State Physics **17**, L233–L236 (1984) 10.1088/0022-3719/17/8/002.

[33]N. R. S. Reddy, N. B. Manson, and E. R. Krausz, "Two-laser spectral hole burning in a colour centre in diamond", Journal of Luminescence **38**, 46–47 (1987) 10.1016/0022-2313(87)90057-3.

[34]E. v. Oort, N. B. Manson, and M Glasbeek, "Optically detected spin coherence of the diamond N-V centre in its triplet ground state", Journal of Physics C: Solid State Physics **21**, 4385–4391 (1988) 10.1088/0022-3719/21/23/020.

[35]A. Gruber, A. Dräbenstedt, C. Tietz, L. Fleury, J. Wrachtrup, and C. v. Borczyskowski, "Scanning Confocal Optical Microscopy and Magnetic Resonance on Single Defect Centers", Science **276**, 2012–2014 (1997) 10.1126/science.276.5321.2012.

[36]A. Dräbenstedt, L. Fleury, C. Tietz, F. Jelezko, S. Kilin, A. Nizovtzev, and J. Wrachtrup, "Low-temperature microscopy and spectroscopy on single defect centers in diamond", Physical Review B **60**, 11503–11508 (1999) 10.1103/PhysRevB.60.11503.

[37]R. Brouri, A. Beveratos, J.-P. Poizat, and P. Grangier, "Photon antibunching in the fluorescence of individual color centers in diamond", Optics Letters **25**, 1294 (2000) 10.1364/OL.25.001294.

[38]J Wrachtrup, S. Y. Kilin, and A. P. Nizovtsev, "Quantum computation using the 13C nuclear spins near the single NV defect center in diamond", Optics and Spectroscopy **91**, 429–437 (2001) 10.1134/1.1405224.

[39]T. A. Kennedy, J. S. Colton, J. E. Butler, R. C. Linares, and P. J. Doering, "Long coherence times at 300 K for nitrogen-vacancy center spins in diamond grown by chemical vapor deposition", Applied Physics Letters **83**, 4190–4192 (2003) 10.1063/1.1626791.

[40]F. Jelezko, T. Gaebel, I. Popa, A. Gruber, and J. Wrachtrup, "Observation of Coherent Oscillations in a Single Electron Spin", Physical Review Letters **92**, 076401 (2004) 10.1103/PhysRevLett.92.076401.

[41]J. M. Taylor, P. Cappellaro, L. Childress, L. Jiang, D. Budker, P. R. Hemmer, A. Yacoby, R. Walsworth, and M. D. Lukin, "High-sensitivity diamond magnetometer with nanoscale resolution", Nature Physics **4**, 810–816 (2008) 10.1038/nphys1075.

[42]N. Y. Yao, L Jiang, A. V. Gorshkov, P. C. Maurer, G Giedke, J. I. Cirac, and M. D. Lukin, "Scalable architecture for a room temperature solid-state quantum information processor.", Nature communications **3**, 800 (2012) 10.1038/ncomms1788.

[43]J. Cai, A. Retzker, F. Jelezko, and M. B. Plenio, "A large-scale quantum simulator on a diamond surface at room temperature", Nature Physics **9**, 168–173 (2013) 10.1038/nphys2519.

[44]Y. Wang, F. Dolde, J. Biamonte, R. Babbush, V. Bergholm, S. Yang, I. Jakobi, P. Neumann, A. Aspuru-Guzik, J. D. Whitfield, and J. Wrachtrup, "Quantum Simulation of Helium Hydride Cation in a Solid-State Spin Register", ACS Nano **9**, 7769–7774 (2015) 10.1021/acsnano.5b01651.

[45]M. Doherty, C. Meriles, A. Alkauskas, H. Fedder, M. Sellars, and N. Manson, "Towards a Room-Temperature Spin Quantum Bus in Diamond via Electron Photoionization, Transport, and Capture", Physical Review X **6**, 041035 (2016) 10.1103/PhysRevX.6.041035.

[46]M. V. G. Dutt, L Childress, L Jiang, E Togan, J Maze, F Jelezko, A. S. Zibrov, P. R. Hemmer, and M. D. Lukin, "Quantum register based on individual electronic and nuclear spin qubits in diamond.", Science (New York, N.Y.) **316**, 1312–6 (2007) 10.1126/science.1139831.

[47]L Jiang, J. S. Hodges, J. R. Maze, P Maurer, J. M. Taylor, D. G. Cory, P. R. Hemmer, R. L. Walsworth, A Yacoby, A. S. Zibrov, and M. D. Lukin, "Repetitive Readout of a Single Electronic Spin via Quantum Logic with Nuclear Spin Ancillae", Science **326**, 267–272 (2009) 10.1126/science.1176496.

[48]C. A. Ryan, J. S. Hodges, and D. G. Cory, "Robust Decoupling Techniques to Extend Quantum Coherence in Diamond", Physical Review Letters **105**, 200402 (2010) 10.1103/PhysRevLett.105.200402.

[49]G de Lange, Z. H. Wang, D. Riste, V. V. Dobrovitski, and R Hanson, "Universal Dynamical Decoupling of a Single Solid-State Spin from a Spin Bath", Science **330**, 60–63 (2010) 10.1126/science.1192739.

[50]P. C. Maurer, J. R. Maze, P. L. Stanwix, L. Jiang, a. V. Gorshkov, a. a. Zibrov, B. Harke, J. S. Hodges, a. S. Zibrov, A. Yacoby, D. Twitchen, S. W. Hell, R. L. Walsworth, and M. D. Lukin, "Far-field optical imaging and manipulation of individual spins with nanoscale resolution", Nature Physics **6**, 912–918 (2010) 10.1038/nphys1774.

[51]P. Neumann, J. Beck, M. Steiner, F. Rempp, H. Fedder, P. R. Hemmer, J. Wrachtrup, and F. Jelezko, "Single-Shot Readout of a Single Nuclear Spin", Science **329**, 542–544 (2010) 10.1126/science.1189075.

[52]P. C. Maurer, G. Kucsko, C. Latta, L. Jiang, N. Y. Yao, S. D. Bennett, F. Pastawski, D. Hunger, N. Chisholm, M. Markham, D. J. Twitchen, J. I. Cirac, and M. D. Lukin, "Room-Temperature Quantum Bit Memory Exceeding One Second", Science **336**, 1283–1286 (2012) 10.1126/science.1220513.

[53]N Bar-Gill, L. M. Pham, A Jarmola, D Budker, and R. L. Walsworth, "Solid-state electronic spin coherence time approaching one second.", Nature communications **4**, 1743 (2013) 10.1038/ncomms2771.

[54]F. Dolde, I. Jakobi, B. Naydenov, N. Zhao, S. Pezzagna, C. Trautmann, J. Meijer, P. Neumann, F. Jelezko, and J. Wrachtrup, "Room-temperature entanglement between single defect spins in diamond", Nature Physics **9**, 139–143 (2013) 10.1038/nphys2545.

[55]H. Bernien, B. Hensen, W. Pfaff, G. Koolstra, M. S. Blok, L. Robledo, T. H. Taminiau, M. Markham, D. J. Twitchen, L. Childress, and R. Hanson, "Heralded entanglement between solid-state qubits separated by three metres", Nature **497**, 86–90 (2013) 10.1038/nature12016.

[56]B. Hensen, H. Bernien, A. E. Dréau, A. Reiserer, N. Kalb, M. S. Blok, J. Ruitenberg, R. F. L. Vermeulen, R. N. Schouten, C. Abellán, W. Amaya, V. Pruneri, M. W. Mitchell, M. Markham, D. J. Twitchen, D. Elkouss, S. Wehner, T. H. Taminiau, and R. Hanson, "Loophole-free Bell inequality violation using electron spins separated by 1.3 kilometres", Nature **526**, 682–686 (2015) 10.1038/nature15759.

[57]D. Maclaurin, M. W. Doherty, L. C. L. Hollenberg, and A. M. Martin, "Measurable Quantum Geometric Phase from a Rotating Single Spin", Physical Review Letters **108**, 240403 (2012) 10.1103/PhysRevLett.108.240403.

[58]C. G. Yale, F. J. Heremans, B. B. Zhou, A. Auer, G. Burkard, and D. D. Awschalom, "Optical manipulation of the Berry phase in a solid-state spin qubit", Nature Photonics **10**, 184–189 (2016) 10.1038/nphoton.2015.278.

[59]S. Choi, J. Choi, R. Landig, G. Kucsko, H. Zhou, J. Isoya, F. Jelezko, S. Onoda, H. Sumiya, V. Khemani, C. von Keyserlingk, N. Y. Yao, E. Demler, and M. D. Lukin, "Observation of discrete time-crystalline order in a disordered dipolar many-body system", Nature **543**, 221–225 (2017) 10.1038/nature21426.

[60]W. B. Wang, X. Y. Chang, F Wang, P. Y. Hou, Y. Y. Huang, W. G. Zhang, X. L. Ouyang, X. Z. Huang, Z. Y. Zhang, L He, and L. M. Duan, "Realization of quantum Maxwell's demon with solid-state spins", arXiv preprint (2017).

[61]J. Klatzow, C. Weinzetl, P. M. Ledingham, J. N. Becker, D. J. Saunders, J. Nunn, I. A. Walmsley, R. Uzdin, and E. Poem, "Experimental demonstration of quantum effects in the operation of microscopic heat engines", arXiv preprint, 1–24 (2017).

[62]J. Hoffmann, C. Spee, O. Gühne, and C. Budroni, "Structure of temporal correlations of a qubit", arXiv preprint (2017).

[63]I. Gross, W. Akhtar, V. Garcia, L. J. Martínez, S. Chouaieb, K. Garcia, C. Carrétéro, A. Barthélémy, P. Appel, P. Maletinsky, J.-V. Kim, J. Y. Chauleau, N. Jaouen, M. Viret, M. Bibes, S. Fusil, and V. Jacques, "Real-space imaging of non-collinear antiferromagnetic order with a single-spin magnetometer", Nature **549**, 252–256 (2017) 10.1038/nature23656.

[64]P. Andrich, C. F.d. l. Casas, X. Liu, H. L. Bretscher, J. R. Berman, F. J. Heremans, P. F. Nealey, and D. D. Awschalom, "Hybrid nanodiamond-YIG systems for efficient quantum information processing and nanoscale sensing", 1–7 (2017).

[65]F. Casola, T. van der Sar, and A. Yacoby, "Probing condensed matter physics with magnetometry based on nitrogen-vacancy centres in diamond", Nature Reviews Materials **3**, 17088 (2018) 10.1038/natrevmats.2017.88.

[66]Y. Kubo, C. Grezes, A. Dewes, T. Umeda, J. Isoya, H. Sumiya, N. Morishita, H. Abe, S. Onoda, T. Ohshima, V. Jacques, A. Dréau, J. F. Roch, I. Diniz, A. Auffeves, D. Vion, D. Esteve, and P. Bertet, "Hybrid quantum circuit with a superconducting qubit coupled to a spin ensemble", Physical Review Letters **107** (2011) 10.1103/PhysRevLett.107.220501.

[67]I. Diniz, S. Portolan, R. Ferreira, J. M. Gérard, P. Bertet, and A. Auffèves, "Strongly coupling a cavity to inhomogeneous ensembles of emitters: Potential for long-lived solid-state quantum memories", Physical Review A - Atomic, Molecular, and Optical Physics **84**, 1–9 (2011) 10.1103/PhysRevA.84.063810.

[68]R. Amsüss, C. Koller, T. Nöbauer, S. Putz, S. Rotter, K. Sandner, S. Schneider, M. Schramböck, G. Steinhauser, H. Ritsch, J. Schmiedmayer, and J. Majer, "Cavity QED with magnetically coupled collective spin states", Physical Review Letters **107**, 1–5 (2011) 10.1103/PhysRevLett.107.060502.

[69]K. Sandner, H. Ritsch, R. Amsüss, C. Koller, T. Nöbauer, S. Putz, J. Schmiedmayer, and J. Majer, "Strong magnetic coupling of an inhomogeneous nitrogen-vacancy ensemble to a cavity", Physical Review A - Atomic, Molecular, and Optical Physics **85**, 1–10 (2012) 10.1103/PhysRevA.85.053806.

[70]D. O. Krimer, S. Putz, J. Majer, and S. Rotter, "Non-Markovian dynamics of a single-mode cavity strongly coupled to an inhomogeneously broadened spin ensemble", Physical Review A - Atomic, Molecular, and Optical Physics **90**, 1–14 (2014) 10.1103/PhysRevA.90.043852.

[71]C. Grezes, B. Julsgaard, Y. Kubo, W. L. Ma, M. Stern, A. Bienfait, K. Nakamura, J. Isoya, S. Onoda, T. Ohshima, V. Jacques, D. Vion, D. Esteve, R. B. Liu, K. Mølmer, and P. Bertet, "Storage and retrieval of microwave fields at the single-photon level in a spin ensemble", Physical Review A **92**, 020301 (2015) 10.1103/PhysRevA.92.020301.

[72]A. O. Sushkov, I. Lovchinsky, N. Chisholm, R. L. Walsworth, H. Park, and M. D. Lukin, "Magnetic Resonance Detection of Individual Proton Spins Using Quantum Reporters", Physical Review Letters **113**, 197601 (2014) 10.1103/PhysRevLett.113.197601.

[73]A. O. Sushkov, N Chisholm, I Lovchinsky, M Kubo, P. K. Lo, S. D. Bennett, D Hunger, A Akimov, R. L. Walsworth, H Park, and M. D. Lukin, "All-Optical Sensing of a Single-Molecule Electron Spin", Nano Letters **14**, 6443–6448 (2014) 10.1021/nl502988n.

[74]F. Shi, Q. Zhang, P. Wang, H. Sun, J. Wang, X. Rong, M. Chen, C. Ju, F. Reinhard, H. Chen, J. Wrachtrup, J. Wang, and J. Du, "Protein imaging. Single-protein spin resonance spectroscopy under ambient conditions.", Science (New York, N.Y.) **347**, 1135–8 (2015) 10.1126/science.aaa2253.

[75]S. J. DeVience, L. M. Pham, I Lovchinsky, A. O. Sushkov, N Bar-Gill, C Belthangady, F Casola, M Corbett, H Zhang, M Lukin, H Park, A Yacoby, and R. L. Walsworth, "Nanoscale NMR spectroscopy and imaging of multiple nuclear species", Nat Nanotechnol **10**, 129–134 (2015) 10.1038/nnano.2014.313.

[76]T. Häberle, T. Oeckinghaus, D. Schmid-Lorch, M. Pfender, F. F. de Oliveira, S. A. Momenzadeh, A. Finkler, and J. Wrachtrup, "Nuclear quantum-assisted magnetometer", Review of Scientific Instruments **88**, 013702 (2017) 10.1063/1.4973449.

[77]I Lovchinsky, A. O. Sushkov, E Urbach, N. P. de Leon, S Choi, K De Greve, R Evans, R Gertner, E Bersin, C Müller, L McGuinness, F Jelezko, R. L. Walsworth, H Park, and M. D. Lukin, "Nuclear magnetic resonance detection and spectroscopy of single proteins using quantum logic", Science (New York, N.Y.) **351**, 836–841 (2016) 10.1126/science.aad8022.

[78]N. Aslam, M. Pfender, P. Neumann, R. Reuter, A. Zappe, F. Fávaro de Oliveira, A. Denisenko, H. Sumiya, S. Onoda, J. Isoya, and J. Wrachtrup, "Nanoscale nuclear magnetic resonance with chemical resolution.", Science (New York, N.Y.) **357**, 67–71 (2017) 10.1126/science.aam8697.

[79]D. B. Bucher, D. R. Glenn, J. Lee, M. D. Lukin, H. Park, and R. L. Walsworth, "High Resolution Magnetic Resonance Spectroscopy Using Solid-State Spins", arXiv preprint 1705.08887 (2017).

[80]D Le Sage, K Arai, D. R. Glenn, S. J. DeVience, L. M. Pham, L Rahn-Lee, M. D. Lukin, A Yacoby, A Komeili, and R. L. Walsworth, "Optical magnetic imaging of living cells", Nature **496**, 486–489 (2013) 10.1038/nature12072.

[81]G Kucsko, P. C. Maurer, N. Y. Yao, M Kubo, H. J. Noh, P. K. Lo, H Park, and M. D. Lukin, "Nanometre-scale thermometry in a living cell.", Nature **500**, 54–8 (2013) 10.1038/nature12373.

[82]D. R. Glenn, K. Lee, H. Park, R. Weissleder, A. Yacoby, M. D. Lukin, H. Lee, R. L. Walsworth, and C. B. Connolly, "Single-cell magnetic imaging using a quantum diamond microscope", Nature Methods **12**, 736–738 (2015) 10.1038/nmeth.3449.

[83]J. F. Barry, M. J. Turner, J. M. Schloss, D. R. Glenn, Y. Song, M. D. Lukin, H. Park, and R. L. Walsworth, "Optical magnetic detection of single-neuron action potentials using quantum defects in diamond", Proceedings of the National Academy of Sciences, 201601513 (2016) 10.1073/pnas.1601513113.

[84]D. Le Sage, L. M. Pham, N. Bar-Gill, C. Belthangady, M. D. Lukin, A. Yacoby, and R. L. Walsworth, "Efficient photon detection from color centers in a diamond optical waveguide", Physical Review B **85**, 121202 (2012) 10.1103/PhysRevB.85.121202.

[85]T. Wolf, P. Neumann, K. Nakamura, H. Sumiya, T. Ohshima, J. Isoya, and J. Wrachtrup, "Subpicotesla diamond magnetometry", Physical Review X **5**, 1–10 (2015) 10.1103/PhysRevX.5.041001.

[86]J. F. Barry, J. M. Schloss, M. J. Turner, E. Bauch, C. A. Hart, and R. L. Walsworth, "Optimizing NV ensemble magnetometer sensitivity", manuscript in preparation (2017).

[87]G. Chatzidrosos, A. Wickenbrock, L. Bougas, N. Leefer, T. Wu, K. Jensen, Y. Dumeige, and D. Budker, "Miniature Cavity-Enhanced Diamond Magnetometer", Physical Review Applied **8**, 044019 (2017) 10.1103/PhysRevApplied.8.044019.

[88]D. F. Jackson Kimball, A. O. Sushkov, and D. Budker, "Precessing Ferromagnetic Needle Magnetometer", Physical Review Letters **116**, 190801 (2016) 10.1103/PhysRevLett.116.190801.

[89]S. Steinert, F. Dolde, P. Neumann, A. Aird, B. Naydenov, G. Balasubramanian, F. Jelezko, and J. Wrachtrup, "High sensitivity magnetic imaging using an array of spins in diamond", Review of Scientific Instruments **81**, 043705 (2010) 10.1063/1.3385689.

[90]L. M. Pham, D Le Sage, P. L. Stanwix, T. K. Yeung, D Glenn, A Trifonov, P Cappellaro, P. R. Hemmer, M. D. Lukin, H Park, A Yacoby, and R. L. Walsworth, "Magnetic field imaging with nitrogen-vacancy ensembles", New Journal of Physics **13**, 045021 (2011) 10.1088/1367-2630/13/4/045021.

[91]M. S. Grinolds, S. Hong, P. Maletinsky, L. Luan, M. D. Lukin, R. L. Walsworth, and A. Yacoby, "Nanoscale magnetic imaging of a single electron spin under ambient conditions", Nature Physics **9**, 215–219 (2013) 10.1038/nphys2543.

[92]K Arai, C Belthangady, H Zhang, N Bar-Gill, S. J. DeVience, P Cappellaro, A Yacoby, and R. L. Walsworth, "Fourier magnetic imaging with nanoscale resolution and compressed sensing speed-up using electronic spins in diamond", Nat Nanotechnol **10**, 859–864 (2015) 10.1038/nnano.2015.171.

[93]J.-P. Tetienne, N. Dontschuk, D. A. Broadway, A. Stacey, D. A. Simpson, and L. C. L. Hollenberg, "Quantum imaging of current flow in graphene", Science Advances **3**, e1602429 (2017) 10.1126/sciadv.1602429.

[94]P. Appel, M. Ganzhorn, E. Neu, and P. Maletinsky, "Nanoscale microwave imaging with a single electron spin in diamond", New Journal of Physics **17**, 112001 (2015) 10.1088/1367-2630/17/11/112001.

[95]L. Shao, R. Liu, M. Zhang, A. V. Shneidman, X. Audier, M. Markham, H. Dhillon, D. J. Twitchen, Y.-F. Xiao, and M. Lončar, "Wide-Field Optical Microscopy of Microwave Fields Using Nitrogen-Vacancy Centers in Diamonds", Advanced Optical Materials, 1075–1080 (2016) 10.1002/adom.201600039.

[96]D. MacLaurin, M. W. Doherty, L. C. L. Hollenberg, and A. M. Martin, "Measurable quantum geometric phase from a rotating single spin", Physical Review Letters **108**, 1–5 (2012) 10.1103/PhysRevLett.108.240403.

[97]A. Ajoy, and P. Cappellaro, "Stable three-axis nuclear-spin gyroscope in diamond", Physical Review A **86**, 062104 (2012) 10.1103/PhysRevA.86.062104.

[98]M. P. Ledbetter, K. Jensen, R. Fischer, A. Jarmola, and D. Budker, "Gyroscopes based on nitrogen-vacancy centers in diamond", Physical Review A **86**, 052116 (2012) 10.1103/PhysRevA.86.052116.

[99]R. R. Fu, B. P. Weiss, E. A. Lima, R. J. Harrison, X.-N. Bai, S. J. Desch, D. S. Ebel, C. Suavet, H. Wang, D. Glenn, D. Le Sage, T. Kasama, R. L. Walsworth, and A. T. Kuan, "Solar nebula magnetic fields recorded in the Semarkona meteorite", Science **346**, 1089–1092 (2014) 10.1126/science.1258022.

[100]R. R. Fu, B. P. Weiss, E. A. Lima, P. Kehayias, J. F. Araujo, D. R. Glenn, J. Gelb, J. F. Einsle, A. M. Bauer, R. J. Harrison, G. A. Ali, and R. L. Walsworth, "Evaluating the paleomagnetic potential of single zircon crystals using the Bishop Tuff", Earth and Planetary Science Letters **458**, 1–13 (2017) 10.1016/j.epsl.2016.09.038.

[101]D. R. Glenn, R. R. Fu, P. Kehayias, D. Le Sage, E. A. Lima, B. P. Weiss, and R. L. Walsworth, "Micrometer-scale magnetic imaging of geological samples using a quantum diamond microscope", Geochemistry, Geophysics, Geosystems **18**, 3254–3267 (2017) 10.1002/2017GC006946.

[102]E. Van Oort, and M. Glasbeek, "Electric-field-induced modulation of spin echoes of N-V centers in diamond", Chemical Physics Letters **168**, 529–532 (1990) 10.1016/0009-2614(90)85665-Y.

[103]F Dolde, H Fedder, M. W. Doherty, T Nöbauer, F Rempp, G Balasubramanian, T Wolf, F Reinhard, L. C. L. Hollenberg, F Jelezko, and J Wrachtrup, "Electric-field sensing using single diamond spins", (2011) 10.1038/NPHYS1969.

[104]F. Dolde, M. W. Doherty, J. Michl, I. Jakobi, B. Naydenov, S. Pezzagna, J. Meijer, P. Neumann, F. Jelezko, N. B. Manson, and J. Wrachtrup, "Nanoscale Detection of a Single Fundamental Charge in Ambient Conditions Using the NV- Center in Diamond", Physical Review Letters **112**, 97603 (2014) 10.1103/PhysRevLett.112.097603.

[105]M. Kim, H. J. Mamin, M. H. Sherwood, K. Ohno, D. D. Awschalom, and D. Rugar, "Decoherence of Near-Surface Nitrogen-Vacancy Centers Due to Electric Field Noise", Physical Review Letters **115**, 1–5 (2015) 10.1103/PhysRevLett.115.087602.

[106]Y. Romach, C. Müller, T. Unden, L. J. Rogers, T. Isoda, K. M. Itoh, M. Markham, A. Stacey, J. Meijer, S. Pezzagna, B. Naydenov, L. P. McGuinness, N. Bar-Gill, and F. Jelezko, "Spectroscopy of Surface-Induced Noise Using Shallow Spins in Diamond", Physical Review Letters **114**, 017601 (2015) 10.1103/PhysRevLett.114.017601.

[107]B. A. Myers, A. Ariyaratne, and A. C. B. Jayich, "Double-Quantum Spin-Relaxation Limits to Coherence of Near-Surface Nitrogen-Vacancy Centers", Physical Review Letters **118**, 197201 (2017) 10.1103/PhysRevLett.118.197201.

[108]V. M. Acosta, E. Bauch, M. P. Ledbetter, A. Waxman, L.-S. Bouchard, and D. Budker, "Temperature Dependence of the Nitrogen-Vacancy Magnetic Resonance in Diamond", Physical Review Letters **104**, 070801 (2010) 10.1103/PhysRevLett.104.070801.

[109]D. M. Toyli, C. F. de las Casas, D. J. Christle, V. V. Dobrovitski, and D. D. Awschalom, "Fluorescence thermometry enhanced by the quantum coherence of single spins in diamond", Proceedings of the National Academy of Sciences **110**, 8417–8421 (2013) 10.1073/pnas.1306825110.

[110]Y. Zhou, J. Wang, X. Zhang, K. Li, J. Cai, and W.-b. Gao, "Self-protected nanoscale thermometry based on spin defects in silicon carbide", 1–7 (2017).

[111]V. Ivády, T. Simon, J. R. Maze, I. A. Abrikosov, and A. Gali, "Pressure and temperature dependence of the zero-field splitting in the ground state of NV centers in diamond: A first-principles study", Physical Review B **90**, 235205 (2014) 10.1103/PhysRevB.90.235205.

[112]J. Cai, F. Jelezko, and M. B. Plenio, "Hybrid sensors based on colour centres in diamond and piezoactive layers", Nature Communications **5** (2014) 10.1038/ncomms5065.

[113]M. W. Doherty, V. V. Struzhkin, D. A. Simpson, L. P. McGuinness, Y. Meng, A. Stacey, T. J. Karle, R. J. Hemley, N. B. Manson, L. C. L. Hollenberg, and S. Prawer, "Electronic properties and metrology applications of the diamond NV - Center under pressure", Physical Review Letters **112**, 1–5 (2014) 10.1103/PhysRevLett.112.047601.

[114]L. Shao, M. Zhang, M. Markham, A. M. Edmonds, and M. Lončar, "Diamond Radio Receiver: Nitrogen-Vacancy Centers as Fluorescent Transducers of Microwave Signals", Physical Review Applied **6**, 064008 (2016) 10.1103/PhysRevApplied.6.064008.

[115]L. Jin, M. Pfender, N. Aslam, P. Neumann, S. Yang, J. Wrachtrup, and R.-B. Liu, "Proposal for a room-temperature diamond maser", Nature Communications **6**, 8251 (2015) 10.1038/ncomms9251.

[116]J. D. Breeze, J. Sathian, E. Salvadori, N. M. Alford, and C. W. M. Kay, "Continuous-wave room-temperature diamond maser", ArXiv e-prints, 1–7 (2017).

[117]L. G. D. Aaron B. Budgor, Leon Esterowitz, *Tunable Solid-State Lasers II*, edited by A. B. Budgor, L. Esterowitz, and L. G. DeShazer, Vol. 52, Springer Series in Optical Sciences (Springer Berlin Heidelberg, Berlin, Heidelberg, 1986), 10.1007/978-3-540-47433-3.

[118]J. Jeske, D. W. M. Lau, L. P. McGuinness, P. Reineck, B. C. Johnson, J. C. McCallum, F. Jelezko, T. Volz, J. H. Cole, B. C. Gibson, and A. D. Greentree, "Stimulated emission from NV centres in diamond", Nature Communications **8**, 1–10 (2016) 10.1038/ncomms14000.

[119]S. Rajendran, N. Zobrist, A. O. Sushkov, R. Walsworth, and M. Lukin, "Directional Detection of Dark Matter using Spectroscopy of Crystal Defects", 1–9 (2017).

[120]*Quantum Diamond Tech. (quantumdiamondtech.com)*, 2018, http://quantumdiamondtech.com.

[121]*Bikanta (bikanta.com)*, 2018.

[122]*Qnami - The Quantum Wave (qnami.ch)*, 2018.

[123]G. Balasubramanian, P. Neumann, D. Twitchen, M. Markham, R. Kolesov, N. Mizuochi, J. Isoya, J. Achard, J. Beck, J. Tissler, V. Jacques, P. R. Hemmer, F. Jelezko, and J. Wrachtrup, "Ultralong spin coherence time in isotopically engineered diamond", Nature Materials **8**, 383–387 (2009) 10.1038/nmat2420.

[124]B. J. Shields, Q. P. Unterreithmeier, N. P. De Leon, H. Park, and M. D. Lukin, "Efficient Readout of a Single Spin State in Diamond via Spin-to-Charge Conversion", Physical Review Letters **114**, 1–5 (2015) 10.1103/PhysRevLett.114.136402.

[125]M. S. J. Barson, P. Peddibhotla, P. Ovartchaiyapong, K. Ganesan, R. L. Taylor, M. Gebert, Z. Mielens, B. Koslowski, D. A. Simpson, L. P. McGuinness, J. McCallum, S. Prawer, S. Onoda, T. Ohshima, A. C. Bleszynski Jayich, F. Jelezko, N. B. Manson, and M. W. Doherty, "Nanomechanical Sensing Using Spins in Diamond", Nano Letters **17**, 1496–1503 (2017) 10.1021/acs.nanolett.6b04544.

[126]P. Udvarhelyi, V. O. Shkolnikov, A. Gali, G. Burkard, and A. Pályi, "Spin-strain interaction in nitrogen-vacancy centers in diamond", (2017).

[127]G. de Lange, T. van der Sar, M. Blok, Z.-H. Wang, V. Dobrovitski, and R. Hanson, "Controlling the quantum dynamics of a mesoscopic spin bath in diamond.", Scientific reports **2**, 382 (2012) 10.1038/srep00382.

[128]N. Bar-Gill, L. Pham, C. Belthangady, D. Le Sage, P. Cappellaro, J. Maze, M. Lukin, a. Yacoby, and R. Walsworth, "Suppression of spin-bath dynamics for improved coherence of multi-spin-qubit systems", Nature Communications **3**, 858 (2012) 10.1038/ncomms1856.

[129]E. Bauch, P. Jungyun, C. Hart, S. Singh, J. M. Schloss, M. J. Turner, J. F. Barry, L. Pham, N. Bar-gill, and R. Walsworth, "Quantum coherence of NV center solid-state spins in diamond", Manuscript in Preparation (2017).

[130]B. A. Myers, A. Das, M. C. Dartiailh, K. Ohno, D. D. Awschalom, and A. C. Bleszynski Jayich, "Probing Surface Noise with Depth-Calibrated Spins in Diamond", Physical Review Letters **113**, 027602 (2014) 10.1103/PhysRevLett.113.027602.

[131]P. Neumann, I. Jakobi, F. Dolde, C. Burk, R. Reuter, G. Waldherr, J. Honert, T. Wolf, A. Brunner, J. H. Shim, D. Suter, H. Sumiya, J. Isoya, and J. Wrachtrup, "High-Precision Nanoscale Temperature Sensing Using Single Defects in Diamond", Nano Letters **13**, 2738–2742 (2013) 10.1021/nl401216y.

[132]E. van Oort, P. Stroomer, and M. Glasbeek, "Low-field optically detected magnetic resonance of a coupled triplet-doublet defect pair in diamond", Physical Review B **42**, 8605–8608 (1990) 10.1103/PhysRevB.42.8605.

[133]P. Jamonneau, M. Lesik, J. P. Tetienne, I. Alvizu, L. Mayer, A. Dréau, S. Kosen, J. F. Roch, S. Pezzagna, J. Meijer, T. Teraji, Y. Kubo, P. Bertet, J. R. Maze, and V. Jacques, "Competition between electric field and magnetic field noise in the decoherence of a single spin in diamond", arXiv **024305**, 1–8 (2015) 10.1103/PhysRevB.93.024305.

[134]M. E. Trusheim, and D. Englund, "Wide-field strain imaging with preferentially aligned nitrogen-vacancy centers in polycrystalline diamond", New Journal of Physics **18**, 123023 (2016) 10.1088/1367-2630/aa5040.

[135]E. Bauch, C. A. Hart, J. M. Schloss, M. J. Turner, J. F. Barry, P. Kehayias, and R. L. Walsworth, "Ultralong Dephasing Times in Solid-State Spin Ensembles via Quantum Control", PRL, 5 (2018).

[136]K. M. C. Fu, C. Santori, P. E. Barclay, L. J. Rogers, N. B. Manson, and R. G. Beausoleil, "Observation of the dynamic Jahn-Teller effect in the excited states of nitrogen-vacancy centers in diamond", Physical Review Letters **103**, 1–4 (2009) 10.1103/PhysRevLett.103.256404.

[137]C. L. Degen, F. Reinhard, and P. Cappellaro, "Quantum sensing", 1–41 (2016).

[138]D. Suter, and F. Jelezko, "Single-spin magnetic resonance in the nitrogen-vacancy center of diamond", Progress in Nuclear Magnetic Resonance Spectroscopy **98-99**, 50–62 (2017) 10.1016/j.pnmrs.2016.12.001.

[139]D. Lee, K. W. Lee, J. V. Cady, P. Ovartchaiyapong, and A. C. B. Jayich, "Topical review: spins and mechanics in diamond", Journal of Optics **19**, 033001 (2017) 10.1088/2040-8986/aa52cd.

[140]L. M. Pham, "Color Centers in Diamond", PhD thesis (Harvard University, 2013).

[141]V. M. Acosta, "Optical Magnetometry with Nitrogen-Vacancy Centers in Diamond by Victor Marcel Acosta A dissertation submitted in partial satisfaction of the requirements for the degree of Doctor of Philosophy in Physics in the Graduate Division of the University of Cali", PhD thesis (Berkeley University, 2011).

[142]M. W. Doherty, N. B. Manson, P. Delaney, F. Jelezko, J. Wrachtrup, and L. C. L. Hollenberg, "The nitrogen-vacancy colour centre in diamond", Physics Reports **528**, 1–45 (2013) 10.1016/j.physrep.2013.02.001.

[143]J.-C. Jaskula, E. Bauch, S. Arroyo-Camejo, M. D. Lukin, S. W. Hell, A. S. Trifonov, and R. L. Walsworth, "Superresolution optical magnetic imaging and spectroscopy using individual electronic spins in diamond", Optics Express **25**, 11048 (2017) 10.1364/OE.25.011048.

[144]J.-C. Jaskula, B. J. Shields, E. Bauch, M. D. Lukin, A. S. Trifonov, and R. L. Walsworth, "Improved quantum sensing with a single solid-state spin via spin-to-charge conversion", 1–11 (2017).

[145]C. Schreyvogel, V. Polyakov, R. Wunderlich, J. Meijer, and C. E. Nebel, "Active charge state control of single NV centres in diamond by in-plane Al-Schottky junctions.", Scientific reports **5**, 12160 (2015) 10.1038/srep12160.

[146]V. M. Acosta, E. Bauch, M. P. Ledbetter, C. Santori, K. M. C. Fu, P. E. Barclay, R. G. Beausoleil, H. Linget, J. F. Roch, F. Treussart, S. Chemerisov, W. Gawlik, and D. Budker, "Diamonds with a high density of nitrogen-vacancy centers for magnetometry applications", Physical Review B - Condensed Matter and Materials Physics **80**, 1–15 (2009) 10.1103/PhysRevB.80.115202.

[147]C Zhang, H Yuan, N Zhang, L. X. Xu, B Li, G. D. Cheng, Y Wang, Q Gui, and J. C. Fang, "Dependence of high density nitrogen-vacancy center ensemble coherence on electron irradiation doses and annealing time", Journal of Physics D: Applied Physics **50**, 505104 (2017) 10.1088/1361-6463/aa97b3.

[148]D. Farfurnik, N. Aharon, I. Cohen, Y. Hovav, A. Retzker, and N. Bar-Gill, "Experimental realization of time-dependent phase-modulated continuous dynamical decoupling", arXiv preprint **1**, 1–6 (2017) 10.1103/PhysRevA.96.013850.

[149]X. Hu, Y. Dai, R. Li, H. Shen, and X. He, "The diffusion of vacancies near a diamond (001) surface", Solid State Communications **122**, 45–48 (2002) 10.1016/S0038-1098(02)00069-8.

[150]J. Orwa, K. Ganesan, J. Newnham, C. Santori, P. Barclay, K. Fu, R. Beausoleil, I. Aharonovich, B. Fairchild, P. Olivero, A. Greentree, and S. Prawer, "An upper limit on the lateral vacancy diffusion length in diamond", Diamond and Related Materials **24**, 6–10 (2012) 10.1016/J.DIAMOND.2012.02.009.

[151]G. Kucsko, S. Choi, J. Choi, P. C. Maurer, H. Zhou, R. Landig, H. Sumiya, S. Onoda, J. Isoya, F. Jelezko, E. Demler, N. Y. Yao, and M. D. Lukin, "Critical thermalization of a disordered dipolar spin system in diamond", arXiv preprint (2016).

[152]J. R. Rabeau, P. Reichart, G. Tamanyan, D. N. Jamieson, S. Prawer, F. Jelezko, T. Gaebel, I. Popa, M. Domhan, and J. Wrachtrup, "Implantation of labelled single nitrogen vacancy centers in diamond using N15", Applied Physics Letters **88**, 023113 (2006) 10.1063/1.2158700.

[153]B. Naydenov, V. Richter, J. Beck, M. Steiner, P. Neumann, G. Balasubramanian, J. Achard, F. Jelezko, J. Wrachtrup, and R. Kalish, "Enhanced generation of single optically active spins in diamond by ion implantation", Applied Physics Letters **96**, 163108 (2010) 10.1063/1.3409221.

[154]J Schwartz, P Michaelides, C. D. Weis, and T Schenkel, "In situ optimization of co-implantation and substrate temperature conditions for nitrogen-vacancy center formation in single-crystal diamonds", New Journal of Physics **13**, 035022 (2011) 10.1088/1367-2630/13/3/035022.

[155]I. Bayn, E. H. Chen, M. E. Trusheim, L. Li, T. Schröder, O. Gaathon, M. Lu, A. Stein, M. Liu, K. Kisslinger, H. Clevenson, and D. Englund, "Generation of Ensembles of Individually Resolvable Nitrogen Vacancies Using Nanometer-Scale Apertures in Ultrahigh-Aspect Ratio Planar Implantation Masks", Nano Letters **15**, 1751–1758 (2015) 10.1021/nl504441m.

[156]F. Fávaro de Oliveira, S. A. Momenzadeh, D. Antonov, H. Fedder, A. Denisenko, and J. Wrachtrup, "On the efficiency of combined ion implantation for the creation of near-surface nitrogen-vacancy centers in diamond", Physica Status Solidi (A) Applications and Materials Science **213**, 2044–2050 (2016) 10.1002/pssa.201600326.

[157]I Jakobi, S. A. Momenzadeh, F. F. de Oliveira, J Michl, F Ziem, M Schreck, P Neumann, A Denisenko, and J Wrachtrup, "Efficient creation of dipolar coupled nitrogen-vacancy spin qubits in diamond", Journal of Physics: Conference Series **752**, 012001 (2016) 10.1088/1742-6596/752/1/012001.

[158]T. Schröder, M. Walsh, J. Zheng, S. Mouradian, L. Li, G. Malladi, H. Bakhru, M. Lu, A. Stein, M. Heuck, and D. Englund, "Scalable fabrication of coupled NV center - photonic crystal cavity systems by self-aligned N ion implantation", Optical Materials Express **7**, 1514 (2017) 10.1364/OME.7.001514.

[159]J. P. Tetienne, R. W. de Gille, D. A. Broadway, T. Teraji, S. E. Lillie, J. M. McCoey, N. Dontschuk, L. T. Hall, A. Stacey, D. A. Simpson, and L. C. L. Hollenberg, "Spin coherence of dense near-surface ensembles of nitrogen-vacancy centres in diamond", (2017).

[160]E. E. Kleinsasser, M. M. Stanfield, J. K. Q. Banks, Z. Zhu, W.-D. Li, V. M. Acosta, H. Watanabe, K. M. Itoh, and K.-m. C. Fu, "High density nitrogen-vacancy sensing surface created via He + ion implantation of 12 C diamond", Applied Physics Letters **108**, 202401 (2016) 10.1063/1.4949357.

[161]T. Yamamoto, T. Umeda, K. Watanabe, S. Onoda, M. L. Markham, D. J. Twitchen, B. Naydenov, L. P. McGuinness, T. Teraji, S. Koizumi, F. Dolde, H. Fedder, J. Honert, J. Wrachtrup, T. Ohshima, F. Jelezko, and J. Isoya, "Extending spin coherence times of diamond qubits by high-temperature annealing", Physical Review B - Condensed Matter and Materials Physics **88**, 1–8 (2013) 10.1103/PhysRevB.88.075206.

[162]D. M. Toyli, C. D. Weis, G. D. Fuchs, T. Schenkel, and D. D. Awschalom, "Chip-Scale Nanofabrication of Single Spins and Spin Arrays in Diamond", Nano Letters **10**, 3168–3172 (2010) 10.1021/nl102066q.

[163]L. M. Pham, S. J. DeVience, F. Casola, I. Lovchinsky, A. O. Sushkov, E. Bersin, J. Lee, E. Urbach, P. Cappellaro, H. Park, A. Yacoby, M. D. Lukin, and R. L. Walsworth, "NMR Technique for Determining the Depth of Shallow Nitrogen-Vacancy Centers in Diamond", Physical Review B **045425**, 1–14 (2016) 10.1103/PhysRevB.93.045425.

[164]M. Schwander, and K. Partes, "A review of diamond synthesis by CVD processes", Diamond and Related Materials **20**, 1287–1301 (2011) 10.1016/j.diamond.2011.08.005.

[165]J. C. Angus, "Diamond synthesis by chemical vapor deposition: The early years", Diamond and Related Materials **49**, 77–86 (2014) 10.1016/j.diamond.2014.08.004.

[166]E. Six, *Element Six CVD Diamond Handbook*, 2015.

[167]H. Sumiya, and S. Satoh, "High-pressure synthesis of high-purity diamond crystal", Diamond and Related Materials **5**, 1359–1365 (1996) 10.1016/0925-9635(96)00559-6.

[168]H Kanda, "Large diamonds grown at high pressure conditions", Brazilian Journal of Physics **30**, 482–489 (2000).

[169]A. M. Zaitsev, *Optical Properties of Diamond* (Springer Berlin Heidelberg, Berlin, Heidelberg, 2001), p. 502, 10.1007/978-3-662-04548-0.

[170]C. B. Hartland, "A study of point defects in CVD diamond using electron paramagnetic resonance and optical spectroscopy", PhD thesis (University of Warwick, 2014).

[171]D. a. Redman, S Brown, R. H. Sands, and S. C. Rand, "Spin dynamics and electronic states of N-V center in diamond by EPR and Four-Wave_Mixing spectroscopy", Physical Review Letters **64**, 3420–3423 (1991) 10.1097/01.NUMA.0000416408.60732.5d.

[172]N. Manson, and J. Harrison, "Photo-ionization of the nitrogen-vacancy center in diamond", Diamond and Related Materials **14**, 1705–1710 (2005) 10.1016/j.diamond.2005.06.027.

[173]N. B. Manson, J. P. Harrison, and M. J. Sellars, "Nitrogen-vacancy center in diamond: Model of the electronic structure and associated dynamics", Physical Review B **74**, 104303 (2006) 10.1103/PhysRevB.74.104303.

[174]R. Hanson, F. M. Mendoza, R. J. Epstein, and D. D. Awschalom, "Polarization and readout of coupled single spins in diamond", Physical Review Letters **97**, 1–4 (2006) 10.1103/PhysRevLett.97.087601.

[175]J. Harrison, M. Sellars, and N. Manson, "Measurement of the optically induced spin polarisation of N-V centres in diamond", Diamond and Related Materials **15**, 586–588 (2006) 10.1016/j.diamond.2005.12.027.

[176]A. Batalov, C. Zierl, T. Gaebel, P. Neumann, I. Y. Chan, G. Balasubramanian, P. R. Hemmer, F. Jelezko, and J. Wrachtrup, "Temporal coherence of photons emitted by single nitrogen-vacancy defect centers in diamond using optical rabi-oscillations", Physical Review Letters **100**, 1–4 (2008) 10.1103/PhysRevLett.100.077401.

[177]P. Delaney, J. C. Greer, and J. A. Larsson, "Spin-Polarization Mechanisms of the Nitrogen-Vacancy Center in Diamond", Nano Letters **10**, 610–614 (2010) 10.1021/nl903646p.

[178]L. Robledo, H. Bernien, T. der Sar, and R. Hanson, "Spin dynamics in the optical cycle of single nitrogen-vacancy centres in diamond", New Journal of Physics **13**, 25013 (2011).

[179]K. Beha, A. Batalov, N. B. Manson, R. Bratschitsch, and A. Leitenstorfer, "Optimum photoluminescence excitation and recharging cycle of single nitrogen-vacancy centers in ultrapure diamond", Physical Review Letters **109**, 1–5 (2012) 10.1103/PhysRevLett.109.097404.

[180]N. Aslam, G. Waldherr, P. Neumann, F. Jelezko, and J. Wrachtrup, "Photo-induced ionization dynamics of the nitrogen vacancy defect in diamond investigated by single-shot charge state detection", New Journal of Physics **15** (2013) 10.1088/1367-2630/15/1/013064.

[181]P. Siyushev, H. Pinto, M. Vörös, A. Gali, F. Jelezko, and J. Wrachtrup, "Optically controlled switching of the charge state of a single nitrogen-vacancy center in diamond at cryogenic temperatures", Physical Review Letters **110**, 1–5 (2013) 10.1103/PhysRevLett.110.167402.

[182]M. Goldman, A. Sipahigil, M. Doherty, N. Yao, S. Bennett, M. Markham, D. Twitchen, N. Manson, A. Kubanek, and M. Lukin, "Phonon-Induced Population Dynamics and Intersystem Crossing in Nitrogen-Vacancy Centers", Physical Review Letters **114**, 145502 (2015) 10.1103/PhysRevLett.114.145502.

[183]H. Jayakumar, J. Henshaw, S. Dhomkar, D. Pagliero, N. B. Manson, R. Albu, M. W. Doherty, and C. A. Meriles, "Optical patterning of trapped charge in nitrogen-doped diamond", Nature Communications **7**, 1–9 (2016) 10.1038/ncomms12660.

[184]M. Pfender, N. Aslam, P. Simon, D. Antonov, G. O. Thiering, S. Burk, F. Fávaro De Oliveira, A. Denisenko, H. Fedder, J. Meijer, J. A. Garrido, A. Gali, T. Teraji, J. Isoya, M. W. Doherty, A. Alkauskas, A. Gallo, A. Grüneis, P. Neumann, and J. Wrachtrup, "Protecting a diamond quantum memory by charge state control", 1–9 (2017).

[185]L. J. Rogers, S Armstrong, M. J. Sellars, and N. B. Manson, "Infrared emission of the NV centre in diamond: Zeeman and uniaxial stress studies", New Journal of Physics **10**, 103024 (2008) 10.1088/1367-2630/10/10/103024.

[186]P. W. Atkins, and R. Friedman, "Molecular Quantum Mechanics", Oxford Universiy Press **134**, 588 (2011).

[187]E. Kim, V. M. Acosta, E. Bauch, D. Budker, and P. R. Hemmer, "Electron spin resonance shift and linewidth broadening of nitrogen-vacancy centers in diamond as a function of electron irradiation dose", Applied Physics Letters **101** (2012) 10.1063/1.4747211.

[188]M. Steiner, P. Neumann, J. Beck, F. Jelezko, and J. Wrachtrup, "Universal enhancement of the optical readout fidelity of single electron spins at nitrogen-vacancy centers in diamond", Physical Review B **81**, 035205 (2010) 10.1103/PhysRevB.81.035205.

[189]L. M. Pham, N. Bar-Gill, C. Belthangady, D. Le Sage, P. Cappellaro, M. D. Lukin, A. Yacoby, and R. L. Walsworth, "Enhanced solid-state multispin metrology using dynamical decoupling", Physical Review B - Condensed Matter and Materials Physics **86**, 1–5 (2012) 10.1103/PhysRevB.86.045214.

[190]A. Dréau, J. R. Maze, M. Lesik, J. F. Roch, and V. Jacques, "High-resolution spectroscopy of single NV defects coupled with nearby 13C nuclear spins in diamond", Physical Review B - Condensed Matter and Materials Physics **85**, 1–7 (2012) 10.1103/PhysRevB.85.134107.

[191]K. Jensen, V. M. Acosta, A. Jarmola, and D. Budker, "Light narrowing of magnetic resonances in ensembles of nitrogen-vacancy centers in diamond", Physical Review B - Condensed Matter and Materials Physics **87**, 1–10 (2013) 10.1103/PhysRevB.87.014115.

[192]S. T. Alsid, "Optimizing Chemical-Vapor-Deposition Diamond for Nitrogen-Vacancy Center Ensemble Magnetometry", PhD thesis (MIT/Lincoln Labs, 2017).

[193]T. Oeckinghaus, R. Stöhr, R. Kolesov, J. Tisler, F. Reinhard, and J. Wrachtrup, "A compact, diode laser based excitation system for microscopy of NV centers", Review of Scientific Instruments **85**, 073101 (2014) 10.1063/1.4885469.

[194]A. Dréau, M. Lesik, L. Rondin, P. Spinicelli, O. Arcizet, J. F. Roch, and V. Jacques, "Avoiding power broadening in optically detected magnetic resonance of single NV defects for enhanced dc magnetic field sensitivity", Physical Review B - Condensed Matter and Materials Physics **84**, 1–8 (2011) 10.1103/PhysRevB.84.195204.

[195]R Hanson, V. V. Dobrovitski, a. E. Feiguin, O Gywat, and D. D. Awschalom, "Coherent Dynamics of a Single Spin Interacting with an Adjustable Spin Bath", Science **320**, 352–355 (2008) 10.1126/science.1155400.

[196]V. V. Dobrovitski, A. E. Feiguin, R. Hanson, and D. D. Awschalom, "Decay of Rabi Oscillations by Dipolar-Coupled Dynamical Spin Environments", Physical Review Letters **102**, 237601 (2009) 10.1103/PhysRevLett.102.237601.

[197]Z. H. Wang, G. De Lange, D. Ristè, R. Hanson, and V. V. Dobrovitski, "Comparison of dynamical decoupling protocols for a nitrogen-vacancy center in diamond", Physical Review B - Condensed Matter and Materials Physics **85**, 57–61 (2012) 10.1103/PhysRevB.85.155204.

[198]F. A. Hopf, R. F. Shea, and M. O. Scully, "Theory of Optical Free-Induction Decay and Two-Photon Superradiance", Physical Review A **7**, 2105–2110 (1973) 10.1103/PhysRevA.7.2105.

[199]J. R. Maze, A Dréau, V. Waselowski, H. Duarte, J.-F. Roch, and V. Jacques, "Free induction decay of single spins in diamond", New Journal of Physics **14**, 103041 (2012) 10.1088/1367-2630/14/10/103041.

[200]V. V. Dobrovitski, A. E. Feiguin, D. D. Awschalom, and R. Hanson, "Decoherence dynamics of a single spin versus spin ensemble", Physical Review B **77**, 245212 (2008) 10.1103/PhysRevB.77.245212.

[201]R. de Sousa, *Electron Spin Resonance and Related Phenomena in Low-Dimensional Structures*, edited by M. Fanciulli, Vol. 115, Topics in Applied Physics (Springer Berlin Heidelberg, Berlin, Heidelberg, 2009), pp. 183–220, 10.1007/978-3-540-79365-6.

[202]K. Fang, V. M. Acosta, C. Santori, Z. Huang, K. M. Itoh, H. Watanabe, S. Shikata, and R. G. Beausoleil, "High-sensitivity magnetometry based on quantum beats in diamond nitrogen-vacancy centers", Physical Review Letters **110**, 2–4 (2013) 10.1103/PhysRevLett.110.130802.

[203]E. L. Hahn, "Spin Echoes", Physical Review **80**, 580–594 (1950) 10.1103/PhysRev.80.580.

[204]V. Stepanov, and S. Takahashi, "Determination of nitrogen spin concentration in diamond using double electron-electron resonance", Physical Review B **94**, 024421 (2016) 10.1103/PhysRevB.94.024421.

[205]S. Meiboom, and D. Gill, "Modified SpinEcho Method for Measuring Nuclear Relaxation Times", Review of Scientific Instruments **29**, 688–691 (1958) 10.1063/1.1716296.

[206]T. Gullion, D. B. Baker, and M. S. Conradi, "New, compensated Carr-Purcell sequences", Journal of Magnetic Resonance (1969) **89**, 479–484 (1990) 10.1016/0022-2364(90)90331-3.

[207]H. J. Mamin, M. H. Sherwood, M. Kim, C. T. Rettner, K. Ohno, D. D. Awschalom, and D. Rugar, "Multipulse double-quantum magnetometry with near-surface nitrogen-vacancy centers", Physical Review Letters **113**, 1–5 (2014) 10.1103/PhysRevLett.113.030803.

[208]A. Angerer, T. Nöbauer, G. Wachter, M. Markham, A. Stacey, J. Majer, J. Schmiedmayer, and M. Trupke, "Subnanotesla quantum-interference magnetometry with a single spin in diamond", Arxiv preprint 1509.01637 (2015).

[209]L. Rowan, E. Hahn, and W. Mims, "Electron-Spin-Echo Envelope Modulation", Physical Review **137**, A61–A71 (1965) 10.1103/PhysRev.137.A61.

[210]T. Gaebel, M. Domhan, I. Popa, C. Wittmann, P. Neumann, F. Jelezko, J. R. Rabeau, N. Stavrias, A. D. Greentree, S. Prawer, J. Meijer, J. Twamley, P. R. Hemmer, and J. Wrachtrup, "Room-temperature coherent coupling of single spins in diamond", Nature Physics **2**, 408–413 (2006) 10.1038/nphys318.

[211]L Childress, M. V. Gurudev Dutt, J. M. Taylor, A. S. Zibrov, F Jelezko, J Wrachtrup, P. R. Hemmer, and M. D. Lukin, "Coherent Dynamics of Coupled Electron and Nuclear Spin Qubits in Diamond", Science **314**, 281–285 (2006) 10.1126/science.1131871.

[212]K. Ohno, F. Joseph Heremans, L. C. Bassett, B. A. Myers, D. M. Toyli, A. C. Bleszynski Jayich, C. J. Palmstrøm, and D. D. Awschalom, "Engineering shallow spins in diamond with nitrogen delta-doping", Applied Physics Letters **101**, 082413 (2012) 10.1063/1.4748280.

[213]L. Childress, "Coherent Manipulation of Single Quantum Systems in the Solid State", PhD thesis (2006).

[214]P. L. Stanwix, L. M. Pham, J. R. Maze, D. Le Sage, T. K. Yeung, P. Cappellaro, P. R. Hemmer, A. Yacoby, M. D. Lukin, and R. L. Walsworth, "Coherence of nitrogen-vacancy electronic spin ensembles in diamond", Physical Review B - Condensed Matter and Materials Physics **82**, 7–10 (2010) 10.1103/PhysRevB.82.201201.

[215]S. C. Lawson, D. Fisher, D. C. Hunt, and M. E. Newton, "On the existence of positively charged single-substitutional nitrogen in diamond", Journal of Physics Condensed Matter **10**, 6171–6180 (1998) 10.1088/0953-8984/10/27/016.

[216]I. Kiflawi, A. Mainwood, H. Kanda, and D. Fisher, "Nitrogen interstitials in diamond", Physical Review B **54**, 16719–16726 (1996) 10.1103/PhysRevB.54.16719.

[217]X. Zhou, G. Watkins, K. McNamara Rutledge, R. Messmer, and S. Chawla, "Hydrogen-related defects in polycrystalline CVD diamond", Physical Review B **54**, 7881–7890 (1996) 10.1103/PhysRevB.54.7881.

[218]J. P. Goss, P. R. Briddon, R Jones, and S Sque, "The vacancynitrogenhydrogen complex in diamond: a potential deep centre in chemical vapour deposited material", Journal of Physics: Condensed Matter **15**, S2903–S2911 (2003) 10.1088/0953-8984/15/39/014.

[219]C. Glover, M. E. Newton, P. M. Martineau, S. Quinn, and D. J. Twitchen, "Hydrogen Incorporation in Diamond: The Vacancy-Hydrogen Complex", Physical Review Letters **92**, 135502 (2004) 10.1103/PhysRevLett.92.135502.

[220]J. R. Maze, J. M. Taylor, and M. D. Lukin, "Electron spin decoherence of single nitrogen-vacancy defects in diamond", Physical Review B - Condensed Matter and Materials Physics **78**, 1–7 (2008) 10.1103/PhysRevB.78.094303.

[221]L. T. Hall, J. H. Cole, and L. C. L. Hollenberg, "Analytic solutions to the central-spin problem for nitrogen-vacancy centers in diamond", Physical Review B **90**, 075201 (2014) 10.1103/PhysRevB.90.075201.

[222]N Mizuochi, P Neumann, F Rempp, J Beck, V Jacques, P Siyushev, K Nakamura, D. J. Twitchen, H Watanabe, S Yamasaki, F Jelezko, and J Wrachtrup, "Coherence of single spins coupled to a nuclear spin bath of varying density", Physical Review B **80**, 041201 (2009) 10.1103/PhysRevB.80.041201.

[223]N. Zhao, S. W. Ho, and R. B. Liu, "Decoherence and dynamical decoupling control of nitrogen vacancy center electron spins in nuclear spin baths", Physical Review B - Condensed Matter and Materials Physics **85**, 1–18 (2012) 10.1103/PhysRevB.85.115303.

[224]A. O. Levchenko, V. V. Vasil'Ev, S. A. Zibrov, A. S. Zibrov, A. V. Sivak, and I. V. Fedotov, "Inhomogeneous broadening of optically detected magnetic resonance of the ensembles of nitrogen-vacancy centers in diamond by interstitial carbon atoms", Applied Physics Letters **106** (2015) 10.1063/1.4913428.

[225]G. Davies, S. C. Lawson, A. T. Collins, A. Mainwood, and S. J. Sharp, "Vacancy-related centers in diamond", Physical Review B **46**, 13157–13170 (1992) 10.1103/PhysRevB.46.13157.

[226]D. J. Twitchen, D. C. Hunt, V Smart, M. E. Newton, and J. M. Baker, "Correlation between ND1 optical absorption and the concentration of negative vacancies determined by electron paramagnetic resonance (EPR)", **8**, 1572–1575 (1999).

[227]J. K. Kirui, J. A. Van Wyk, and M. J. R. Hoch, "Dynamics of negatively charged divacancies in neutron irradiated type Ib diamond", Diamond and Related Materials **39**, 78–81 (2013) 10.1016/j.diamond.2013.08.003.

[228]A Jarmola, A Berzins, J. Smits, K Smits, J Prikulis, F Gahbauer, R Ferber, D Erts, M Auzinsh, and D. Budker, "Longitudinal spin-relaxation in nitrogen-vacancy centers in electron irradiated diamond", Applied Physics Letters **107**, 242403 (2015) 10.1063/1.4937489.

[229]J. Choi, S. Choi, G. Kucsko, P. C. Maurer, B. J. Shields, H. Sumiya, S. Onoda, J. Isoya, E. Demler, F. Jelezko, N. Y. Yao, and M. D. Lukin, "Depolarization Dynamics in a Strongly Interacting Solid-State Spin Ensemble", Physical Review Letters **118**, 093601 (2017) 10.1103/PhysRevLett.118.093601.

[230]I. B. Bersuker, "The Jahn-Teller effect as a general tool for solving molecular and solid state problems: Novel findings", Journal of Molecular Structure **838**, 44–52 (2007).

[231]T. A. Abtew, Y. Y. Sun, B. C. Shih, P. Dev, S. B. Zhang, and P. Zhang, "Dynamic Jahn-Teller effect in the NV- center in diamond", Physical Review Letters **107**, 146403 (2011) 10.1103/PhysRevLett.107.146403.

[232]X. Xiao, and N. Zhao, "Proposal for observing dynamic JahnTeller effect by single solid-state defects", New Journal of Physics **18**, 103022 (2016) 10.1088/1367-2630/18/10/103022.

[233]P. Keller, *Basic Principles of Magnetic Resonance*, Vol. 1, Springer Series in Solid-State Sciences (Springer Berlin Heidelberg, Berlin, Heidelberg, 2010), pp. 1–30, 10.1007/978-3-662-09441-9.

[234]T. Ishikawa, K.-M. C. Fu, C. Santori, V. M. Acosta, R. G. Beausoleil, H. Watanabe, S. Shikata, and K. M. Itoh, "Optical and Spin Coherence Properties of Nitrogen-Vacancy Centers Placed in a 100 nm Thick Isotopically Purified Diamond Layer", Nano Letters **12**, 2083–2087 (2012) 10.1021/nl300350r.

[235]L. Cywiński, R. M. Lutchyn, C. P. Nave, and S. Das Sarma, "How to enhance dephasing time in superconducting qubits", Physical Review B **77**, 174509 (2008) 10.1103/PhysRevB.77.174509.

[236]J. A. Van Wyk, E. C. Reynhardt, G. L. High, and I Kiflawi, "The dependences of ESR line widths and spin - spin relaxation times of single nitrogen defects on the concentration of nitrogen defects in diamond", Journal of Physics D: Applied Physics **30**, 1790–1793 (1997) 10.1088/0022-3727/30/12/016.

[237]L. Cywiński, W. M. Witzel, and S. Das Sarma, "Pure quantum dephasing of a solid-state electron spin qubit in a large nuclear spin bath coupled by long-range hyperfine-mediated interactions", Physical Review B - Condensed Matter and Materials Physics **79**, 1–23 (2009) 10.1103/PhysRevB.79.245314.

[238]S. Takahashi, R. Hanson, J. van Tol, M. S. Sherwin, and D. D. Awschalom, "Quenching Spin Decoherence in Diamond through Spin Bath Polarization", Physical Review Letters **101**, 047601 (2008) 10.1103/PhysRevLett.101.047601.

[239]A. Jarmola, V. M. Acosta, K. Jensen, S. Chemerisov, and D. Budker, "Temperature- and magnetic-field-dependent longitudinal spin relaxation in nitrogen-vacancy ensembles in diamond", Physical Review Letters **108**, 1–5 (2012) 10.1103/PhysRevLett.108.197601.

[240]M. Mrózek, D. Rudnicki, P. Kehayias, A. Jarmola, D. Budker, and W. Gawlik, "Longitudinal spin relaxation in nitrogen-vacancy ensembles in diamond", EPJ Quantum Technology **2**, 22 (2015) 10.1140/epjqt/s40507-015-0035-z.

[241]L. T. Hall, P. Kehayias, D. A. Simpson, A. Jarmola, A. Stacey, D. Budker, and L. C. L. Hollenberg, "Detection of nanoscale electron spin resonance spectra demonstrated using nitrogen-vacancy centre probes in diamond", Nature Communications **7**, 10211 (2016) 10.1038/ncomms10211.

[242]A Norambuena, E Muñoz, H. T. Dinani, A Jarmola, P Maletinsky, D Budker, and J. R. Maze, "Spin-lattice relaxation of individual solid-state spins", (2017).

[243]H. S. Knowles, D. M. Kara, and M. Atatüre, "Observing bulk diamond spin coherence in high-purity nanodiamonds", Nature Materials **13**, 21–25 (2014) 10.1038/nmat3805.

[244]E. C. Reynhardt, G. L. High, E. C. Reynhardt, and G. L. High, "Dynamic nuclear polarization of diamond . I . Solid state and thermal mixing effects Dynamic nuclear polarization of diamond . I . Solid state and thermal mixing effects", **4090** (2012) 10.1063/1.477009.

[245]W. M. Witzel, M. S. Carroll, A. Cywiński, and S. Das Sarma, "Quantum decoherence of the central spin in a sparse system of dipolar coupled spins", Physical Review B - Condensed Matter and Materials Physics **86**, 1–27 (2012) 10.1103/PhysRevB.86.035452.

[246]G. E. Uhlenbeck, and L. S. Ornstein, "On the Theory of the Brownian Motion", Physical Review **36**, 823–841 (1930) 10.1103/PhysRev.36.823.

[247]J. Klauder, and P. Anderson, "Spectral Diffusion Decay in Spin Resonance Experiments", Physical Review **125**, 912–932 (1962) 10.1103/PhysRev.125.912.

[248]A. V. Khaetskii, D. Loss, and L. Glazman, "Electron spin decoherence in quantum dots due to interaction with nuclei", Physical Review Letters **88**, 1868021–1868024 (2002) 10.1103/PhysRevLett.88.186802.

[249]F. M. Cucchietti, J. P. Paz, and W. H. Zurek, "Decoherence from spin environments", Physical Review A - Atomic, Molecular, and Optical Physics **72** (2005) 10.1103/PhysRevA.72.052113.

[250]A. Abragam, *The principles of nuclear magnetism* (Clarendon Press, 1983), p. 599.

[251]D. C. Johnston, "Stretched exponential relaxation arising from a continuous sum of exponential decays", Physical Review B - Condensed Matter and Materials Physics **74**, 1–7 (2006) 10.1103/PhysRevB.74.184430.

[252]J. S. Hyde, and J. B. Feix, "Electron-Electron Double Resonance", in *Biomedical epr, part b: methodology, instrumentation, and dynamics*, Vol. 24/B (1989), pp. 305–307, 10.1007/978-1-4613-0743-3{_}6.

[253]C. Belthangady, N. Bar-Gill, L. M. Pham, K. Arai, D. Le Sage, P. Cappellaro, and R. L. Walsworth, "Dressed-state resonant coupling between bright and dark spins in diamond", Physical Review Letters **110**, 1–5 (2013) 10.1103/PhysRevLett.110.157601.

[254]A. M. Tyryshkin, J. J. Morton, A. Ardavan, and S. A. Lyon, "Davies electron-nuclear double resonance revisited: Enhanced sensitivity and nuclear spin relaxation", Journal of Chemical Physics **124** (2006) 10.1063/1.2204915.

[255]L Rondin, J.-P. Tetienne, S Rohart, A Thiaville, T Hingant, P Spinicelli, J.-F. Roch, and V Jacques, "Stray-field imaging of magnetic vortices with a single diamond spin", Nature Communications **4** (2013) 10.1038/ncomms3279.

[256]T. van der Sar, F. Casola, R. Walsworth, and A. Yacoby, "Nanometre-scale probing of spin waves using single-electron spins.", Nature communications **6**, 7886 (2015) 10.1038/ncomms8886.

[257]G. Balasubramanian, I. Y. Chan, R. Kolesov, M. Al-Hmoud, J. Tisler, C. Shin, C. Kim, A. Wojcik, P. R. Hemmer, A. Krueger, T. Hanke, A. Leitenstorfer, R. Bratschitsch, F. Jelezko, and J. Wrachtrup, "Nanoscale imaging magnetometry with diamond spins under ambient conditions", Nature **455**, 648–651 (2008) 10.1038/nature07278.

[258]M. S. Grinolds, M Warner, K. D. Greve, Y Dovzhenko, L Thiel, R. L. Walsworth, S Hong, P Maletinsky, and A Yacoby, "Subnanometre resolution in three-dimensional magnetic resonance imaging of individual dark spins", Nature Nanotechnology **9**, 279–284 (2014) 10.1038/nnano.2014.30.

[259]V. Zablotskii, T. Polyakova, O. Lunov, and A. Dejneka, "How a High-Gradient Magnetic Field Could Affect Cell Life", Scientific Reports **6**, 37407 (2016) 10.1038/srep37407.

[260]X.-d. Chen, C.-l. Zou, F.-w. Sun, and G.-c. Guo, "Optical manipulation of the charge state of nitrogen-vacancy center in diamond Optical manipulation of the charge state of nitrogen-vacancy center in diamond", **013112** (2013) 10.1063/1.4813120.

[261]M. Pfender, N. Aslam, G. Waldherr, P. Neumann, and J. Wrachtrup, "Single-spin stochastic optical reconstruction microscopy", Proceedings of the National Academy of Sciences **111**, 14669–14674 (2014) 10.1073/pnas.1404907111.

[262]D. Wildanger, J. R. Maze, and S. W. Hell, "Diffraction Unlimited All-Optical Recording of Electron Spin Resonances", Physical Review Letters **107**, 17601 (2011) 10.1103/PhysRevLett.107.017601.

[263]S Arroyo-Camejo, M.-P. Adam, M Besbes, J.-P. Hugonin, V Jacques, J.-J. Greffet, J.-F. Roch, S. W. Hell, and F Treussart, "Stimulated emission depletion microscopy resolves individual nitrogen vacancy centers in diamond nanocrystals", ACS Nano **7**, 10912–10919 (2013) 10.1021/nn404421b.

[264]E. H. Chen, O. Gaathon, M. E. Trusheim, and D. Englund, "Wide-Field Multispectral Super-Resolution Imaging Using Spin-Dependent Fluorescence in Nanodiamonds", Nano Letters **13**, 2073–2077 (2013) 10.1021/nl400346k.

[265]E. Rittweger, K. Y. Han, S. E. Irvine, C. Eggeling, and S. W. Hell, "STED microscopy reveals crystal colour centres with nanometric resolution", Nature Photonics **3**, 144–147 (2009) 10.1038/nphoton.2009.2.

[266]K. Y. Han, S. K. Kim, C. Eggeling, and S. W. Hell, "Metastable dark States enable ground state depletion microscopy of nitrogen vacancy centers in diamond with diffraction-unlimited resolution.", Nano Letters **10**, 3199–3203 (2010) 10.1021/nl102156m.

[267]T Staudacher, F Shi, S Pezzagna, J Meijer, J Du, C. A. Meriles, F Reinhard, and J Wrachtrup, "Nuclear Magnetic Resonance Spectroscopy on a (5-Nanometer)3 Sample Volume", Science **339**, 561–563 (2013) 10.1126/science.1231675.

[268]H. J. Mamin, M Kim, M. H. Sherwood, C. T. Rettner, K Ohno, D. D. Awschalom, and D Rugar, "Nanoscale Nuclear Magnetic Resonance with a Nitrogen-Vacancy Spin Sensor", Science **339**, 557–560 (2013) 10.1126/science.1231540.

[269]S. Arroyo-Camejo, A. Lazariev, S. W. Hell, and G. Balasubramanian, "Room temperature high-fidelity holonomic single-qubit gate on a solid-state spin", Nature Communications **5** (2014) 10.1038/ncomms5870.

[270]I. Lovchinsky, A. O. Sushkov, E. Urbach, N. P. de Leon, S. Choi, K. De Greve, R. Evans, R. Gertner, E. Bersin, C. Muller, L. McGuinness, F. Jelezko, R. L. Walsworth, H. Park, and M. D. Lukin, "Nuclear magnetic resonance detection and spectroscopy of single proteins using quantum logic", Science **351**, 836–841 (2016) 10.1126/science.aad8022.

[271]J.-P. Tetienne, T. Hingant, J.-V. Kim, L. H. Diez, J.-P. Adam, K. Garcia, J.-F. Roch, S. Rohart, A. Thiaville, D. Ravelosona, and V. Jacques, "Nanoscale imaging and control of domain-wall hopping with a nitrogen-vacancy center microscope", Science **344**, 1366–1369 (2014) 10.1126/science.1250113.

[272]S Kolkowitz, A Safira, A. A. High, R. C. Devlin, S Choi, Q. P. Unterreithmeier, D Patterson, A. S. Zibrov, V. E. Manucharyan, H Park, and M. D. Lukin, "Probing Johnson noise and ballistic transport in normal metals with a single-spin qubit", Science **347**, 1129–1132 (2015) 10.1126/science.aaa4298.

[273]M Pelliccione, A Jenkins, P Ovartchaiyapong, C Reetz, E Emmanouilidou, N Ni, and A. C. Bleszynski Jayich, "Scanned probe imaging of nanoscale magnetism at cryogenic temperatures with a single-spin quantum sensor", Nat Nanotechnol **11**, 700–705 (2016) 10.1038/nnano.2016.68.

[274]D. A. Hopper, R. R. Grote, A. L. Exarhos, and L. C. Bassett, "Near-Infrared-Assisted Charge Control and Spin Readout of the Nitrogen-Vacancy Center in Diamond", arXiv **241201**, 1–5 (2016) 10.1103/PhysRevB.94.241201.

[275]D. Wildanger, B. R. Patton, H. Schill, L. Marseglia, J. P. Hadden, S. Knauer, A. Schönle, J. G. Rarity, J. L. O'Brien, S. W. Hell, and J. M. Smith, "Solid Immersion Facilitates Fluorescence Microscopy with Nanometer Resolution and Sub-Ångström Emitter Localization", Advanced Materials **24**, OP309–OP313 (2012) 10.1002/adma.201203033.

[276]L. Li, E. H. Chen, J. Zheng, S. L. Mouradian, F. Dolde, T. Schröder, S. Karaveli, M. L. Markham, D. J. Twitchen, and D. Englund, "Efficient Photon Collection from a Nitrogen Vacancy Center in a Circular Bullseye Grating", Nano Letters **15**, 1493–1497 (2015) 10.1021/nl503451j.

[277]M. J. Burek, N. P. de Leon, B. J. Shields, B. J. M. Hausmann, Y. Chu, Q. Quan, A. S. Zibrov, H. Park, M. D. Lukin, and M. Lončar, "Free-Standing Mechanical and Photonic Nanostructures in Single-Crystal Diamond", Nano Letters **12**, 6084–6089 (2012) 10.1021/nl302541e.

[278]G Waldherr, J Beck, M Steiner, P Neumann, A Gali, T. Frauenheim, F Jelezko, and J Wrachtrup, "Dark States of Single Nitrogen-Vacancy Centers in Diamond Unraveled by Single Shot NMR", Physical Review Letters **106**, 157601 (2011) 10.1103/PhysRevLett.106.157601.

[279]J. R. Maze, "Quantum manipulation of nitrogen-vacancy centers in diamond: from basic properties to applications", PhD Thesis, 1–206 (2010).

[280]A. Ajoy, Y. X. Liu, and P. Cappellaro, "DC Magnetometry at the T_2 Limit", 2016.

[281]C Bonato, M. S. Blok, H. T. Dinani, D. W. Berry, M. L. Markham, D. J. Twitchen, and R Hanson, "Optimized quantum sensing with a single electron spin using real-time adaptive measurements", Nat Nanotechnol **11**, 247–252 (2016) 10.1038/nnano.2015.261http://www.nature.com/nnano/journal/v11/n3/abs/nnano.2015.261.html{\#}supplementary-information.

[282]G Davies, "Dynamic Jahn-Teller distortions at trigonal optical centres in diamond", Journal of Physics C: Solid State Physics **12**, 2551–2566 (1979) 10.1088/0022-3719/12/13/019.

[283]E. R. MacQuarrie, T. a. Gosavi, a. M. Moehle, N. R. Jungwirth, S. a. Bhave, and G. D. Fuchs, "Coherent control of a nitrogen-vacancy center spin ensemble with a diamond mechanical resonator", Optica **2**, 233 (2015) 10.1364/OPTICA.2.000233.

[284]P. London, J. Scheuer, J. M. Cai, I. Schwarz, A. Retzker, M. B. Plenio, M. Katagiri, T. Teraji, S. Koizumi, J. Isoya, R. Fischer, L. P. McGuinness, B. Naydenov, and F. Jelezko, "Detecting and polarizing nuclear spins with double resonance on a single electron spin", Physical Review Letters **111**, 1–5 (2013) 10.1103/PhysRevLett.111.067601.

[285]J. C. O. Chubar, P. Elleaume, *Radia software package*, 2017.

[286]A. M. Edmonds, U. F. S. D'Haenens-Johansson, R. J. Cruddace, M. E. Newton, K. M. C. Fu, C. Santori, R. G. Beausoleil, D. J. Twitchen, and M. L. Markham, "Production of oriented nitrogen-vacancy color centers in synthetic diamond", Physical Review B - Condensed Matter and Materials Physics **86**, 1–7 (2012) 10.1103/PhysRevB.86.035201.

[287]R. de Sousa, and S. D. Sarma, "Electron spin coherence in semiconductors: Considerations for a spin-based solid state quantum computer architecture", Physical Review B **67**, 33301 (2003) 10.1103/PhysRevB.67.033301.

[288]W. M. Witzel, K. Young, and S. Das Sarma, "Converting a real quantum spin bath to an effective classical noise acting on a central spin", Physical Review B - Condensed Matter and Materials Physics **90**, 1–6 (2014) 10.1103/PhysRevB.90.115431.

[289]P. Szańkowski, G. Ramon, J. Krzywda, D. Kwiatkowski, and. Cywiński, "Environmental noise spectroscopy with qubits subjected to dynamical decoupling", 1–37 (2017).

[290]J. J.J. J. Sakurai, and J. Napolitano, *Modern quantum mechanics* (Addison-Wesley, 2011), p. 550.